

KAUNAS UNIVERSITY OF TECHNOLOGY

MONICA SUSANA CAMPOS COVARRUBIAS

INFLUENCE OF DOPANTS ON THE  
PROPERTIES OF BARIUM CERATE AND  
BARIUM ZIRCONATE THIN FILMS

Doctoral dissertation  
Natural Sciences, Physics (N 002)

2023, Kaunas

This doctoral dissertation was prepared at Kaunas University of Technology, Faculty of Mathematics and Natural Sciences, Department of Physics during the period of 2018–2022.

The doctoral right has been granted to Kaunas University of Technology together with University of Southern Denmark.

**Scientific Supervisor:**

Prof. Dr. Giedrius LAUKAITIS (Kaunas University of Technology, Natural Sciences, Physics, N 002).

Edited by: English language editor Brigita Brasienė (Publishing House *Technologija*), Lithuanian language editor Rozita Znamenskaitė (Publishing House *Technologija*)

**Dissertation Defense Board of Physics Science Field:**

Prof. Dr. Tomas TAMULEVIČIUS (Kaunas University of Technology, Natural Sciences, Physics, N 002) - **chairperson**;

Prof. Dr. Liutauras MARCINAUSKAS (Kaunas University of Technology, Natural Sciences, Physics, N 002);

Chief Researcher Dr. Šarūnas MEŠKINIS (Kaunas University of Technology, Natural Sciences, Physics, N 002);

Prof. Dr. Yogendra Kumar MISHRA (University of Southern Denmark, Denmark, Natural Sciences, Physics, N 002);

Assoc. Prof. Dr. Tomas ŠALKUS (Vilnius University, Technological Sciences, Materials Engineering, T 008).

The public defense of the dissertation will be held at 10 a.m. on 27 November, 2023 at the public meeting of the Dissertation Defense Board of Physics Science Field in Rectorate Hall at Kaunas University of Technology.

Address: K. Donelaičio 73-402, LT-44249 Kaunas, Lithuania

Phone: (+370) 608 28 527; e-mail doktorantura@ktu.lt

The doctoral dissertation was sent out on 27 October, 2023.

The doctoral dissertation is available on the internet <http://ktu.edu> and at the libraries of Kaunas University of Technology (Gedimino 50, Kaunas, LT-44239, Lithuania) and University of Southern Denmark (Campusvej 55, Odense M, DK-5230, Denmark).

© M.S.C. Covarrubias, 2023

KAUNO TECHNOLOGIJOS UNIVERSITETAS

MONICA SUSANA CAMPOS COVARRUBIAS

LEGIRAVIMO ĮTAKA BARIO CERATO IR  
BARIO CIRKONATO PLONŲ DANGŲ  
SAVYBĖMS

Daktaro disertacija  
Gamtos mokslai, fizika (N 002)

2023, Kaunas

Disertacija rengta 2018–2022 metais Kauno technologijos universiteto Matematikos ir gamtos mokslų fakultete, Fizikos katedroje.

Doktorantūros teisė Kauno technologijos universitetui suteikta kartu su Pietų Danijos universitetu.

**Mokslinis vadovas:**

prof. dr. Giedrius LAUKAITIS (Kauno technologijos universitetas, gamtos mokslai, fizika, N 002).

Redagavo: anglų kalbos redaktorė Brigita Brasienė (leidykla „Technologija“), lietuvių kalbos redaktorė Rozita Znamenskaitė (leidykla „Technologija“)

**Fizikos mokslo krypties disertacijos gynimo taryba:**

prof. dr. Tomas TAMULEVIČIUS (Kauno technologijos universitetas, gamtos mokslai, fizika, N 002) – **pirmininkas**;

prof. dr. Liutauras MARCINAUSKAS (Kauno technologijos universitetas, gamtos mokslai, fizika, N 002);

vyr. m. d. dr. Šarūnas MEŠKINIS (Kauno technologijos universitetas, gamtos mokslai, fizika, N 002);

prof. dr. Yogendra Kumar MISHRA (Pietų Danijos universitetas, Danija, gamtos mokslai, fizika, N 002);

doc. dr. Tomas ŠALKUS (Vilniaus universitetas, technologijos mokslai, medžiagų inžinerija, T 008).

Disertacija bus ginama viešame fizikos mokslo krypties disertacijos gynimo tarybos posėdyje 2023 m. lapkričio 27 d. 10 val. Kauno technologijos universiteto Rektorato salėje.

Adresas: K. Donelaičio g. 73-402, LT-44249 Kaunas, Lietuva

Tel. (+370) 608 28 527; el. paštas [doktorantura@ktu.lt](mailto:doktorantura@ktu.lt)

Disertacija išsiųsta 2023 m. spalio 27 d.

Su disertacija galima susipažinti interneto svetainėje <http://ktu.edu>, Kauno technologijos universiteto (Gedimino g. 50, LT-44239 Kaunas, Lietuva) ir Pietų Danijos universiteto (Campusvej 55, Odense M, DK-5230, Danija) bibliotekose.

© M.S.C. Covarrubias, 2023

## CONTENT

<b>LIST OF FIGURES.....</b>	<b>7</b>
<b>LIST OF TABLES.....</b>	<b>11</b>
<b>LIST OF ABBREVIATIONS AND TERMS .....</b>	<b>14</b>
<b>1. INTRODUCTION.....</b>	<b>18</b>
<b>2. LITERATURE OVERVIEW .....</b>	<b>26</b>
2.1. Description of the perovskite structure .....	26
2.2. Proton conduction explanation by Grotthuss mechanism .....	27
2.3. Barium cerates.....	36
2.3.1. Lattice parameters and phases of undoped and doped barium cerates .....	36
2.3.2. Grain size of undoped and doped barium cerates.....	37
2.3.3. Crystal size of undoped and doped BaCeO <sub>3</sub> .....	39
2.3.4. Density of undoped and doped BaCeO <sub>3</sub> .....	41
2.4. Barium zirconates.....	43
2.4.1. Lattice parameters of undoped BaZrO <sub>3</sub> and doped BaZrO <sub>3</sub> .....	43
2.4.2. Grain size of undoped BaZrO <sub>3</sub> and doped BaZrO <sub>3</sub> .....	44
2.5. Microstructure of barium cerate and barium zirconates thin films formed by PVD.....	46
2.5.1. Formation of thin films of barium cerates and barium zirconates.....	46
2.6. Degradation of barium cerates and barium zirconates .....	57
2.7. Summary of the literature review .....	59
<b>3. EXPERIMENTAL TECHNIQUE AND METHODS.....</b>	<b>60</b>
3.1. Sample preparation .....	60
3.2. Profilometer .....	62
3.3. X-ray diffraction (XRD).....	63
3.4. Scanning electron microscopy (SEM) .....	65
3.5. Energy dispersive X-ray spectroscopy (EDS) .....	66
3.6. Electrochemical impedance spectroscopy (EIS) .....	66
3.7. Nanoindentation .....	71
<b>4. RESULTS AND DISCUSSION .....</b>	<b>72</b>
4.1. Barium cerates thin films formed at low temperatures (<400 °C).....	72
4.1.1. Elemental composition of the formed barium cerate thin films.....	72
4.1.2. Crystal structure of the formed barium cerate thin films .....	73
4.1.3. Microstructure of the formed barium cerate thin films.....	77
4.1.4. Nano-indentation analysis of the formed barium cerate thin films .....	81
4.1.5. Electrical properties of the formed barium cerate thin films.....	82
4.2. Barium cerates thin films formed at intermediate temperatures (500–700 °C).....	85
4.2.1. Crystal structure of the formed barium cerate thin films .....	86
4.2.2. Microstructure of the formed barium cerate thin films.....	90
4.2.3. Electrical properties of the formed barium cerate thin films .....	94

4.3.	Formation and investigation of barium cerate doped yttrium.....	99
4.3.1.	Elemental composition of the formed BCY thin films .....	99
4.3.2.	Crystal structure of the formed BCY thin films.....	100
4.3.3.	Microstructure of the formed BCY thin films .....	104
4.3.4.	Electrical properties of the formed BCY thin films .....	109
4.4.	Formation and investigation of barium zirconate thin films .....	111
4.4.1.	Elemental composition of the formed barium zirconate thin films .....	111
4.4.2.	Crystal structure of the formed barium zirconate thin films.....	111
4.4.3.	Microstructure of the formed barium zirconate thin films .....	115
<b>5.</b>	<b>CONCLUSIONS .....</b>	<b>122</b>
<b>6.</b>	<b>SUMMARY .....</b>	<b>125</b>
<b>7.</b>	<b>REFERENCES.....</b>	<b>155</b>
<b>8.</b>	<b>CURRICULUM VITAE.....</b>	<b>171</b>
<b>9.</b>	<b>LIST OF PUBLICATIONS AND SCIENTIFIC CONFERENCES .....</b>	<b>172</b>
<b>10.</b>	<b>ACKNOWLEDGEMENTS.....</b>	<b>174</b>

## LIST OF FIGURES

<b>Fig. 1.</b> Schematic representation of a) hydrogen energy fuel cell and b) hydrogen separator cell [19] .....	19
<b>Fig. 2.</b> Schematic representation of the proton conduction mechanism to the synthesis of ammonia [25] and the reactions occurring at the interface with the electrodes ....	20
<b>Fig. 3.</b> Graph that shows the effect of yttrium dopant concentration on (o) barium zirconate and ( $\Delta$ ) for barium cerates supported ruthenium catalysts [26] .....	20
<b>Fig. 4.</b> Schematic representation of proton mechanism for Syngas production [32]	21
<b>Fig. 5.</b> Perovskites structure with orthorhombic phase for $\text{BaCeO}_3$ at 25 °C .....	26
<b>Fig. 6.</b> Grotthuss mechanism for intra-octahedral diffusion of the proton on oxygen lattice .....	28
<b>Fig. 7.</b> Proton hopping at the oxygen site on the octahedron in the perovskite: a) hydrogen tunnelling movement at low temperatures, b) intra-octahedron and c) inter-octahedron at the oxygen sites (1), (2) and (3); the potential energy barriers are lower for b) and c) jumps, and a) proton hopping contains a higher potential barrier at high temperatures [52].....	29
<b>Fig. 8.</b> Comparison of conductivities at low operating temperature for the main fast ion conductors: BCY [57, 58], BZCYYb [59], BZY, $\text{TiO}_2$ and YSZ [36].....	31
<b>Fig. 9.</b> Factors influencing grain size (a) ionic radii for doped barium cerate (BCO) [91, 100], (b) concentration of sintering aid of BCY20-Ni [102] , BCG-Co [101], BCG-Co/Ni/Zn [103], (c) sintering time (1600 °C) [104] .....	38
<b>Fig. 10.</b> (a) Dependence of BCY10 grain size on the sintering times and its effect on the relative density; (b) SEM images show the microstructure at four sintering times: 1 h (1 b), 6 h (2 b), 10 h (3 b) and 24 h (4 b) [104] .....	39
<b>Fig. 11.</b> Effect of different process and sintering temperatures on the crystal size for BCO, BCY and BCG: conventional precipitation method (CPM) [103], spray pyrolysis [108], high energy ball milling (HEBM) [109], synthesis by nitrates [110], sol-gel [111], hydrothermal synthesis [112], solid-state reaction (SSR) [111, 113], reverse micelle [114] and hydrogelation of acrylates [114] .....	40
<b>Fig. 12.</b> Different sintering metal aids (0.01) vs. density (%) [103, 116] for $\text{BaCe}_{0.9-x}\text{Gd}_{0.1}\text{O}_{3-\delta}$ formed by SSR and ultrasonic assisted precipitation .....	41
<b>Fig. 13.</b> Effect of % of sintering aid in the relative density for BCO, BCY and BCG [90, 102, 103, 120, 121] .....	42
<b>Fig. 14.</b> Effect of temperature on the density by different synthesis strategies without the use of aid sintering: BCG – ultrasonic assisted [103], BCY10 – hydrogelation of acrylates [114], BCY – SSRS [102], BCO and BCY10 – freeze dried [124], BCY20 – ball milling (BCNd) [125], BCG – conventional precipitation [126].....	43
<b>Fig. 15.</b> (a) Different dopants vs. lattice parameters [127] and (b) dopant concentration vs. lattice parameter [73, 130, 131, 132], (c) sintering aids concentration that modifies the lattice parameters [133] and (d) dopants under wet and dry conditions that influence the lattice parameters [134] .....	44
<b>Fig. 16.</b> SEM micrographs of BZO-doped sintered at 1600 °C for 8 h [135] .....	44
<b>Fig. 17.</b> (a) Grain size vs. dopant concentration [73, 132, 135, 136, 137, 138] and (b) barium deficiency vs. grain size .....	45

<b>Fig. 18.</b> Relative density of doped barium zirconate at different ionic radii [135] ...	46
<b>Fig. 19.</b> Schematic representation of the arriving of adatoms to the substrate and their diffusion process.....	47
<b>Fig. 20.</b> Growth modes at different interfacial energies.....	48
<b>Fig. 21.</b> Thornton zone diagram at different temperatures and ion energies for films formed by the physical vapor deposition [142].....	49
<b>Fig. 22.</b> BZY formed on MgO and Al <sub>2</sub> O <sub>3</sub> [40].....	50
<b>Fig. 23.</b> SEM image of BZY with Zone 2 formed on MgO [151].....	51
<b>Fig. 24.</b> Cross-section view of BZY, BCY/BZY/BCY textured layers formed on Si <sub>3</sub> N <sub>4</sub> substrates [152].....	51
<b>Fig. 25.</b> BaZr <sub>0.2</sub> Ce <sub>0.7</sub> Y <sub>0.1</sub> O <sub>3-d</sub> film formed by e-beam evaporation deposition method on LSGM-BZCY layer as deposited (a) and after annealing (b) [41].....	52
<b>Fig. 26.</b> (a) Single layer (2S) electrolyte BaCe <sub>0.5</sub> Zr <sub>0.35</sub> Y <sub>0.15</sub> O <sub>3-δ</sub> and b) gradient (2G)Ni-BaCe <sub>0.5</sub> Zr <sub>0.35</sub> Y <sub>0.15</sub> O <sub>3-δ</sub> – BaCe <sub>0.5</sub> Zr <sub>0.35</sub> Y <sub>0.15</sub> O <sub>3-δ</sub> [153].....	52
<b>Fig. 27.</b> Schematic representation of the mixture of hetero-epitaxial (layer by layer growth) and polycrystalline on BZY formed by PLD at 600–900 °C.....	57
<b>Fig. 28.</b> Schematic representation of degradation morphology for barium zirconate doped yttrium [176].....	58
<b>Fig. 29.</b> Schematic representation of e-beam evaporation deposition method and e-beam interaction with the evaporated target gas [179].....	61
<b>Fig. 30.</b> Schematic representation of vapor source speed that is modified with collision regions; $u$ is hydrodynamic flow velocity, thermal velocity is $vt$ , and final speed is $v = u + vt$ [180].....	62
<b>Fig. 31.</b> Schematic representation of the electrons emitted at different energies [191].....	66
<b>Fig. 32.</b> Schematic representation of bulk and grain boundary polarization (resistance) contribution in the electrochemical impedance spectroscopy (EIS) (1), and on the right, the Nyquist diagram (2), ideal (a) and real (b) spectra with their equivalent circuits, (3) resistance (R) and constant phase element (CPE) [194].....	67
<b>Fig. 33.</b> Schematic representation of the output signal for AC voltage after its conversion to the exponential function by Euler equation [196].....	69
<b>Fig. 34.</b> Schematic representation of Nyquist and Bode plot [195].....	70
<b>Fig. 35.</b> Effect of deposition rate on Ba excess (Ce/Ba).....	73
<b>Fig. 36.</b> BaCeO <sub>3</sub> formed at 25 °C, 100 °C, 250 °C and 400 °C at 2 Å/s on Inconel 600 substrate [A1].....	74
<b>Fig. 37.</b> Schematic representation of the deposition rate on the crystallization of the film at three different support interactions: I) non bonded with support, II) bonded with support, III) high bonding with support.....	75
<b>Fig. 38.</b> BaCeO <sub>3</sub> formed at 400 °C at 2 Å/s, 4 Å/s, 8 Å/s and 12 Å/s formed on Inconel 600 [A1].....	75
<b>Fig. 39.</b> Crystalline evolution of BCO at different substrates SST, Inconel 600 GSA and Invar formed at 12 Å/s and 400 °C.....	76
<b>Fig. 40.</b> SEM images of BCO formed at I) 2 Å/s and II) 12 Å/s.....	77
<b>Fig. 41.</b> SEM image for BCO formed on (a) Stainless steel A301 (SST), (b) Glass sealing alloy (GSA), (c) Inconel 600 and (d) Invar from 25 °C to 400 °C and from 2 to	

12 Å/s [A1] .....	80
<b>Fig. 42.</b> High magnification SEM images of BCO formed at 12 Å/s and 400 °C on (a) SST, (b) Invar, (c) Inconel 600 and (d) GSA .....	80
<b>Fig. 43.</b> Load-displacement curves of the nanoindentation test obtained by Berkovich indenter; the elastic part of the BCO film (thickness 1 µm) before the break presented for (a) Stainless steel A301 (SST), (b) Glass sealing alloy (GSA), Inconel 600 (Inconel) and Invar [A1] to evaluate the residual stress .....	81
<b>Fig. 44.</b> I) The linear dependency between the load (mN) representing the residual stress and the thermal expansion coefficient ( $\alpha_s$ ), II) the dependency between the load and the compression and relaxation on the unit cell.....	82
<b>Fig. 45.</b> Ion conductivity on wet (0.02 atm H <sub>2</sub> O/Ar) for BaCeO <sub>3</sub> formed on Inconel, Invar, GSA and SST .....	83
<b>Fig. 46.</b> Nyquist plot for BCO formed on Stainless steel, Glass sealing alloy and fitting curves [A1] .....	84
<b>Fig. 47.</b> XRD diffractogram of BaCeO <sub>3</sub> surface with (a) $\omega = 0$ and (b) $\omega = 1^\circ$ grazing incident scan after EIS experiments and exposure to air [A1] .....	85
<b>Fig. 48.</b> XRD diffraction of BCO at 500 °C, 600 °C and 700 °C formed on Inconel 600 .....	86
<b>Fig. 49.</b> XRD diffractogram for highly oriented BCO formed at 600 °C and 700 °C on MgO (001) (a), YSZ (001) (b) and Al <sub>2</sub> O <sub>3</sub> (0001) (c).....	87
<b>Fig. 50.</b> Effect of support and its temperature on the unit cell volume of BCO formed on MgO (001), Al <sub>2</sub> O <sub>3</sub> (001) and YSZ (001) .....	89
<b>Fig. 51.</b> XRD diffraction of BaCeO <sub>3</sub> as deposited and after 1 week and 3 months; there is no presence of BaCO <sub>3</sub> or other phases.....	90
<b>Fig. 52.</b> Effect of substrate temperature on grain growth size in Zone 2 towards the formation of different microstructures on x and y directions at (1) 500 °C, (2) 600 °C, (3) 610 °C and (4) 700 °C substrate temperature [A4].....	91
<b>Fig. 53.</b> SEM images of BaCeO <sub>3</sub> formed at 500 °C (a, b), 600 °C (c, d) and 700 °C (e, f) on Inconel .....	92
<b>Fig. 54.</b> SEM images of BaCeO <sub>3</sub> thin films formed on MgO (001) at 600 °C (Ia, Ib) and 700 °C (IIa, Iib), Al <sub>2</sub> O <sub>3</sub> (1000) at 600 °C (Ic, Id) and 700 °C (Iic, Iid), YSZ (001) at 600 °C (Ie, If) and 700 °C (Iie, Iif) and deposited at 2 Å/s .....	93
<b>Fig. 55.</b> Grain size lateral growth (x-direction) vs. temperature for BCO formed on Inconel, Al <sub>2</sub> O <sub>3</sub> , MgO and YSZ at 700 °C .....	94
<b>Fig. 56.</b> Ion conductivity for BCO formed at 500 °C, 600 °C and 700 °C on Inconel 600 at 0.02 atm H <sub>2</sub> O/N <sub>2</sub> [A4] .....	94
<b>Fig. 57.</b> Humidity effect on the ionic conductivity of BaCeO <sub>3</sub> [A4].....	96
<b>Fig. 58.</b> Nyquist plot for BaCeO <sub>3</sub> deposited on Inconel at 700 °C tested at 300 °C (main plot) and cooling (inset plot) in wet nitrogen [A4] .....	97
<b>Fig. 59.</b> Ion conductivity (0.02 atm H <sub>2</sub> O/N <sub>2</sub> ) of BCO formed on YSZ, MgO and Al <sub>2</sub> O <sub>3</sub> at 2 Å/s and 600 °C [A4] .....	98
<b>Fig. 60.</b> XRD spectra of BCY10 (a) and BCY20 (b) at 500 °C [A3], 600 °C and 700 °C .....	101
<b>Fig. 61.</b> Unit cell volume variation with temperature for BCY10 and BCY20 thin films .....	102

<b>Fig. 62.</b> Dependency of crystal size on temperature between BCY10 and BCY20	102
<b>Fig. 63.</b> Schematic representation of temperature on nucleation and growth on the microstructure of BCO columns as an effect of relaxation at 500 °C and 600 °C ...	105
<b>Fig. 64.</b> Cross-section of BCY10 formed at (a) 500 °C [A3] a) and (b) 600 °C, BCY20 formed at (c) 500 °C [A3] and (d) 600 °C.....	105
<b>Fig. 65.</b> SEM image of surface morphology of BCY10 formed on Inconel 600 at 500 °C (Ia, Ib) [A3], 600 °C (Ic, Id), 700 °C (Ie, If), BCY20 at 500 °C (IIa, IIb) [A3], 600 °C (IIc, IId), 700 °C (IIe, IIf).....	106
<b>Fig. 66.</b> SEM image at two magnifications of BCY10 at 600 °C in MgO (Ia, Ib), Al <sub>2</sub> O <sub>3</sub> (Ic, Id), YSZ (Ie, If) and 700 °C (e, h), BCY10 at 700 °C in MgO (IIa, IIb), Al <sub>2</sub> O <sub>3</sub> (IIc, IId), YSZ (IIe, IIf) and 700 °C (IIe, IIh) .....	107
<b>Fig. 67.</b> SEM image at two magnifications of BCY20 at 600 °C in MgO (Ia, b), Al <sub>2</sub> O <sub>3</sub> (Ic, Id), YSZ (Ie, If) and 700 °C (e, h), BCY20 at 700 °C in MgO (IIa, IIb), Al <sub>2</sub> O <sub>3</sub> (IIc, IId), YSZ (IIe, IIf) and YSZ (IIe, IIh).....	108
<b>Fig. 68.</b> Ionic conductivity on heating and cooling for BaCe <sub>0.9</sub> Y <sub>0.1</sub> O <sub>3</sub> formed at 600 °C and 700 °C on Inconel 600, measured in the range between 200 °C and 400 °C in Wet N <sub>2</sub> [A4].....	110
<b>Fig. 69.</b> XRD diffractogram of BZO, BZY20 and BZCY thin films formed at 500 °C, 600 °C and 700 °C on Inconel 600.....	112
<b>Fig. 70.</b> Unit cell volume vs. substrate temperature for BZO, BZY20 and BZCY thin films formed at 500 °C, 600 °C and 700 °C; the lines are for eye guidance.....	113
<b>Fig. 71.</b> Cross-section of the SEM image of BZO 500 °C (a) [A3] (a) and 600 °C (b), BZY20 500 °C [A3] (c) and 600 °C (d), BZCY 500 °C [A3] (e) and 600 °C (f) formed on Inconel 600 at Å/s, (g) picture of BZY20 formed at 600 °C stable at room conditions .....	116
<b>Fig. 72.</b> SEM image of (I) BZO formed on Inconel 600 at 500 °C [A3] (a, b), 600 °C (c, d) and 700 °C (e, f), (II) BZY20 at 500 °C [A3] (a, b), 600 °C (c, d) and 700 °C (e, f) and (III) BZCY at 500 °C [A3] (a, b), 600 °C (c, d) and 700 °C (e, f) .....	118
<b>Fig. 73.</b> SEM image of BZO formed on MgO (Ia, Ib), Al <sub>2</sub> O <sub>3</sub> (Ic, Id), YSZ (Ie, If) at 600 °C and MgO (IIa, IIb), Al <sub>2</sub> O <sub>3</sub> (IIc, IId), YSZ (IIe, IIf) 700 °C (e-h) at two different magnifications .....	119
<b>Fig. 74.</b> SEM image of BZY20 formed on MgO (Ia, Ib), Al <sub>2</sub> O <sub>3</sub> (Ic, Id), YSZ (Ie, If) at 600 °C and MgO (IIa, IIb), Al <sub>2</sub> O <sub>3</sub> (IIc, IId), YSZ (IIe, IIf) 700 °C (e-h) at two different magnifications .....	120
<b>Fig. 75.</b> SEM image of BZCY formed on MgO (Ia, Ib), Al <sub>2</sub> O <sub>3</sub> (Ic, Id), YSZ (Ie, If) at 600 °C and MgO (IIa, IIb), Al <sub>2</sub> O <sub>3</sub> (IIc, IId), YSZ (IIe, IIf) 700 °C (e-h) at two different magnifications .....	121

## LIST OF TABLES

<b>Table 1.</b> Example of barium cerates and barium zirconates for H <sub>2</sub> purification .....	19
<b>Table 2.</b> Examples of electrolytes are barium cerate and barium zirconate based used in the formation of ethylene.....	21
<b>Table 3.</b> Ionic conductivity $\sigma$ for doped and undoped barium cerates .....	32
<b>Table 4.</b> Ionic conductivity of barium zirconates and their doped compositions .....	32
<b>Table 5.</b> Ionic conductivity of barium cerate perovskites and their doped compositions .....	33
<b>Table 6.</b> Activation energies $E_a$ values for doped barium cerates .....	34
<b>Table 7.</b> Activation energies $E_a$ values for doped barium zirconates .....	35
<b>Table 8.</b> Activation energies $E_a$ values for doped barium zirconates cerates .....	35
<b>Table 9.</b> Phase transitions for BaCeO <sub>3</sub> at different temperatures and assets methods .....	36
<b>Table 10.</b> Influences of the dopant concentration on the phase variation for barium cerate doped yttrium .....	37
<b>Table 11.</b> Lattice parameters and cell volume variations for different dopants in polycrystalline samples [91] .....	37
<b>Table 12.</b> Formation parameters of different barium cerates thin films deposited using magnetron sputtering.....	54
<b>Table 13.</b> Formation parameters of barium zirconates thin films deposited using magnetron sputtering.....	54
<b>Table 14.</b> Formation parameters of barium cerates thin films deposited using PLD .....	55
<b>Table 15.</b> Formation parameters of barium zirconates thin films deposited using PLD .....	55
<b>Table 16.</b> Crystalline planes obtained by XRD for BZY thin films on different substrates.....	56
<b>Table 17.</b> Lattice parameter variation for BZY20 on different oriented support [131].....	57
<b>Table 18.</b> Thermal expansion coefficients (TEC) and chemical composition for Invar, Glass sealing alloy (GSA), Inconel 600 and Stainless steel A302 .....	60
<b>Table 19.</b> Technical parameters.....	63
<b>Table 20.</b> Impedance for the equivalent circuits elements .....	69
<b>Table 21.</b> Capacitance values and a plausible interpretation [197] .....	70
<b>Table 22.</b> Atomic concentration of BCO thin films formed at 25 °C and 400 °C.....	72
<b>Table 23.</b> Lattice parameter for BCO thin film (thickness: 1 $\mu\text{m}$ ) formed on different substrates by e-beam evaporation deposition method at 400 °C formed at 12 Å/s [A1].....	76

<b>Table 24.</b> Grain size of BaCeO <sub>3</sub> formed at 12 Å/s at 400 °C .....	81
<b>Table 25.</b> Electrical and mechanical properties of BaCeO <sub>3</sub> formed in metallic supports [A1] .....	84
<b>Table 26.</b> Crystalline properties of BaCeO <sub>3</sub> [A4] .....	88
<b>Table 27.</b> Texture coefficients of the thin films deposited on Inconel 600, YSZ (001), MgO (001), Al <sub>2</sub> O <sub>3</sub> (0001) compared to Pnma reference structure diffractogram (01-078-4102) [A4].....	89
<b>Table 28.</b> Microstructure properties of BaCeO <sub>3</sub> obtained by SEM image [A4] .....	91
<b>Table 29.</b> Conductivity, activation energies and relaxation temperatures in BaCeO <sub>3</sub> formed at 500 °C, 600 °C and 700 °C .....	95
<b>Table 30.</b> Conductivity, activation energies and relaxation temperatures of BaCeO <sub>3</sub> formed at 600 °C under wet and dry atmospheres .....	96
<b>Table 31.</b> Conductivity, activation energy and relaxation temperature of BaCeO <sub>3</sub> formed at 600 °C .....	99
<b>Table 32.</b> Atomic % of BCY10 and BCY20 film formed at 500 °C and 600 °C on Inconel 600 obtained by EDX analysis and on the right columns, the non stoichiometry obtained from atomic % between Ba and Ce and Y .....	100
<b>Table 33.</b> Lattice parameters for BaCe <sub>0.9</sub> Y <sub>0.1</sub> O <sub>3-δ</sub> with Pbnm phase and BaCe <sub>0.8</sub> Y <sub>0.2</sub> O <sub>3-δ</sub> with Pm3m phase formed at 500 ° [A3], 600 °C and 700 °C on Inconel 600.....	103
<b>Table 34.</b> Texture coefficients of formed BCY10 compared with reference diffractogram of Pbnm 01-083-5709 and BCY20 thin films compared with the reference diffractogram of Pm3m 01-084-7856 .....	104
<b>Table 35.</b> Grain size BCY10 and BCY20 film formed on Inconel 600 at 2 Å/s .....	106
<b>Table 36.</b> BCY10 grain size at 600 °C and 700 °C on YSZ, Al <sub>2</sub> O <sub>3</sub> and MgO .....	109
<b>Table 37.</b> BCY20 grain size at 600 °C and 700 °C on YSZ, Al <sub>2</sub> O <sub>3</sub> and MgO .....	109
<b>Table 38.</b> Conductivity, activation energy in the dry and wet atmosphere and relaxation temperature in BCY10 formed at 600 °C .....	110
<b>Table 39.</b> Elemental composition of barium zirconate thin films formed at 500 °C and 600 °C substrate temperatures from EDX and ratio of Ba between Zr, Y and Ce to determine Ba excess in the thin film.....	111
<b>Table 40.</b> Texture coefficient for BZO compared with the reference diffractogram of Pm3m 04-012-3448, BZY20 compared with the reference diffractogram of Pm3m of 04-015-2511 and BZCY Pm3m of 04-021-6507 formed at 2Å/s on Inconel 600 at three different temperatures: 500 °C [A3], 600 °C and 700 °C; the main orientation is marked in bold.....	113
<b>Table 41.</b> Lattice parameter and crystal size for BZO, BZY20 and BZCY	

initial powder and formed on Inconel 600 at three different temperatures: 500 °C [A3], 600 °C and 700 °C.....	115
<b>Table 42.</b> Grain size of BZO, BZY20 and BZCY formed at 500 °C, 600 °C and 700 °C on Inconel 600 at 2 Å/s .....	119
<b>Table 43.</b> Grain size for BZO, BZY20 and BZCY formed on YSZ, Al <sub>2</sub> O <sub>3</sub> and MgO at 600 °C and 2Å/s .....	121

## LIST OF ABBREVIATIONS AND TERMS

### Abbreviations

- $\sigma_H^+$  – proton conduction  
AC – alternating current  
AHM – argon hydrogen mixture  
Atm. – atmosphere  
BCO – barium cerate  
BCY10 – barium cerate doped yttrium 10% ( $\text{BaCe}_{0.9}\text{Y}_{0.1}\text{O}_{3-\delta}$ )  
BCY20 – barium cerate doped yttrium 20% ( $\text{BaCe}_{0.8}\text{Y}_{0.2}\text{O}_{3-\delta}$ )  
BZCY – barium zirconate cerate doped yttrium ( $\text{BaZr}_{0.7}\text{Ce}_{0.2}\text{Y}_{0.1}\text{O}_{3-\delta}$ )  
BZO – barium zirconate ( $\text{BaZrO}_{3-\delta}$ )  
BZY20 – barium zirconate doped yttrium 20% ( $\text{BaZr}_{0.8}\text{Y}_{0.2}\text{O}_{3-\delta}$ )  
CPE – constant phase  
 $d$  – grain size  
D – the interplanar spacing  
DSC – differential scanning calorimetry  
E-beam – electron beam  
EDS – energy dispersive X-spectroscopy  
EIS – electrochemical impedance spectroscopy  
eV – electron volts  
 $F$  – Faraday constant  
GOF – goodness-of-fit  
GSA – glass sealing alloy  
J – joules  
 $K_B$  – Boltzmann constant  
 $K_w$  – water equilibrium constant  
L – inductance  
 $L$  – length  
N – newtons  
 $N_A$  – Avogadro number  
nm – nanometer  
Pa – pascals  
PLD – pulsed laser deposition  
 $PO_2$  – oxygen pressure  
PT – proton transfer  
PVD – physical vapor deposition  
 $R$  – resistance  
 $R$  – universal gas constant  
RE – rare earth  
RF – radio frequency  
 $R_{wp}$  – Bragg error  
S/cm – siemens per centimetre  
SEM – scanning electron microscopy  
SST – stainless steel

$T$  – temperature  
TC – texture coefficient  
 $T_{cr}$  – critical temperature  
TEC – thermal expansion coefficient  
 $Z$  – impedance  
 $\Omega$  – quantum tunneling frequency  
 $\theta$  – scattering angle  
 $\lambda$  – wavelength

### Terms

High operation temperature – between 650 °C and 1000 °C.

High sintering temperature – above 900 °C.

Ionic conductivity – the electric conductivity created by the transport of ions in an electrolyte.

Low operation temperature – temperature below 650 °C [1].

Low sintering temperature – temperature below 900 °C [2].

Proton conduction – the ionic conduction under wet atmosphere minus the ionic conductivity under dry atmosphere.

Relative density – (density of the film/theoretical density) \* 100. A 100% density means that the theoretical density calculated from modelling from date base (TOPAS 4.1) matches with the experimental values, and the porosity is not present.

Residual stress – stress generated by the growth process of the thin film.

Thin films – a two-dimensional material layer of solid-state material deposited on a substrate from a few nanometers to a few micrometers.

$$\sigma_H^+ = \sigma(H_2O) - \sigma(dry) \quad (1)$$

## SUMMARY

Barium cerate and barium zirconate-based materials are well known for their ionic conductivity properties at temperatures between 200 and 1000 °C. The properties of these materials vary from random-oriented crystal to highly oriented heteroepitaxial films. The orientation forms surfaces with different textures. Textured structure is a result of the residual stress in the film that affects the surface. The residual stress as well affects the entire film that results on the hetero-epitaxial ultra-thin films, offering an advantage to obtain a detailed study of the surface and interfaces: they exhibit a bending or formation of cracks in the entire film effect due to the mismatch or poor mechanical properties. Textured thin films and the stress in the formed structures influence their chemical stability and catalytic, mechanical and electronic properties. There are two main issues for the production of microsystems on metal supports, i.e., processing cost and scalability [3]. Moreover, the use of metal-supported fuel cell causes another problem, which is the degradation of the metal and the migration of atoms, such as Ni, which decomposes the crystal at high sintering temperatures [4]. High sintering temperatures are necessary to obtain a high percentage of crystallinity, high-density and thin films with large grain size. Physical vapor deposition (PVD) techniques have the advantage of forming dense, crystalline films at low forming temperatures. A variation in the deposition parameters controls the microstructure and properties of the formed thin film. In this work, there were investigated the formation of barium cerate ( $\text{BaCeO}_{3-\delta}$ , BCO) and their doped composition with variation in the atomic concentration as barium cerate doped yttrium 10% ( $\text{BaCe}_{0.9}\text{Y}_{0.1}\text{O}_{3-\delta}$ , BCY10), barium cerate doped yttrium 20% ( $\text{BaCe}_{0.8}\text{Y}_{0.2}\text{O}_{3-\delta}$ , BCY20), barium zirconate ( $\text{BaZrO}_{3-\delta}$ , BZO) and their doped composition with variation in the atomic concentration as barium zirconate doped yttrium 20% ( $\text{BaZr}_{0.8}\text{Y}_{0.2}\text{O}_{3-\delta}$ , BZY) and barium zirconate 10% yttrium with 10% Ceria ( $\text{BaZr}_{0.8}\text{Ce}_{0.1}\text{Y}_{0.1}\text{O}_{3-\delta}$ , BZCY) thin films, formed using the e-beam evaporation method. The influence of the microstructure of the formed thin films on ionic conductivity, chemical and mechanical stability was investigated. The e-beam evaporation process of barium cerates and barium zirconates demonstrated the formation of textured thin films. The microstructure of the formed thin films is influenced by the kinetic energy of the arriving particles gained from the evaporation process [5, 6], substrate temperature and the relaxation processes. The dopant concentration as well influences the microstructure and residual stress of the formed thin films. The Thornton diagram clearly describes the dependence of technological parameters on the microstructure [7]. The microstructure is classified into different zones (Zone 1, Zone T, Zone 2 and Zone 3). Zone 1 is characterized by a porous and fibrous amorphous phase structure in the cross-section due to the diffusion limited movements of adatoms. The increase of the substrate temperature enhances the diffusion of adatoms filling the voids and forming the Zone T, but the amorphous phases are still present in the thin films. By further increasing the temperature, in Zone 2, the diffusion of the adatom is further enhanced resulting in the formation of broad highly crystalline phases columns. At the higher temperatures, in Zone 3, the bulk and boundary diffusions participate by forming near-equiaxed and highly crystalline

structures [8, 9]. Barium cerate thin films with columnar growth (Zone T) and highly dense structure with the smallest grain sizes were obtained when the support temperature was below 400 °C. Although the support temperature is higher than 500 °C, thin films exhibit columnar growth (Zone 2) with improved grain sizes compared to the Zone T. Ionic conductivity varies due to the change in microstructure. The barium cerate (BCO) thin film formed on Al<sub>2</sub>O<sub>3</sub> (0001), YSZ (001) and MgO (001) supports corresponds to Zone 2. It demonstrates the influence of residual stress on the ionic conductivity. The highest ionic conductivity in BCO thin films (~0.1 S/cm, 400 °C) was obtained when the thin films were formed on YSZ support at 600 °C formation temperature. YSZ support induces oxygen vacancy formation in BaCeO<sub>3</sub> and then enhances the ionic conductivity. Furthermore, barium zirconates thin films were highly unstable when the formation temperatures were below 400 °C. Then, they exhibit stability when support temperature is higher than 500 °C. Summarising, it was shown how the microstructure and ion conductivity of the formed barium cerates and barium zirconates thin films are influenced by the deposition parameters (deposition rate and substrate temperature) and lattice mismatch between the thin films and supports, which have different thermal and ionic conductivities.

## 1. INTRODUCTION

Thin films are gaining attention as potential fuel cell membranes due to their ability to lower the operating temperatures, reduce internal resistance and increase conductivity. Proton-conducting oxides, such as barium cerates ( $\text{BaCeO}_3$ ), barium zirconates ( $\text{BaZrO}_3$ ) and strontium cerates ( $\text{SrCeO}_3$ ), are studied as electrolytes. Alkaline cerates ( $\text{ACeO}_3$ ) and zirconates ( $\text{AZrO}_3$ ) exhibit protonic conductivity in perovskite oxides ( $A = \text{Ca}, \text{Sr}, \text{or Ba}$ ). Rare earth elements, e.g., Yb, Gd, Nd and Y, are common dopants in barium/strontium cerates due to their similar ionic radii to cerium/zirconium. Cerates have shown good protonic conductivity but react in acidic environments to form carbonates in the presence of  $\text{CO}_2$  and  $\text{H}_2\text{O}$ . Zirconates are chemically stable, possess better mechanical properties, resist acidic conditions, are stable in  $\text{CO}_2$ , but have lower proton conductivity. Balancing high protonic conductivity and stability involves adjusting parameters and dopant concentrations. Proton conductivity and properties depend on dopants, concentration, and thin film methods that influence structural composition, microstructure, and proton diffusion factors, such as density and grain size. When analysing formation methods and parameters, it is crucial to achieve dense, crystalline films with predictable microstructure. Dopants and concentrations impact chemical stability, phase, lattice parameters, grain size and material strains. Low crystallinity adds ion conductivity resistance, emphasizing the need for highly dense electrolytes with strong crystallinity [A3].

Barium cerates and barium zirconates are the most studied perovskite structures, in which different dopants readily accommodate. The change in their composition results in a variation of the chemical, electronic and mechanical properties. The composition and stoichiometry as well influence the chemical and mechanical stability, as in the case of their degradation in different atmospheres. Barium cerate has the highest proton conductivity at temperatures above  $800\text{ }^\circ\text{C}$ . The main reason is the stability and smaller lattice parameters of its cubic phase. Below  $800\text{ }^\circ\text{C}$ , the degradation of materials is observed with an orthorhombic phase reducing the ionic conductivity properties. Then, barium zirconates with cubic phase are a better choice for working at lower temperatures. One of its disadvantages is the difficulty to obtain single phase and large grains that improve ionic conductivity values. Ionic conductivity is an important property for the main application of both materials as electrolytes in fuel cells and electrolyzers.

The aim of reducing the consumption of fossil fuels in recent years makes fuel cells and electrolyzers an alternative to produce  $\text{CO}_2$ -free energy. Proton conductive fuel cell electrolyzers offer a variety of environmentally friendly energy generation applications, such as energy generation (stationary or mobile), energy storage [10] for solar cells, alternative to solar cells, sensors, bioelectricity, and in the chemical industry for hydrogen [11–16], ethylene [17] and ammonia production. Proton conductive fuel cells and electrolyzers have recently gained attention as efficient systems compared to the oxygen ion cells. In proton conduction electrochemical cells, each application has different requirements for increasing fuel cell efficiency.

Compared to different hydrocarbon fuels, hydrogen has the highest energy density of all of them, i.e.,  $143 \text{ MJ kg}^{-1}$  [18]. Nowadays, hydrogen is a valuable molecule for high-efficiency power generation. The main requirements for power generation by hydrogen fuel cells (Fig. 1) is a high degree of proton conduction on the materials, stability under a wide range of oxygen pressures [19] and low ohmic resistance. The ohmic resistance represents the ionic resistance of the electrolyte and the electronic resistance on the electrodes. Another application is hydrogen purification. Hydrogen purification is as well necessary to prevent it from losing its efficiency as a fuel. Table 1 shows two main examples of the composition of barium cerates for their application as electrolytes in  $\text{H}_2$  separation (Table 1).

**Table 1.** Example of barium cerates and barium zirconates for  $\text{H}_2$  purification

	$\text{H}_2$ flux $\text{ml} \cdot \text{cm}^{-2} \cdot \text{min}^{-1}$	T ( $^\circ\text{C}$ )	Ref
$\text{BaCe}_{0.7}\text{Zr}_{0.1}\text{Y}_{0.1}\text{Sn}_{0.1}\text{O}_3$	0.11	850	[20]
$\text{BaCe}_{0.85}\text{Fe}_{0.15}\text{O}_3/\text{BaCe}_{0.15}\text{Fe}_{0.85}\text{O}_3$ 50:50	0.76	950	[21]

Hydrogen is purified from a mixture of  $\text{CO}_2$  (from the atmosphere) and  $\text{H}_2$ . In the cell,  $\text{CO}_2$  is not absorbed, and  $\text{H}_2$  is oxidized. Subsequently, the proton is guided to the anode for hydrogen reformation (Fig. 1 a) or together with the electron (Fig. 1 b). Hydrogen storage by electrochemical cells is another challenge for proton conduction cells. The materials must contain a large amount of  $\text{H}^+$  [22].

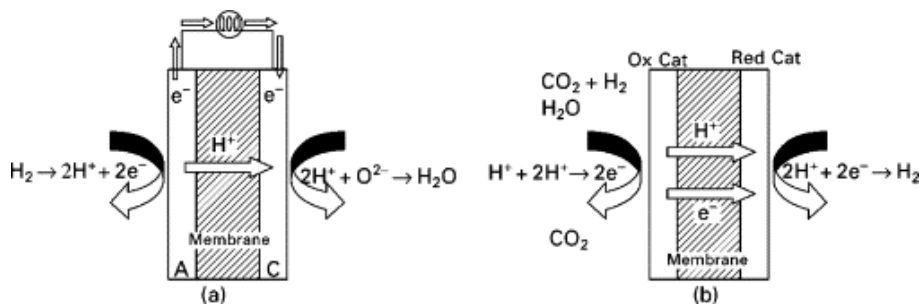


**Fig. 1.** Schematic representation of a) hydrogen energy fuel cell and b) hydrogen separator cell [19]

The proton conduction fuel cell is used as well for the synthesis of ammonia molecules [23] (Fig. 2). Ammonia is a highly demanded molecule in the agricultural industry for its use in the production of fertilizer. Additionally, the electrochemical cells have shown that ammonia produces high-density yields to produce carbon-free power. Ammonia has the advantage of being easily transported compared to the hydrogen molecules. Ammonia can liquefy at ambient temperature and compressed twice as compared to the hydrogen gas. Therefore, ammonia is ideally suited to be a carrier of  $\text{H}_2$ .

In the fuel cell, the effectiveness of proton conduction in the electrolyte in the fuel cell affects the ammonia production yield [24]. Fast proton transport is required to prevent reformation and evaporation of hydrogen gas within the cell. Electrolyte compositions based on barium cerates and barium zirconates-based electrolyte compositions have shown high rates of  $\text{NH}_3$  formation [25] (Fig. 3).

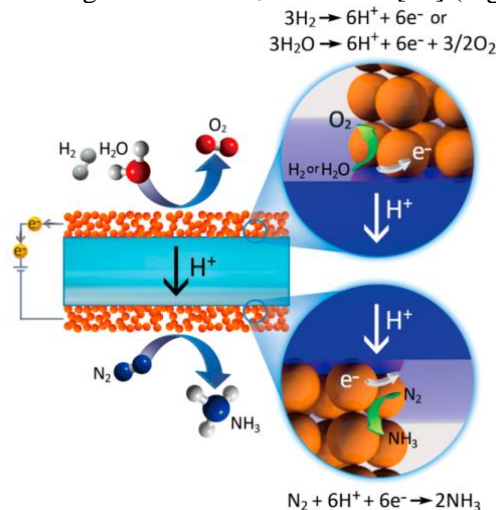


**Fig. 2.** Schematic representation of the proton conduction mechanism to the synthesis of ammonia [25] and the reactions occurring at the interface with the electrodes

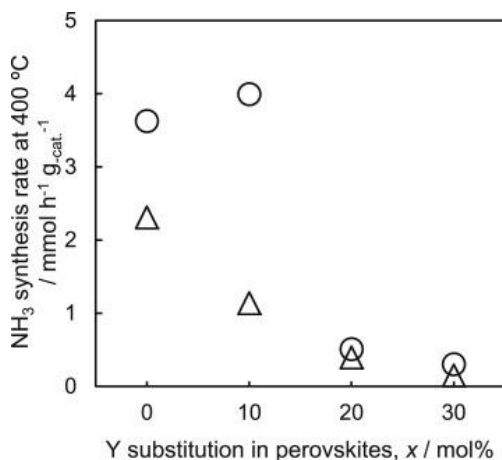


**Fig. 3.** Graph that shows the effect of yttrium dopant concentration on (o) barium zirconate and (Δ) for barium cerates supported ruthenium catalysts [26]

Hydrocarbon fuel cells are applied to the chemical industry for the production of energy from methane, biogas, ethanol and oxidation of natural gas. The main electrolyte for this application is  $\text{BaZr}_{0.8}\text{Y}_{0.2}\text{O}_{3-\delta}$  [27]. The main characteristics of the electrolyte for this application are resistance to  $\text{CO}_2$ , sulphur and high prolonged thermal stability in high humidity conditions. Furthermore, BZY20 is known to have a high water absorption capacity [28].

Syngas production is another application of proton-conducting fuel cells (Fig. 4). Syngas is a mixture of CO and H<sub>2</sub> used for the production of methanol, ammonia and as a fuel. The proton conductive cell converts CO<sub>2</sub> and CH<sub>4</sub> (from biomass) to CO and H<sub>2</sub>. One of the main issues of the electrochemical cell is the high operating temperature. Undesired reactions with gas contaminants, irreversible structural changes and delamination occur resulting in poor cell performance [29]. Another case is carbon deposition at 650 °C, which prevents gas diffusion and decreases the number of active sites [16]. Therefore, BaZrO<sub>3</sub> compositions are mainly investigated [31]. Fig. 4 as well shows that the diffusion processes are important at the interface between the electrode and electrolyte.

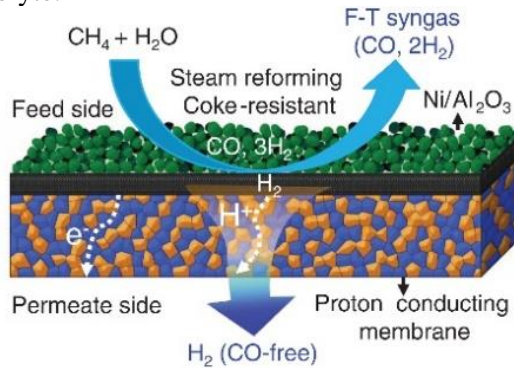


**Fig. 4.** Schematic representation of proton mechanism for Syngas production [32]

Proton conduction cells have shown good performance in ethylene production as well. Ethylene is a precursor in the plastic industry. It is formed from ethane and O<sub>2</sub> stream. The advantage of proton fuel cells over oxygen-ion cells is that the produced ethylene is not oxidized at the anode site. Then, it limits the formation of carbon oxides caused by the presence of water. Therefore, anhydrous conditions improve the cell performance in BaCe<sub>0.85</sub>Y<sub>0.15</sub>O<sub>3-δ</sub> [17] (BCY) (Table 2). Moreover, BCY formed at high sintering temperature (1700 °C) demonstrates an increase in ethylene production [19]. The ethylene fuel cell as well produces hydrogen as a by-product.

**Table 2.** Examples of electrolytes are barium cerate and barium zirconate based used in the formation of ethylene

Electrolyte	Sintering temperature (°C)	Temperature (°C)	Ethylene conversion (%)	Ref.
BaCe <sub>0.85</sub> Y <sub>0.15</sub> O <sub>3-δ</sub>	1500	700	27.9	[17]
BaCe <sub>0.85</sub> Y <sub>0.15</sub> O <sub>3-δ</sub>	1700	700	35.0	[33]
BaCe <sub>0.7</sub> Y <sub>0.17</sub> Zr <sub>0.1</sub> Nd <sub>0.03</sub> O <sub>3-δ</sub>	1500	700	23.0	[34]

Thus, for different applications, electrolytes need to have high stability against CO<sub>2</sub>, H<sub>2</sub>S, humidity conditions, low operation temperature, high-density materials, low ohmic resistance [29] and avoid recombination fast proton conduction. Barium

zirconates have been shown to be the ideal electrolytes that function at low operating temperatures (<650 °C). The only drawbacks in proton conductive fuel cells are the need for precious metal cathodes and anodes that are resistant to acid conditions.

The proton conduction occurs via oxygen vacancies that under humidified conditions, form proton defects. Dopants with lower oxidation numbers integrate into the unit cell to form oxygen vacancies. However, different dopants and their concentration have been shown to modify the ionic conductivity, electronic defects and microstructure [34].

The protons move according to the Grotthuss mechanism in the unit cell at low operation temperature. Other proton pathways include grain boundaries and pores at temperatures below 150 °C [36]. Above this temperature, the formation of space charge depletion regions increases the resistance to the proton path [37]. In some cases, the ionic conductivity may be higher in grain boundaries [38]. Aidhy and Weber [39] report on the effect of dopant segregation at grain boundaries that reduces ionic conductivity for fast oxygen conduction. Therefore, the microstructure plays a crucial role in proton transport when low operational temperatures (<650 °C) are used.

Proton conductive electrolytes were previously manufactured by different techniques that require high sintering temperatures to obtain high-density materials as one of the requirements for proton conductive electrolytes. However, it has been found that a decrease in the thickness reduces the value of the ohmic resistance. Therefore, physical vapor deposition (PVD) is another way to obtain high-density materials with homogenous and thicknesses lower than 1 μm. PVD systems operate at low temperatures, and the mobility of the atoms can be controlled by the deposition parameters. Thin films with grain-free microstructure were reported to enhance the proton conductivity [40]. BaZr<sub>0.2</sub>Ce<sub>0.7</sub>Y<sub>0.1</sub>O<sub>3</sub> were previously fabricated by PVD systems as magnetron sputtering, pulsed laser deposition and e-beam at low temperatures. The thin film that was formed before by the e-beam evaporation method is a mixture of barium zirconate and cerium with low crystallinity and grain sizes of approximately 600 nm [41]. Then, the post-annealing step at 1300 °C formed grain sizes that were greater than 5 μm. Other compositions were not reported beforehand.

In this work, the microstructure and phase formation of barium cerates and barium zirconates doped and undoped compositions are investigated at different deposition rates (2 Å/s, 4 Å/s, 8 Å/s and 12 Å/s), formed by e-beam evaporation method at support temperatures ranging from 25 °C to 700 °C. Other properties, such as degradation and ionic conductivity were evaluated as well for the future applications in fuel cells and electrolyzers.

## **Research problem**

The current research is characterized by the limitations in understanding the formation and characteristics of thin films composed of barium cerates and barium zirconates. These limitations are particularly pronounced when considering films with thicknesses under 1 μm. These materials exhibit altered lattice parameters due to a mismatch effect when grown on certain support. This phenomenon is well-documented in the case of barium zirconates, where the cubic phase lattice parameter undergoes modification due to the support mismatch. Conversely, in the case of

barium cerates with an orthorhombic phase, the extent of this lattice parameter alteration remains unexplored. A notable outcome of the lattice parameter change in barium zirconates is its significant impact on the trapping of protons and the ultimate values of ionic conductivity. However, the influence of various deposition parameters and support materials on the phase formation, microstructure, chemical stability and mechanical durability of thin films composed of different compositions of barium cerate and barium zirconate has not been the subject of prior investigation. This research gap is particularly relevant within the temperature range from 25 °C to 700 °C, which encompasses the film formation process. Furthermore, the ionic conductivity evaluation of barium cerates and barium zirconates is conventionally performed at temperatures exceeding 600 °C. Consequently, the information concerning the behaviour of these films at temperatures below 600 °C is notably scarce. In summary, the gap of comprehensive research addressing the formation, properties and behaviour of thin films made from barium cerates and barium zirconates within specific temperature ranges, as well as the influence of deposition parameters and support variations, poses a significant research problem in the field.

### **Aim of the research**

The aim of the research is to investigate the formation of barium cerates and barium zirconates thin films deposited by using e-beam evaporation method, along with an examination of their characteristics.

### **Objectives of the research**

1. To analyse the microstructure of barium cerates and barium zirconates thin films formed at different technological parameters.
2. To evaluate the crystal phase and preferred orientation of formed barium cerates and barium zirconates thin films and their dependencies on technological parameters.
3. To investigate the ionic conductivity of the selected barium cerates thin films at temperatures below 500 °C.

### **Scientific novelty and practical value**

The novelty is to obtain new knowledge about the influence of technological parameters (support temperature and deposition rate), the type of support on the formation and properties of the formed thin films of barium cerates and barium zirconates by the e-beam evaporation method evaporating BaCeO<sub>3</sub> (BCO), BaCe<sub>0.9</sub>Y<sub>0.1</sub>O<sub>3-δ</sub> (BCY10), BaCe<sub>0.8</sub>Y<sub>0.2</sub>O<sub>3-δ</sub> (BCY20), BaZrO<sub>3</sub> (BZO), BaZr<sub>0.8</sub>Y<sub>0.2</sub>O<sub>3-δ</sub> (BZY), BaZr<sub>0.8</sub>Ce<sub>0.1</sub>Y<sub>0.1</sub>O<sub>3-δ</sub> (BZCY) powders, including:

1. The influence of technological parameters on the chemical and mechanical stability of the formed barium cerates and barium zirconates thin films.
2. The formation and variation of the microstructure caused by different factors, such as deposition rate, support temperature, thermal expansion mismatch between the formed barium cerates and barium zirconates thin film and used support, lattice mismatch, support composition, support thermal properties, dopants and the concentration of dopants.

3. The influence of the unit cell size, the orientation of the crystal and the shape of the grain on the ionic conductivity of the formed barium cerates and barium zirconates thin films.

### **Key statements for the defense**

1. Deposition rate, thermal expansion coefficient (TEC) and substrate temperature affect the microstructure and surface morphology of barium cerate and barium zirconate thin films formed by the electron beam evaporation.
2. Ionic conductivity can be induced by controlling the residual stresses in barium cerate thin films formed by the electron beam evaporation.
3. In undoped barium cerate and barium cerate doped with 10% yttrium, at substrate temperatures below 500 °C, the conductivity of protons and oxygen ions is most influenced by the residual strain.
4. By controlling the deposition parameters (type of substrate, substrate temperature, deposition rate), barium cerate thin films can be formed in columnar structures belonging to Zones 2 and T of the Thornton zone diagram and barium zirconate thin films with columnar growth, which are formed according to the Stranski–Krastanov growth pattern.

### **Structure of the dissertation**

The dissertation is structured in 4 chapters. The first chapter introduces the main aim of the research, the methods and the main results. The second chapter aims to present the microstructural properties of barium cerates and barium zirconates formed under different conditions. This chapter starts by introducing the effect of microstructure on ionic conductivity. It is divided into 7 sections. It includes the description of the perovskites as the main structure, followed by its ionic conductivity, formation of the materials by conventional methods and finalizes with the formation of films by physical vapor deposition methods. The third chapter includes the methods used in this research. The fourth chapter covers the results and is divided into four sections. The first section includes undoped barium cerates formed at temperatures below 400 °C and at different deposition rates of 2, 4, 8 and 12 Å/s by the e-beam evaporation method on Inconel 600, Invar, Stainless steel and Glass sealing alloy. The second section includes undoped barium cerate formed at 2 Å/s and temperatures of 500 °C, 600 °C and 700 °C. These films were formed on MgO (001), YSZ (001) and Al<sub>2</sub>O<sub>3</sub> (0001). The third section aims to investigate the formation of barium cerate doped yttrium formed by e-beam evaporation method and temperatures of 500 °C, 600 °C and 700 °C, 2 Å/s on Inconel 600, MgO (001), YSZ (001) and Al<sub>2</sub>O<sub>3</sub> (0001). The fourth section shows barium zirconates thin films including the microstructure of doped yttrium and doped yttrium and cerium formed by the e-beam evaporation method at 600 °C and 700 °C, 2 Å/s on Inconel 600, MgO (001), YSZ (001) and Al<sub>2</sub>O<sub>3</sub> (0001). In chapter 5, there is the main summary and conclusions. The chapter 6 contains the references.

## Contribution of the author and others

The contribution of the author consists of the main part of the research consisting of the experimental work, ceramic system, investigation, measurements, calculation and data analysis. The contributions could be summarised as follows:

- Deposition of  $\text{BaCeO}_3$  by e-beam evaporation method on Invar, Inconel 600, Glass sealing alloy (GSA) and Stainless steel at 4 different rates, 2 Å/s, 4 Å/s, 8 Å/s and 12 Å/s, and 4 different temperatures, 150 °C, 300 °C, 450 °C and 600 °C.
- Deposition of  $\text{BaCeO}_3$ ,  $\text{BaCe}_{0.9}\text{Y}_{0.1}\text{O}_{3-\delta}$ ,  $\text{BaCe}_{0.8}\text{Y}_{0.2}\text{O}_{3-\delta}$ ,  $\text{BaZrO}_3$ ,  $\text{BaZr}_{0.8}\text{Y}_{0.2}\text{O}_{3-\delta}$ ,  $\text{BaZr}_{0.8}\text{Ce}_{0.1}\text{Y}_{0.1}\text{O}_{3-\delta}$  by e-beam evaporation method at the selected deposition rate 2 Å/s at 500 °C on Inconel 600.
- Deposition of  $\text{BaCeO}_3$ ,  $\text{BaCe}_{0.9}\text{Y}_{0.1}\text{O}_{3-\delta}$ ,  $\text{BaCe}_{0.8}\text{Y}_{0.2}\text{O}_{3-\delta}$ ,  $\text{BaZrO}_3$ ,  $\text{BaZr}_{0.8}\text{Y}_{0.2}\text{O}_{3-\delta}$ ,  $\text{BaZr}_{0.8}\text{Ce}_{0.1}\text{Y}_{0.1}\text{O}_{3-\delta}$  by e-beam evaporation method at the selected deposition rate 2 Å/s at 600 °C and 700 °C on Inconel 600,  $\text{Al}_2\text{O}_3$ , YZS and MgO.
- Scanning electron microscopy and energy dispersive X-ray spectroscopy in collaboration with Dr. Mantas Sriubas and Dr. Kristina Bočkutė.
- X-ray diffraction measurement and analysis in collaboration with Prof. Dr. Maria Gazda from Gdansk University in Poland.
- Measurements and analysis of data from impedance spectroscopy in collaboration with Dr. Piotr Winiarz and Dr. Kacper Dzierzgowski from Gdansk University in Poland.
- Data analysis, interpretation, writing of articles and presentation of the results in scientific conferences in collaboration with Dr. Mantas Sriubas, Dr. Kristina Bočkutė, Prof. Dr. Maria Gazda, Dr. Piotr Winiarz, Prof. Dr. Giedrius Laukaitis.

All the information presented in this work was supervised by Prof. Dr. Giedrius Laukaitis. The experiments and methodology of the scientific plan were written in collaboration with all co-authors.

## 2. LITERATURE OVERVIEW

Ionic conductivity in barium cerates and barium zirconates perovskites and their doped compositions is influenced by microstructure, chemical and mechanical stability. Therefore, at the beginning of this chapter, the structure of the perovskite is described in sub-chapter 2.1. Afterwards, the Grotthuss mechanism that occurs on the perovskites is explained in sub-chapter 2.2. Sub-chapters 2.3 and 2.4 describe the properties of barium cerates and barium zirconates when they are formed by the conventional methods. Further on, sub-chapter 2.5 describes the advances in the formation of barium cerate and barium zirconate thin film by the PVD technique. Then, the observed degradation mechanisms are present in sub-chapter 2.6. The summary of the literature overview is presented in sub-chapter 2.7.

### 2.1. Description of the perovskite structure

Barium cerate and barium zirconate have a perovskite structure. The main advantage of this structure is the addition of different metals in A and B sites in  $ABO_3$  without influencing the main arrangement of atoms that characterize perovskites. Perovskites are considered the most common type of mineral on earth. The lattice structure includes connected systems of three-dimensional  $BO_6$  octahedrons and  $AO_{12}$  cube-octahedrons (Fig. 5). Perovskite structures follow the Goldschmidt tolerance factor ( $t$ ) [42] to predict their formation at 300 K under atmospheric pressure. The size of O, A and B are spherical approximations. Therefore, for ideal structures,  $t = 1$  as the maximum value, and 0.8 is the minimum value to obtain a stabilized cell.

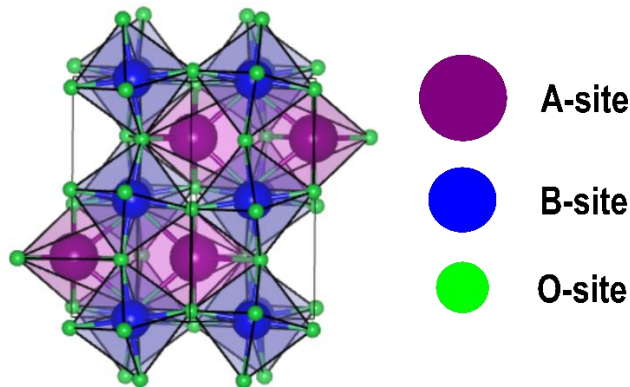
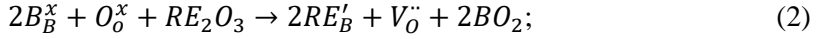


**Fig. 5.** Perovskites structure with orthorhombic phase for  $BaCeO_3$  at 25 °C

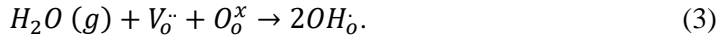
The main difference between the two perovskites is the degree of covalence between the Ce-O and Zr-O bonds. Zr-O has higher a degree of covalence [43]. It is explained by difference in molecular orbitals  $f$  for Ce and  $d$  for Zr. Another property is basicity:  $BaCeO_3$  is a very basic oxide compared to  $BaZrO_3$ . Then,  $BaCeO_3$  can easily accept the protons compared to  $BaZrO_3$ . The addition of different dopants in the A or B sites modifies the basicity and covalency.

The addition of dopants at the B site, which contains a lower oxidation number or rare earths with oxidation number +3 ( $RE^{3+}$ ) than B site ( $^{4+}$ ), form oxygen vacancies according to the equation (Kroger–Vink notation) [44] (Eq. 2). In  $RE'_B$ , B is the site replaced by the dopant, while  $B_B^x$  represents the B on atom at the B site before the addition of dopant in  $ABO_3$ :



where  $2RE'_B$  is the acceptor dopant at the B-sites,  $O_o^x$  is the neutral oxide ion and  $V_o^{\cdot\cdot}$  is the oxygen vacancy. The substitution of dopants at different sites (A, B or interstitial) in the lattice alters the ionic conductivity.

Oxygen vacancies react with water to form proton defects (Eq. 3):



Common rare earth elements used as dopants in  $BaCeO_3$  and  $BaZrO_3$  are as follows [45]:

1. Metallic atoms, such as In, Y, Yb, Sn, Gd, Nd, Hf and Sc, and their mixtures;
2. Halogen atoms (F-, Cl-);
3. Co-doping with other atoms, such as  $Ga^{3+}$ ,  $In^{3+}$ ,  $Y^{3+}$ ,  $Mo_3^+$ , to enhance ionic conductivity;
4. Isovalent elements, such as  $Ti^{4+}$ ,  $Sn^{4+}$ ,  $Zr^{4+}$  and even the donor  $Nb^{5+}$  and  $Ta^{5+}$  dopants, enhance the perovskite stability.

In order to improve  $BaCeO_3$  stability, it requires doping with dopants of small ionic size and high electronegative to increase the Goldschmit tolerance factor. Thus, acceptor ( $Ga^{3+}$ ,  $In^{3+}$ ,  $Y^{3+}$ ), isovalent ( $Ti^{4+}$ ,  $Sn^{4+}$ ,  $Zr^{4+}$ ) and even donor ( $Nb^{5+}$  and  $Ta^{5+}$ ) dopants [45] can be used.

## 2.2. Proton conduction explanation by Grotthuss mechanism

The conduction of protons at intermediate temperatures is explained by the Grotthuss mechanism (Fig. 6). Once proton defects are created, the proton attached to the oxygen atoms jumps from one oxygen to another. This jump requires a certain amount of activation energy. Unlike oxygen jumps, hydrogen bonds require less energy to diffuse from cathode to anode. Proton conductivity has been observed at low operating temperatures, and compared to oxygen ion conduction, the activation energies are less than 0.6 eV.

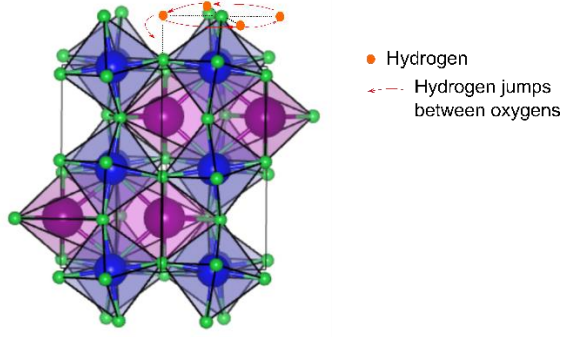


**Fig. 6.** Grotthuss mechanism for intra-octahedral diffusion of the proton on oxygen lattice

Dopants and crystal structure have a strong influence on the diffusion of protons and their activation energies for ionic conduction. The proton diffusion pathway is a phonon-assisted transport. The proton interacts with the vibration of the crystal lattice. For example, with a doping of 10% yttrium ( $\text{BaZr}_{0.9}\text{Y}_{0.1}\text{O}_{3-\delta}$ ), the proton jump time decreases with increasing temperature [46]. The simulation for barium zirconate doped with yttrium demonstrated that yttrium tilts the unit cell, and this tilt facilitates the formation of hydrogen bonds that helps bringing oxygen closer to the oxygen vacancies [47].

The incorporation of water is another factor to produce proton defects. Eq. 4 describes the energy required to produce proton defects and includes the formation of oxygen vacancies:

$$\Delta H_{\text{H}_2\text{O}} = 2E_{\text{OH}} - E(V_{\text{O}^{\cdot\cdot}}) + E_{\text{PT}}; \quad (4)$$

where  $\Delta H_{\text{H}_2\text{O}}$  is the enthalpy of water intake,  $E_{\text{OH}}$  is the energy involved with the replacement of  $\text{O}^{2-}$  by the hydroxyl group  $\text{OH}^-$ ,  $E(V_{\text{O}^{\cdot\cdot}})$  is the energy required to form an oxygen-ion vacancy and  $E_{\text{PT}}$  is the energy of the gas phase of proton-transfer reaction from one side to another.

The oxygen vacancies and water pressures are related to the water incorporation or equilibrium constant of water incorporation ( $K_w$ ) (Eq. 4):

$$K_w = \frac{[\text{OH}_o^-]^2}{P_{\text{H}_2\text{O}}[\text{V}_{\text{O}^{\cdot\cdot}}][\text{O}_o^{\cdot\cdot}]}. \quad (4)$$

The enthalpy of water incorporation fluctuates with crystallography symmetry, dopants (oxygen vacancies), dopants concentrations, crystal orientation, microstructure, density and strain in the lattice. High dopant concentration is known to retain more water above 200 °C [48]. For example, BCY [49], the equilibrium constant of this reaction has a standard enthalpy of 162.2 kJ/mol (released heat).

Proton diffusivity ( $D_H$ ) dependence on temperature and its concentration is obtained [50] by Eq. 5:

$$D_H = \frac{\sigma_H RT}{F^2 C_H}; \quad (5)$$

where  $C_H$  is the proton concentration,  $\sigma_H$  is bulk conductivity,  $F$  is Faraday's constant,  $R$  is the universal gas constant and  $T$  is temperature. Moreover, the small distance between the atoms turns out in a change on proton trapping effect. Small proton trapping means high diffusion and consequently high total ionic conductivity [51] (Eq. 6):

$$\sigma_{total} = N_A / (K_B T) \sum_{i=1}^n (c_i q_i^2 D_i); \quad (6)$$

where  $\sigma$  is the total electrical conductivity of the material,  $N_A$  is the Avogadro number,  $K_B$  is the Boltzmann constant,  $T$  is the absolute temperature, and  $c_i$ ,  $q_i^2$  and  $D_i$  are the concentration charge and diffusion coefficient of ions at responsible species.

Proton conductivity on different orthorhombic perovskites, such as  $\text{SrTiO}_3$ ,  $\text{SrZrO}_3$  and  $\text{CaZrO}_3$ , suggests proton quantum path at low temperatures. It includes a proton jumping from corner-linked to edge-sharing type [52] that has the minimum distance from all three different steps.

Fig. 7 illustrates the Grotthuss mechanism path a), b) and c) on different directions on the perovskite with a) as the proton tunnelling jump. The numbers 1, 2 and 3 indicate the oxygen sites in the perovskite. Proton tunnelling is suggested to occur at low temperatures and in only one oxygen to oxygen direction [52]. The quantum tunnelling at the critical temperature ( $T_{cr}$ ) is described in Eq. 7.

$$\epsilon e^{-\frac{Q}{K_B T}} \sim \Omega \quad (8)$$

The probability of Q coincides with the quantum tunnelling frequency  $\Omega$ . E is the difference in energy level between the ground and the first excited states.

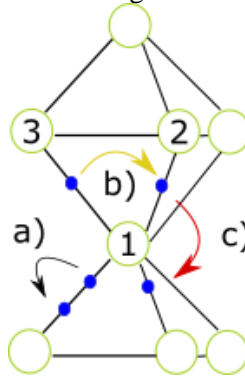
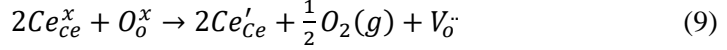


**Fig. 7.** Proton hopping at the oxygen site on the octahedron in the perovskite: a) hydrogen tunnelling movement at low temperatures, b) intra-octahedron and c) inter-octahedron at the oxygen sites (1), (2) and (3); the potential energy barriers are lower for b) and c) jumps, and a) proton hopping contains a higher potential barrier at high temperatures [52]

The formation of proton defects, oxygen vacancies, interstitial defects and other charges influence electrolytes total charge or energy gap. The total charge is modified as well by reducing or oxidizing (air) atmospheres (Brouwer diagram [53]) at high temperatures. The material can be converted from an n-type semiconductor for  $\text{H}_2$  atmospheres to a p-type at high oxygen pressure or air under high temperatures (Eq.

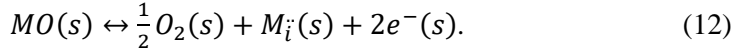
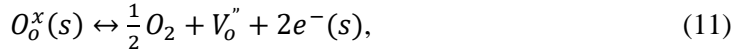
8). For example, undoped barium cerate does not contain oxygen vacancies, but under reduction conditions (e.g., H<sub>2</sub>) and high temperatures, Ce<sup>+4</sup> becomes Ce<sup>+3</sup> [54].



The oxygen atoms in the lattice are sensitive to different reactions at high temperatures. At a high oxygen pressure (PO<sub>2</sub>) and high temperatures, oxygen interstitials are formed along with holes [*h*'] that enhance electric conductivity (Eq. 10). Interstitial oxygen takes one electron from the lattice [53].



At low PO<sub>2</sub> and high temperatures, the lattice is charged negatively due to the release of molecular oxygen from the lattice (Eqs. 11 and 12) [53].



MO is neutral metal oxide, and *M<sub>i</sub><sup>+</sup>* is cation interstitials. In order to avoid electronic conductivity, high temperatures are selected for oxygen ion conductors. Conversely, a proton conductor works at low temperatures without electric effects in an ideal proton conductor. In mixed ion conduction, holes and electrons diminish the ion conductivity at low temperature as in the case of BaCeO<sub>3</sub>.

The total conductivity  $\sigma_{bulk}$  includes all the charges (protons, holes, electrons and ions) as described by Nerst–Einstein equation (Eqs. 13 and 14) [53]:

$$\mu = \frac{qD}{kT}, \quad (13)$$

$$\sigma_{total} = n_{ionic} \left( \frac{q^2 D_{ionic}}{kT} \right) + n_{electrons} \left( \frac{q^2 D_{electrons}}{kT} \right) + n_{holes} \left( \frac{q^2 D_{holes}}{kT} \right). \quad (14)$$

Ionic mobility is much smaller than electron mobility. The contribution of ions is higher than electrons for the electrolytes. The Arrhenius equation relates the total ion conductivity at different temperatures with the activation energy (Eq. 15). Then, low activation energies (<0.6 eV) exhibit a prominent proton conduction behaviour, while higher values show an oxygen ion conductivity [53].

$$\sigma_{total} = \sigma_0/T \cdot \exp\left(-\frac{E_A}{K_B T}\right); \quad (15)$$

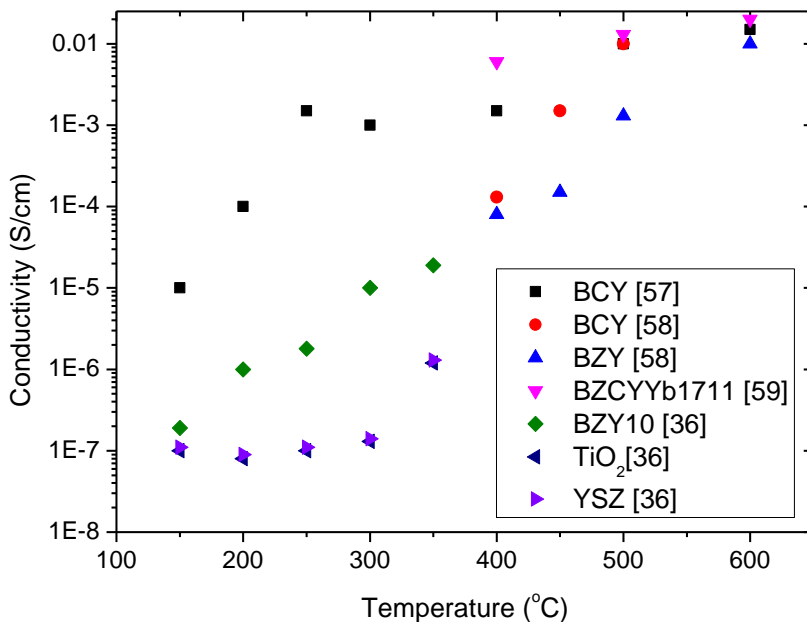
where  $\sigma_{total}$  is the ionic conductivity at T temperature,  $\sigma_0$  is the initial total ionic conductivity,  $E_A$  is the activation energy and  $K_B$  is the Boltzmann constant.

Table 3 shows the ionic conductivities achieved by barium cerates and barium zirconates. The conductivities for barium cerates at 600 °C were in the range of 10<sup>-5</sup> S/cm with the lowest values for undoped BCO and BCY10 formed under the same conditions. Barium cerates are mixed ionic conductor. Therefore, the variation of the atmospheres enhances the ionic conductivity.

Table 4 presents the activation energies for different barium cerates and barium zirconates under different atmospheres. It was mentioned before that the atmosphere

influences the charges and consequently the type of ionic/electronic conduction. Therefore, different values are observed in different temperature ranges.  $E_A$  values for dominant proton conduction are less than 0.6 eV, while oxygen ion conductors have a value greater than 0.6 eV. Undoped barium cerate is a conductor of oxygen ion at low temperatures and a mixed conductor of protons and oxygens at high temperatures. However, under reduced conditions and high temperatures,  $Ce^{4+}$  is reduced to  $Ce^{3+}$ . The lowest activation energy for BCO under  $H_2$  (reduced condition) was 0.31 eV [55]. The lowest  $E_A$  for barium cerates was only observed under a hydrogen atmosphere. The lowest  $E_A$  for barium zirconates of 0.38 eV was observed under humid air conditions [56]. Water absorption is the primary mechanism for enhancing ionic conductivity for doped barium zirconate. Therefore, a mixture of barium zirconates and barium cerates offers the advantage of both compositions.  $BaCe_{0.6}Zr_{0.2}Y_{0.2}O_{3-6}$  exhibits ionic conductivity of  $2.86 \times 10^{-2}$  S/cm at 300 °C [57]. The mixture has low activation energies for BZCY, i.e., 0.39 eV above 600 °C in the humid air atmosphere [56].

Figure 8 compares the ionic conductivity of different fast ion conductors with barium cerates and zirconates in the range between 150 °C and 600 °C. BCY exhibits high ion conductivity under nominal water and  $CO_2$  conditions. Otherwise, it degrades.



**Fig. 8.** Comparison of conductivities at low operating temperature for the main fast ion conductors: BCY [57, 58], BZCYYb [59], BZY,  $TiO_2$  and YSZ [36]

**Table 3.** Ionic conductivity  $\sigma$  for doped and undoped barium cerates

Material	$\sigma$ , S/cm	Temperature, (°C)	Ref.
BaCe <sub>0.8</sub> Y <sub>0.2</sub> O <sub>3</sub>	$5.79 \times 10^{-2}$	300	[57]
BaCe <sub>0.7</sub> Nb <sub>0.1</sub> Sm <sub>0.2</sub> O <sub>3-<math>\delta</math></sub>	$2.6 \times 10^{-3}$	700	[60]
BaCe <sub>0.7</sub> Ta <sub>0.1</sub> Y <sub>0.2</sub> O <sub>3-<math>\delta</math></sub>	$2.3 \times 10^{-3}$	600	[61]
BaCe <sub>0.7</sub> In <sub>0.2</sub> Yb <sub>0.1</sub> O <sub>3-<math>\delta</math></sub>	$2.7 \times 10^{-3}$	600	[62]
BaCe <sub>0.8</sub> Sm <sub>0.2</sub> O <sub>3-<math>\delta</math></sub>	$6.62 \times 10^{-3}$	600	[63]
BaCe <sub>1-x</sub> Y <sub>x</sub> O <sub>3-<math>\delta</math></sub>	$1.04 \times 10^{-2}$	600	[64]
BaCe <sub>0.85</sub> Dy <sub>0.15</sub> O <sub>3-<math>\delta</math></sub>	$0.93 \times 10^{-2}$	600	[65]
BaCe <sub>0.9</sub> Gd <sub>0.1</sub> O <sub>3-<math>\delta</math></sub>	$1.4 \times 10^{-2}$	600	[66]
BaCeO <sub>3</sub>	$1.72 \times 10^{-5}$	600	[67]
BaCe <sub>0.9</sub> Gd <sub>0.1</sub> O <sub>3</sub>	$4.16 \times 10^{-5}$	600	[67]
BaCe <sub>0.9</sub> Nd <sub>0.1</sub> O <sub>3</sub>	$2.53 \times 10^{-5}$	600	[67]
BaCe <sub>0.9</sub> Sm <sub>0.1</sub> O <sub>3</sub>	$3.41 \times 10^{-5}$	600	[67]
BaCe <sub>0.9</sub> Y <sub>0.1</sub> O <sub>3</sub>	$1.86 \times 10^{-5}$	600	[67]

The ionic conductivity is measured in different temperature ranges. It aims for high values at temperatures below 600 °C. The barium cerates and their doped composition presents values lower than  $5.79 \times 10^{-2}$  S/cm (Table 3). The lowest values are obtained for undoped composition as a consequence of a lower amount of oxygen vacancies. Similar compositions with variation in the microstructure show different ionic conductivity values. The ionic conductivity value of 0.11 S/cm at 600 °C (Table 4) for barium zirconates doped yttrium was an effect of microstructure and thickness. The microstructure formed by PVD systems differs from the solid-state reaction. The BaCe<sub>0.6</sub>Zr<sub>0.2</sub>Y<sub>0.2</sub>O<sub>3- $\delta$</sub>  mixture exhibits the highest ionic conductivity value of  $2.86 \times 10^{-2}$  at 300 °C (Table 5). The low amount of zirconium made BaCe<sub>0.6</sub>Zr<sub>0.2</sub>Y<sub>0.2</sub>O<sub>3- $\delta$</sub>  unstable under water and CO<sub>2</sub>. In comparison, stable BaCe<sub>0.2</sub>Zr<sub>0.6</sub>Y<sub>0.2</sub>O<sub>3- $\delta$</sub>  had an ionic conductivity value of  $1.79 \times 10^{-2}$  S/cm with a tolerance factor closer to the barium zirconates.

**Table 4.** Ionic conductivity of barium zirconates and their doped compositions

Material	$\sigma$ , S/cm	Temperature, (°C)	Ref.
BaZr <sub>0.8</sub> Y <sub>0.2</sub> O <sub>3-<math>\delta</math></sub>	$5.79 \times 10^{-2}$	300	[57]
BaZr <sub>0.8</sub> Y <sub>0.2</sub> O <sub>3-<math>\delta</math></sub>	0.11	500	[68]
BaZr <sub>0.7</sub> Pr <sub>0.1</sub> Y <sub>0.2</sub> O <sub>3-<math>\delta</math></sub>	0.01	600	[69]
BaZr <sub>0.8</sub> Y <sub>0.2</sub> O <sub>3-<math>\delta</math></sub>	$1 \times 10^{-2}$	450	[70]
BaZr <sub>0.8</sub> Y <sub>0.2</sub> O <sub>3-<math>\delta</math></sub>	$1.0 \times 10^{-3}$	550	[71]
BaZr <sub>0.8</sub> Y <sub>0.2</sub> O <sub>3-<math>\delta</math></sub>	$4.45 \times 10^{-3}$	600	[72]

**Table 5.** Ionic conductivity of barium cerate perovskites and their doped compositions

Material	$\sigma$ , S/cm	Temperature, (°C)	Ref.
BaCe <sub>0.9-x</sub> Zr <sub>x</sub> Nd <sub>0.1</sub> O <sub>2.95</sub>	$7.6 \times 10^{-6}$	600	[73]
BaCe <sub>0.05</sub> Zr <sub>0.3</sub> Y <sub>0.16</sub> Zn <sub>0.04</sub> O <sub>3-<math>\delta</math></sub>	$1.46 \times 10^{-3}$	550	[74]
BaCe <sub>0.7</sub> In <sub>0.2</sub> Yb <sub>0.1</sub> O <sub>3-<math>\delta</math></sub>	$8 \times 10^{-3}$	800	[62]
BaCe <sub>0.9-x</sub> Zr <sub>x</sub> Sm <sub>0.1</sub> O <sub>3-<math>\delta</math></sub>	$1.93 \times 10^{-2}$	800	[75]
BaCe <sub>0.4</sub> Zr <sub>0.4</sub> Gd <sub>0.1</sub> Dy <sub>0.1</sub> O <sub>3-<math>\delta</math></sub>	$1.93 \times 10^{-3}$	700	[76]
BaCe <sub>0.8</sub> Zr <sub>0.1</sub> Y <sub>0.1</sub> O <sub>3-<math>\delta</math></sub>	$12 \times 10^{-3}$	700	[77]
BaZr <sub>0.5</sub> Ce <sub>0.3</sub> Y <sub>0.2</sub> O <sub>3</sub>	$2.5 \times 10^{-2}$	600	[56]
BaZr <sub>0.5</sub> Ce <sub>0.3</sub> Sm <sub>0.2</sub> O <sub>3</sub>	$4.5 \times 10^{-2}$	600	[56]
BaZr <sub>0.5</sub> Ce <sub>0.3</sub> Gd <sub>0.2</sub> O <sub>3</sub>	$4.5 \times 10^{-3}$	600	[56]
BaZr <sub>0.5</sub> Ce <sub>0.3</sub> Dy <sub>0.2</sub> O <sub>3</sub>	$6.8 \times 10^{-2}$	600	[56]
BaCe <sub>0.45</sub> Zr <sub>0.45</sub> In <sub>0.1</sub> O <sub>3-<math>\delta</math></sub>	$0.5 \times 10^{-2}$	800	[78]
BaCe <sub>0.45</sub> Zr <sub>0.45</sub> Y <sub>0.1</sub> O <sub>3-<math>\delta</math></sub>	$1.06 \times 10^{-2}$	800	[78]
BaCe <sub>0.45</sub> Zr <sub>0.45</sub> Gd <sub>0.1</sub> O <sub>3-<math>\delta</math></sub>	$0.82 \times 10^{-2}$	800	[78]
BaCe <sub>0.45</sub> Zr <sub>0.45</sub> Sm <sub>0.1</sub> O <sub>3-<math>\delta</math></sub>	$0.69 \times 10^{-2}$	800	[78]
BaCe <sub>0.6</sub> Zr <sub>0.2</sub> Y <sub>0.2</sub> O <sub>3-<math>\delta</math></sub>	$2.86 \times 10^{-2}$	300	[57]
BaCe <sub>0.4</sub> Zr <sub>0.4</sub> Y <sub>0.2</sub> O <sub>3-<math>\delta</math></sub>	$2.00 \times 10^{-2}$	300	[57]
BaCe <sub>0.2</sub> Zr <sub>0.6</sub> Y <sub>0.2</sub> O <sub>3-<math>\delta</math></sub>	$1.79 \times 10^{-2}$	300	[57]
BaCe <sub>0.5</sub> Zr <sub>0.3</sub> Y <sub>0.2</sub> O <sub>3</sub> – Zn	$7.66 \times 10^{-3}$	700	[79]
BaCe <sub>0.5</sub> Zr <sub>0.3</sub> Y <sub>0.2</sub> O <sub>3</sub> – Na <sub>2</sub> CO <sub>3</sub> .	$7.68 \times 10^{-3}$	700	[79]
BaCe <sub>0.85-x</sub> Zr <sub>x</sub> Er <sub>0.15</sub> O <sub>3-<math>\delta</math></sub>	$3.5 \times 10^{-3}$	700	[80]
BaZr <sub>0.1</sub> Ce <sub>0.7</sub> Y <sub>0.1</sub> Yb <sub>0.1</sub> O <sub>3</sub>	$7.4 \times 10^{-2}$	750	[81]
BaZr <sub>0.1</sub> Ce <sub>0.7</sub> Y <sub>0.1</sub> Yb <sub>0.1</sub> O <sub>3</sub>	$1.3 \times 10^{-2}$	500	[82]
BaZr <sub>0.1</sub> Ce <sub>0.7</sub> Y <sub>0.1</sub> Yb <sub>0.1</sub> O <sub>3</sub>	$2.07 \times 10^{-2}$	800	[83]
Ba <sub>0.5</sub> Sr <sub>0.5</sub> Ce <sub>0.5</sub> Zr <sub>0.35</sub> Y <sub>0.1</sub> Sm <sub>0.05</sub> O <sub>3</sub>	$2.391 \times 10^{-3}$	700	[84]
BaZr <sub>0.1</sub> Ce <sub>0.7</sub> Y <sub>0.1</sub> Yb <sub>0.1</sub> O <sub>3</sub>	$1.41 \times 10^{-2}$	600	[85]
Ba <sub>0.9</sub> K <sub>0.1</sub> Ce <sub>0.6</sub> Zr <sub>0.2</sub> Y <sub>0.2</sub> O <sub>3</sub>	0.012	800	[86]

Activation energies ( $E_a$ ) for proton conduction have the values less than 0.5 eV. Table 6 displays values for barium cerate and its composition with  $E_a$  less than 0.6 eV. The pellets were kept in a dry atmosphere at 700 °C before measurements at lower temperatures [87] to avoid degradation. Due to this reason, ionic conductivities are measured above 400 °C [55]. Undoped barium cerate exhibits the lowest (0.31 eV) and highest (1.05 eV) activation energies. While the lowest values were under inert atmosphere, such as wet Ar in the temperature range of 400–700 °C, the highest values were under air and hydrogen/argon in the low temperature range of 250–850 °C. The highest values were a consequence of its change in the electronic defects.

In dry conditions, for barium zirconates (Table 7), the  $E_a$  is higher than 0.6 eV, but under humid conditions, it decreases to 0.5 eV as a consequence of the formation of proton defects. The lowest values are for the mixture between barium zirconate and praseodymium [69]. High activation energy values were observed in a high range of temperatures. The reduced concentration of water enhances oxygen ion conduction

instead of proton conduction. The mixture between barium cerate and zirconates (Table 8) exhibits similar behaviour under wet and dry conditions as previous barium zirconate alone. The mixture was tested above 573 °C.  $\text{BaZr}_{0.5}\text{Ce}_{0.3}\text{Dy}_{0.2}\text{O}_3$  has the lowest activation energy value (0.38 eV) in the range between 600 °C and 700 °C.

**Table 6.** Activation energies  $E_a$  values for doped barium cerates

Sample	Testing atmosphere	Temperature, °C	$E_a$ , eV	Ref
$\text{BaCe}_{0.80}\text{Sm}_{0.20}\text{O}_{3-x}$	$\text{H}_2\text{O-Ar}$	475–750	0.534	[88]
$\text{BaCe}_{0.6}\text{Sm}_{0.2}\text{In}_{0.2}\text{O}_{3-\delta}$	$\text{H}_2\text{O-Ar}$	475–750	0.226	[88]
$\text{BaCe}_{0.9}\text{Y}_{0.1}\text{O}_{3-\delta}$	Wet $\text{H}_2$	550–750	0.37	[89]
$\text{BaCe}_{0.85}\text{Y}_{0.1}\text{In}_{0.05}\text{O}_{3-\delta}$	Wet $\text{H}_2$	550–750	0.34	[89]
$\text{BaCe}_{0.85}\text{Y}_{0.1}\text{Zr}_{0.05}\text{O}_{3-\delta}$	Wet $\text{H}_2$	550–750	0.38	[89]
$\text{BaCe}_{0.85}\text{Y}_{0.1}\text{Nb}_{0.05}\text{O}_{3-\delta}$	Wet $\text{H}_2$	550–750	0.38	[89]
$\text{BaCe}_{0.7}\text{In}_{0.2}\text{Y}_{0.1}\text{O}_{3-\delta}$	Dry air	500–800	0.47	[79]
$\text{BaCe}_{0.7}\text{In}_{0.2}\text{Y}_{0.1}\text{O}_{3-\delta}$	Wet air	500–800	0.63	[79]
$\text{BaCe}_{0.7}\text{In}_{0.2}\text{Y}_{0.1}\text{O}_{3-\delta}$	Wet $\text{H}_2$	500–800	0.25	[79]
$\text{BaCe}_{0.7}\text{In}_{0.2}\text{Y}_{0.1}\text{O}_{3-\delta}$	Wet $\text{N}_2$	500–800	0.4	[79]
$\text{BaCe}_{0.9}\text{La}_{0.1}\text{O}_{3-\delta}$	Wet air	150–250	0.53	[87]
$\text{BaCe}_{0.9}\text{Nd}_{0.1}\text{O}_{3-\delta}$	Wet air	150–250	0.53	[87]
$\text{BaCe}_{0.9}\text{Sm}_{0.1}\text{O}_{3-\delta}$	Wet air	150–250	0.49	[87]
$\text{BaCe}_{0.9}\text{Gd}_{0.1}\text{O}_{3-\delta}$	Wet air	150–250	0.49	[87]
$\text{BaCe}_{0.9}\text{Y}_{0.1}\text{O}_{3-\delta}$	Wet air	150–250	0.48	[87]
$\text{BaCe}_{0.9}\text{Y}_{0.1}\text{O}_{3-\delta}$	Wet air	150–250	0.47	[87]
$\text{BaCe}_{0.9}\text{Tb}_{0.1}\text{O}_{3-\delta}$	Wet air	150–250	0.46	[87]
$\text{BaCeO}_3$	Argon hydrogen mixture (AHM)	400–700	0.31	[55]
$\text{BaCe}_{0.82}\text{Er}_{0.9}\text{Yb}_{0.9}\text{O}_3$	AHM	400–700	0.43	[55]
$\text{BaCe}_{0.82}\text{Er}_{0.9}\text{Sc}_{0.9}\text{O}_3$	AHM	400–700	0.46	[55]
$\text{BaCeO}_3$	Dry-air	400–700	0.51	[55]
$\text{BaCe}_{0.82}\text{Er}_{0.9}\text{Yb}_{0.9}\text{O}_3$	Dry-air	400–700	0.44	[55]
$\text{BaCe}_{0.82}\text{Er}_{0.9}\text{Sc}_{0.9}\text{O}_3$	Dry-air	400–700	0.60	[55]
$\text{BaCeO}_3$	Air	250–800	1.05	[91]
$\text{BaCe}_{0.9}\text{Gd}_{0.1}\text{O}_3$	Air	250–800	0.68	[91]
$\text{BaCe}_{0.9}\text{Nd}_{0.1}\text{O}_3$	Air	250–800	0.90	[91]
$\text{BaCe}_{0.9}\text{Sm}_{0.1}\text{O}_3$ (Sm)	Air	250–800	0.68	[91]
$\text{BaCe}_{0.9}\text{Y}_{0.1}\text{O}_3$ (Y)	Air	250–800	0.54	[91]
$\text{BaCeO}_3$	5% $\text{H}_2$ –95% Ar	250–800	0.88	[91]
$\text{BaCe}_{0.9}\text{Gd}_{0.1}\text{O}_3$	5% $\text{H}_2$ –95% Ar	250–800	0.78	[91]
$\text{BaCe}_{0.9}\text{Nd}_{0.1}\text{O}_3$	5% $\text{H}_2$ –95% Ar	250–800	0.82	[91]
$\text{BaCe}_{0.9}\text{Sm}_{0.1}\text{O}_3$	5% $\text{H}_2$ –95% Ar	250–800	0.72	[91]

BaCe <sub>0.9</sub> Y <sub>0.1</sub> O <sub>3</sub>	5% H <sub>2</sub> -95% Ar	250-800	0.56	[91]
---	------------------------------	---------	------	------

**Table 7.** Activation energies  $E_a$  values for doped barium zirconates

Sample	Testing atmosphere	Temperature, °C	$E_a$ , eV	Ref
BaZr <sub>0.8</sub> Y <sub>0.2</sub> O <sub>3-δ</sub>	2% H <sub>2</sub> O/H <sub>2</sub>	550-700	0.59	[92]
BaZr <sub>0.9</sub> Pr <sub>0.1</sub> O <sub>3-δ</sub>	Dry air	550-700	0.6	[69]
	Wet hydrogen	550-700	0.59	[69]
BaZr <sub>0.8</sub> Y <sub>0.1</sub> Pr <sub>0.1</sub> O <sub>3-δ</sub>	Dry air	550-700	0.66	[69]
	Wet hydrogen	550-700	0.51	[69]
BaZr <sub>0.7</sub> Y <sub>0.2</sub> Pr <sub>0.2</sub> O <sub>3-δ</sub>	Dry air	550-700	0.68	[69]
	Wet hydrogen	550-700	0.51	[69]
BaZr <sub>0.8</sub> Y <sub>0.2</sub> O <sub>3</sub>	5% H <sub>2</sub> in Argon	350-650	0.61-0.63	[68]
	O <sub>2</sub> /dry	350-650	0.96	[68]
	Ar/dry	350-650	0.89	[68]

**Table 8.** Activation energies  $E_a$  values for doped barium zirconates cerates

Sample	Testing atmosphere	Temperature, °C	$E_a$ , eV	Ref
BaZr <sub>0.1</sub> Ce <sub>0.7</sub> Y <sub>0.1</sub> Yb <sub>0.1</sub> O <sub>3</sub>	Air	573-723	0.79	[85]
	Dry H <sub>2</sub>	573-723	0.76	[85]
	Wet H <sub>2</sub>	573-723	0.67	[85]
BaZr <sub>0.1</sub> Ce <sub>0.7</sub> Y <sub>0.2</sub> O <sub>3</sub>	Air	573-723	0.79	[85]
	Dry H <sub>2</sub>	573-723	0.77	[85]
	Wet H <sub>2</sub>	573-723	0.73	[85]
BaZr <sub>0.1</sub> Ce <sub>0.7</sub> Y <sub>0.1</sub> Yb <sub>0.1</sub> O <sub>3</sub>	Air	400-600	0.75	[83]
	Wet H <sub>2</sub>	400-600	0.66	[83]
	Wet O <sub>2</sub>	400-600	0.68	[83]
BaZr <sub>0.5</sub> Ce <sub>0.3</sub> Y <sub>0.2</sub> O <sub>3</sub>	Dry air	600-700	0.73	[56]
	Wet air	600-700	0.39	[56]
BaZr <sub>0.5</sub> Ce <sub>0.3</sub> Sm <sub>0.2</sub> O <sub>3</sub>	Dry air	600-700	0.89	[56]
	Wet air	600-700	0.50	[56]
BaZr <sub>0.5</sub> Ce <sub>0.3</sub> Gd <sub>0.2</sub> O <sub>3</sub>	Dry air	600-700	0.88	[56]
	Wet air	600-700	0.43	[56]
BaZr <sub>0.5</sub> Ce <sub>0.3</sub> Dy <sub>0.2</sub> O <sub>3</sub>	Dry air	600-700	0.71	[56]
	Wet air	600-700	0.38	[56]

The dopants, the unit cell and the test conditions (temperature and atmosphere) determine the value of the total ionic conductivity. Furthermore, it has been shown that the change in microstructure influences the ionic conductivity below 600 °C as a consequence of the grain boundaries. The mechanical stability in barium cerates and zirconates is controlled by the microstructure as well. The microstructure includes lattice parameters, grain size, grain orientation, grain boundaries (width and composition), crystallinity, crystal phase, crystal size, crystal orientation and density.

## 2.3. Barium cerates

### 2.3.1. Lattice parameters and phases of undoped and doped barium cerates

The microstructure of barium cerates and barium zirconates formed at high temperatures is well documented. In this sub-chapter, the microstructure of barium cerates and zirconates is presented.

The dopant, the temperature and the sintering aids show a strong effect on the variation on the lattice parameters and the phase transitions (Table 9). It varies from orthorhombic > rhombohedral > cubic with rising temperature for BaCeO<sub>3</sub>. The lattice parameter changes for  $a = 8.840 \text{ \AA}$ ,  $b = 6.2020 \text{ \AA}$ ,  $c = 6.2390 \text{ \AA}$  from orthorhombic to  $a = 6.234 \text{ \AA}$  rhombohedral above 400 °C.

The cubic phase is ideal for barium cerates due to the smallest lattice parameters contributing to have a rapid proton jump. However, this phase begins to form above 800 °C. At room temperature, orthorhombic phase is usually observed.

**Table 9.** Phase transitions for BaCeO<sub>3</sub> at different temperatures and assets methods

Phase	Transition temperature [93] (°C)	Inductive melting [94] (°C)	High-temperature X-ray [93] (°C)	Neutron powder diffraction [95] (°C)	Time of flight neutron powder diffraction [96] (°C)	DSC in high purity Argon [97] (°C)	TEC (x 10 <sup>-6</sup> K <sup>-1</sup> ) [93]	Lattice parameters (Å) [93]		
								a	b	c
Orthorombic (P)	0–250	260	260	290	300	267	11.0	8.784	6.220	6.239
Orthorombic (I)	250–450	357					11.0	8.784	6.220	6.239
Rhombohedral	400–800		385	400	400	327	11.0	6.234	-	-
Cubic	>800		895	900	880	907	10.4	~4		

The concentration of the dopant is another factor that modifies the phase and the unit cell. For example, adding yttrium at different concentrations results in a phase change [98] (Table 10). The high concentration of dopant adds more oxygen vacancies resulting in a higher diffusion for BCY. Meanwhile, for other dopants, such as Nd, its phase is stable in the range <0.2 [99]. It is known that Nd occupies site A and B. At the A-site, oxygen vacancies are consumed. Therefore, the mobility of the atoms is low, and the phase is stable.

**Table 10.** Influences of the dopant concentration on the phase variation for barium cerate doped yttrium

Y	Crystall phase (at 800 °C)
$\leq 0.1$	Orthorhombic (Pmcn)
$\geq 0.15$	Rhombohedral (R3c)
$0.2 \leq x \leq 0.25$	Monoclinic (I2/m) and rhombohedral (R3c)

The cell volume varies in size with the addition of dopants and can expand or contract from the undoped unit cell (Table 11). The unit cell is compressed for BCO (Gd). Meanwhile, the unit cell BCO (Nd) is expanding. The doped position is located in A or B in  $ABO_3$ . The position that the atoms take and the strain generated in the unit cell are influenced by the size of the atom compared with the initial B atom.

**Table 11.** Lattice parameters and cell volume variations for different dopants in polycrystalline samples [91]

Compound	Dopant	Crystal Phase	Lattice parameters (Å)	Cell volume (Å <sup>3</sup> )
<b>BaCeO<sub>3</sub></b>	-	Orthorhombic	a = 8.724, b = 6.230, c = 6.211	337.57
<b>BaCe<sub>0.9</sub>Gd<sub>0.1</sub>O<sub>3</sub></b>	Gd	Orthorhombic	a = 8.746, b = 6.183, c = 6.170	333.65
<b>BaCe<sub>0.9</sub>Nd<sub>0.1</sub>O<sub>3</sub></b>	Nd	Orthorhombic	a = 8.744, b = 6.323, c = 6.161	340.63
<b>BaCe<sub>0.9</sub>Sm<sub>0.1</sub>O<sub>3</sub></b>	Sm	Orthorhombic	a = 8.753, b = 6.226, c = 6.220	338.97
<b>BaCe<sub>0.9</sub>Y<sub>0.1</sub>O<sub>3</sub></b>	Y	Orthorhombic	a = 8.749, b = 6.230, c = 6.211	338.54

### 2.3.2. Grain size of undoped and doped barium cerates

Different dopants modify the binding arrangements by adding strain to the structure in  $BaCeO_3$  (Fig. 9). Hence, the lattice parameters change as well. The strain can be released with a change in grain size. The grain size is 4  $\mu\text{m}$  for undoped  $BaCeO_3$ . The addition of dopants reduces grain growth below 2  $\mu\text{m}$  (Fig. 9 a). M. Amsif et al. [100], demonstrate the effect of ionic radii on the development of the microstructure. Atoms that are larger than Ce exhibit large grain sizes. Large atoms substitute A sites instead of B sites. Another way to develop the microstructure is by adding sintering aids (Fig. 9 b). The grain size increases up to 50  $\mu\text{m}$  for BCG doping with 5% mol Cobalt (Co). Large grains reduce the grain boundary resistance [101]. Co is incorporated into the grain and boundaries. This behaviour is opposite to the large size dopants, which increase the grain size by doping at the A site. A large concentration of Co can be found as well at the B site. Long sintering times and high

temperatures as well influence the grain size value as a consequence of the diffusion enhancement (Fig. 9 c). It was observed that at high sintering times, the dislocations start to appear. In fact, the relative density drops from 98.6% to 97.6% as a consequence of the dislocations (Fig. 10).

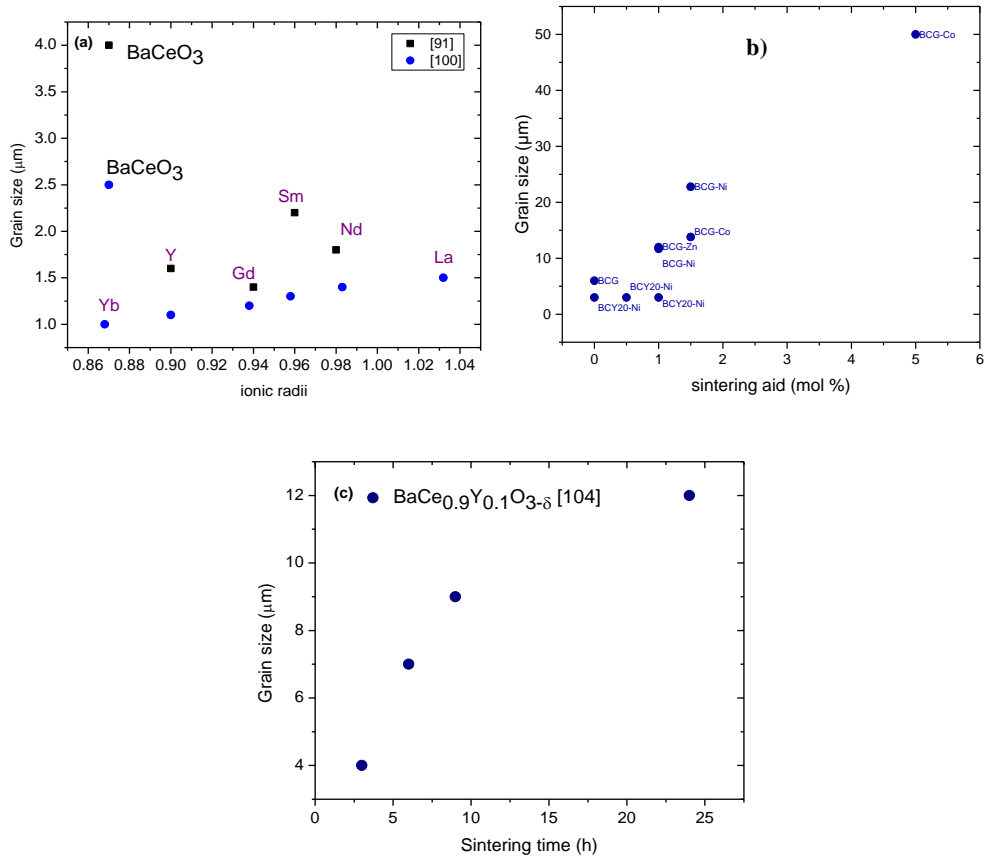
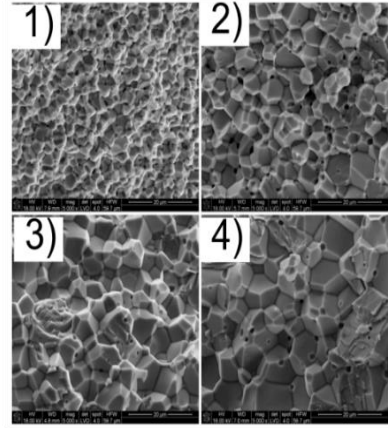
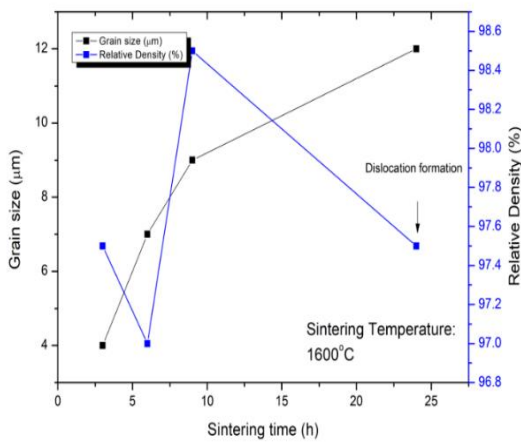


**Fig. 9.** Factors influencing grain size (a) ionic radii for doped barium cerate (BCO) [91, 100], (b) concentration of sintering aid of BCY20-Ni [102], BCG-Co [101], BCG-Co/Ni/Zn [103], (c) sintering time (1600 °C) [104]



(a)

(b)

**Fig. 10.** (a) Dependence of BCY10 grain size on the sintering times and its effect on the relative density; (b) SEM images show the microstructure at four sintering times: 1 h (1 b), 6 h (2 b), 10 h (3 b) and 24 h (4 b) [104]

As mentioned, the addition of energy results in an enhancement of the diffusion of the atoms and microstructure. This behaviour is explained with the coefficient of thermal expansion (TEC) (Eq. 16):

$$TEC = \frac{(L-L_0)/L_0}{T-T_0}; \quad (16)$$

where  $L$  is the initial length and  $L_0$  the final length, while  $T$  and  $T_0$  are the initial and final temperature. This parameter describes the effect of temperature on the expansion of the lattice parameter under a given atmosphere. There is a step from heating to cooling. Although it is expected that the material recovers its initial state (spalling resistance), this does not occur [105]. The expansion of the lattice occurs with the rise in temperature, which as well enhances the mobility of the atom. The grain size increased after cooling from dilatometry measurements. The dilatometry results showed an expansion of the lattice from 30 °C to 1000 °C in  $BaCe_{0.54}Zr_{0.36}Y_{0.1}O_{3-\delta}$  (TEC of  $8.53 \times 10^{-6} K^{-1}$ ). The dopants and oxygen vacancies modify the TEC turning out in the modification of the binding energy in the crystal lattice [106]. The TEC for  $BaCeO_3$  is  $13.8 \times 10^{-6} K^{-1}$  [107], which is higher compared to the Zr-containing.

### 2.3.3. Crystal size of undoped and doped $BaCeO_3$

The largest crystal size for  $BaCeO_3$  is 60 nm by spray pyrolysis [108]. Different high temperature/energy processes allow for enhanced diffusion towards crystal size growth. Another technique to obtain large crystals is a combination of solid-state with ball milling achieving a crystal size value of 54 nm [109]. The energy for the

ultrasonic-assisted reaction results in crystal size values of 20 nm. This energy was not sufficient to reach more than 50 nm [103] (Fig. 11). Different processes add different amounts of energy to the atoms to diffuse.

The addition of dopants, such as yttrium and gadolinium, reduces the crystal size values. These dopants elevate the activation energies for crystallization. Then, large energies are required to obtain large crystals (Fig. 11). Although, the self-diffusion process is faster for yttrium than for the other dopants, it seems that the energy is not enough to achieve large crystals. The use of spray pyrolysis to obtain large crystals is explained by the additional kinetic energy that the atoms receive during the spray process. The addition of metal, such as Ag, Au, V and Pt, seems to increase the activation energy of crystallization. This rise in activation energy can be attributed to the strong Ag, Au, V and Pt bonds that prevent diffusion of barium cerate atoms [110]. Then, BaCeO<sub>3</sub> nanocrystals were formed by sol-gel with a size of 16 nm for the undoped composition and its mixtures, i.e., V-BaCeO<sub>3</sub>, Ag-BaCeO<sub>3</sub>, Au-BaCeO<sub>3</sub> and Pt-BaCeO<sub>3</sub>, the values for which were 15 nm, 14 nm, 12 nm and 10 nm respectively.

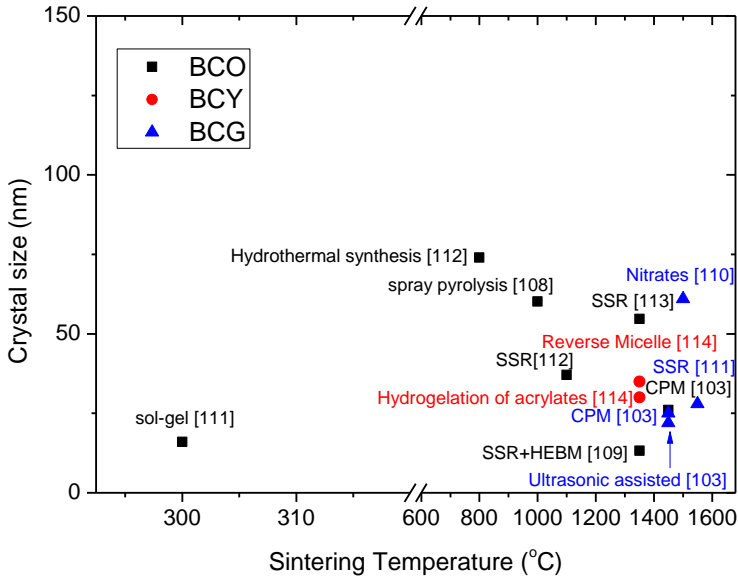


**Fig. 11.** Effect of different process and sintering temperatures on the crystal size for BCO, BCY and BCG: conventional precipitation method (CPM) [103], spray pyrolysis [108], high energy ball milling (HEBM) [109], synthesis by nitrates [110], sol-gel [111], hydrothermal synthesis [112], solid-state reaction (SSR) [111, 113], reverse micelle [114] and hydrogelation of acrylates [114]

The use of sintering aids, such as Co [14] on barium cerate doped gadolinium (BCG) enhances the crystal size to 216 nm. Then, Co has the effect of weakening the bonds to enhance the self-diffusion process. Moreover, additional oxygen vacancies are created when Co<sup>+2</sup> is present.

### 2.3.4. Density of undoped and doped BaCeO<sub>3</sub>

High-density materials (>90% relative density) are obtained in undoped and doped BaCeO<sub>3</sub> with La, Nd, Sm, Gd, Y, Yb and Tb [100] by freeze drying synthesis. Other atoms, such as Ca, have a strong effect on density. Barium cerate doped Ca showed a clear effect of dopant concentration on porosity. Less amount of dopant of 0.02 presents lower porosity. Above 0.05 to 0.15 of dopant, the porosity increases up by 46% with sintering temperatures of 1450 °C. A small amount of dopant results in a large grain size ( $x = 0.02$ ,  $d = 1.1 \mu\text{m}$ ) compared to high a concentration. The conductivity increases to  $\sim 2.2 \times 10^{-3} \text{ S/cm}$  with a dopant concentration of 0.1. After that, its value decreases [115].

Sintering aids reduce the surface energy and particle diffusion, which enhance relative density [103, 116]. Excessive aid content can proportionate a negative ion conductivity results due to the introduction of unwanted electronic conductivity. For example, the use of different metallic aids with the purpose of increasing the density of barium cerate doped gadolinium ( $\text{BaCe}_{0.9-x}\text{Gd}_{0.1}\text{O}_{3-d}$ ) [116] demonstrate that Zn improves the grain density. Zinc lowers the grain boundary as well as the activation energy value for ion conduction. Fig. 12 shows the effect of ionic radii on relative density. Ni and Co were the best sintering aids to enhance density in barium cerates.

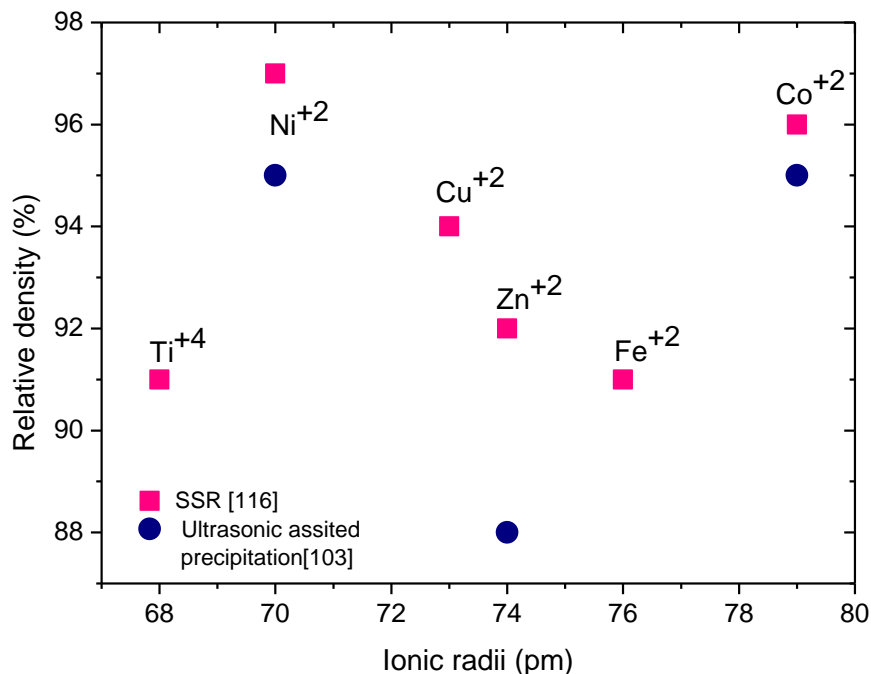


**Fig. 12.** Different sintering metal aids (0.01) vs. density (%) [103, 116] for  $\text{BaCe}_{0.9-x}\text{Gd}_{0.1}\text{O}_{3-\delta}$  formed by SSR and ultrasonic assisted precipitation

Sintering aids are usually located within the grains. Sintering aids located at grain boundaries have the disadvantage of decreasing the mechanical properties of the

material [117]. Liu et al. [118] report the effect of Ni, Fe and both on  $\text{BaCe}_{0.7}\text{Zr}_{0.1}\text{Y}_{0.2}\text{O}_{3-d}$  (BCZY). This material is porous after sintering at 1400 °C. The combination of Ni and Fe as well enhances the grain size. Then, the power density rises in the fuel cell [118].

Different sintering aids improve the density of doped barium cerates (Fig. 13). However, it is reported that for solid-state reactive sintering, CuO should be selected as a sintering aid for three main reasons: 1) it leads to a rapid densification of  $\text{BaCeO}_3$ -based materials at lower sinter aid concentration, 2) it is fully solubilized in the Ce-sublattice of  $\text{BaCeO}_3$ , and 3) it does not form any low-conductivity impurity phases under the heat treatments [119]. In addition to Medvedev et al. [119], there were studied  $\text{BaCe}_{0.6}\text{Zr}_{0.3}\text{Y}_{0.1}\text{O}_{3-d}$  with different sintered aids. Ni, Zn, Cu and Co were reported to form dense ceramics at low sintering temperatures, whereas for Fe and Mn to form dense ceramics at high sintering temperatures, other sintering aids that function at high sintering temperatures are as follows: Pd, Bi, Ag, Ta, Ti, Cr and Nb.

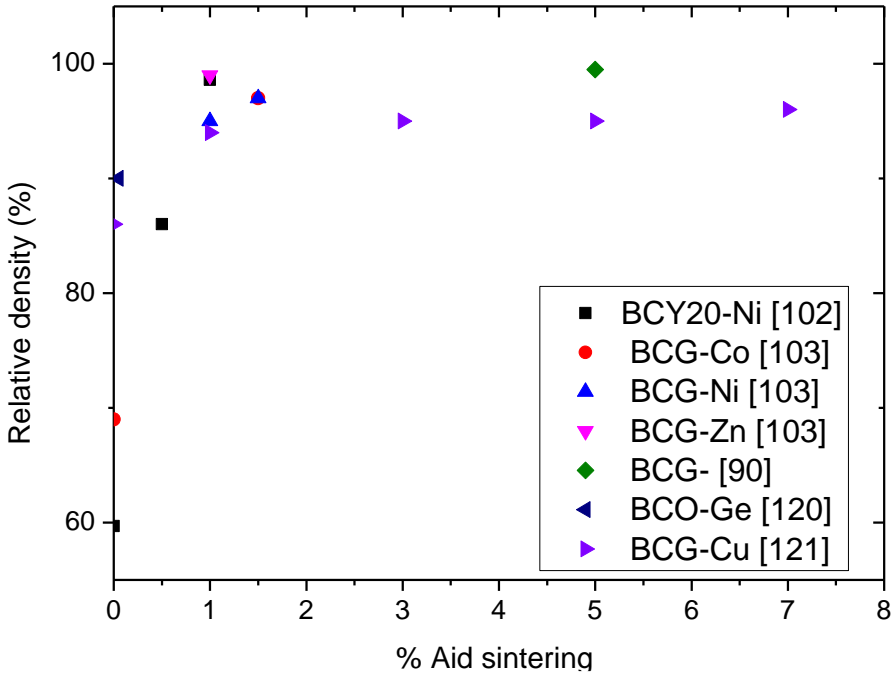


**Fig. 13.** Effect of % of sintering aid in the relative density for BCO, BCY and BCG [90, 102, 103, 120, 121]

High porosity reduces the ionic conductivity. The  $\text{BaCe}_{0.9}\text{Nd}_{0.1}\text{O}_3$  porous membranes fabricated by the screen printing process showed lower conductivity than their dense membranes and bulk part [122]. The manufacturing process and the temperature as well interfere in the density of the material. The freeze dried process proved to be the most effective method to achieve densities above 90% (Fig. 14). The relative density for BCY20 rises from 96.3% at 1250 °C to 98% at 1450 °C [123].

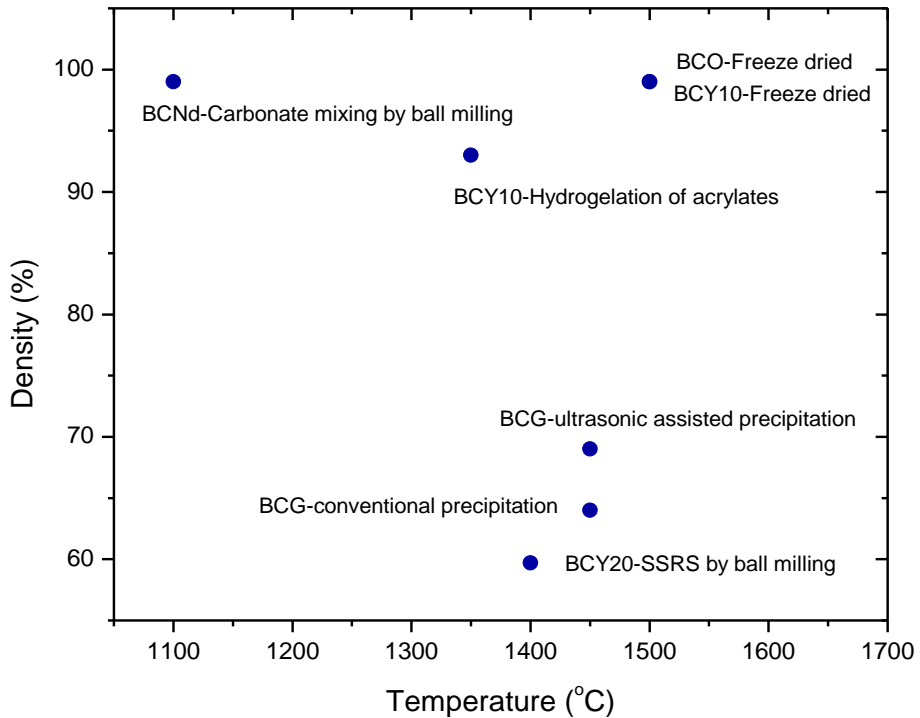


**Fig. 14.** Effect of temperature on the density by different synthesis strategies without the use of aid sintering: BCG – ultrasonic assisted [103], BCY10 – hydrogelation of acrylates [114], BCY – SSRS [102], BCO and BCY10 – freeze dried [124], BCY20 – ball milling (BCNd) [125], BCG – conventional precipitation [126]

## 2.4. Barium zirconates

### 2.4.1. Lattice parameters of undoped BaZrO<sub>3</sub> and doped BaZrO<sub>3</sub>

The phase for barium zirconates is Pm3m. The phase is stable even above 800 °C, contrary to the barium cerates. The lattice parameter expands with temperature and the size of the dopant as a strain effect following Vegard's law. After adding a larger size dopant to the yttrium size, there is a drop in the lattice parameter. Large atoms replace the A-site instead of B-site [127]. The atoms used for doping had lower atomic radii for barium zirconates than Ba (Fig. 15). The mismatch of ionic radii with Zr influences the solubility of the dopant in the cell [128]. Due to this, at the high % of yttrium, the strain in the cell increases, and there is an increase in lattice parameter. Sintering aids have a shrinking effect on barium zirconates with increasing concentration. The aids were added at the site B instead of the interstitials at high concentrations. The Zn-aids are the main exception to this trend with the occupation of interstitial sites causing expansion in the lattice. Strain in the lattice has been observed as well when the unit cell absorbs water causing an expansion.

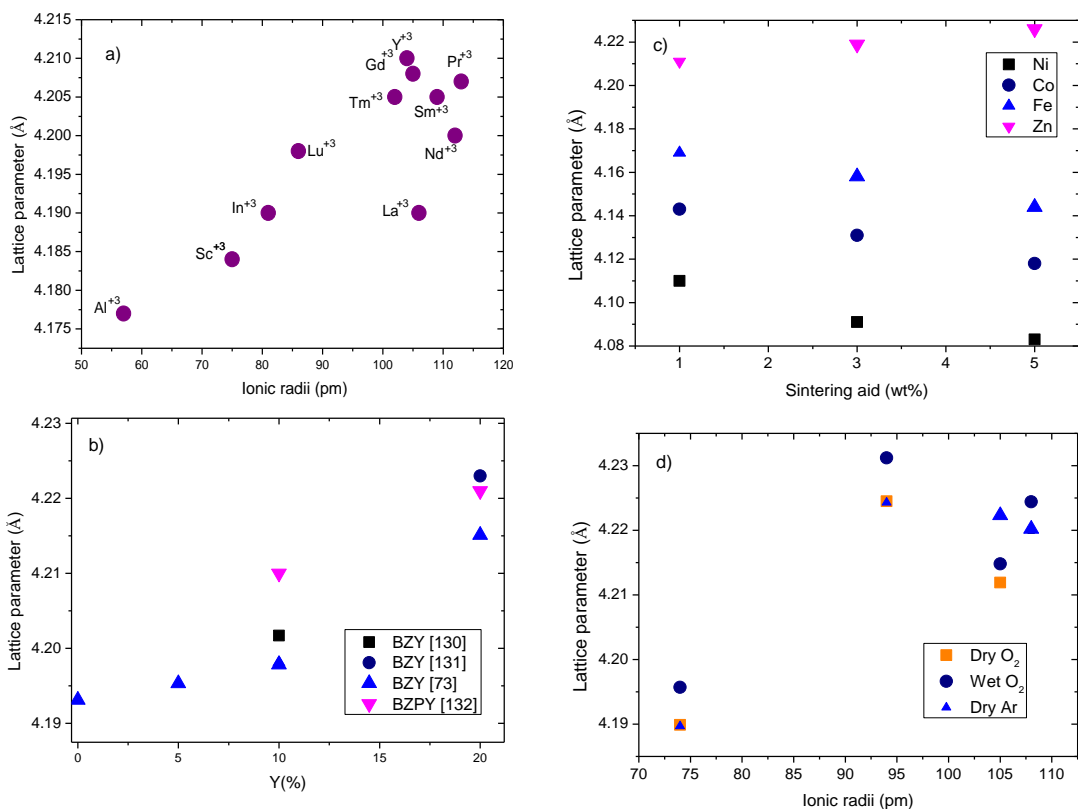


**Fig. 15.** (a) Different dopants vs. lattice parameters [127] and (b) dopant concentration vs. lattice parameter [73, 130, 131, 132], (c) sintering aids concentration that modifies the lattice parameters [133] and (d) dopants under wet and dry conditions that influence the lattice parameters [134]

## 2.4.2. Grain size of undoped BaZrO<sub>3</sub> and doped BaZrO<sub>3</sub>

Sm-, Nd- and La-doped barium zirconate exhibit grain size values of 4, 5 and 8  $\mu\text{m}$ , respectively. Meanwhile, Gd- and In-doped BaZrO<sub>3</sub> showed values of 1  $\mu\text{m}$ . The grain sizes were lower than 1  $\mu\text{m}$  for Lu, Sc and Tm [135] (Fig. 16).

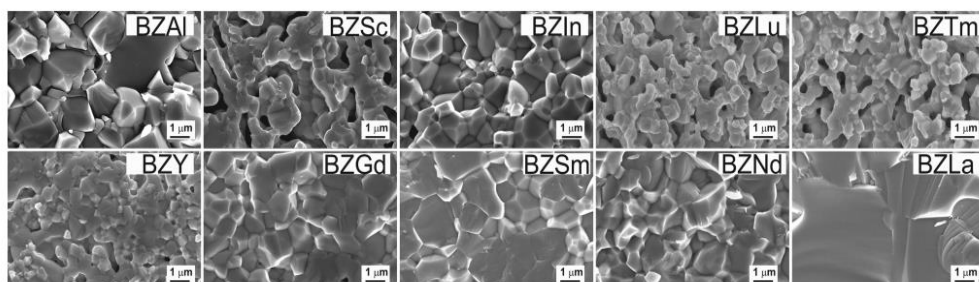


**Fig. 16.** SEM micrographs of BZO-doped sintered at 1600 °C for 8 h [135]

The formation of large grain size in La-BZO was explained by the substitution of Lanthane (La) at the A-site. The remaining amorphous phase of BaO liquified at high temperatures, enhancing the diffusion of the atoms. The grain size values rise at higher dopant concentrations (Fig. 17 a). Moreover, Ba deficiencies occur as an effect of high sintering temperatures and result in a grain size decrease up to 50% when the deficiency is 0.1 (Fig. 17 b).

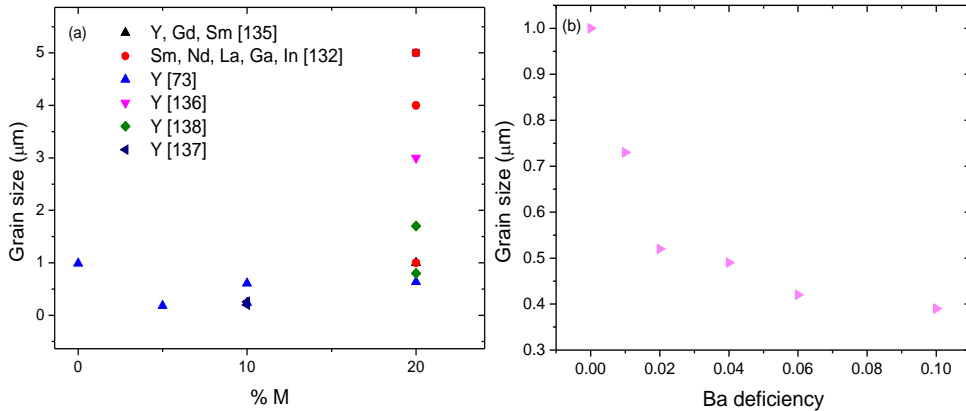


**Fig. 17.** (a) Grain size vs. dopant concentration [73, 132, 135, 136, 137, 138] and (b) barium deficiency vs. grain size

Relative densities correlate with the composition sintering and grain size formation. Small grain sizes form in porous structures [135]. Furthermore, the relative density is enhanced by large dopants that displace the atom at the A site of the perovskite (Fig. 18).

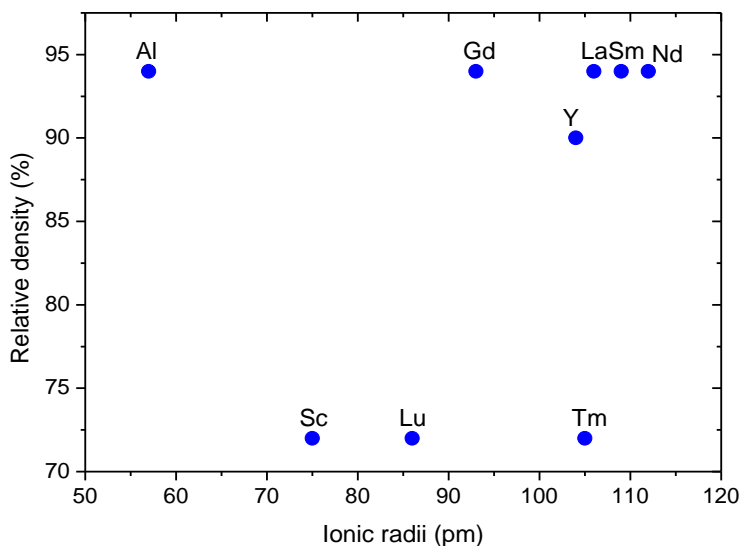


**Fig. 18.** Relative density of doped barium zirconate at different ionic radii [135]

## 2.5. Microstructure of barium cerate and barium zirconates thin films formed by PVD

The thin film microstructure is divided into randomly oriented and highly oriented. There are different processes to obtain highly oriented thin films with different microstructures. The microstructure depends on the deposition conditions. The conditions are summarized as the kinetic energy available for adatom diffusion obtained from substrate temperature, gas pressure, e-beam energy, composition, growth rate and heat diffusion (composition and thickness). Growth velocity implies a different process [139].

### 2.5.1. Formation of thin films of barium cerates and barium zirconates

The formation of the film begins with the arrival of adatoms to the substrate as an effect of condensation. Once there, there is diffusion, nucleation, coalescence and reevaporation (Fig. 19). The diffusion of adatoms varies with wetting effects between the substrate and the film or when the adatoms are strongly bound to each other instead of the film leading to the cluster formation and columnar growth [140].

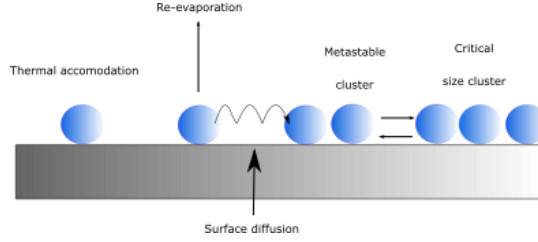


**Fig. 19.** Schematic representation of the arriving of adatoms to the substrate and their diffusion process

### 2.5.1.1. Nucleation

The specific shape of the microstructure begins with the formation of the nucleus that is described in the following lines [141]. The size and number of nucleus follow a driving force, which is the free-energy per unit volume,  $\Delta G_V$ . The interfacial forces are added for heteroepitaxial growth. Then,  $\Delta G_V$  becomes  $\Delta G^*$  (Eq. 17).

$$\Delta G^* = a_3 r^3 \Delta G_V + a_1 r^2 \gamma_{fV} + a_2 r^2 \gamma_{fS} - a_2 r^2 \gamma_{SV}; \quad (17)$$

where  $r$  is the average dimension of the nuclei. The interfacial energies are  $\gamma_{fV}$  for film-vapor,  $\gamma_{fS}$  for film-substrate,  $\gamma_{SV}$  for substrate-vapor (Eq. 18).

$$\gamma_{SV} = \gamma_{fS} + \gamma_{fS} \cos \theta; \quad (18)$$

where  $\theta$  is the wetting angle and depends on the materials involved (Eq. 19).

$$\Delta G^* = \frac{4(a_1 \gamma_{fV} + a_2 \gamma_{fS} - a_2 \gamma_{SV})^3}{27 a_3^2 \Delta G_V^2} \quad (19)$$

Surface energy and substrate chemistry affect the nucleation rate. The substrate can catalyse the vapor condensation by reducing  $\Delta G^*$  and reduction of the contact angle. Then, Eq. 20 is as follows:

$$\Delta G^* = \frac{16\pi(\gamma_{fV})^3}{3(\Delta G_V)^2} \left\{ \frac{2-3 \cos \theta + \cos^3 \theta}{4} \right\}. \quad (20)$$

In the opposite case, the mismatch of the bond between the substrate and the film adds elastic strain and then increases the barrier to nucleation or high  $\Delta G^*$ . In the equation, the  $\Delta G_S$  values are added together with  $\Delta G_V$ .  $\Delta G_S$  is the strain free-energy change per unit volume. Strained substrates can release their strain during the nucleation process at different temperatures. Then, the value of  $\Delta G^*$  is reduced. Other cases with reduced  $\Delta G^*$  includes impurities.

$\Delta G^*$  will affect the nucleation density, and it is associated with the Boltzman factor (Eq. 21):

$$N^* = n_s \exp - \Delta G^* / k_B T; \quad (21)$$

where  $n_s$  is the total nucleation site density.

### 2.5.1.2. Thin film growth

The wetting effect or interfacial energy between the film and substrate controls the growth modes in PVD (Fig. 20). Interfacial energy limits the adatom diffusion; with high wetting or easy diffusion of adatoms on the surface, they follow a layer-by-layer growth 2D. A lower wetting Stranski–Krastanov shape forms with island growth at the surface as a way to release the stress. A lower wetting substrate Stranski–Krastanov growth is formed. An island growth of less wetting substrate is achieved. PVD systems usually follow a Volmer–Weber growth mode [139]. The chemical potential ( $\mu$ ) gradient  $\frac{\delta\mu}{\delta n}$  is the driving force for obtaining an equilibrium microstructure. A high chemical potential means high flux of atoms at the surface, while low chemical potential is a low flux of atoms.

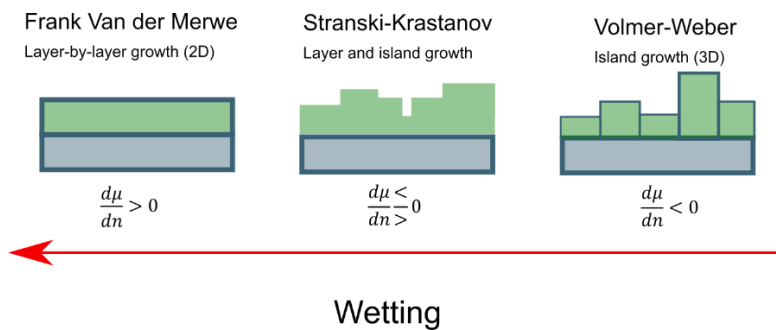


**Fig. 20.** Growth modes at different interfacial energies

Barium cerates and barium zirconates could be formed by using physical vapor deposition methods (PVD), such as magnetron sputtering, pulsed laser deposition (PLD) and electron beam (e-beam) evaporation method. The microstructure of PVD films follows the Thornton zone diagrams for Volmer–Weber growth [142]. The diagram considers the temperature of the substrate and the flow of energy added to the system. Control of deposition parameters (e.g., energy flux) is another way to control the microstructure instead of using high temperatures. The activation energy for the grain growth process is roughly 10 times less than the activation energy by solid-state calcination in a furnace. Therefore, the thermally activated ionization process that occurs on the growth surface was considered a rapid crystallization mechanism [143]. PVD processes add higher thermal energy (1–100 eV) to the crystal formation even at low substrate temperatures due to the significant contribution of the kinetic energy and electronic excitation.

Microstructure studies of thin-film growth have been reviewed by different authors [144] and involve the physical vapor deposition process, kinetic energies from the arrival particles, the ion energy added during sputtering and the temperature of the substrate. In the e-beam evaporation method, the microstructure follows the Thornton diagram in the region of low ionization energy where it is almost negligible. In these regions, three zones are dominant: Zone 1, 2 and 3. Another type of e-beam method is the reactive e-beam evaporation method, which includes the addition of different gases [145] and the change in the kinetic energies of the arriving particles and ion.

The diagram (Fig. 21) includes a very dense Zone T compared to the other zones. The diagram contains the ion etching zone when the thickness starts to turn negative. Thornton diagram as well indicates zones with high tensile stress, compressive stress and the zone in between. Film growth is a continuous process of surface growth.

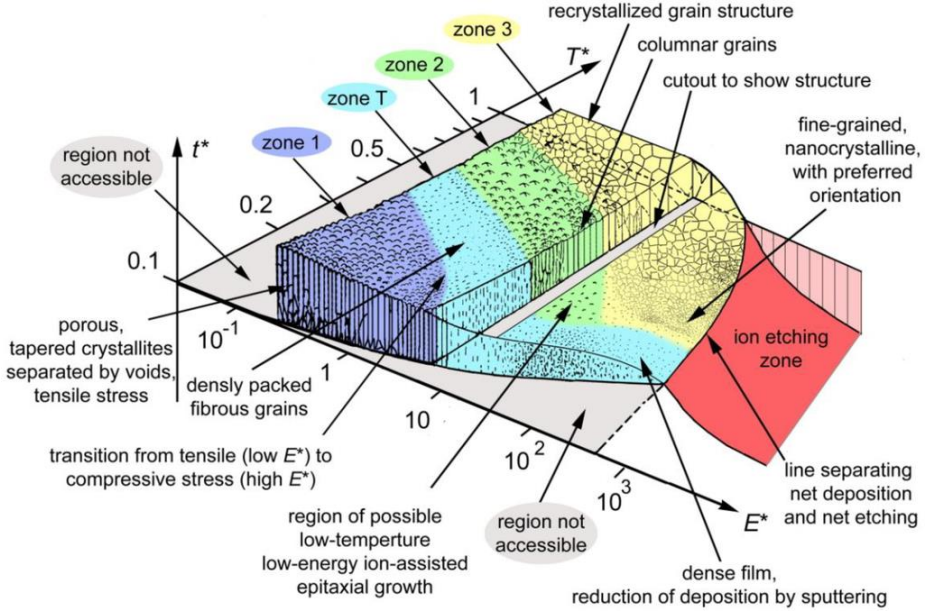


**Fig. 21.** Thornton zone diagram at different temperatures and ion energies for films formed by the physical vapor deposition [142]

The axes of the Thornton diagram are  $E^*$  and  $T^*$  that represent the kinetic energy of the arriving particles and  $T^*$ , which is the generalized temperature [142]. The general equation of kinetic energy of the particles [146] (Eq. 22) is as follows:

$$E^* = \frac{\sum_{\alpha} ((\epsilon_{kin,\alpha} M_{\alpha}) / (\epsilon_{ce} M_s)) J_{\alpha}}{\sum_{\alpha} J_{\alpha}}; \quad (22)$$

where  $M_{\alpha}$  is the mass of the energetic particles,  $M_s$  is the mass of atoms in the deposited film,  $\epsilon_{ce}$  is the heat of sublimation or the cohesive energy,  $J_{\alpha}$  is the ion current density on the substrate,  $N_{moved,\alpha}$  is the number of atoms that are rearranged on the surface,  $E^*$  is the normalized energy flux.

The generalized temperature or total temperature of the arriving particles is defined by (Eq. 23):

$$T^* = T_h + \frac{1}{k} \frac{\sum_{\alpha} (\epsilon_{pot} J_{\alpha} / N_{moved,\alpha})}{\sum_{\alpha} J_{\alpha}}; \quad (23)$$

where  $T_h = T/T_m$  is the film temperature normalized by the melting point  $T_m$  of the deposited film,  $N_{moved,\alpha}$  is the number of atoms that rearrange on the surface, and the potential energy (Eq. 24) is as follows:

$$\varepsilon_{pot} = \varepsilon_{ce} + (\varepsilon_{iz} - \phi); \quad (24)$$

where  $\varepsilon_{iz}$  is the ionization energy and  $\phi$  is the work function of the electron for neutralization. However, for the e-beam evaporation deposition method,  $T^*$  is the post-vapor expansion temperature. Another parameter that influences the microstructure is the level of pressure or vacuum inside the chamber. Dense film are formed under high vacuum pressures [147].

Moreover, the diagram shows variation in stress levels from one zone to another. Zone 1 has the presence of tensile stress, while Zone T is a transition between tensile and compressive stress, and Zone 2 is compressive stress. Tensile stress is consistent with rapid growth and small grain size formed at high growth rates and compressive for slow growth rate [148].

The formation of single phase randomly oriented barium cerates and barium zirconates films under different formation parameters as substrate temperature, gas pressure, gas composition influence the composition, microstructure [149] and intrinsic and extrinsic defects [150].

The first highly dense and highly oriented barium zirconate doped yttrium film was formed by physical vapor deposition, specifically by pulsed laser deposition (PLD) at 600 °C. Barium zirconate doped yttrium transparent ceramics thin film was formed with the main purpose of obtaining high proton conductivity at low temperatures with low ohmic resistance for solid fuel cell application. Therefore, in order to obtain high power, the electrolytes are tested under diverse temperatures, voltage and atmospheres to study the effect of microstructure and their composition as an electrolyte. The BZY20 film formed by PLD showed columnar growth [40]. The films formed between 400 °C and 600 °C. It did not show grain boundary resistance compared with the randomly oriented pellets. The films were formed on MgO and Al<sub>2</sub>O<sub>3</sub>. The author attributed the difference between the films to the orientation of the crystals. However, there is a difference in the microstructure. The first film formed on MgO was composed of very dense continuous columns (Zone 2). Conversely, the films formed on Al<sub>2</sub>O<sub>3</sub> were made up of small columns one on top of the other (Zone 1) (Fig. 22). The grain boundaries are known to add resistance to the conduction at temperatures lower than 200 °C.

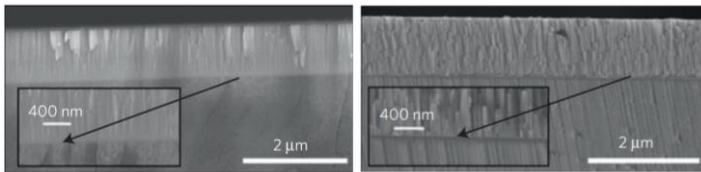


**Fig. 22.** BZY formed on MgO and Al<sub>2</sub>O<sub>3</sub> [40]

The same composition was formed at 900 °C by PLD resulting in hetero-epitaxial films with high density and crystallinity. It demonstrated the effect of crystallinity and high density on the activation energy and ionic conductivity. The work of Pergolesi et al. [40] turned out in the activation energy of 0.63 eV in MgO with a value similar to that of the sintered pellet. However, Kim et al. [151] increased the deposition temperature and managed to obtain larger grain sizes or Zone 2 (~20 nm lateral grain

size, Fig. 23) than BZY20 formed by Pergolesi. The activation energies were 0.44 eV for 130 nm thickness. Moreover, at 200 °C, no grain boundary resistance or oxygen diffusion was observed.

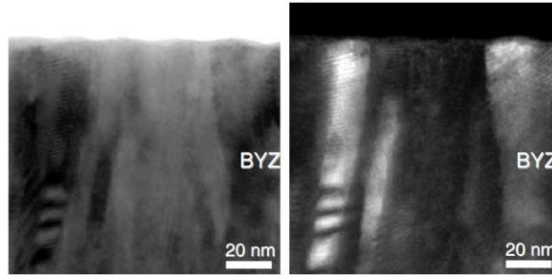


**Fig. 23.** SEM image of BZY with Zone 2 formed on MgO [151]

Multilayer formation of thin films demonstrated that the BCY between the electrodes and BZY achieved 3 times more power ( $62 \text{ mWcm}^{-2}$ ) [152] than the bare BZY at 475 °C. The total thickness of the electrolyte was 200 nm, and platinum electrodes were used on both sides and DC current. It was fabricated by PLD at 750 °C. The microstructures exhibited Zone 2 with lateral grain size between approximately 20–70 nm (Fig. 24). The formation of Zone 2 for BCY10 and BZY20 at 750 °C could be attributed to the high energy density in PLD parameters plus a rising in the deposition temperature compared to Pergolesi work.

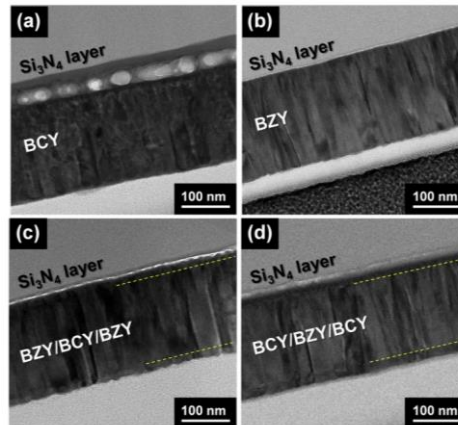


**Fig. 24.** Cross-section view of BZY, BCY/BZY/BCY textured layers formed on  $\text{Si}_3\text{N}_4$  substrates [152]

$\text{BaZr}_{0.2}\text{Ce}_{0.7}\text{Y}_{0.1}\text{O}_{3-\delta}$  formed by the e-beam evaporation deposition method [41] at 200 °C showed a highly dense (Zone 1) (Fig. 25 (a)) and highly crystalline structure with a gun power ranging from 0.9 to 1.05 kW (Fig. 25). However, additional sintering at 1300 °C was required to enhance density and crystallinity (Zone 3) (Fig. 25 (b)). Afterwards, the cell was tested above 500 °C. The maximum power was  $1.21 \text{ Wcm}^{-2}$  at 650 °C for 1  $\mu\text{m}$  thickness.

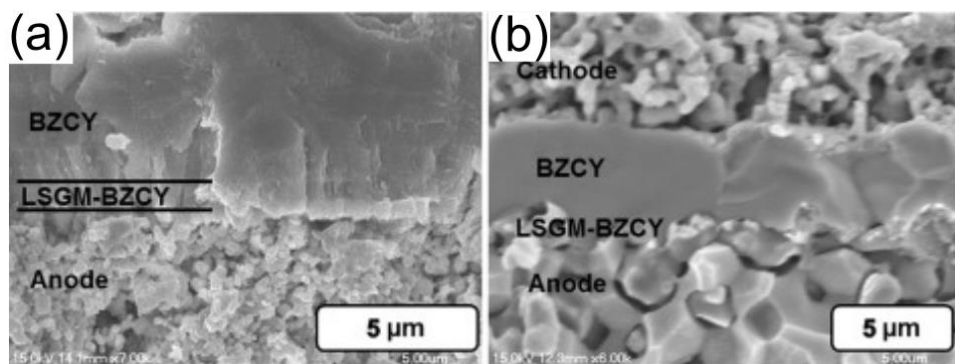


**Fig. 25.**  $\text{BaZr}_{0.2}\text{Ce}_{0.7}\text{Y}_{0.1}\text{O}_{3-d}$  film formed by e-beam evaporation deposition method on LSGM-BZCY layer as deposited (a) and after annealing (b) [41]

Another attempt to increase the power was the formation of a thick gradient electrode-electrolyte  $\text{Ni-BaCe}_{0.5}\text{Zr}_{0.35}\text{Y}_{0.15}\text{O}_{3-\delta} - \text{BaCe}_{0.5}\text{Zr}_{0.35}\text{Y}_{0.15}\text{O}_{3-\delta}$  with  $653 \text{ mWcm}^{-2}$  at  $600 \text{ }^\circ\text{C}$  with a total thickness of  $2 \text{ } \mu\text{m}$  [153], compared to a single layer that results in delamination with the anode surface (Fig. 26 (a)). Due to this, a possible gradient layer will offer better mechanical stability (Fig. 26 (b)). Lower thickness has shown to be weaker and tended to accumulate a large amount of stress.

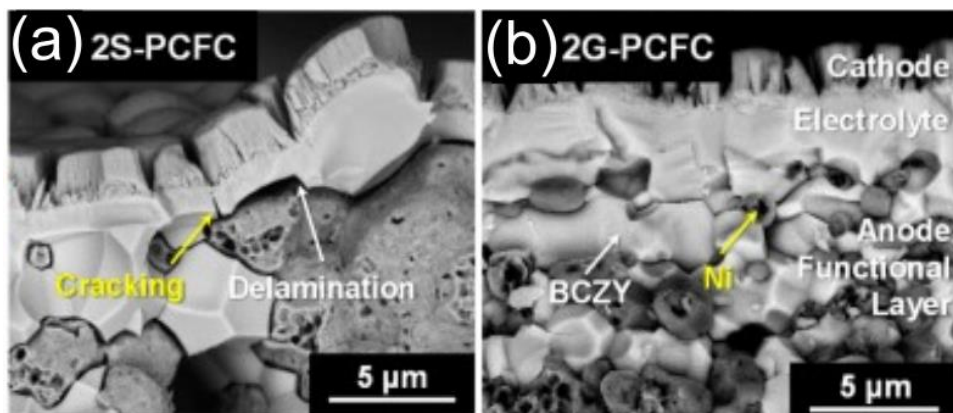


**Fig. 26.** (a) Single layer (2S) electrolyte  $\text{BaCe}_{0.5}\text{Zr}_{0.35}\text{Y}_{0.15}\text{O}_{3-\delta}$  and b) gradient (2G) $\text{Ni-BaCe}_{0.5}\text{Zr}_{0.35}\text{Y}_{0.15}\text{O}_{3-\delta} - \text{BaCe}_{0.5}\text{Zr}_{0.35}\text{Y}_{0.15}\text{O}_{3-\delta}$  [153]

An attempt to obtain lower BZY thickness ( $<50 \text{ nm}$ ) to reduce the ohmic resistance showed no cracking but bending in MgO supports due to the inhomogeneous strain (compression/tensile) in hetero-epitaxial films with a layer-by-layer growth [130]. In order to solve this problem, an intermediate layer (40% Ce in BZO) was added to obtain a relaxed film and avoid the build-up of high residual stress. The base support was MgO, and the lattice parameters of the films were closer to each other. However, the thickness was too low to release a small amount of strain ( $-0.3$  to  $0.7\%$ ). The activation energy for the relaxed structure of  $0.44 \text{ eV}$  was obtained with the thicknesses of  $22 \text{ nm}$  and  $87 \text{ nm}$ , for compression,  $0.47 \text{ eV}$  and  $0.42\text{--}0.39 \text{ eV}$  for tensile. Kim et al. [151] obtained similar activation values for relaxed structures at

130 nm on MgO with high crystallinity. The low activation in tensile stress showed that the shrinking of the lattice parameters as well play a role in the proton jump distance.

As mentioned before, the microstructure varies with the deposition parameters and the formed techniques that influence the final properties. Therefore, selecting the proper deposition parameters is essential to achieve the desired microstructure and properties. Table 12 includes the deposition parameters for the films formed by magnetron sputtering for barium cerate. The films formed by magnetron sputtering form according to the Thornton diagram. Barium cerates with Zone 1 were previously formed by magnetron sputtering. The thickness of this film was above 1  $\mu\text{m}$ . Moreover, an enhancement in crystallinity was observed with an increase in temperature to 500  $^{\circ}\text{C}$  under argon. The mass of argon allows more kinetic energy to be added to the sputtering process [154]. Thus, the film growth is enhanced compared to oxygen. While oxygen has two effects, i.e., increasing the interaction (collisions) of ejected atoms and molecules resulting in enhanced crystallinity [155] and enhanced direct exchange of background oxygen with the growth layer [156]. Therefore, the variation between the pressure of Ar and  $\text{O}_2$  as well helps to regulate the adatom energy or final microstructure.

Barium zirconates and barium zirconate doped yttrium were not formed before by the magnetron sputtering (Table 13). However, the mixtures of barium zirconates with titanium and ceria have been previously reported at 400  $^{\circ}\text{C}$ , 500  $^{\circ}\text{C}$  and 600  $^{\circ}\text{C}$ . Adding Ce enhances the roughness and reduces the dissipation factor [157] under AC-current, improving the mechanical properties. Single crystals of doped barium zirconates were previously formed by magnetron sputtering under a mixture of Ar and  $\text{O}_2$ . The formation of grains was observed when the pressure was mainly Ar and temperature of 500  $^{\circ}\text{C}$ . The mass of argon permits a higher momentum transfer compared to the oxygen for large atoms. Sputtering is a less energetic process compared to PLD and e-beam. As a result, the microstructures are located mainly in Zone 1. The main advantage of sputtering techniques is that they cover large areas.

**Table 12.** Formation parameters of different barium cerates thin films deposited using magnetron sputtering

	Vacuum pressure (Pa)	Gases	RF	Deposition rate ( $\mu\text{m/h}$ )	T ( $^{\circ}\text{C}$ )	Microstructure	Crystallinity	Ref.
$\text{BaCe}_{0.65}\text{Zr}_{0.2}\text{Y}_{0.15}\text{O}_{3-\delta}$	$10^{-5}$	Ar:O <sub>2</sub> 4:1 (2 Pa)	Up 10 Wcm <sup>2</sup>	0.7	400	Zone 1	Random oriented	[158]
$\text{BaCe}_{1-x}\text{Y}_x\text{O}_{3-\delta}$	$<10^{-4}$	Ar20–50 sccm O2 5 sccm (0.3–2 Pa)	15 V and 30 V	NA	RT	Zone 1	Random oriented	[149]
$\text{BaCe}_{0.9}\text{Y}_{0.1}\text{O}_{3-\delta}$	Not applied	Ar:O <sub>2</sub> 10:0 (1.4 Pa)	NM	0.4	500	NA	Crystalline, (110) oriented	[159]

**Table 13.** Formation parameters of barium zirconates thin films deposited using magnetron sputtering

	Vacuum pressure (Pa)	Gas type/Pressure (Pa)	RF (W)	Temperature ( $^{\circ}\text{C}$ )	Thickness (nm)	Roughness (nm)	Ref.
$\text{BaZr}_{0.2}\text{Ti}_{0.8}\text{O}_3$	0.67	Ar:O <sub>2</sub> 4:1 0.0003	80	400, 500, 600	150	0.57–0.62	[157]
$\text{BaZr}_{0.2}\text{Ti}_{0.8}\text{O}_{3-\delta}$ 0.5%Ce	0.67	Ar:O <sub>2</sub> 4:1 0.0003	80	400, 500, 600	150	0.40–0.53	[157]
$\text{Pb}_{0.6}\text{Ba}_{0.4}\text{ZrO}_3$	0.007	Ar:O <sub>2</sub> 0:4/ 0.39Pa	60	500	NA	NA	[160]

Barium cerates and barium zirconates were formed as well by pulsed laser deposition (PLD) (Table 14). A highly dense Zone 2 microstructure with a single phase is observed for BCY at 600  $^{\circ}\text{C}$ . Table 6 shows that Zone 2 is formed with an energy density of 2.5 J/cm<sup>2</sup> to 3 J/cm<sup>2</sup> under O<sub>2</sub> atmosphere.

**Table 14.** Formation parameters of barium cerates thin films deposited using PLD

	Vacuum pressure (Pa)	Gas (Pa)	Energy density (Jcm <sup>-2</sup> )	Deposition rate (nm/pulse)	Temperature (°C)	Thickness (nm)	Microstructure	Crystallinity	Ref
<b>BaCe<sub>0.9</sub>Y<sub>0.10</sub>O<sub>3-δ</sub></b>	<4.0 ×10 <sup>-3</sup>	O <sub>2</sub>	2.5	0.13	NA	200	Zone 2	Single phase	[152]
	1×10 <sup>-4</sup>	O <sub>2</sub> /1.0	2.5	NA	400	300	Zone 2	Single phase	[161]
		O <sub>2</sub> / 0.1	3	0.02	700	30	NA	Single phase	[162]

The T-Zone films for barium zirconates were previously formed by PLD (Table 15). The temperatures above 600 °C were needed to obtain a single phase. The deposition rates were lower than 3 Å/s. The table shows that a change in energy density from 1.5 J/cm<sup>2</sup> to 5 J/cm<sup>2</sup> changes the growth microstructure from layer-by-layer to columnar growth in Zone T.

**Table 15.** Formation parameters of barium zirconates thin films deposited using PLD

	O <sub>2</sub> pressure (Pa)	Energy density (J/cm <sup>2</sup> )	Deposition rate (Å/s)	Temperature (°C)	Thickness (nm)	Microstructure	Crystallinity	Ref
<b>BaZr<sub>0.8</sub>Y<sub>0.2</sub>O<sub>3-δ</sub></b>	10	5	3	650	1000	Zone T	Single phase	[163]
	0.1	3	0.22	700	30	NA	Single phase	[162]
	13–2.6	1–2.5	NA	25–600	100–600	NA	Amorphous to single phase	[164]
	13.3–3	1.8	0.3	600–900	130	Epitaxial	Amorphous to crystalline	[151]
	5.33	1.5	3	750	500	Epitaxial	Single phase	[165]

Layer by layer growth was observed when the energy density decreased, the temperature increased from 600 °C to 750 °C, and the thickness decayed to less than 200 nm. Therefore, less energy is needed to obtain layer-by-layer growth. The films were formed on different supports. Each support results in a different orientation (Table 16). The orientation of the support and lattice mismatch influences the surface energy and directs the growth direction of the crystal [166]. Epitaxial films of BZY and BCY were formed as ultra-thin films by PLD.

**Table 16.** Crystalline planes obtained by XRD for BZY thin films on different substrates

<b>Substrate</b>	<b>Crystal growth</b>	<b>Planes</b>	<b>Ref</b>
<b>Pt</b>	Randomly oriented	(110), (200), (211), (220)	[167]
<b>Al<sub>2</sub>O<sub>3</sub></b>	Layer by layer	(002), (004)	[168]
<b>Al<sub>2</sub>O<sub>3</sub></b>	Columnar	(111)	[40]
<b>MgO</b>	Layer by layer	(001), (002), (003), (004)	[131]
<b>MgO</b>	Layer by layer	(001), (002)	[130]
<b>MgO</b>	Columnar	(001), (002)	[40]
<b>MgO (001)</b>	Columnar	(001)	[162]
<b>BCZ-MgO</b>	Layer by layer	(001), (002)	[130]
<b>GSO</b>	Layer by layer	(001), (002), (003), (004)	[131]
<b>STO</b>	Layer by layer	(001), (002), (003), (004)	[131]
<b>NGO</b>	Layer by layer	(001), (002), (003), (004)	[131]
<b>NGO</b>	Columnar	(001), (002)	[40]
<b>LAO</b>	Layer by layer	(001), (002), (003), (004)	[131]
<b>BCY (pellet)</b>	Randomly oriented	(110), (200), (211), (220)	[163]
<b>BCY (thin film)</b>	Columnar	(001)	[162]
<b>BZY-Ni (pellet)</b>	Randomly oriented	(100), (110), (111), (200), (211), (220)	[169]

A mixture of layer-by-layer random crystal growth was reported at 900 °C by PLD for barium zirconate doped yttrium [151]. There is a hypothesis that the layer-by-layer region next to the substrate helps in the proton conduction (Fig. 27).

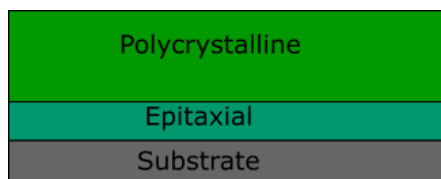


**Fig. 27.** Schematic representation of the mixture of hetero-epitaxial (layer by layer growth) and polycrystalline on BZY formed by PLD at 600–900 °C

### 2.5.1.3. Strain in formed barium zirconate thin films

Strain in lattice parameters for the same composition has shown variation with an oxygen partial pressure during PLD deposition [131]. Fluri et al. [130] report that in BZY with layer-by-layer growth, the thin film has a mismatch between the substrates, resulting in compressive or tensile strain. This strain influences the lattice parameters and the phase (Table 17). The lattice mismatch demonstrates that the stress provides a force for the atoms to move, and it comes from the support.

**Table 17.** Lattice parameter variation for BZY20 on different oriented support [131]

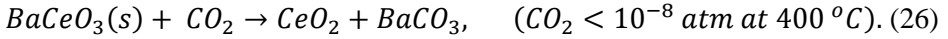
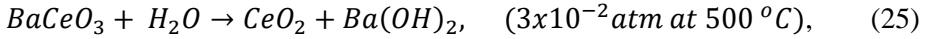
Substrate	In-plane (Å)	Out-of-plane (Å)
<b>MgO</b>	4.166+/-0.005	4.200+/-0.002
<b>GSO</b>	4.168+/-0.003	4.192+/-0.002
<b>STO</b>	4.163+/-0.002	4.193+/-0.002
<b>NGO</b>	4.195+/-0.003	4.206+/-0.002
<b>LAO</b>	4.189+/-0.005	4.193+/-0.003

Monolayers can only accommodate a 9% mismatch. Above this percentage, the misfit dislocation forms. Thinner films tend to bend the support due to the high stress levels. The stress for thicker films releases through the thickness with the rearrangement of the atoms, whereas for thin films, the Volmer–Weber growth forms films that are free to rearrange in the out-of-plane to release some of the stress, while the in-plane direction is under biaxial strain [170]. However, with the increasing thickness, the elastic energy increases and makes relaxation energetically favourable.

## 2.6. Degradation of barium cerates and barium zirconates

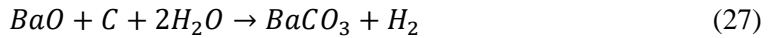
Barium cerates and barium zirconates degrade in the presence of CO<sub>2</sub>. The stability under CO<sub>2</sub> for each composition is different. The same degradation mechanism was observed in bulk and thin films.

What concerns BaCeO<sub>3</sub>, Loureiro et al. [171] studied the pressure and temperature limits of CO<sub>2</sub> and water for barium cerates to avoid the formation of barium carbonates and their degradation with water: H<sub>2</sub>O < 3 x 10<sup>-2</sup> atm at 500 °C (Eq. 25). The high basicity of BaCeO<sub>3</sub> was reported to be the main reason for its reaction with CO<sub>2</sub> above 400 °C (Eq. 26).

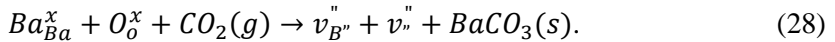


BaCeO<sub>3</sub> can be applied in hydrogenation and dehydrogenation reactions at low humidity pressure (10<sup>-4</sup> atm). Although basicity was the main issue CO<sub>2</sub> reaction, the microstructure of BCY10 showed that the excess of Ba results in rapid degradation of the mechanical properties due to BaCO<sub>3</sub> formation [149].

Another reaction involved in the degradation of barium cerates is the reaction with carbon. BaO oxidizes carbon with the formation of CO and Ba. The products adsorb and decompose water to form BaCO<sub>3</sub> and H<sub>2</sub> [172] (Eq. 27). The reaction is reversible above 1100 °C [173].



While Barium zirconate is more acid to react with CO<sub>2</sub>, the doped compositions react with pure CO<sub>2</sub> from 550 °C [174]. The formation of BaCO<sub>3</sub> creates Ba deficiencies in barium zirconates and barium cerates. The reaction is described by the following reaction (Eq. 28):



Afterwards, Ba deficiencies are filled with yttrium ions [12, 175] (Eq. 29). The reaction is faster than undoped BaZrO<sub>3</sub> (Fig. 28). Ba deficiencies form at high sintering temperatures due to the low boiling point of BaO (730 °C).

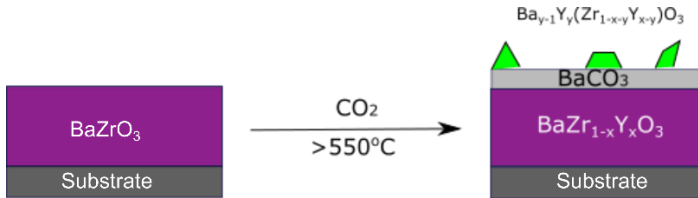
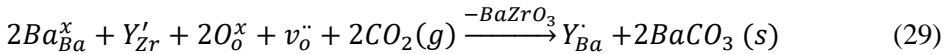


**Fig. 28.** Schematic representation of degradation morphology for barium zirconate doped yttrium [176]

The disadvantage of BaCO<sub>3</sub> formation is the degradation of the mechanical and electrical properties. Another source of degradation is the addition of NiO as a sintered aid. It was observed that under hydrogen atmospheres, NiO tends to reduce and degrade barium zirconates [177]. Opposite to barium zirconates, NiO enhances the stability of barium cerates [58]. In barium cerates, Ni migrates to the surface after high sintering temperatures. Therefore, the surface is protected against CO<sub>2</sub> and water attack towards BaO.

The control of stoichiometry is crucial in barium cerates and barium zirconates in both directions. The excess or lack of Ba leads to the formation of BaCO<sub>3</sub> due to the presence of BaO. The control of the degradation process is important to avoid the

degradation of the material properties. The control of stoichiometry at high sintering temperatures is not an easy task.

## **2.7. Summary of the literature review**

The conductivity in  $\text{BaCeO}_3$  and  $\text{BaZrO}_3$  is closely related to their microstructure. The microstructure varies from bulk to thin film, and it is modulated by dopants, temperature and technological parameters.

The microstructure influences the defect formation, such as oxygen vacancies, intrinsic and extrinsic defects, strain and dislocations [A2]. The microstructure of  $\text{BaCeO}_3$  and  $\text{BaZrO}_3$  affects the chemical reactivity and mechanical stability. The formation of barium cerates and barium zirconates thin films by physical vapor deposition adds specific orientations to the films, growth modes, grain shapes, strain and defects to improve and study their properties for a fast proton conductive material.

### 3. EXPERIMENTAL TECHNIQUE AND METHODS

#### 3.1. Sample preparation

The initial powders, (BCO), 99.9% purity, barium cerate doped with 10% (BCY10) and 20% yttrium (BCY20), 99.9% purity, (Goodfellow Cambridge Ltd, Huntingdon, UK), BZO, 99.9% purity, barium zirconate doped with 20% yttrium (BZY20) and barium zirconate doped with yttrium and cerium (BZCY), 99.9% purity, were used as target materials to form the thin films.

The already prepared pellet was used as a target for barium cerates. The target container was filled up to 2/3 of its capacity with the pellets to reduce any particle contamination to the substrate.

The powders were pressed for the formation of pellets with a size of 1 cm length and diameter for barium zirconates. Three pellets were added to the container inside the chamber.

#### Deposition at 25–400 °C substrate temperature

An e-beam physical evaporation deposition system (Kurt J. Lesker 61 EB-PVD 75, Hastings, UK) was used for all the films. Substrate temperature was from 25 °C to 400 °C. The acceleration voltage of the electron gun was 7.9 kV. The current was adjusted in the range of 30–100 mA. The initial pressure was  $1 \times 10^{-4}$  Pa and working pressure  $1 \times 10^{-2}$  Pa. The substrates were cleaned with acetone bath before moving them to the chamber. Once in the chamber, having obtained high vacuum, the substrates were treated with Ar<sup>+</sup> plasma for 10 min before starting the film deposition. The growth rates were 2 Å/s, 4 Å/s, 8 Å/s and 12 Å/s. The substrates rotate during deposition at 8 rpm. Four different Fe-Ni alloy substrates with different thermal expansion were used to form BaCeO<sub>3</sub>. The substrates were Invar, Glass sealing alloy, Inconel 600 and Stainless steel AISI A301 (Goodfellow Cambridge Ltd, Huntingdon, UK) (Table 18). The thickness and deposition rate were controlled with an INFICON (Inficon, Bad Ragaz, Switzerland) crystal sensor.

**Table 18.** Thermal expansion coefficients (TEC) and chemical composition for Invar, Glass sealing alloy (GSA), Inconel 600 and Stainless steel A302

Substrate	Thermal expansion coefficient (TEC) 10 <sup>-6</sup> , K <sup>-1</sup> / TEC range	Chemical composition
Invar	1.7–2.0/20–90 °C	Fe, 64%, Ni 36%, traces of Mn, Si and C
Glass sealing alloy	4.8/20–200 °C	Fe 54%, Ni 29%, Co 17%, traces of Cu, Mn, Si and C
Inconel alloy 600	11.5–13.3/20–100 °C	Fe 8%, Ni 72%, Cr 16%, traces of Cu, Mn, Si, C and S
Stainless steel AISI 301	18/20–100 °C	Fe 73%, Ni 7%, Cr 17%, Mn 2% and Si 1%.
BaCeO <sub>3</sub>	11.2 [178]	

## Deposition at 500–700 °C substrate temperature

The e-beam physical evaporation deposition system (Kurt J. Lesker 61 EB-PVD 75, Hastings, UK) was used to form the films. The substrate temperatures were 500 °C, 600 °C and 700 °C that were achieved by ultrahigh vacuum heater (15 V) and controlled model 101303-23C (Heatwaves labs, Inc. CA, US). The acceleration voltage of the electron gun was 7.9 kV. The current was adjusted in the range of 30–100 mA. The initial pressure was  $1 \times 10^{-8}$  Pa, and the working pressure was  $1 \times 10^{-5}$  Pa. The substrates were cleaned with an ultrasonic bath of Isopropanol and after with acetone bath one after the other before moving them into the chamber. The deposition rate was 2 Å/s. The used substrate was Inconel 600 of 0.2 mm thickness (Goodfellow Cambridge Ltd, Huntingdon, UK), MgO (001), YSZ (001) and Al<sub>2</sub>O<sub>3</sub> (0001). The thickness and deposition rates were controlled with an INFICON (Inficon, Bad Ragaz, Switzerland) crystal sensor.

## E-beam evaporation deposition process

The e-beam evaporation deposition method consists of the vaporization of an ingot by introducing electrons with high kinetic energy. As a result of this interaction, ions, X-ray and IR emissions are released (Fig. 29). The emissions interact with the vapor and form a collision region. The deposition rate and the composition influence the size of the collision region. The size of the collision region is influenced by the deposition rate and composition. Released electrons are captured by the copper covers to avoid the increment of temperature on the substrate.

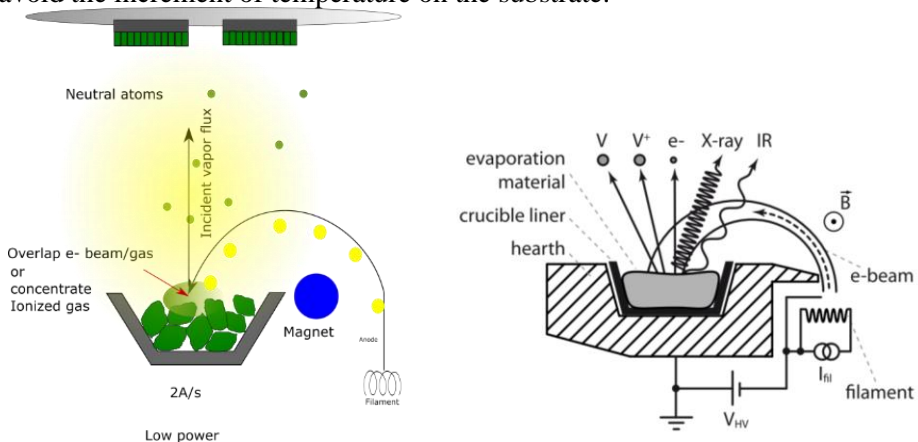


**Fig. 29.** Schematic representation of e-beam evaporation deposition method and e-beam interaction with the evaporated target gas [179]

The formation of the collision region usually is far from the substrate and does not interact with it. However, it can interfere with the ejection speed of the atoms. The collision regions change the angle of ejection and add a negative value to the total ejection speed (Fig. 30). At low deposition rates, this effect is minimal. In the collision region, the atoms are in hydrodynamic flowing velocity  $\vec{u}$  with a decrease in the thermal velocity  $\vec{v}_t$ . Therefore, the last speed is  $\vec{v} = \vec{u} + v_t$ .

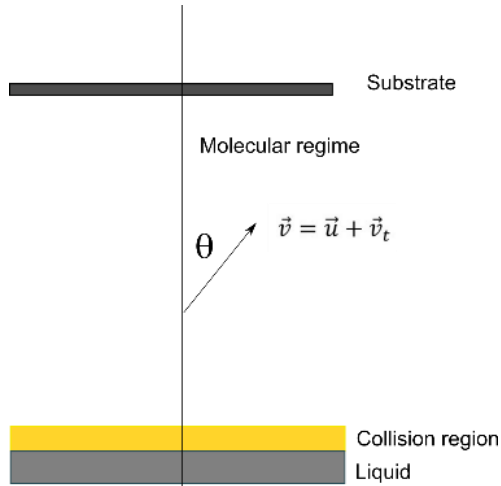


**Fig. 30.** Schematic representation of vapor source speed that is modified with collision regions;  $\vec{u}$  is hydrodynamic flow velocity, thermal velocity is  $\vec{v}_t$ , and final speed is  $\vec{v} = \vec{u} + \vec{v}_t$  [180]

The melting process occurs when the e-beam is directed towards the target by bombarding electrons, which increase the temperature and reduce the resistance in the target. The temperature at the target increases until it reaches its melting point. Then, there is no more temperature rise. This is explained by the decrease in temperature at the target due to the evaporation [181]. The acceleration of atoms in some cases is a consequence of the voltage applied between the target and the substrate [182]. One main feature of EB-PVD is its high energy transfer [183]. The electrons are not in thermal equilibrium with the neutral species and ions [184]. The control in the ionization or collision region increases the possibility to manipulate the speed of atoms and the chemical composition that influences the crystal phases and microstructure of the formed films [185]. However, the ionization region is localized further to the substrate compared to the sputtering or plasma laser deposition. Then, the effect of ions and the speed is minimum compared to other PVD process. Moreover, vacuum pressure is much lower in the range of ultra-high vacuum ( $1 \times 10^{-8}$  mbar) than other process and direct the speed of the atoms out of the ionization region [147].

### 3.2. Profilometer

Profilometer XP-200 (Ambios 73 Technology) was used to investigate the thickness of the formed films. The thickness was measured three times in three different points where the film-substrate step was observed. The thickness was calculated as a difference between the maximum height (film) and minimum height (substrate) contour.

The system is described as an electromagnetic sensor, which follows the displacement of the tip as it traces the contour of a film-substrate step. The film thickness is directly measured as the height of the resulting step-contour trace [186]. The x and z direction is recorded in 1D scan. The x-y resolution is  $5 \mu\text{m}$ , and the z

resolution of 0.01  $\mu\text{m}$ . Compared to atomic force microscopy with a stylus force of 1  $\mu\text{N}$ , the mechanical stylus has a force of 5 mN [187]. The parameters are added in Table 19.

**Table 19.** Technical parameters

Technical parameters	Value
Styli	Diamond
Vertical range ( $\mu\text{m}$ )	400 max
Vertical resolution ( $\text{\AA}$ )	1
Used scan length (mm)	1
Stylus force range (mg)	0.05 to 10
Repeatability ( $\text{\AA}$ )	+/-10

### 3.3. X-ray diffraction (XRD)

X-ray diffractometer (XRD) is D8 Discover Bruker. The measurements were performed using Cu  $K\alpha$  ( $\lambda = 0.154059$  nm) radiation in the  $2\theta$  range of  $20\text{--}70^\circ$  with a  $0.01^\circ$  step.

The diffraction principle is based on bending on the monochromatic X-ray wave after encountering an atom. The wave has a wavelength of  $\lambda = 0.01\text{--}10$  nm, comparable to the size of the atoms, frequency in the range of  $3 \times 10^{16}\text{--}3 \times 10^{19}$  Hz and photon energies in the range of 100 eV–100 keV [102]. Therefore, the energetic X-rays can reach deep into the materials, analyse the bulk structure and interact with the electrons of atoms. The collision results in an elastic scattering (momentum transfer,  $Q$ ). The resulting scattered wave can constructively interfere when the atoms have a crystalline distribution with the formation of the diffracted beam. Then, the Bragg equation expresses the constructive interference (Eq. 30).

$$n\lambda = 2d\sin\theta; \quad (30)$$

where  $n$  is the order of diffraction,  $\lambda$  is the wavelength,  $d$  is the interplanar spacing and  $\theta$  is the scattering angle.

Considering  $d$ -spacing calculation for a  $\theta$  approximation after the fitting process, the lattice parameter is calculated according to the expected phase. For example, in orthorhombic structure, the lattice parameters are  $a$ ,  $b$  and  $c$ ; for  $h$ ,  $k$ ,  $l$ , the peak values are calculated with Eq. 31.

$$\frac{1}{d_{hkl}^2} = \frac{h^2}{a^2} + \frac{k^2}{b^2} + \frac{l^2}{c^2} \quad (31)$$

The crystal sizes and lattice parameters were obtained by XRD diffractogram analysis using software TOPAS 4.1 and Le Bail method [189] to fit the experimental data. The technique consists of analysing the intensities and fitting them into a model. The model uses theoretical lattice parameters, phase information and functions to integrate until it obtains the closest approximation. In the first step of the fitting, the observed intensity is calculated according to Eq. 32.

$$I_k(obs) = \sum_j \{w_{j,k} \cdot S_k^2(calc) \cdot y_j(obs)/y_j(calc)\}; \quad (32)$$

where  $w_{j,k}$  is a measure of contribution (standard deviation) of the Bragg peak at position  $2\theta_k$  to the diffraction profile  $y_j$  at position  $2\theta_j$ . The sum is for all  $y_j(obs)$ , which can theoretically contribute to the integrated intensity  $I_k(obs)$ . For the iteration,  $S_k^2$  values are calculated and re-injected in the equation to obtain the closest approximation.

The unit cell parameter values for each theoretical composition and substrates composition were added during the fitting process.

The parameters that were entered into software include:

- Profile function: Lorentz (natural solution to the differential equation);
- Background corrections: Chebyshev polynomial from 9–12 points;
- Peak asymmetry: fundamental Approach (Cheary–Coelho);
- Errors calculation: the weighted profile R-factor ( $R_{wp}$ ) and goodness-of-fit (GOF or  $\chi$ ).

## Different R-Bragg factors

### $R_{wp}$

R-Bragg factors are used to know how good is the fitting or the error. The standard deviation of the Bragg peak intensity measurements is known as standard uncertainty [190]. The intensities ( $y_i$ ) are measured as an infinite number of times for each observed and calculated  $\theta_i$  value. The calculation is summarized in this equation:  $w_i = 1/\sigma^2[y_{o,i}]$ , o term is for observed intensity and  $\sigma$  is the standard deviation.  $R_{wp}$  values that are lower than 4 are ideal (Eq. 33).

$$R_{wp} = \sqrt{\frac{\sum_i w_i (y_i(obs) - y_i(calc))^2}{\sum_i w_i y_i(obs)^2}} \cdot 100; \quad (33)$$

where  $w_i = \frac{1}{\sigma^2[y_i(obs)]}$ . The experimental R factor calculation (Eq. 34) is needed to obtain the goodness-of-fit (G.O.F).

$$R_{exp} = \sqrt{\frac{\sum_i w_i y_i(obs)^2}{n-p}} \cdot 100; \quad (34)$$

where  $n$  is the number of profile data points,  $p$  is number of refined parameters.

### GOF

Goodness-of-fit (G.O.F) (Eq. 35) exhibits the relation between  $R_{wp}$  and  $R_{exp}$ , were lower G.O.F or  $\chi$  is ideal.

$$GOF = \frac{R_{wp}}{R_{exp}} \quad (35)$$

In case of unknown phase, each phase can be analysed until the lower GOF is obtained.

## Crystal size (D)

Crystal sizes were calculated on the base of the Scherrer Eq. 36.

$$D = \frac{(k\lambda)}{\beta_{hkl} \cos\theta}; \quad (36)$$

where  $\lambda = 0.15\text{nm}$ ,  $\beta_{hkl}$  is the full width at half maximum (FWHM) of the diffraction peak.  $\beta_{hkl}$  values were calculated for each peak according to the peak refined values from Le Bail method and Lorentzian function (Eq. 37).

$$L(b_L, x) = \frac{2}{\pi} \frac{1}{1+(2x/b_L)^2}; \quad (37)$$

where  $b_L = H_L$ ,  $H_L$  is full-width at half-maximum.  $x = \theta - \theta_h$ , which is the difference of the actual position with the expected position, and a and b are the coefficients (Eq. 38).

Then,

$$D = 360K\lambda/(\pi^2 L). \quad (38)$$

## Texture coefficient

The texture coefficients (TC) (Eq. 40) determine the preferential crystallite orientation in the thin films. The intensities were obtained from the diffractogram after removing all background. The values are obtained for each plane.

$$TC_{(h_i, k_i, l_i)} = \frac{I(h_i, k_i, l_i)}{I_o(h_i, k_i, l_i)} \left\{ \frac{1}{N} \sum_{i=1}^N \frac{I(h_i, k_i, l_i)}{I_o(h_i, k_i, l_i)} \right\}^{-1}; \quad (39)$$

where  $I(h_i, k_i, l_i)$  is the intensity of  $(h_i, k_i, l_i)$  peak determined by the diffractograms.  $I_o(h_i, k_i, l_i)$  corresponds to the standard intensities from ICDD data base. N is the number of peaks that appears in the obtained diffractogram.

## 3.4. Scanning electron microscopy (SEM)

The surface topography and cross-section images were obtained by using the scanning electron microscope (SEM) “Hitachi S-3400N” (Hitachi High-Technologies, Tokyo, Japan). The principle of scanning electron microscopy is based on the interaction of e-beam with an acceleration voltage from 0.1 keV to 50 KeV with the atoms of the film. The interaction of electrons with the electrons from the target atoms results in the release of electrons with different energies as secondary electrons (SE), back scattering electrons (BSE), Auger electron (AE) and low-loss electrons (LLE) (Fig. 31). The distance between the sample and the detector is short. Then, a high amount of SE is expected.

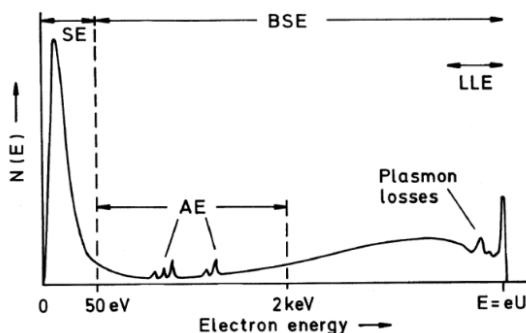


**Fig. 31.** Schematic representation of the electrons emitted at different energies [191]

The surface topography and cross-section images were obtained using the scanning electron microscope (SEM) Hitachi S-3400N. In-plane grain sizes were evaluated by ImageJ software. The cracking of the film was done to obtain the cross-section. The surface and cross-section of the samples were directly measured without any coating to reduce the charging effects. ImageJ software was used to measure the grain size. Grain size statistical analysis was obtained in Origin8. The mean value and error were calculated with 30 measurements or  $n = 30$ .

### 3.5. Energy dispersive X-ray spectroscopy (EDS)

The elemental composition was analysed by using the energy-dispersive X-ray spectroscope (EDS) “BrukerXFlash QUAD 5040” (Bruker AXS GmbH, Billerica, MA, USA). The e-beam gun interaction with the electrons in the atom removes one electron from its K shell. Then, the vacancy is filled by an electron dropping from L shell. The decay on the energy releases a photon or X-ray. The energy of the X-ray is the difference between the initial energy for L-shell electron and the final state to K-shell (Eq. 40).

$$E_v = E_k - E_L = eV \quad (40)$$

The emission of different X-rays varies with the atomic number. Large atomic number increases the X-ray fluorescence yield, and low atomic number increases the probability of Auger emission. Therefore, X-ray fluorescence yields drop.

Electrons can pass close to the nucleus and bend its direction as well. The bending releases an X-ray at different energies as a consequence of loss of momentum. Therefore, Bremsstrahlung-electrons are observed at different energies and form a part of the background.

### 3.6. Electrochemical impedance spectroscopy (EIS)

The electrical properties of the films were studied with Electrochemical Impedance Spectroscopy (EIS). The measurements were performed using Gamry Reference 600 + potentiostat in the frequency range of 1 Hz–1 MHz in humidified and/or dry nitrogen gas. The wetting stage consisted of a bubbler with deionized H<sub>2</sub>O ( $p_{H_2O} = 0.02$  atm) connected in series with a bubbler with deionized H<sub>2</sub>O and KBr ( $p_{H_2O} = 0.02$  atm). The temperature range of 200–400 °C with 20 °C steps was used for Inconel substrates and from 200 to 500 °C with 20 °C steps for MgO, YSZ, and

Al<sub>2</sub>O<sub>3</sub> substrates. The conductivity of the films deposited on the metallic substrate was measured perpendicularly to the plane using two platinum discs as electrodes [A4].

EIS measures the circuit resistance to the flow of an electrical current. The electrochemical cell is built to measure the current through a cell. The technique that uses an AC current is called Electrochemical impedance spectroscopy. The usual electrochemical cell to measure thin film impedance consists of two platinum electrodes that touch the film surface. Frequency, current and temperature are the main parameters to study the electrical properties in the film. Moreover, the cell can be measured in different environments from oxidizing (e.g., O<sub>2</sub>) to reduction (H<sub>2</sub>) or inert atmospheres (e.g., Ar or N<sub>2</sub>). For example, at high oxygen pressure PO<sub>2</sub> and high temperature (Eq. 41), the film could become *p*-type conductor:



where  $O_i''$  is interstitial oxygen,  $h'$  is the holes formation as an effect of oxygen interstitials that takes 2 electrons from the lattice. Brouwer diagrams study and model the relation between the chemical conditions and defects in the lattice. Recently, density functional theory (DFT) based on semiconductor physics explain the defects of the lattice and its contribution to the energy gaps [192]. Then, the multidimensional Brouwer diagrams are created.

Electrochemical Impedance Spectroscopy measurements were performed using Gamry Reference 3000 potentiostat in the temperature range of 20 °C to 600 °C with 50 °C steps and the frequency range of 1 Hz to 1 MHz. ProboStat unit (Norecs AS) was used to mount and prepare the sample for through-plane measurements, which were carried out in dry and wet argon or nitrogen. The wetting stage consisted of a bubbler with deionized H<sub>2</sub>O (pH<sub>2</sub>O = 0.02 atm). The obtained data were fitted using ZView Software (Scribner Associates Inc., 150 E Connecticut Ave, Southern Pines, NC, USA). The spectra were deconvoluted to two separate semicircles described by (RQ)+(RQ) equivalent circuits, expressed in Circuit Description Code [193]. Two equivalent circuits usually belong to the bulk and grain boundary contribution (Fig. 28).

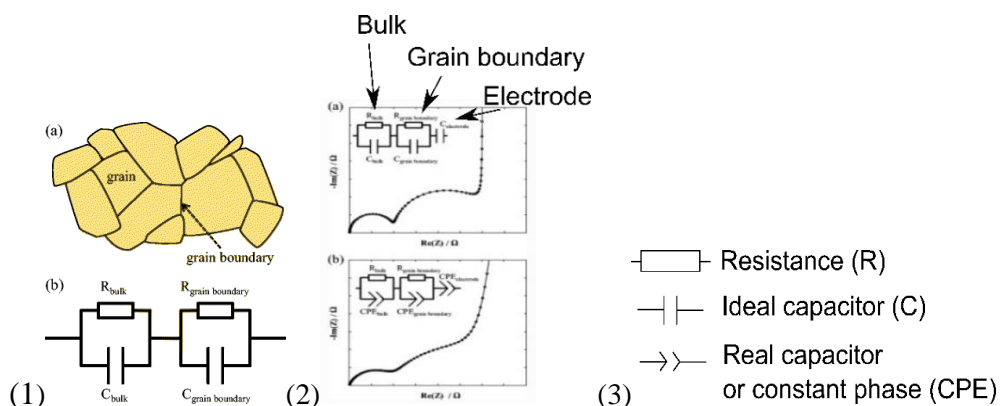


**Fig. 32.** Schematic representation of bulk and grain boundary polarization (resistance) contribution in the electrochemical impedance spectroscopy (EIS) (1), and on the right, the

Nyquist diagram (2), ideal (a) and real (b) spectra with their equivalent circuits, (3) resistance (R) and constant phase element (CPE) [194]

The impedance is  $Z = \frac{V(\omega)}{I(\omega)}$  (41); the graph between  $V$  and  $I$  at difference frequencies results in an oval or Lissajous, a figure which was used in the past to interpret the signals. Nowadays, Euler relationship (Eq. 41) is used to convert the obtained data in an exponential complex function. This conversion will allow to have terms in Cartesian form (Eq. 42):

$$\exp(j\varphi) = \cos\varphi + j\sin\varphi; \quad (42)$$

where  $\varphi$  is the phase shift.

First, the  $V$  and  $I$  are converted to an exponential function [195] (Eqs. 43 and 44):

$$V_t = V_0 \exp(j\omega t), \quad (43)$$

$$I_t = I_0 \exp(j\omega t - \varphi). \quad (44)$$

Then, the values are added to the impedance equation (Eq. 45):

$$Z = \frac{V(\omega)}{I(\omega)} = \frac{V_0 \exp(j\omega t)}{I_0 \exp(j\omega t - \varphi)} = Z \exp j\varphi. \quad (45)$$

The result is substituted in the Euler equation (Eq. 35) to obtain the axes for the Nyquist plot in two dimensions.

Therefore, the Nyquist plot consists of the real impedance and imaginary impedance. The real impedance belongs to the resistance term (Eq. 46) and the imaginary to the capacitance and inductance (Eq. 47). The Nyquist semicircle is composed of the effect of those terms in the total impedance. Fig. 33 illustrates the AC output signal frequency on the Nyquist diagram.

$$Z'_{real} = Z_0 \cos(\theta) : R \text{ (Resistance)}, \quad (46)$$

$$Z''_{img} = Z_0 \sin(\theta) : C \text{ (capacitance)} + L \text{ (inductance)}. \quad (47)$$

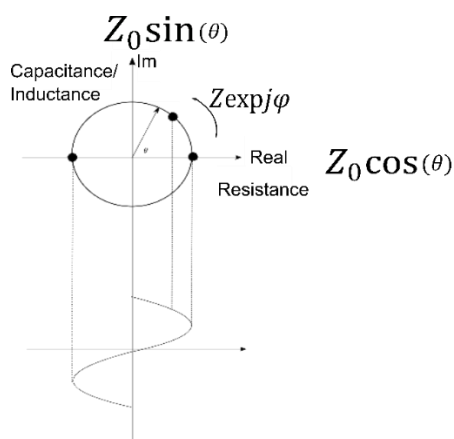


**Fig. 33.** Schematic representation of the output signal for AC voltage after its conversion to the exponential function by Euler equation [196]

According to Eq. 45, it is possible to calculate the equivalent circuit elements (Table 20), where  $\omega$  is  $2\pi f$  and the angular frequency in AC voltage. R is the resistance, L is the inductance, and C is the capacitance.

**Table 20.** Impedance for the equivalent circuits elements

Element	Impedance (Z) component
Resistor	$R$
Inductor	$j\omega L$
Capacitor	$\frac{1}{j\omega C}$

Impedance data exists as the Nyquist plot or the Bode plot (Fig. 34). Bode plot shows changes in the impedance magnitude (capacitance or induction), and phase angles vary at different frequencies. The Nyquist plot is the most valuable and useful tool to observe the other different charge-related phenomena occurring in electrolytes and electrodes.

The fitting of the circuit considers the shape and the number of semicircles present. Different values of capacitances and resistance are added (Table 21). Second semicircles at low frequencies are considered as grain boundaries according to the Brick model [197].

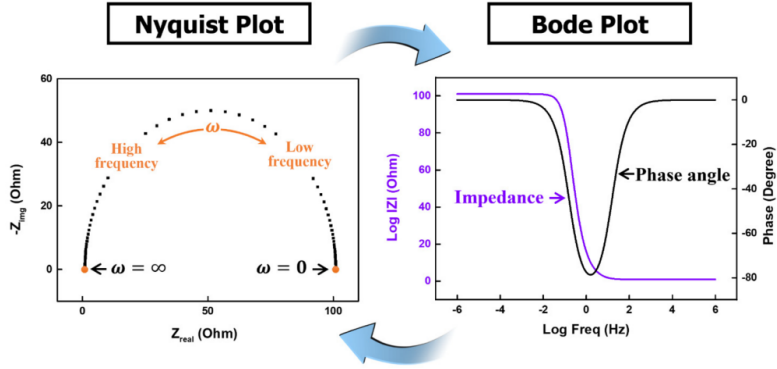


**Fig. 34.** Schematic representation of Nyquist and Bode plot [195]

**Table 21.** Capacitance values and a plausible interpretation [197]

Capacitance (F)	Phenomenon responsible
$10^{-12}$	Bulk
$10^{-11}$	Minor, second phase
$10^{-11}$ – $10^{-8}$	Grain boundary
$10^{-10}$ – $10^{-9}$	Bulk ferroelectric
$10^{-9}$ – $10^{-7}$	Surface layer
$10^{-7}$ – $10^{-5}$	Sample-electrode interface
$10^{-4}$	Electrochemical reactions

Based on the calculated resistance and total conductivity, the activation energy was determined by using Arrhenius conductivity equation (Eq. 48):

$$\sigma = \sigma_0/T \cdot \exp\left(-\frac{E_a}{k_B T}\right). \quad (48)$$

The term  $\sigma_0$  is the pre-exponential factor,  $E_a$  is the activation energy,  $k$  is the Boltzmann constant, and  $T$  is the absolute temperature. The activation energy is calculated from the conductivity measurements and Arrhenius equation (Eq. 49–51):

$$\sigma = \sigma_0/T \cdot \exp\left(-\frac{E_a}{k_B T}\right) \text{ is divided by } T, \quad (49)$$

$$\sigma T = \sigma_0 \cdot \exp\left(-\frac{E_a}{k_B T}\right) \text{ is divided by } \ln, \quad (50)$$

$$\ln(\sigma T) = \ln\sigma_0 - \frac{E_a}{kT}; \quad (51)$$

which is equal to  $y = b - a\frac{1}{T}$  and follows a linear graph of  $y = ax + b$ . The activation energy is calculated from the slope (Eq. 52).

$$a = \frac{E_a}{k}, E_a = a * k [J] \quad (52)$$

### **3.7. Nanoindentation**

In order to analyse the residual stress in the film, a nanoindenter (NanoTest Vantage, Micro Materials Ltd., Wrexham, UK) with a pyramidal, diamond, three-sided Berkovich indenter with an apical angle of  $124.4^\circ$  was used. The maximum penetration deep is 300 nm. Then, 15 independent measurements were obtained for each of the samples with the loading time fixed to 15 s. The highest load at the same displacement indicates high residual compressive stress [198].

## 4. RESULTS AND DISCUSSION

### 4.1. Barium cerates thin films formed at low temperatures (<400 °C)

In order to optimize the film properties, a series of 64 films were prepared. Four deposition temperatures (25 °C, 100 °C, 250 °C and 400 °C) and four deposition speeds (2 Å/s, 4 Å/s, 8 Å/s and 12 Å/s) were tested for each temperature. The films were prepared with temperatures below 400 °C. The films were characterized by XRD and SEM to evaluate the microstructure. Subsequently, the electrical and mechanical properties were evaluated.

#### 4.1.1. Elemental composition of the formed barium cerate thin films

In order to investigate the phase purity and composition of the thin film, the EDS spectrum was analyzed. EDS provides a half-width X-rays free path conversely for the electron of similar energy. The result of the analysis turns out to be an integrated composition that covers the entire thickness [199]. Both temperatures exhibit excess Ba at different rates (Table 22) compared to the stoichiometry in the powder. The unusual stoichiometry has different explanations, the effect of collision regions and different vapor pressure of each atom.

**Table 22.** Atomic concentration of BCO thin films formed at 25 °C and 400 °C

Element	Deposition rate (Å/s)			
<b>25 °C (at. %)</b>				
	2	4	8	12
<b>Ba</b>	9.37	10.44	10.83	8.87
<b>Ce</b>	4.43	4.65	4.73	6.01
<b>O</b>	86.2	84.91	84.44	85.12
<b>Ce/Ba</b>	0.47	0.44	0.43	0.67
<b>400 °C (at. %)</b>				
<b>Ba</b>	15.23	15.42	11.96	14.04
<b>Ce</b>	6.74	7.33	6.08	6.97
<b>O</b>	78.03	77.25	81.96	78.99
<b>Ce/Ba</b>	0.44	0.47	0.50	0.49

Low deposition rates  $<5 \text{ nms}^{-1}$ , the atomic velocity distribution of the atoms is described by the Maxwell shape. On the contrary, with a high deposition rate, this law is not valid. The angular dependence change, and as a consequence, the speed changes as well. As an effect of the emissive properties between the target and the e-beam, a collision region is higher at high deposition rates, and the speed of atoms decreases (Fig. 35). This effect was observed at 25 °C. In the collision region, the atoms have a hydrodynamic flow velocity  $u$ , and the thermal velocity  $u_t$  is minimized. Therefore, the last velocity is  $v=u+u_t$ . Due to this, Ce/Ba ratio decreases from 2 Å/s to 8 Å/s. However, at 12 Å/s, another phenomenon was observed that increases the velocity of the particles. High velocity means a higher energy transfer to the translation energy that could either surpass the constructed collision region or minimize the collision region formation.

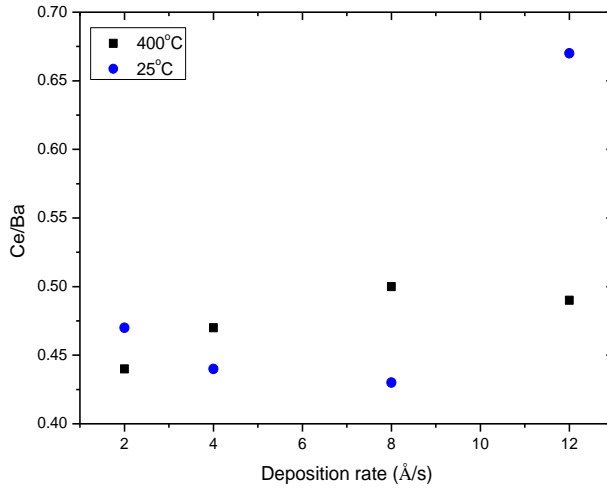


**Fig. 35.** Effect of deposition rate on Ba excess (Ce/Ba)

The substrate is close to the region of low or no collision; as a result, a change in the temperature of the substrate influences their velocity and collision (Eq. 53):

$$\alpha = (2kT/m)^{1/2}; \quad (53)$$

where  $\alpha$  is the most probable velocity in the gas with Maxwellian velocity distribution at temperature T, which is the post-expansion temperature of the gas. The atoms gain speed until they reach a limit that is explained by the increase in collisions. Atoms have different masses; thus, their velocity is influenced by the mass as well. As a result, the film composition improves at higher temperatures.

A stoichiometric atomic % ratio between Ba and Ce is important in order to avoid an excess of Ba, resulting in the formation of  $\text{BaCO}_3$  on contact with the atmosphere. Another important atom is oxygen, it determines the amount of present oxygen vacancies. However, the amount of oxygen in the films was greater than 60 at.%. The amount of oxygen decreases with temperature. The excess Ba results in the formation of  $\text{BaO}$  and  $\text{BaCO}_3$ , when the amount of oxygen is higher (Table 18), but with low oxygen content, the vacancies are formed and could result in oxygen migration between the substrate and film [200].

#### 4.1.2. Crystal structure of the formed barium cerate thin films

Fig. 36 presents the X-ray diffractograms (XRD) pattern of the formed film at 25 °C, 100 °C, 250 °C and 400 °C substrate temperatures and 12 Å/s. At 25 °C, a mixture of  $\text{CeO}_2$  and  $\text{BaCO}_3$  that are the precursor components of  $\text{BaCeO}_3$  were observed. The maximum intensities of  $\text{BaCO}_3$  and  $\text{CeO}_2$  were minimized at 100 °C as an effect of integration in an amorphous phase. A semi-crystalline phase was observed at 250 °C. The intensity of the crystalline peak is stronger at 600 °C as an effect of the increase of crystalline phase. The crystalline phase was Orthorombic Pbnm. The crystallographic orientations of the film were towards (002) and (242) at 2 Å/s and 12

Å/s. Meanwhile, amorphous phases were observed at 4 Å/s and 8 Å/s. Then, XRD diffractograms demonstrate that the deposition rates of 2 Å/s and 12 Å/s formed at 400 °C are ideal for BaCeO<sub>3</sub> crystal formation. According to the atomic composition, 2 Å/s and 12 Å/s showed a greater excess of Ba. The change in crystallinity with temperature and deposition rate for the film deposited by e-beam evaporation was observed previously in Sm-doped Ceria [201].

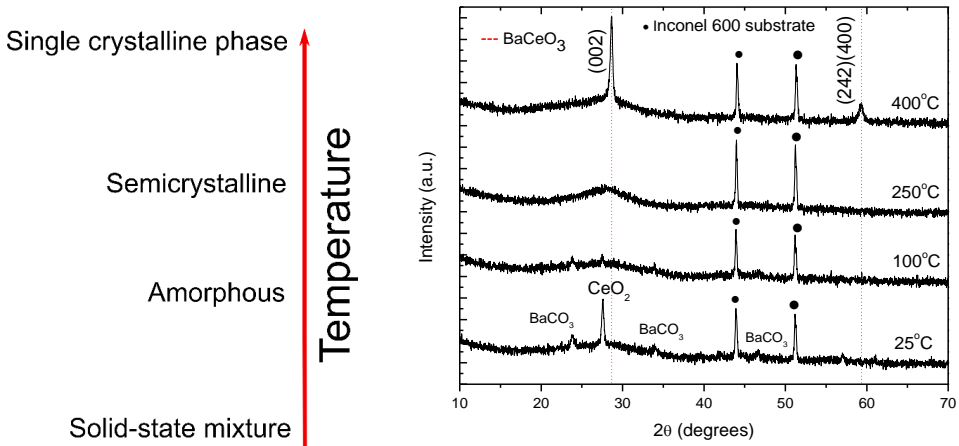


**Fig. 36.** BaCeO<sub>3</sub> formed at 25 °C, 100 °C, 250 °C and 400 °C at 2 Å/s on Inconel 600 substrate [A1]

The interaction of the particles with the support demonstrates its influence on the activation energy of crystallization. The presence of less bound particles at low deposition rates (2 Å/s) on the support enhances the diffusion process and decreases the crystallization activation energy. At the high deposition rate (12 Å/s), it is a combination of 1) high kinetic energy particles interacting with the support and 2) a large number of particles with higher diffusion energies rearranging into a crystal order [202] (Fig. 37, 38).

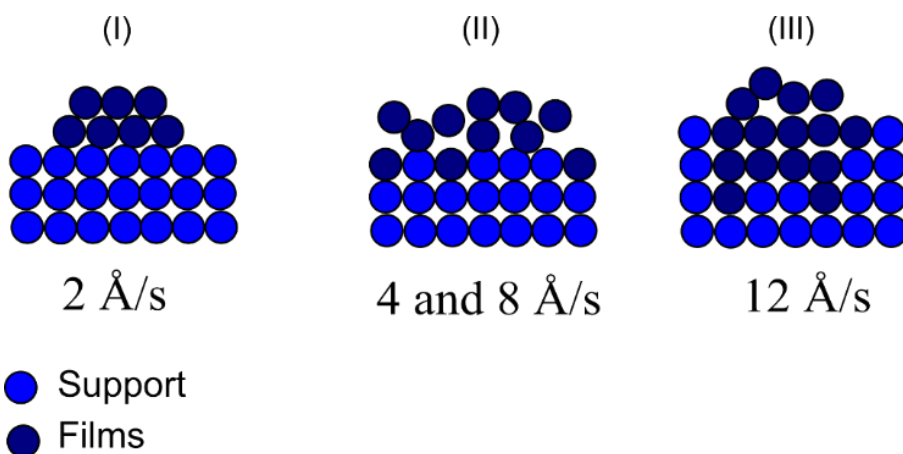


**Fig. 37.** Schematic representation of the deposition rate on the crystallization of the film at three different support interactions: I) non bonded with support, II) bonded with support, III) high bonding with support

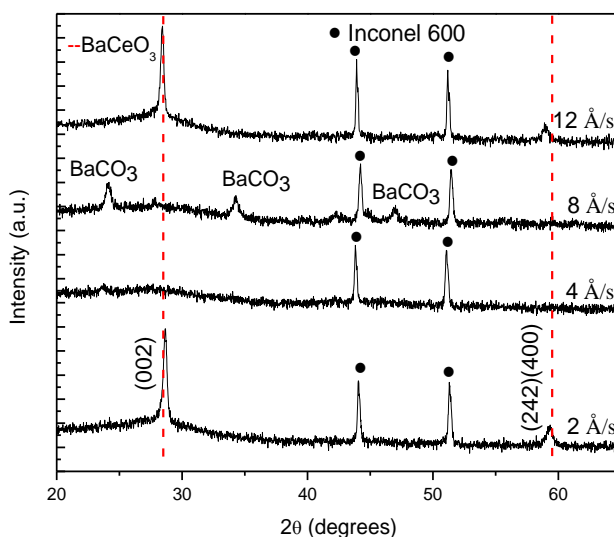


**Fig. 38.** BaCeO<sub>3</sub> formed at 400 °C at 2 Å/s, 4 Å/s, 8 Å/s and 12 Å/s formed on Inconel 600 [A1]

Due to the rapid crystallization and substrate interaction, the properties of the films were assessed at 12 Å/s and 400 °C in the formation of BaCeO<sub>3</sub> on four different FeNi alloys substrates: Stainless steel A301, Inconel 600, Glass sealing alloy and Invar. The XRD diffractogram showed crystallization on the four substrates with orientations (002) and (004) (422) (Fig. 39).

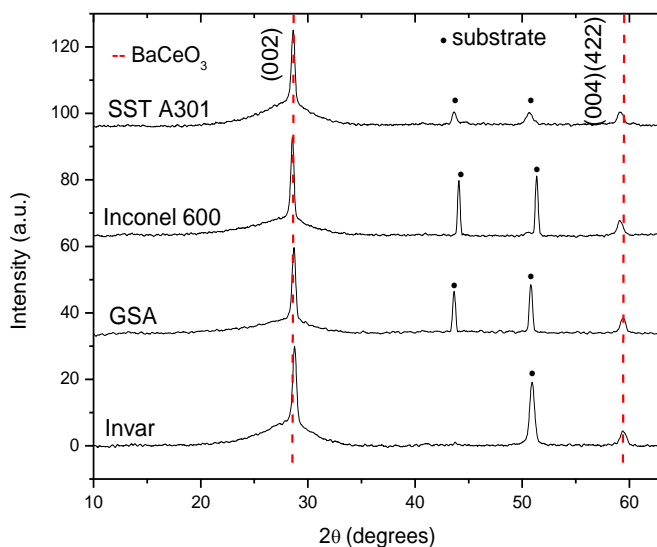


**Fig. 39.** Crystalline evolution of BCO at different substrates SST, Inconel 600 GSA and Invar formed at 12 Å/s and 400 °C.

In Table 23, the volume of the unit cell is compressed when the TEC coefficient is less or greater than the TEC of BaCeO<sub>3</sub>. However, the lattice parameter ‘a’ is more compressed in Inconel 600 than in the other films.

**Table 23.** Lattice parameter for BCO thin film (thickness: 1 μm) formed on different substrates by e-beam evaporation deposition method at 400 °C formed at 12 Å/s [A1]

	Composition (%)	TEC ( $\times 10^{-6} \text{K}^{-1}$ )	a (Å)	b (Å)	c (Å)	Vol (Å <sup>3</sup> )	Crystal size (002) (nm)	Density (%)
<b>Invar</b>	Fe 64% Ni 36%	1.7	6.2096	8.7640	6.2400	339.59	22	99
<b>GSA</b>	Fe 54% Ni 29% Co 17%	4.8	6.3937	8.7425	6.4578	360.00	25	99
<b>Inconel 600</b>	Fe 8% Ni 72% Cr 16%	11.5	5.5955	8.4463	7.6653	362.27	26	99
<b>SST A301</b>	Fe 76% Ni 7% Cr 17%	17.3	6.1770	8.9109	6.4409	354.17	72	99

The relaxation process started from the strain generated as a consequence of difference in the thermal expansion between the substrate and film [203] (Eq. 54). The Inconel 600 substrate showed the lowest strain and the most relaxed film that resulted in the largest unit cell volume. Eq. 54 shows the strain ( $\varepsilon$ ) at initial temperature  $T_0$  and final temperature  $T_1$ . The coefficient of the thermal expansion for the film is  $\alpha_f$ , and for the substrate, it is  $\alpha_s$ .

$$\varepsilon = \int_{T_0}^{T_1} (\alpha_s - \alpha_f) dT \quad (54)$$

#### 4.1.3. Microstructure of the formed barium cerate thin films

SEM micrographs at 25 °C show Zone 1 at 2 Å/s, 4 Å/s, 8 Å/s and 12 Å/s on Invar, GSA and Inconel. There were fewer defects in the films at 400 °C and at 2 Å/s and 12 Å/s. Fig. 40 showed that the films formed at 2 Å/s had a larger grain size values than films formed at 12 Å/s.

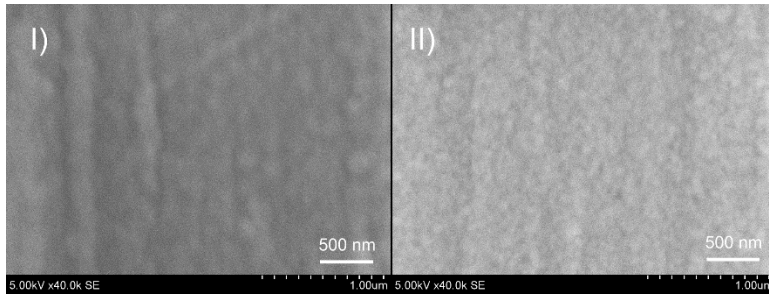


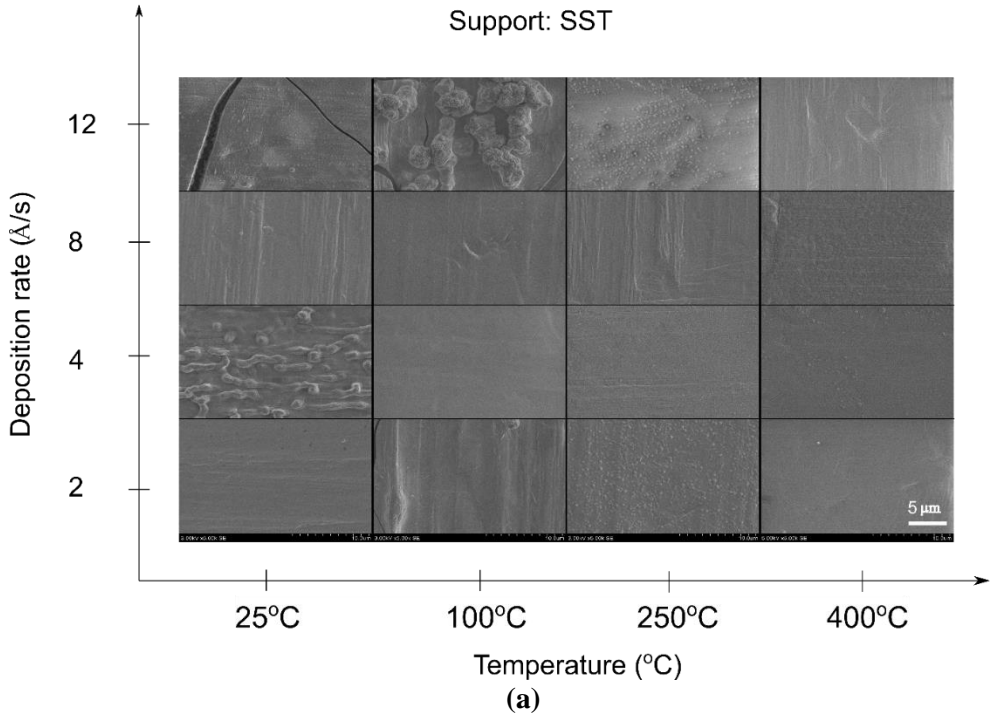
**Fig. 40.** SEM images of BCO formed at I) 2 Å/s and II) 12 Å/s

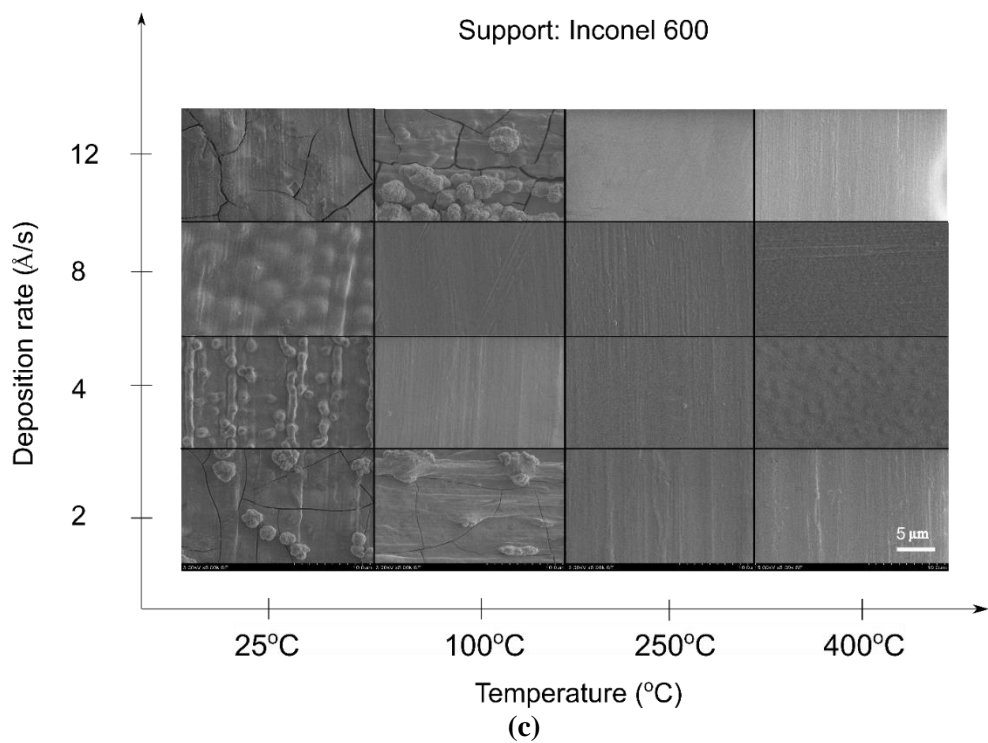
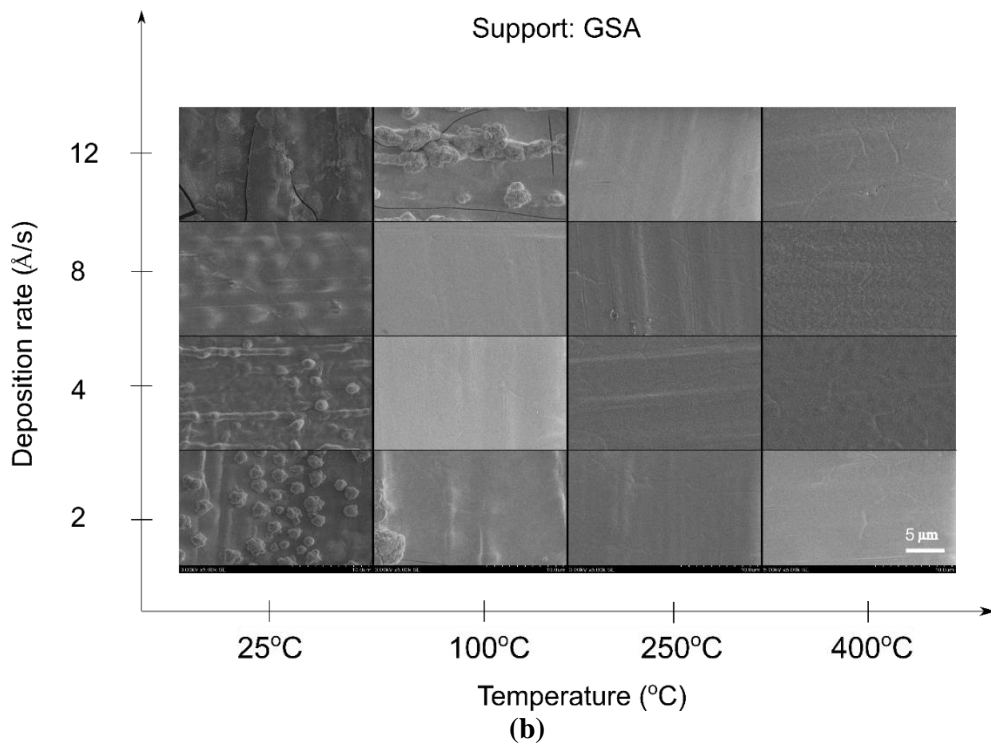
At higher magnification, the highly dense surfaces demonstrate the formation of T-Zone microstructure for BaCeO<sub>3</sub> from 100 °C to 400 °C.  $T_s/T_m$  ratio is the starting point for locating the microstructure in the zone diagrams.  $T_m$  is the melting temperature of BaCeO<sub>3</sub>, which is 1743 °C,  $T_s$  is the temperature of the substrate.  $T_s/T_m$  ratio changed to 0.08, 0.17, 0.26, 0.34 for substrate temperatures of 25 °C, 100 °C, 250 °C and 400 °C. Zone 1 corresponds to  $T_s/T_m < 0.2$ , and Zone T is  $T_s/T_m < 0.3$ . The  $T_s/T_m$  ratio corresponds to the expected Zone 1. Zone 1 is characterized by groves, voids or fibrous shapes. The surface is smooth and the cross-section is very dense for Zone T. SEM micrographs (Fig. 41) showed the corrugate formation on the surface as an effect of tensile stress according to the Thornton diagram. A similar microstructure was observed for Zone 1 in ZnO thin film formed by sputtering [204]. The rise in temperature with the formation of Zone T results in a release of stress and the formation of less corrugated surfaces. High deposition rates exhibit higher corrugated surfaces than lower deposition rates. The accumulation of a large amount of stress is a consequence of rapid growth.

SEM images show the formation of cracks at the support temperature of 25–100 °C (Fig. 41). This effect is known as a consequence of reaction between the free BaO and CO<sub>2</sub> in the atmosphere that expands the film with the formation of BaCO<sub>3</sub>. Low deposition temperatures are not enough to complete the reaction. In order to avoid

unreacted BaO, the temperature of the substrate must be increased. Non-stoichiometric films result in unreacted BaO as well.

The only film that showed cracks on the surface at 400 °C was BCO deposited in Invar at 4 Å/s. The cause was thermal stress, lattice mismatch and thermal expansion mismatch. Additionally, the level of binding between the film and the substrate and the energy of the particles at 4 Å/s could be other effects that influence the relaxation of the microstructure.





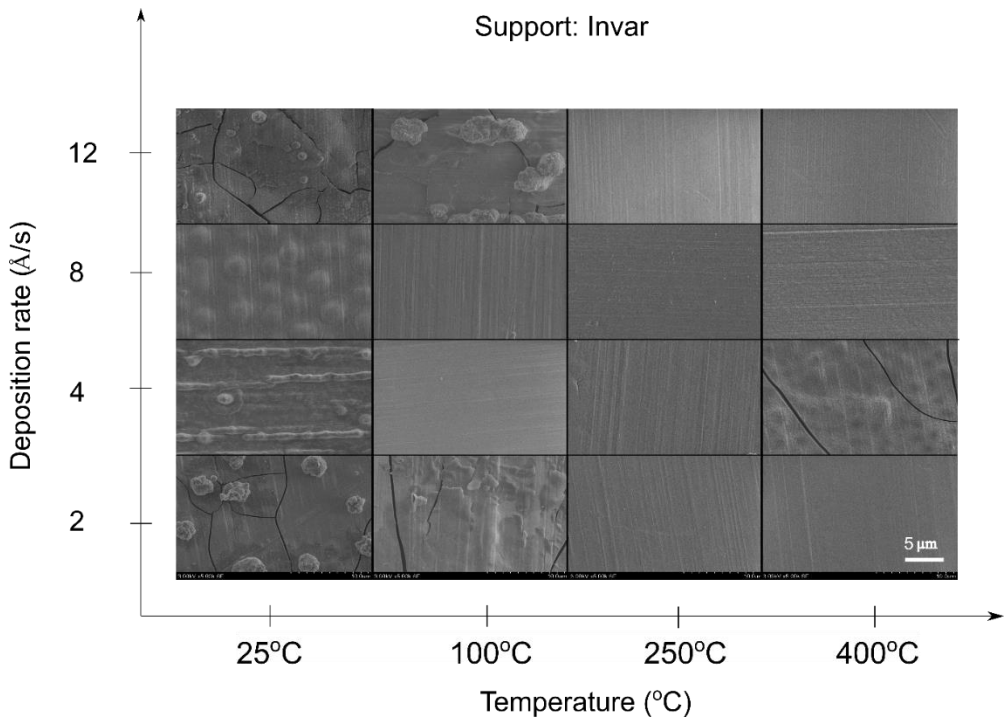


**Fig. 41.** SEM image for BCO formed on (a) Stainless steel A301 (SST), (b) Glass sealing alloy (GSA), (c) Inconel 600 and (d) Invar from 25 °C to 400 °C and from 2 to 12 Å/s [A1]

The high SEM magnification for the films formed at 12 Å/s and 400 °C is shown in Fig. 42. The surfaces show rounded shapes for GSA, Invar and Stainless steel.

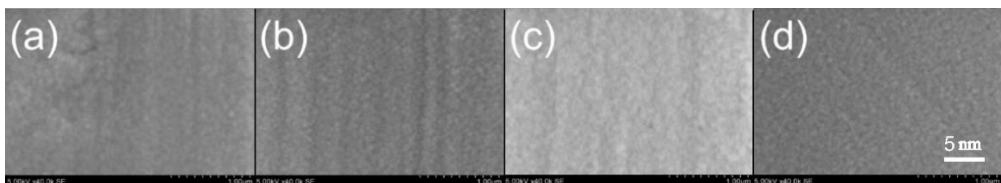


**Fig. 42.** High magnification SEM images of BCO formed at 12 Å/s and 400 °C on (a) SST, (b) Invar, (c) Inconel 600 and (d) GSA

The grain sizes of the samples formed at 12 Å/s and 400 °C on Invar, GSA, Inconel 600 and Invar were 87.87 nm, 85.30 nm, 120.53 nm and 109.06 nm, respectively (Table 24). The difference of 35 nm was observed between the lowest and highest value. High values were obtained on Inconel 600 with the TEC value closest to BaCeO<sub>3</sub>.

**Table 24.** Grain size of BaCeO<sub>3</sub> formed at 12 Å/s at 400 °C

Support	Grain size (nm)
Invar	87.86+/-3.0
GSA	85.30+/-3.4
Inconel	120.53+/-5.3
SST	109.06+/-4.2

Those experiments showed that in addition to temperature, there is a relaxation effect at different TECs.

#### 4.1.4. Nano-indentation analysis of the formed barium cerate thin films

Nano-indentation results show differences in hardness (Fig. 43). The greater force that is necessary in the same displacement represents the greater hardness. Inconel had the the highest hardness from four substrates. High hardness is related to a large amount of residual stress. Inconel showed the highest load and slope compared to the other substrates. High slope is related to compressive stress, while small slope is related to the tensile stress perpendicular to the indenter.

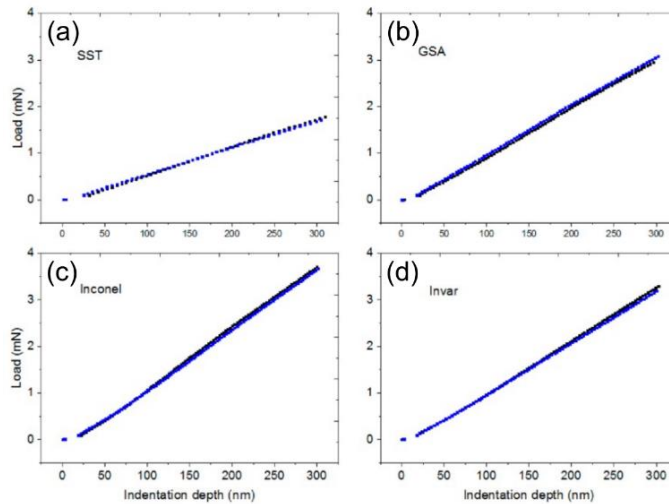


**Fig. 43.** Load-displacement curves of the nanoindentation test obtained by Berkovich indenter; the elastic part of the BCO film (thickness 1 μm) before the break presented for (a) Stainless steel A301 (SST), (b) Glass sealing alloy (GSA), Inconel 600 (Inconel) and Invar [A1] to evaluate the residual stress

The values of the coefficient of thermal expansion have a linear dependence on the load or residual stress (Fig. 44 I). The low coefficient of thermal expansion exhibits higher load values compared to the coefficient of thermal expansion. There is an exception with Inconel. It showed the highest residual stress. Fig. 44 II) relates the compression and relaxation of the unit cell with the residual stress. Thus, both the

high compression and high tensile unit cell volume showed high residual stress. High residual stress is consistent with high values of ion conductivity. Tensile stress on the unit cell has been previously reported to enhance the ionic conductivity [130]. Tensile stress reduces the distance between the oxygens perpendicular to the stress in the perovskite structure. Then, the Grotthuss mechanism is enhanced in one direction. Similar thermal expansion between the film and support did not guarantee a fully relaxed film at low formation temperatures compared with the thermal expansion mismatch at different annealing temperatures [205]. The columnar microstructure and low formation temperatures could be the reason. The biaxial stress for columnar growth is generally observed with relaxation or freedom perpendicular to the substrate. The BCO formed on Invar, the load value (residual stress) and unit cell values agree with the formation of small grain size, i.e., 87 nm. It is suggested that the microstructure for Invar cross-section has a rapid nucleation rate that evolves towards the formation of columnar shape with high biaxial stress. The nucleation and growth rate of BCO for Inconel support suggest a higher diffusion: the reason could be its composition. Inconel and SST supports had the highest grain size, and both substrate had a similar amount of Chromium (Cr).

The graph between the load and coefficient of thermal expansion demonstrates that high residual stress is formed with low TEC in the substrate (Fig. 44). The TEC for Inconel was expected to match the TEC of the film and low residual stress values. The thermal conductivity in Invar is  $2 \text{ W m}^{-1}\text{K}^{-1}$  lower than Inconel  $11 \text{ W m}^{-1}\text{K}^{-1}$ , which for Glass sealing is  $17 \text{ W m}^{-1}\text{K}^{-1}$  and Stainless steel,  $16 \text{ W m}^{-1}\text{K}^{-1}$ . The thermal conductivities that are higher than 11 showed lower residual stress. Then, it was suggested that the thermal conductivity in the support could be one of the reasons for high residual stress in Inconel compared with other supports.

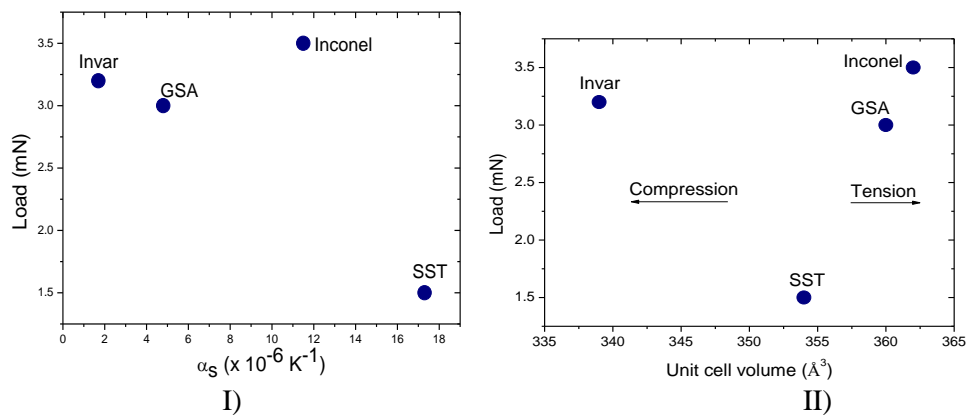


**Fig. 44.** I) The linear dependency between the load (mN) representing the residual stress and the thermal expansion coefficient ( $\alpha_s$ ), II) the dependency between the load and the compression and relaxation on the unit cell

#### 4.1.5. Electrical properties of the formed barium cerate thin films

Figure 45 shows the ionic conductivity in  $\text{BaCeO}_3$  films formed at  $12 \text{ \AA/s}$  and  $400 \text{ }^\circ\text{C}$  support temperature formed on the four metal supports. The graph indicates

that the temperatures below 400 °C result in ionic conductivity values between  $10^{-8}$  and  $10^{-10}$  S/cm. BaCeO<sub>3</sub>-based materials are mixed ion conductors. At low temperatures, the conduction of protons dominates, and at high-temperature, the conductivity of oxygen ions is prominent [206]. However, the temperatures, at which this phenomenon occurs, are higher than the values obtained. The ionic conductivity was closer to the values of the pellet shape [207] ( $10^{-9}$ - $10^{-10}$  Scm<sup>-1</sup>). The relaxed and compressed films showed the same behaviour at different conductivity values. The main difference between Inconel and other films is the size of the grain. A similar effect was observed in BaTiO<sub>3</sub>; the nanograins added grain boundary resistance compared to the coarse grains [208].

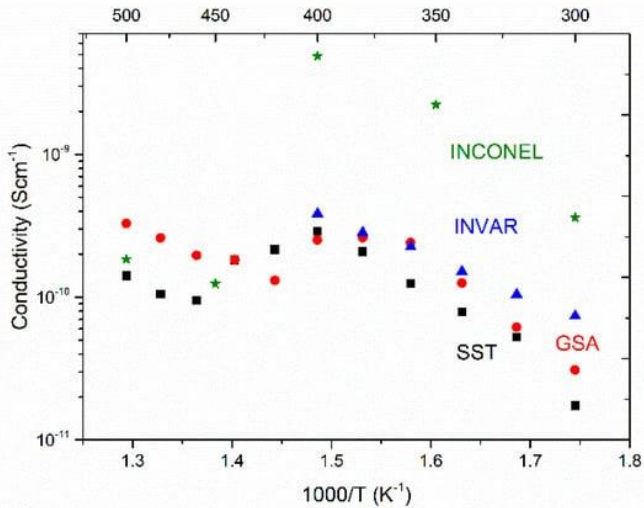


**Fig. 45.** Ion conductivity on wet (0.02 atm H<sub>2</sub>O/Ar) for BaCeO<sub>3</sub> formed on Inconel, Invar, GSA and SST

The activation energies depend on the type of ion that is being transported. The values are above 0.6 eV only for the oxygen ion, and for the proton, they are below 0.6 eV. The obtained results show that in both cases, the mixed oxygen and proton diffusion are influenced by the lattice parameters. Comparing BCO formed in Invar and Inconel, BCO formed in Invar had the lowest activation energy (0.6 eV) and was consistent with its compressed unit cell, while BCO formed on Inconel had the activation energy of 0.9 eV with the unit cell relaxed (Table 25). The film formed on Inconel had the highest compressed lattice parameter ‘a’. Although the compressed lattice parameter showed low activation energies, the reason for high ion conductivity and high activation energy on Inconel is not clear at this point. Depending on the volume of the unit cell, the film formed on Inconel has a high tensile strain. Previous reports on films with high tensile stress showed that oxygen vacancies increase near the interface and can induce vacancies in the substrate [209]. Although the unit cell is not absolutely compressed to reduce the activation energy, the increase in ion conductivity in the film could be due the formation of oxygen vacancies due to the residual stress.

**Table 25.** Electrical and mechanical properties of BaCeO<sub>3</sub> formed in metallic supports [A1]

Substrate	Composition	$\sigma$ (350 °C), wet /cm) $\times 10^{-10}$	$E_A$ (eV)	Relaxation temperature (°C)
Invar	Fe 64% Ni 36%	1.9	0.6	400
Glass sealing alloy (GSA)	Fe 54% Ni 29% Co 17%	2.2	1.13	360
Inconel alloy (600)	Fe 8% Ni 72% Cr 16%	22	0.9	400
Stainless steel (SST)	Fe 76% Ni 7% Cr 17%	1.0	0.95	400

At temperatures below 400 °C, a mixed conduction of oxygen and proton was observed. This effect was observed before in Ba<sub>7</sub>NbMoO<sub>20</sub> in humid atmosphere. Above 400 °C, there was a drop in ionic conductivity [210]. Similar studies show that the effect of hydration at low temperatures and dehydration at higher temperatures lead to a decline in ionic conductivity value [211].

The fit of the semicircles in the Nyquist plot (Fig. 46) shows that the resistance changes according to the residual stress. Residual stress affects the oxygen vacancies and charge transfer, which influences the transport properties and total ion conduction [209]. GSA with tensile effect in the unit cell showed higher charge transfer resistance compared to the SST with relaxed unit cell.

Another factor contributing to the resistance is catalytic activity at the surface between the film and electrode. The lower frequency semicircle is related to the diffusion processes and grain boundary resistance. The films measured at 380 °C showed higher grain boundary resistance compared to the films above 420 °C. The reason could be thermally activated processes, such as oxygen diffusion, phase transitions or changes in microstructure.

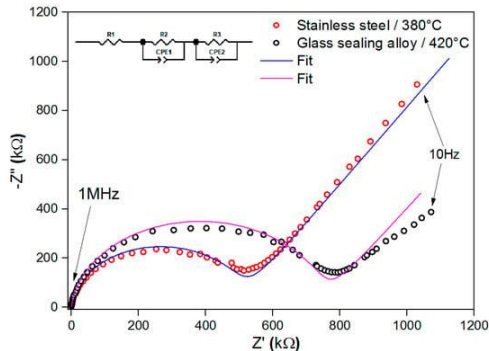
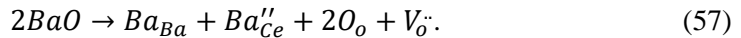


**Fig. 46.** Nyquist plot for BCO formed on Stainless steel, Glass sealing alloy and fitting curves [A1]

XRD diffractograms show the decomposition of the material after EIS measurements and exposure to air (Fig. 47). The grazing angle of incidence that measured the crystallinity with a thin film thickness showed that  $BaCeO_3$  is mainly on the surface. Usually,  $BaCeO_3$  reacts with  $CO_2$  above  $500\text{ }^\circ\text{C}$ . The reaction is reversible above  $800\text{ }^\circ\text{C}$  [212]. Another reason is the presence of excess  $BaO$ . The unreactive  $BaO$  has three different routes of incorporation (Eq. 55–57). According to those equations, oxygen vacancies are formed. According to Haile et al. [212], Barich undoped composition follows Eqs. 53 and 55. Therefore, high ionic conductivities are expected with excess  $Ba$  as a consequence of crystalline defects.



The excess of  $Ba$  in  $BaCeO_3$  to form oxygen vacancies has other consequences: 1) increase in lattice, 2) water uptake increases, 3) sintering increases, but 4) material instability appears with  $BaCO_3$  formation [149]. The water absorption is related to Eqs. 55 and 56. Other authors demonstrate that the excess  $Ba$  only forms a small number of oxygen vacancies, and  $Ba$ -deficiency is better for obtaining stable materials [212].

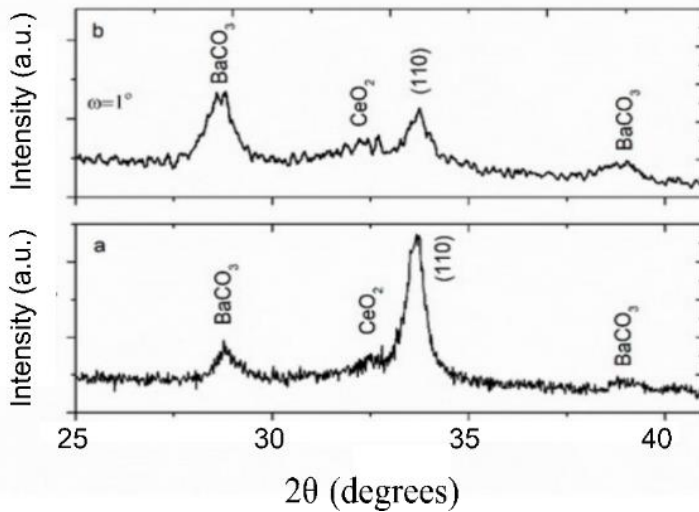


**Fig. 47.** XRD diffractogram of  $BaCeO_3$  surface with (a)  $\omega = 0$  and (b)  $\omega = 1^\circ$  grazing incident scan after EIS experiments and exposure to air [A1]

#### 4.2. Barium cerates thin films formed at intermediate temperatures (500–700 $^\circ\text{C}$ )

In order to enhance the diffusion and promote grain growth and crystallinity, the selected deposition rate was  $2\text{ \AA/s}$  compared to the methodology 1, and the system was modified to obtain precise temperatures of  $500\text{ }^\circ\text{C}$ ,  $600\text{ }^\circ\text{C}$  and  $700\text{ }^\circ\text{C}$ . The

selected metal alloy was Inconel 600. Subsequently, the film formation was tested on three other substrates with different compositions:  $\text{Al}_2\text{O}_3$  (0001),  $\text{MgO}$  (001) and YSZ (001) at 600 °C and 700 °C. Metal alloys substrates start to degrade at higher temperatures. Therefore,  $\text{BaCeO}_3$  thin film was formed in the selected metal oxide supports.

#### 4.2.1. Crystal structure of the formed barium cerate thin films

The XRD diffractogram (Fig. 48) shows a clear, highly crystalline and textured (oriented) single phase  $\text{BaCeO}_3$  film formed on Inconel 600 at 500 °C, 600 °C and 700 °C. The phase was *Pnma* orthorhombic, and the size of the crystallites rose from 110 nm to 177 nm with an increase in the deposition temperature from 500 °C to 600 °C. Afterwards, there was a decay in the value towards 68 nm. Crystallinity changes were previously reported in e-beam evaporation deposition methods as a change in elemental composition [213]. An improvement in diffusion and crystallinity is as well a consequence of energy change of the particles [149]. Temperature is a parameter that has a strong influence to reach the crystallization activation energy. The obtained results show that the energy transferred from the electrons contributes to obtaining large crystals.

The decay in the value of the crystal size is a consequence of relaxation by the formation of dislocations that result in the rearrangement of atoms and change in the orientation of crystal [214]. The largest crystal size reported for barium cerates was obtained by solid-state reaction with gadolinium as dopant and Co as sintering aid, resulting in 216 nm [14] above 1400 °C sintering temperature. The largest reported crystal size for undoped  $\text{BaCeO}_3$  is 60 nm [108] after sintering.

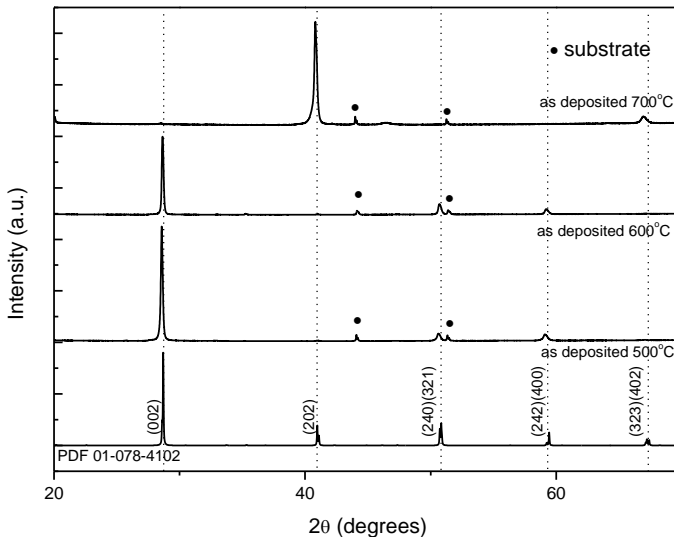


**Fig. 48.** XRD diffraction of BCO at 500 °C, 600 °C and 700 °C formed on Inconel 600

Fig. 49 shows the XRD diffractograms of the single phase of  $\text{BaCeO}_3$  formed on  $\text{MgO}$  (001), YSZ (001) and  $\text{Al}_2\text{O}_3$  (0001) at 600 °C and 700 °C. The peaks show no signs of semi-crystalline region formation, and random orientation was minimal.

Highly oriented barium cerate-based material has shown highly oriented single crystals but under stress [130] due to the ultra-thin thickness. Then, it is suggested that the films that were formed are highly aligned and partially relaxed.

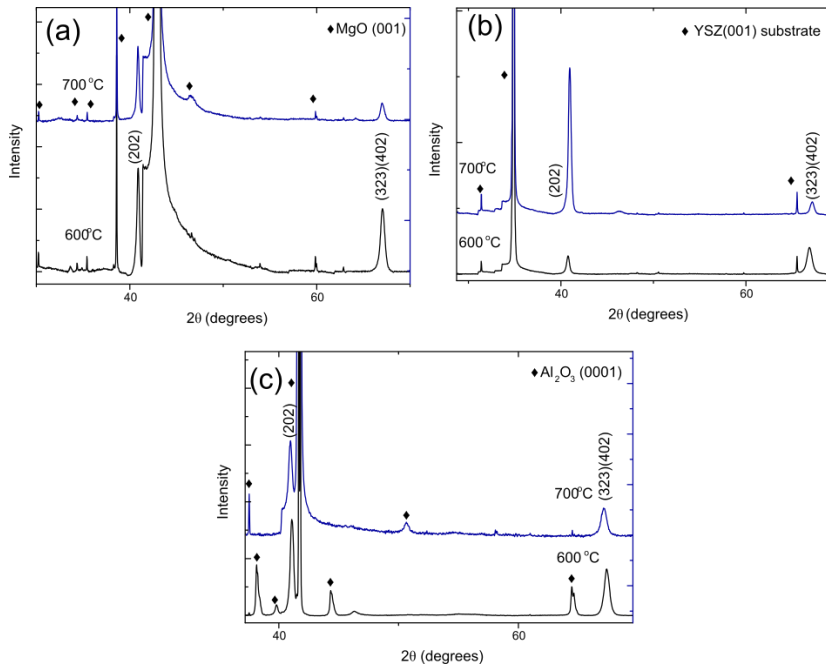


**Fig. 49.** XRD diffractogram for highly oriented BCO formed at 600 °C and 700 °C on MgO (001) (a), YSZ (001) (b) and Al<sub>2</sub>O<sub>3</sub> (0001) (c)

The Inconel 600 substrate formed the largest crystal size for BCO with a value of 177 nm at 600 °C. The heat transfer is maximized on metal supports rather than oxides. This result supports the idea that crystallinity in highly oriented barium cerates films improves by adding more energy and controlling the support heat transfer.

The unit cell volume for BCO on Inconel (Å<sup>3</sup>) decreased from 345.91 Å<sup>3</sup> at 500 °C to 343.98 Å<sup>3</sup> at 610 °C (Table 26). Afterwards, there is an increase in the volume at 700 °C to 350.60 Å<sup>3</sup>. BCO unit cell for Al<sub>2</sub>O<sub>3</sub> increases barely from 339.28 Å<sup>3</sup> to 339.94 Å<sup>3</sup> from 600 °C to 700 °C. In YSZ, the volume decreases from 340 Å<sup>3</sup> to 339.97 Å<sup>3</sup> from 600 °C to 700 °C, and in MgO, from 339.57 to 338.40 Å<sup>3</sup>.

**Table 26.** Crystalline properties of BaCeO<sub>3</sub> [A4]

Substrate	Deposition temperature, °C	Lattice parameters			Crystallite size, nm	Plane	Volume, Å <sup>3</sup>	Rwp, %
		a, Å	b, Å	c, Å				
Inconel	500	6.2686	8.8188	6.2583	110	(002)	345.97	2.74
	600	6.2339	8.8313	6.2533	177	(002)	344.20	2.81
	610	6.2455	8.8146	6.2385	159	(002)	343.98	2.89
	700	6.2839	8.8223	6.3240	68	(202)	350.60	3.86
Al <sub>2</sub> O <sub>3</sub>	500	N/A, multiphase structure						
	600	6.2910	8.8084	6.1227	34	(202)	339.28	5.73
	700	6.1734	8.9664	6.1415	14	(202)	339.95	9.27
YSZ	500	N/A, multiphase structures						
	600	6.1378	8.6372	6.4212	16	(202)	340.41	8.8
	700	6.1934	8.7451	6.2768	27	(202)	339.97	9.96
MgO	500	N/A, multiphase structures						
	600	6.1698	8.6516	6.3616	10	(202)	339.57	7.07
	700	6.1918	8.6584	6.3120	19	(202)	338.40	9.51

Fig. 50 compares the reference value of the unit cell volume for undoped BCO (340.8 Å<sup>3</sup>) with the values obtained at different supports and temperatures. The different unit cell values show that the films formed on metal oxides were compressed, and the films formed on Inconel 600 were relaxed. Moreover, it demonstrates that the reported reference value obtained in pellets at high sintering temperature belongs to the compressed BaCeO<sub>3</sub>.

The texture coefficients were measured for each film and temperature (Table 27). The orientation changes with the type of support and temperature as an effect of relaxation. The films formed on Inconel 600 show a (002) orientation. The orientation changes in the metal oxide support towards (402) (323). An exception was observed at 700 °C for Inconel 600 and YSZ with orientation to (002). The increase in temperature aligns the crystals towards (002) as a re-arrangement of the atoms to release the stress created at high temperatures. In fact, (002) orientation was previously observed in 300 nm thick doped barium cerates thin films formed by PLD [215] on silicon nitride deposited at 400 °C. The change of orientation towards a single plane or mode of growth with rising in support temperature was previously observed in BZY thin film deposited with a thickness of 120 nm [151] on MgO(001) formed at 900 °C.

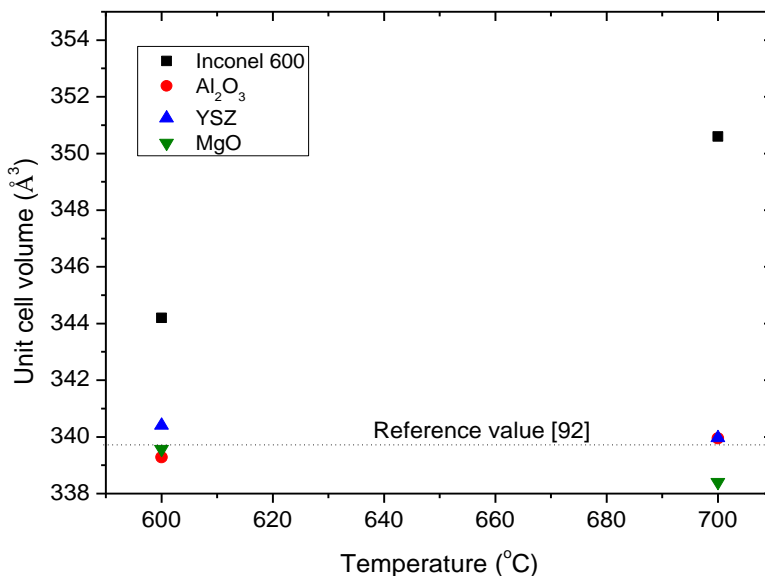


**Fig. 50.** Effect of support and its temperature on the unit cell volume of BCO formed on MgO (001), Al<sub>2</sub>O<sub>3</sub> (001) and YSZ (001)

**Table 27.** Texture coefficients of the thin films deposited on Inconel 600, YSZ (001), MgO (001), Al<sub>2</sub>O<sub>3</sub> (0001) compared to Pnma reference structure diffractogram (01-078-4102) [A4]

Substrate type and temperature		Texture coefficients				
Inconel	(°C)	(002)	(202)	(240) (321)	(242) (400)	(402) (323)
	500	2.89	0.05	0.73	1.20	0.11
	600	1.92	0.05	1.13	0.88	0.0
	610	1.65	1.03	0.81	0.79	0.71
	700	0.00	2.75	0.0	0.24	0.0
<b>YSZ (001)</b>	600	0.0	0.40	0.0	0.0	1.59
	700	0.0	1.60	0.0	0.0	0.40
<b>MgO (001)</b>	600	0.0	0.23	0.0	0.0	1.77
	700	0.0	0.42	0.0	0.0	1.58
<b>Al<sub>2</sub>O<sub>3</sub> (0001)</b>	600	0.0	0.82	0.0	0.0	1.17
	700	0.09	1.66	0.34	0.0	1.91

Figure 51 demonstrates the stability of BaCeO<sub>3</sub> under atmospheric conditions following the XRD diffractogram. The stability of the formed BaCeO<sub>3</sub> thin film above 500 °C is attributed to the preferred orientation when compared to sintered high

temperature, large and randomly oriented crystal from the pellets. Small displacement on the peak at around  $28^\circ$  suggests stress relaxation.

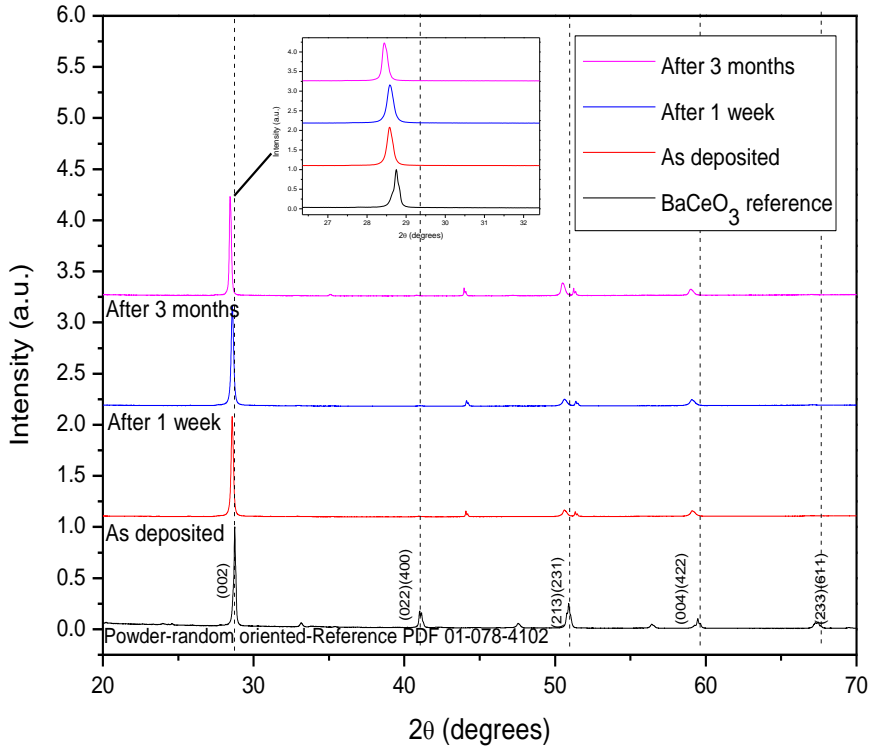


**Fig. 51.** XRD diffraction of BaCeO<sub>3</sub> as deposited and after 1 week and 3 months; there is no presence of BaCO<sub>3</sub> or other phases

#### 4.2.2. Microstructure of the formed barium cerate thin films

SEM micrographs for BCO formed on Inconel 600 exhibit Zone 2 (Fig. 52, 53). Zone 2 with different sizes is observed in Al<sub>2</sub>O<sub>3</sub> (0001), MgO (001) and YSZ (001) (Fig. 54). The grain size (y-axis) does not follow a dependence on temperature. The difference in grain morphology is attributed to the sum of TEC mismatch stress relaxation, surface energy on the supports and deposition conditions influencing the total diffusion energy of diffusion at the surface to modify the nucleation and grain growth. (Table 28). However, grain size values (x-axis) have a clear temperature dependence for Inconel 600. Inconel had the lowest values with 39 nm for grain growth on the x-axis and 296 nm for grain size in the y direction. The highest grain size was 437 nm, and x-axis grain size was 215 nm at 700 °C. Al<sub>2</sub>O<sub>3</sub> showed to obtain the most stable grain size at high temperature with the minimum value of 68 nm for grain growth in the x-axis and 294 nm for the grain size in the y-axis growth. The grain size values formed by the e-beam evaporation methods were lower than those formed by the solid-state reaction [14] sintered above 1400 °C. This is a consequence of rapid growth of the grain perpendicular to the support, which does not allow rapid diffusion parallel to the support or Zone 1. There, the rise in temperature of the

substrate allows obtaining a greater diffusion and coalescence parallel to the substrate or Zone 2. The grain sizes for barium cerates are usually above 4  $\mu\text{m}$  for undoped and 1  $\mu\text{m}$  for doped [124] in pellets. Temperature influences the nucleation growth next to the substrate and coalescence mechanisms [214]. The relaxation process during and after the formation of the film dictates the final morphology.

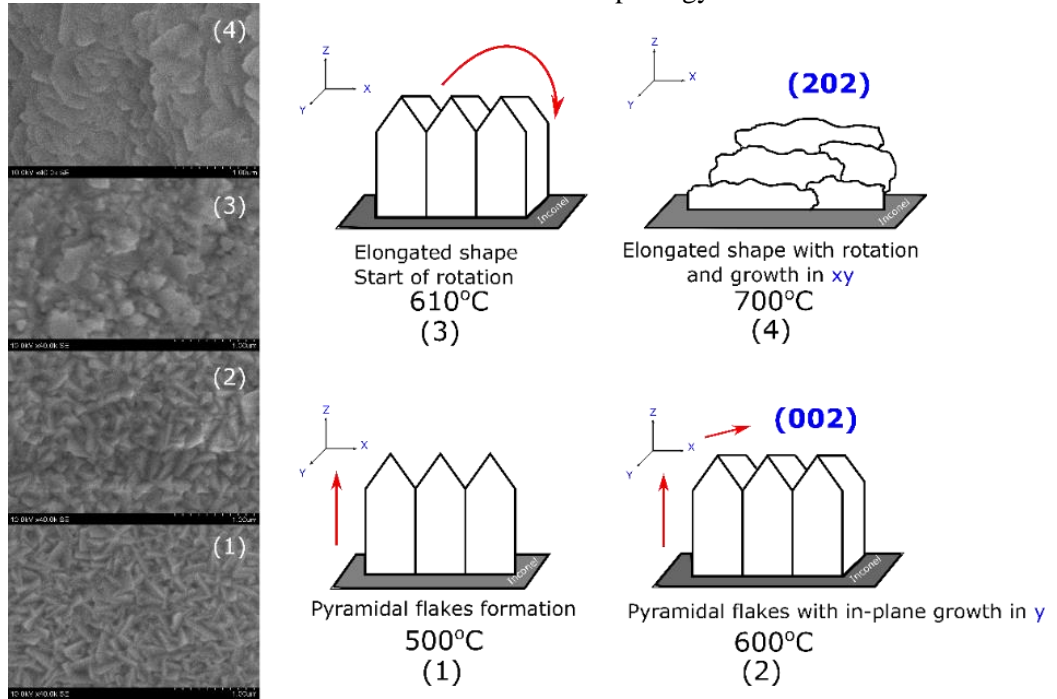


**Fig. 52.** Effect of substrate temperature on grain growth size in Zone 2 towards the formation of different microstructures on x and y directions at (1) 500 °C, (2) 600 °C, (3) 610 °C and (4) 700 °C substrate temperature [A4]

**Table 28.** Microstructure properties of  $\text{BaCeO}_3$  obtained by SEM image [A4]

Substrate	Temperature	Morphology	Lateral grain size, x direction (nm)	Grain size, y direction (nm)
$\text{Al}_2\text{O}_3$	600 °C	Pyramidal flakes	46	336
	700 °C	Pyramidal flakes and elongated	68	294
$\text{MgO}$	600 °C	Pyramidal flakes and elongated	47	290
	700 °C	Elongated	152	334
$\text{YSZ}$	600 °C	Fibrous	55	283
	700 °C	Pyramidal flakes and elongated	88	359

<b>Inconel 600</b>	500 °C	Pyramidal flakes	39	296
	600 °C	Elongated	103	273
	700 °C	Elongated	215	437

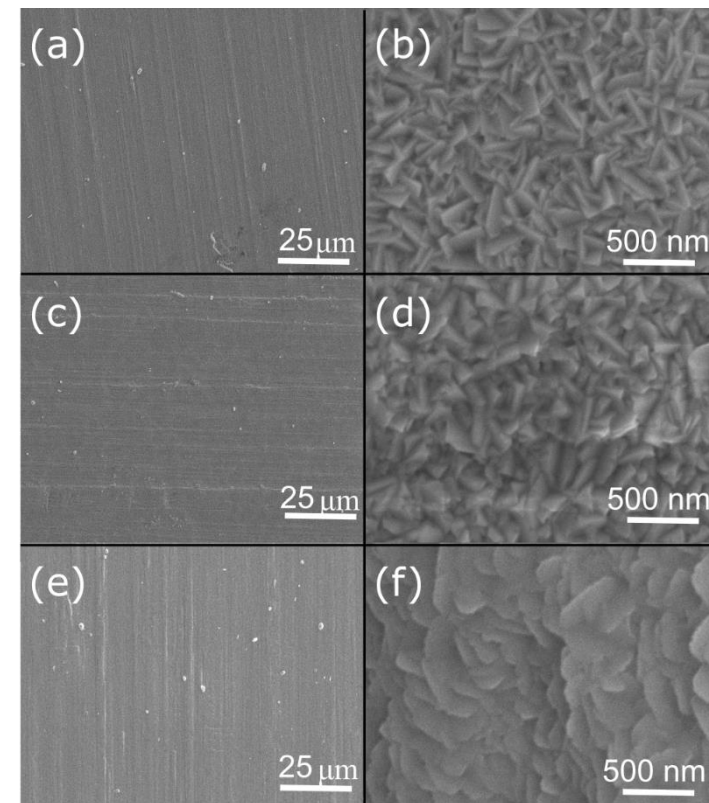


**Fig. 53.** SEM images of BaCeO<sub>3</sub> formed at 500 °C (a, b), 600 °C (c, d) and 700 °C (e, f) on Inconel

(I) 600°C

(II) 700°C

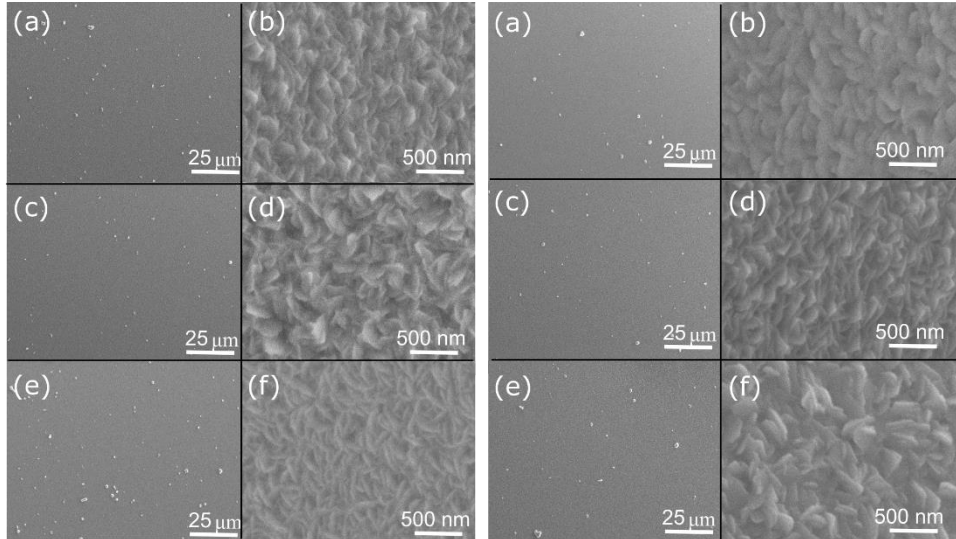


**Fig. 54.** SEM images of BaCeO<sub>3</sub> thin films formed on MgO (001) at 600 °C (Ia, Ib) and 700 °C (IIa, Iib), Al<sub>2</sub>O<sub>3</sub> (1000) at 600 °C (Ic, Id) and 700 °C (Iic, Iid), YSZ (001) at 600 °C (Ie, If) and 700 °C (Iie, Iif) and deposited at 2 Å/s

The Inconel and MgO (001) supports demonstrate faster x-axis grain growth kinetic among the four supports (Fig. 54 I). The slowest growth rate was for Al<sub>2</sub>O<sub>3</sub> (Fig. 55). The non-linear crystal growth rate in a different direction is a result of relaxation process and deformation mechanism that occurs. It was reported that for thicker films, the strain will be elastic and given by:  $\varepsilon_e = \int_{T_0}^{T_1} (\alpha_s - \alpha_f) dT$  where  $\alpha_s$  and  $\alpha_f$  are the coefficient of thermal expansion for the support and film. Other authors describe the relaxation of thin films in terms of three mechanisms, creep, grain boundary sliding and plastic deformation through dislocation glide [216].

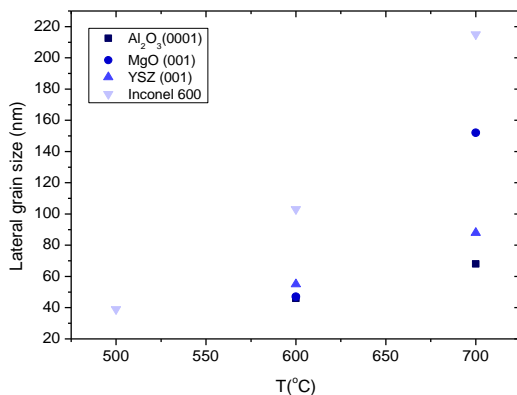


**Fig. 55.** Grain size lateral growth (x-direction) vs. temperature for BCO formed on Inconel, Al<sub>2</sub>O<sub>3</sub>, MgO and YSZ at 700 °C

### 4.2.3. Electrical properties of the formed barium cerate thin films

Ionic conductivity measurements (Fig. 56) demonstrate the effect of microstructure on the ion conductivity of BaCeO<sub>3</sub> in comparison to the pellets [207] ( $10^{-9}$  S/cm -  $10^{-10}$  Scm<sup>-1</sup>) with two higher orders of magnitude. Moreover, those values were higher than BaCeO<sub>3</sub> formed before by the e-beam evaporation deposition methods with grain size values that were three times lower [A4].

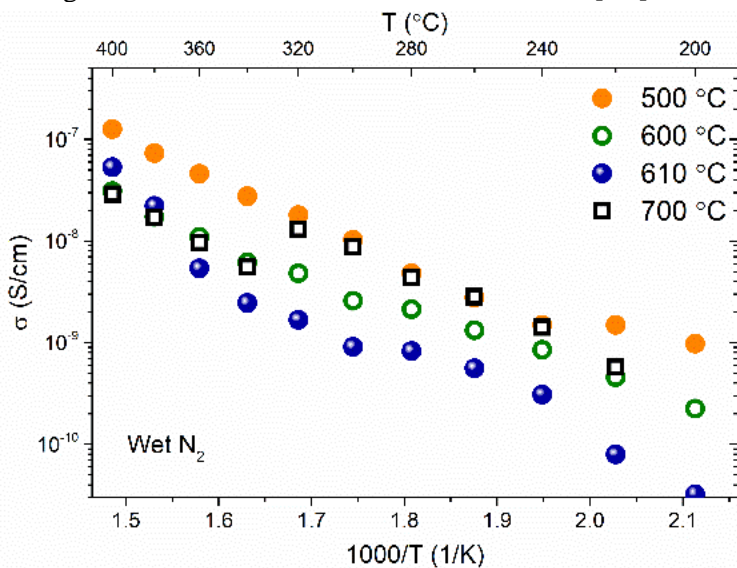


**Fig. 56.** Ion conductivity for BCO formed at 500 °C, 600 °C and 700 °C on Inconel 600 at 0.02 atm H<sub>2</sub>O/N<sub>2</sub> [A4]

A decrease in ionic conductivity has been still observed at different measured temperatures (Table 29). The size of the slope increases at high temperatures. The main reason is the relaxation effects that take place during the heating of the film. The film formed at 500 °C showed to be compressed and obtained the highest ionic

conductivity and activation energy value of 0.87 eV. A value higher than 0.6 eV shows mixed ionic conductivity. Then, the oxygen diffusion took place during the measurements. According to the unit cell volume, the film that was formed at 700 °C was the most relaxed film with expected low oxygen diffusion from microstructure relaxation. The film obtained the lowest activation energy (0.57 eV) or mostly proton conduction. Nevertheless, it shows a strong change in slope at 320 °C with high activation energy values (1.03 eV) and minimization of the overall conductivity. The relaxation of the unit cell decreases the trapping of protons, resulting in the loss of water and reducing the ionic conductivity. Relaxed film tends to lose more water. Additionally, for the relaxation of the lattice, the re-arrangement of the microstructure shows that it follows a process of oxygen diffusion contributing to the total conductivity.

**Table 29.** Conductivity, activation energies and relaxation temperatures in BaCeO<sub>3</sub> formed at 500 °C, 600 °C and 700 °C

Substrate T(°C)	$\sigma_{\text{ion}}$ (400 °C) (S/cm)	Ea (eV) (Slope high T/ slope low T)	Relaxation temperature (°C)
500	$1.25 \times 10^{-7}$	0.87	220
600	$3.09 \times 10^{-8}$	0.89/0.82	280
700	$2.87 \times 10^{-8}$	1.03/0.57	320

Fig. 57 shows the effect of BaCeO<sub>3</sub> in a wet and dry N<sub>2</sub> atmosphere. As expected, the film under humidity conditions showed higher ionic conductivity due to the proton diffusion. Under dry conditions, the conductivity of oxygen ions is present. Therefore, BaCeO<sub>3</sub> has proton conductivity at high temperatures as well as low temperatures. In both cases, the activation energies were similar. It was observed that under humidity conditions, the relaxation is pronounced compared to the diffusion of oxygen ions, which means that the structure is under more stress due to the water molecules and could result in the relaxation of structure and release of water. This could explain the similar activation energies with the film under dry atmosphere (0.80 eV (dry) and 0.87 eV (wet)) (Table 30). The enhancement of the charge transfer process due to the proton and oxygen ion conduction is demonstrated. The presence of proton conduction could be due to the presence of Ce<sup>+3</sup>. The reduction of Ce<sup>+4</sup> to Ce<sup>+3</sup> could be a part of e-beam evaporation methods as in the case of ceria. The formation of ceria thin films by e-beam evaporation methods at 2 Å/s exhibited the presence of Ce<sup>+3</sup> with a concentration between 25% and 29% [201]. Other authors claim that the target already contains Ce<sup>+3</sup>.

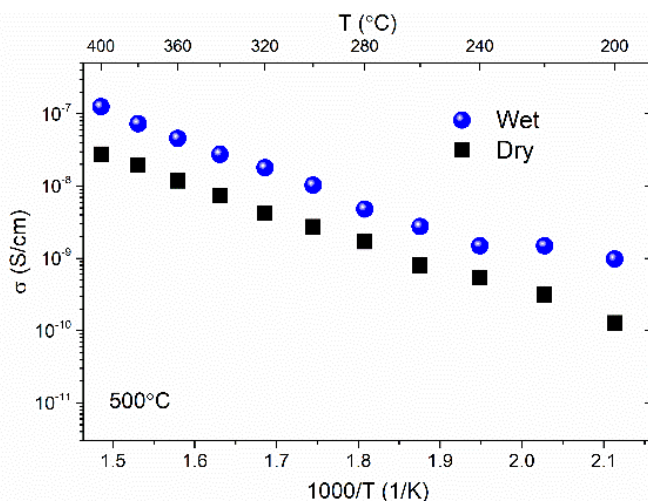


**Fig. 57.** Humidity effect on the ionic conductivity of BaCeO<sub>3</sub> [A4]

**Table 30.** Conductivity, activation energies and relaxation temperatures of BaCeO<sub>3</sub> formed at 600 °C under wet and dry atmospheres

Substrate T (°C)	$\sigma_{ion}$ (400 °C) (S/cm)	Ea (eV)	Relaxation temperature (°C)
<b>Wet</b>	1.25 × 10 <sup>-7</sup>	0.87	220
<b>Dry</b>	2.7 × 10 <sup>-8</sup>	0.80	-

The grain boundary resistance of films is usually observed at low frequencies on the Nyquist plot (Fig. 57) as the beginning of the second semicircle. The second semicircle is a diffusion-controlled process, compared to the kinetic control of the first semicircle. In the cooling process, the increase in the resistance of the first semicircle is explained by the decrease in the contribution of oxygen diffusion. In the work of Xiao et al. [168], for films above 50 nm with columnar growth, the interface effect such as strain or lattice dislocation are neglected in the Nyquist plot. Therefore, the residual stress found throughout the film and its effect on the oxygen ion diffusion as an activated thermal process was observed at low frequencies.

The ionic conductivities of the BaCeO<sub>3</sub> formed on MgO (001) and Al<sub>2</sub>O<sub>3</sub> (0001) show a similar behaviour to BaCeO<sub>3</sub> formed on Inconel 600 (Fig. 58) but with 3 orders of magnitude high value. The slopes occur at different temperatures. The support for BaCeO<sub>3</sub> formed on MgO (001) is at 320 °C and for BaCeO<sub>3</sub> formed on Al<sub>2</sub>O<sub>3</sub>, at 400 °C. Then, the ionic conductivities in BaCeO<sub>3</sub> formed on oxide supports exhibit a higher ionic conductivity than the films formed on Inconel 600 °C. The ionic conductivities of the supports alone follow the same behaviour, but three orders of magnitude less. The ionic conductivity is obtained with 1.5 μm thickness. Then, the actual thickness at the calculated ionic conductivity could be larger than the added and include the substrate-film interface and the substrate. However, higher thickness values usually result in high resistance, which decreases ionic conductivity [217]. The semicircle at intermediate frequencies (Fig. 58) shows a faradaic impedance. The

semicircle at high frequency was previously reported corresponding to the migration of protons from the electrolyte to the triple phase boundary, and at intermediate frequency, it is the dissociative adsorption and diffusion of oxygen [167]. However, they do not take into account the self-diffusion process on the surface or the entire film. Then, the microstructure is rearranged. The rearrangement at the surface enhances the oxygen ion diffusion process ( $E_a = 0.82$  eV), but when the film relaxes, the process stops until the equilibrium is reached. In polycrystalline solids, the high diffusion of grain boundaries did not contribute to the total ionic conductivity. In contrast, nanocrystalline solid films possess high grain boundary mobility that contributes to the overall ionic conductivity with space charge overlap [218]. Then, the density of defects is less than that of the bulk solids. A relaxed film (formed at 700 °C) has low conductivity as well as low activation values, 0.57 eV. Different changes in slope demonstrate different relaxation processes in the microstructure that decrease ionic conductivity as a result of two effects: 1) the volume expansion in the unit cell volume affecting the Grotthuss mechanism and trapping of proton and 2) the oxygen ion diffusion or change in the microstructure. Then, the dynamic microstructure in BaCeO<sub>3</sub> affects the total conductivity.

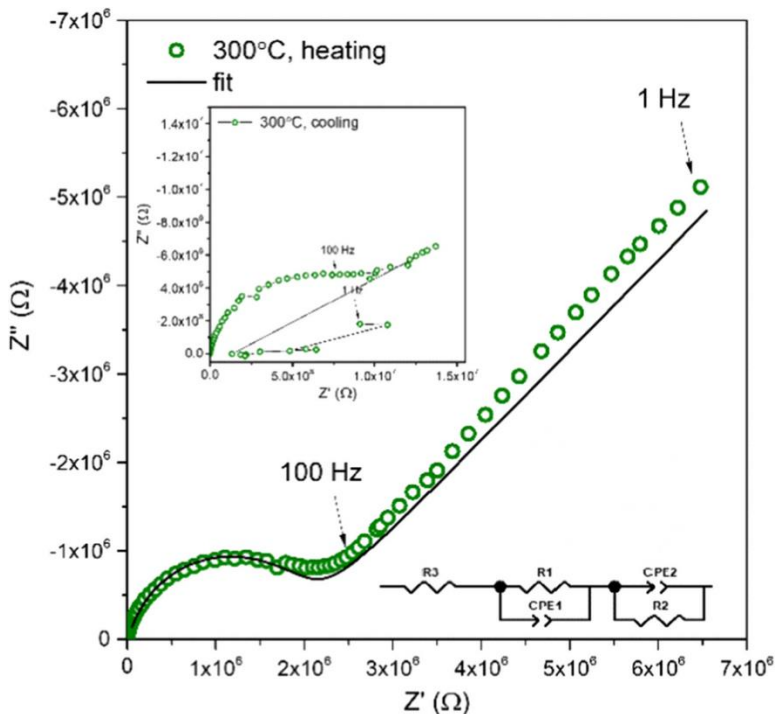


**Fig. 58.** Nyquist plot for BaCeO<sub>3</sub> deposited on Inconel at 700 °C tested at 300 °C (main plot) and cooling (inset plot) in wet nitrogen [A4]

The films formed with the (402) (323) orientation in metal oxides showed a higher ionic conductivity (Fig. 59) than the film formed with the (002) orientation. One of the reasons is the compressed volume of the unit cell. However, the activation

energy changed with the properties of the supports for the films formed at 600 °C (Table 31). The film formed in MgO support showed the lowest activation energy with the value of 0.65 eV. The other supports presented higher values, i.e., for Al<sub>2</sub>O<sub>3</sub>, with 0.80 eV and for YSZ, with 1.24 eV. The film formed in YSZ showed the highest conductivity. Compared to MgO and Al<sub>2</sub>O<sub>3</sub>, YSZ contains oxygen vacancies for oxygen ion transport. YSZ is a stable structure. Then, the oxygen ion conduction could be a result of the relaxation process on the film that in contact with YSZ forms oxygen vacancies and enhances the total conductivity. The effect of multilayers with different ion transport was previously reported for gadolinium doped ceria formed on barium zirconate doped yttrium (GDC/BZY) [167]. The protons move into the layer with oxygen ion transport to form new proton defects. As a result, the power density improved.

According to the graph, it has been observed that the relaxation process in BCO is minimal compared to the films formed in Inconel 600. It is suggested that the thermal conductivity of the metal oxide supports slow down the relaxation of the structure. This effect could reduce the oxygen ion conduction due to the less movement on the film and decrease the activation energy. Nevertheless, the ionic conductivity increased as an effect of oxygen ion conduction transfer from the supports. Then, the activation energies were above 0.6 eV.

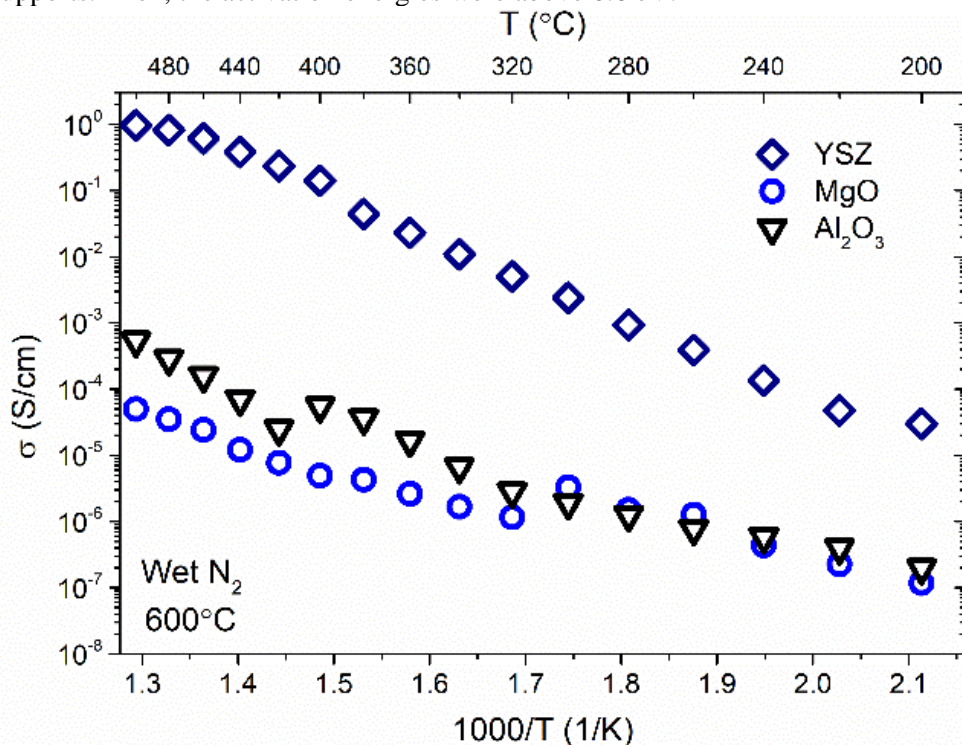


**Fig. 59.** Ion conductivity (0.02 atm H<sub>2</sub>O/N<sub>2</sub>) of BCO formed on YSZ, MgO and Al<sub>2</sub>O<sub>3</sub> at 2 Å/s and 600 °C [A4]

**Table 31.** Conductivity, activation energy and relaxation temperature of BaCeO<sub>3</sub> formed at 600 °C

Substrate T (°C)	$\sigma_{\text{ion}}$ (400 °C) (S/cm)	Ea (eV)	Relaxation temperature (°C)
YSZ	0.13	1.24	-
MgO	$4.8 \times 10^{-6}$	0.65	380
Al <sub>2</sub> O <sub>3</sub>	$5.5 \times 10^{-5}$	0.80	400

The changes in dielectric constant in the barium zirconate cerate materials show that the oxygen vacancies were generated due to the substitution of Ce<sup>+4</sup> with the formation of Ce<sup>+3</sup> due to the oxygen ionic conduction that creates holes. Films with high amount of Ce<sup>+3</sup> had high ionic conductivity [219]. Maxwell–Wagner polarization explains the increase in dielectric constant and conductivity in the whole multilayer film [220]. The general equation (Eq. 58) is as follows:

$$\sigma_{\text{total}} = \frac{d}{(d_1/\sigma_1)+(d_2/\sigma_2)}; \quad (58)$$

where  $\sigma$  is the conductivity,  $d$  – thickness as a sum of  $d_1$  and  $d_2$ ,  $d_1$  film,  $d_2$  interface,  $\sigma_1$  and  $\sigma_2$  – their respective conductivities. Other theories in the enhancement of ionic conduction include the formation of a 2D interface between the film and the substrate, which is highly strained. This effect could allow the enhancement of 2D proton conduction [221]. The results show that the main effect of the support was the transfer of oxygen ions and oxygen vacancies.

### 4.3. Formation and investigation of barium cerate doped yttrium

A series of six films was formed for doped barium cerate. The starting powders contained two different concentrations of yttrium, i.e., 10% and 20%, and the substrate temperatures were tested at 600 °C and 700 °C.

#### 4.3.1. Elemental composition of the formed BCY thin films

The elemental composition of the film changed with temperature for BCY10 and BCY20. The excess of Ba at 500 °C is higher compared to the undoped BaCeO<sub>3</sub>. The yttrium dopant concentration decreases the Ce evaporation compared with the stoichiometry of BaCeO<sub>3</sub> formed at 500 °C. The films with higher amounts of yttrium at the target and support temperature showed lower ratio of yttrium to ceria, compared to barium in the film (Table 32). The mechanism for reducing the concentration of yttrium and cerium in the film could be explained by strong binding between them, compared to barium. Then, barium is vaporized first.

**Table 32.** Atomic % of BCY10 and BCY20 film formed at 500 °C and 600 °C on Inconel 600 obtained by EDX analysis and on the right columns, the non stoichiometry obtained from atomic % between Ba and Ce and Y

Element	Composition, at. %			
	BCY10		BCY20	
	500 °C	600 °C	500 °C	600 °C
<b>Ba</b>	12.87	11.47	14.62	12.2
<b>Ce</b>	9.9	7.97	10.2	6.25
<b>Y</b>	0.43	0.42	1.03	0.44
<b>O</b>	76.8	80.14	74.15	81.11
<b>Ce/Ba</b>	0.80	0.73	0.76	0.54

#### 4.3.2. Crystal structure of the formed BCY thin films

X-ray diffraction (XRD) patterns (Fig. 60) and Rietveld refinement confirmed a single-phase film at support temperatures of 500 °C, 600 °C and 700 °C in BCY10. A *Pbnm* orthorhombic phase was observed for BCY10 and *Pm3m* cubic phase for BCY20. At 700 °C, a mixture between BCY20 and  $\text{Ce}_{0.8}\text{Y}_{0.2}\text{O}_{1.19}$  was observed for BCY20. High temperature sintering of BCY20 reports the formation of  $\text{Y}_{0.2}\text{Ce}_{0.8}\text{O}_{1.19}$  [222]. According to  $R_{\text{wp}}$  values, the closest structure that fitted the diffractogram was an orthorhombic *Pbnm*. The crystallinity was observed to have changes in the size and orientation of the crystal without a linear dependence with temperature. Increasing temperatures resulted in a different diffusion process and crystalline defects that modify crystallinity in BCY10 and BCY20, such as exchange, interstitial, vacancy, sub-boundary and relaxation [223]. Moreover, the driving force of the different diffusion processes includes thermomigration and stress field in the film. Therefore, different temperatures add different levels of stress that result in a change in the microstructure, crystallinity and orientation. This effect was studied before at different thicknesses during the deposition process [224]. Compared to  $\text{BaCeO}_3$ , BCY10 shows the start of crystal orientation at lower temperatures and an increase in crystal size. However, BCY20 does not increase the size of the crystal, but there is a change in the orientation. This non-linear behaviour is explained by the strain created by a different thermal expansion mismatch that results in a different relaxation process. The % of yttrium influences the relaxation process.

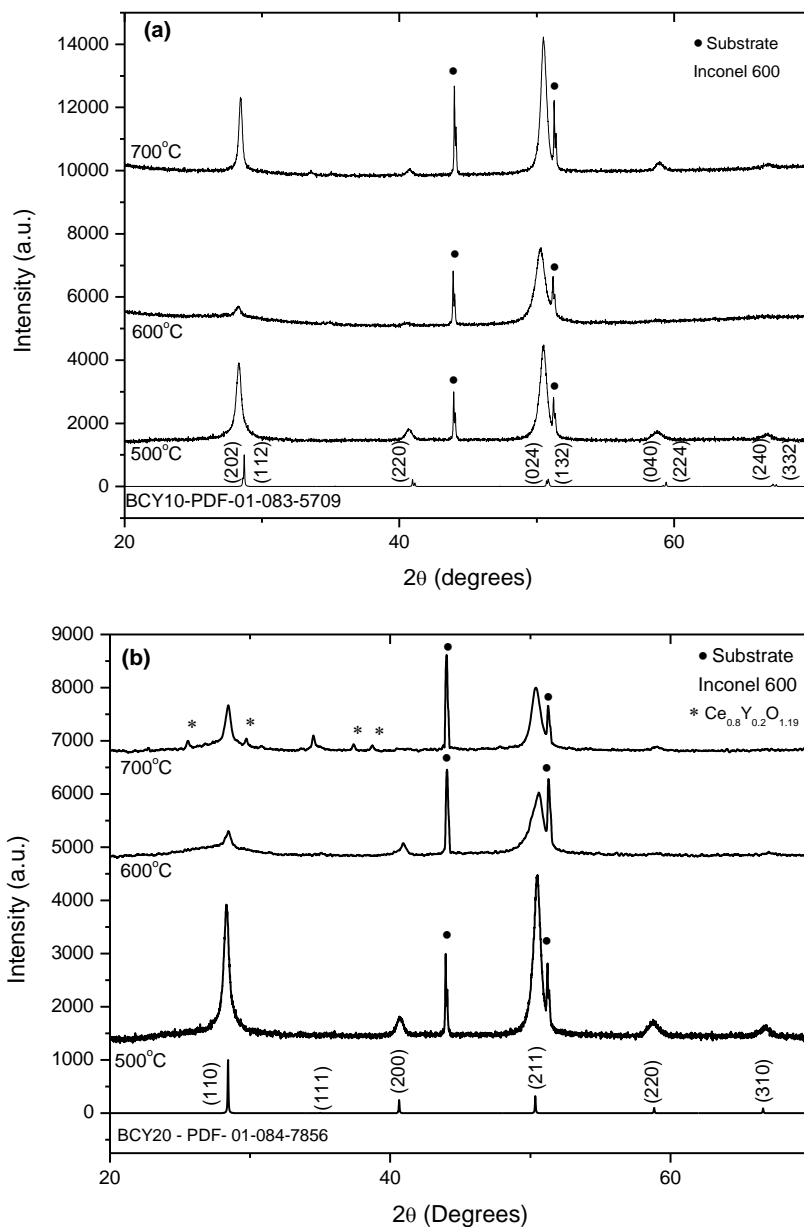


**Fig. 60.** XRD spectra of BCY10 (a) and BCY20 (b) at 500 °C [A3], 600 °C and 700 °C

The unit cell volume for BCY10 for the films formed at 500 °C were expanded compared with the unit cell volume in the powder (Table 33). This is a consequence of the high thermal conductivity obtained by the Inconel 600 support. The unit cell volume of the film for BCY20 was closer to the powder values. The unit cell volume was compressed with temperature (Fig. 61) due to the effect of stress. Unit cell values at 600 °C and 700 °C were similar to the reference values of  $340 \text{ \AA}^3$  [58].

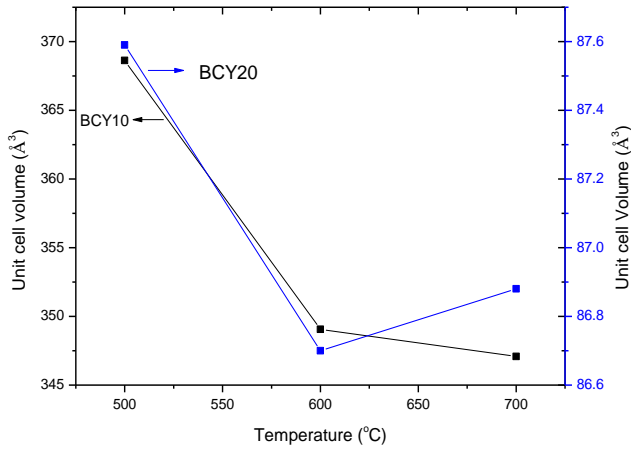


**Fig. 61.** Unit cell volume variation with temperature for BCY10 and BCY20 thin films

Crystal sizes increase with temperature (Fig. 62) as a result of the sum of the total diffusion energies involved in the film formation. Furthermore, the highest crystallite size for BCY10 was 33.7 nm at 700 °C and for BCY20, 14.8 nm. The crystallization activation energy is suggested to be lower with decreasing yttrium content. The crystal growth was faster for BCY10 than BCY20. Therefore, it is suggested that high yttrium concentration stabilizes the microstructure. The values of the lattice parameters for BCY20 at three different temperatures were similar.

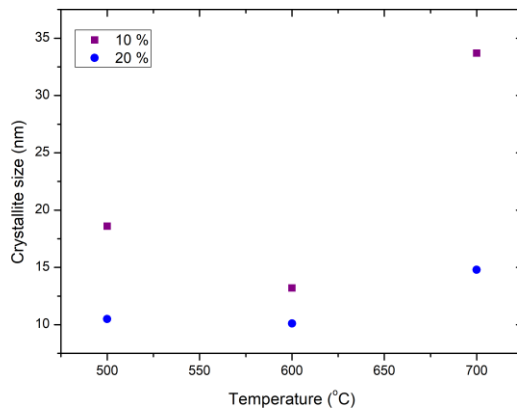


**Fig. 62.** Dependency of crystal size on temperature between BCY10 and BCY20

**Table 33.** Lattice parameters for  $\text{BaCe}_{0.9}\text{Y}_{0.1}\text{O}_{3-\delta}$  with  $Pbnm$  phase and  $\text{BaCe}_{0.8}\text{Y}_{0.2}\text{O}_{3-\delta}$  with  $Pm3m$  phase formed at 500 ° [A3], 600 °C and 700 °C on Inconel 600

Substrate temperature (°C)	Crystal phase	Lattice parameters			Unit cell volume (Å <sup>3</sup> )	Rwp %	GOF	Crystal size (nm)
		a, Å	b, Å	c, Å				
<b>BCY10</b>								
<b>Powder</b>	<i>Pbnm</i>	6.3033	6.2473	8.6764	341.66	3.8	1.27	24.2
<b>500</b>	<i>Pbnm</i>	6.7349	6.2173	8.8036	368.63	3.63	1.16	18.6
<b>600</b>	<i>Pbnm</i>	5.7928	6.2915	9.5774	349.06	3.35	1.07	13.2
<b>700</b>	<i>Pbnm</i>	6.2194	6.2523	8.9257	347.08	3.39	1.11	33.7
<b>BCY20</b>								
<b>Powder</b>	<i>Pm3m</i>	4.4393			87.48	3.67	1.31	10.3
<b>500</b>	<i>Pm3m</i>	4.4410			87.59	3.46	1.10	10.5
<b>600</b>	<i>Pm3m</i>	4.4249			86.70	3.32	1.13	10.1
<b>700</b>	<i>Pm3m</i>	4.4291			86.88	4.04	1.25	14.8

The preferred crystal orientation (024) for BCY10 and (211) for BCY20 were influenced by the deposition temperature (Table 34). The orientation of BCY10 towards (024) is enhanced at high temperature, while for BCY20, the orientation occurs the plane (110).

Although surface orientation is usually the result of growing, the surface with the lowest surface energy [225], orientation at BCY10 and BCY20 is influenced by the decrease in stress created by the residual stress. Then, different orientations were reported before at different temperatures and supports. For example, the thin film BCY10 was formed before by PLD with orientation towards (020) [161] and BCY10 formed by RF-magnetron sputtering reports towards (110) orientation [159]. In addition, randomly oriented crystallographic BCY10 thin film [93, 162, 165] were formed before, above 700 °C. Different processes add different amount of kinetic energy resulting in different diffusion and stress. PLD adds 10 eV, sputtering 1–10 eV and e-beam 0.1–1 eV [227].

**Table 34.** Texture coefficients of formed BCY10 compared with reference diffractogram of *Pbnm* 01-083-5709 and BCY20 thin films compared with the reference diffractogram of *Pm3m* 01-084-7856

Substrate temperature (°C)	Crystal phase	Texture coefficients				
		BCY10*				
		(020)	(220)	(024)	(040)	(240)
500	<i>Pbnm</i>	0.51	0.35	<b>2.76</b>	0.58	0.77
600	<i>Pbnm</i>	0.11	0.17	<b>2.71</b>	0	0
700	<i>Pbnm</i>	0.45	0.20	<b>3.49</b>	0.43	0.41
		BCY20**				
		(110)	(200)	(211)		
500	<i>Pm3m</i>	0.17	0.32	<b>2.49</b>		
600	<i>Pm3m</i>	0.24	0.60	<b>2.15</b>		
700	<i>Pm3m</i>	0.36	0	<b>1.63</b>		

\* Values closer to 5 means a preferred orientation for the plane.

\*\* Values closer to 3 means a preferred orientation for the plane.

#### 4.3.3. Microstructure of the formed BCY thin films

SEM images of the cross-section of BCY10 display Zone 1 microstructure with different layers at 500 °C (Fig. 63). At 600 °C, the grain size increases, and it has a columnar growth with Zone 2 (Fig. 64). The formation of many columnar layers was previously explained by the relaxation of new adsorbed atoms after the start of columnar growth that localizes the atoms in different sites close to the column [228]. The growth process is a quasi-equilibrium process. Thus, the adsorption energy is the sum of the binding energy and motion of atoms. Then, the temperature changes the growth rates of the grains. The rate enhances at 600 °C, and the grain size on the surface decreases. At 700 °C (Fig. 65 Ia–If), local plastic yield, interfacial slips and collapse between grain are suggested [229, A4]. Another reason is the migration of atoms from grain boundaries to grain to release the stress [230]. The cross-section of BCY20 at 500 °C as well shows Zone 2 (Fig. 65 c, d). At 600 °C, it changes to Zone T [231]. In contrast to BCY10, it is suggested that BCY20 adds have more diffusion energy available towards the formation of Zone T according to the Thornton diagram.

However, the differences in the stress could be another reason. SEM on the BCY20 surfaces (Fig. 65 IIa–IIf) show that the surface microstructure decreases in grain sizes at 600 °C but with the corrugate surface formation. This effect could indicate a change from tensile to compressive stress. According to the XRD at 600 °C, the film decreases the crystal size and starts to change the orientation (Fig. 65 IIc, II d). Pyramidal flake shapes were observed on the surfaces. The shape of the surfaces is a consequence of quenching that reduces the mobility [231] and restructures the surface [232] to reduce the strain created during heating and surface energy [232]. BCY20 that was formed earlier by PLD at 700 °C shows a superdense or T-Zone structure [162]. The relative densities were 98% and 99% for BCY10 and BCY20 at 600 °C.

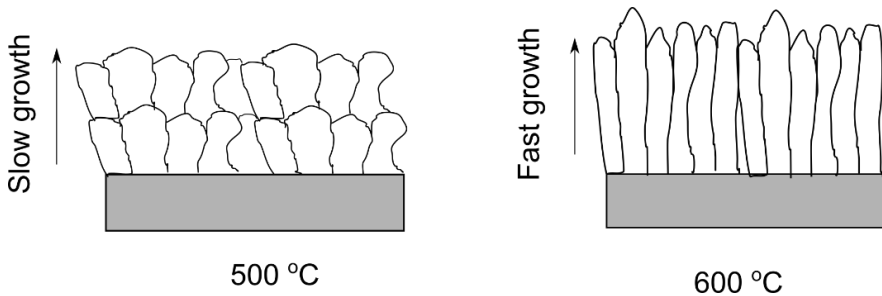


**Fig. 63.** Schematic representation of temperature on nucleation and growth on the microstructure of BCO columns as an effect of relaxation at 500 °C and 600 °C

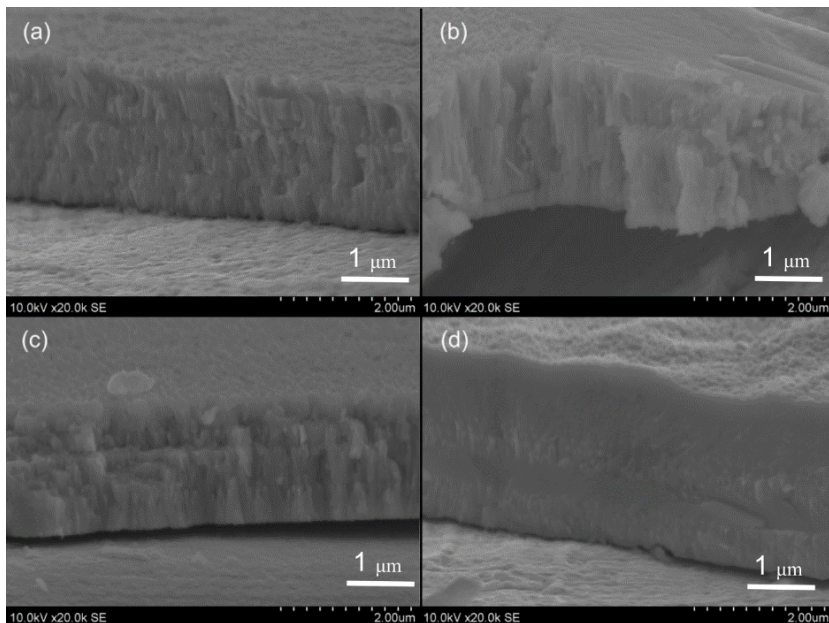


**Fig. 64.** Cross-section of BCY10 formed at (a) 500 °C [A3] a) and (b) 600 °C, BCY20 formed at (c) 500 °C [A3] and (d) 600 °C

At high magnification, the surface defects in the form of corrugated surface are present for BCY10 and BCY20 (Fig. 63 c, d and Fig. 64). Those defects varied with temperature.

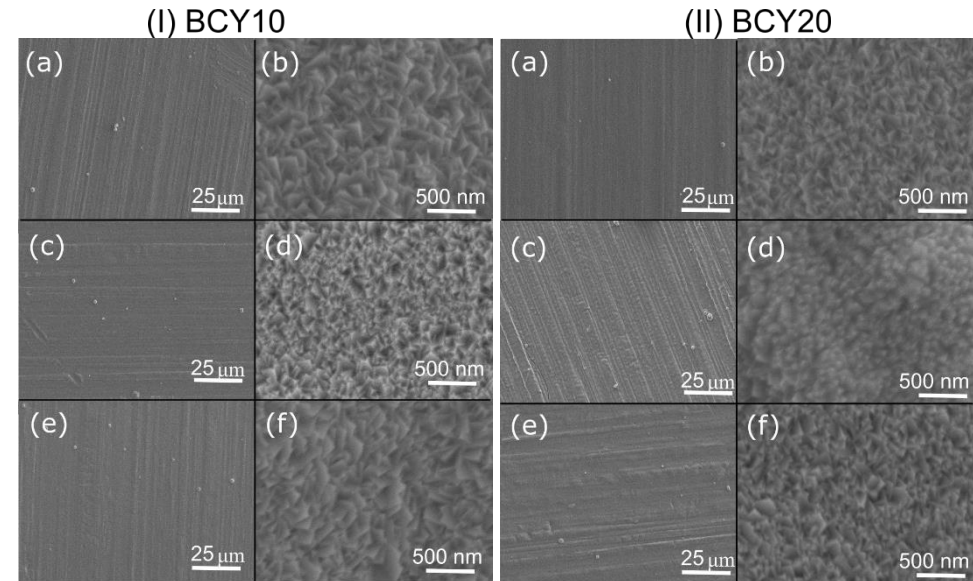


**Fig. 65.** SEM image of surface morphology of BCY10 formed on Inconel 600 at 500 °C (Ia, Ib) [A3], 600 °C (Ic, Id), 700 °C (Ie, If), BCY20 at 500 °C (IIa, IIb) [A3], 600 °C (IIc, IId), 700 °C (IIe, II f)

The grain size values for BCY10 and BCY20 did not show a linear dependency with temperature (Table 35). The grain size values were higher for BCY10 than BCY20. The largest grain size value for BCY10 was 326 nm at 700 °C, and for BCY20, it was 241 nm at 500 °C. It is known that a high % of yttrium stabilizes different structures [113]. A decay in grain size values for BCY20 could be a consequence of slow relaxation of residual stress. The grain sizes for BCY10 were larger than BCY10 formed by PLD at 750 °C [152] prepared on Si<sub>3</sub>N<sub>4</sub> and BZY20 films. The E-beam could transfer the higher amount of energy to the diffusion process than PLD.

**Table 35.** Grain size BCY10 and BCY20 film formed on Inconel 600 at 2 Å/s

Temperature (°C)	Grain size (nm)	
	BCY10	BCY20
500	307.6+/-10.8	241.86+/-6.2
600	178.73+/-10.6	140.26+/-7.1
700	326.4+/-11.0	189.56+/-7.5

SEM images for BCY10 formed in YSZ, MgO and Al<sub>2</sub>O<sub>3</sub> at 600 °C show crack-free films with fibrous morphology and flake shape formation (Fig. 66 I, II). BCY10 columnar growth was observed before in Pt (111) [215] and Si<sub>3</sub>N<sub>4</sub> [152], but nano structured surfaces were reported before by the team [A2] at 500 °C.

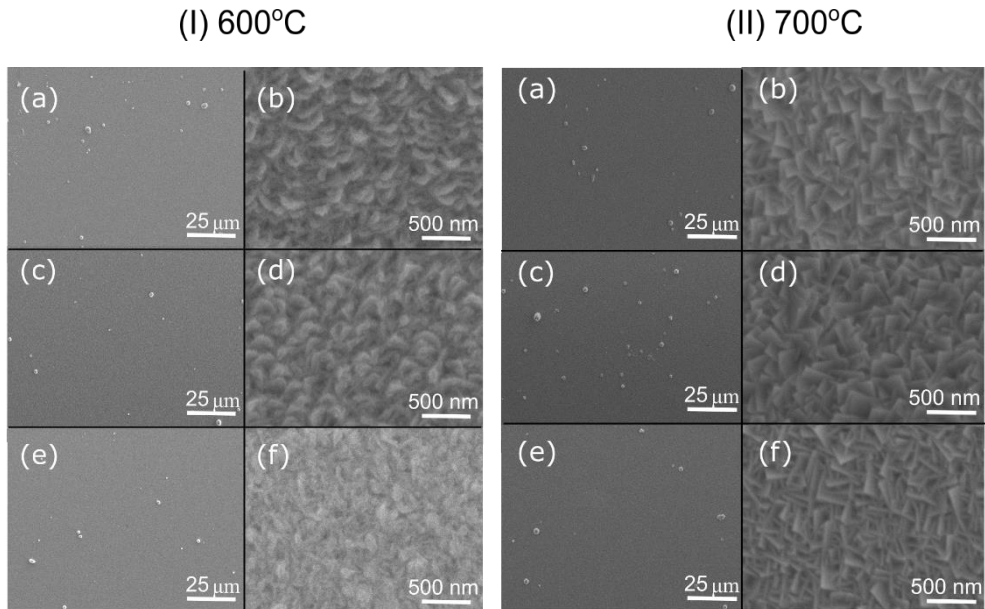


**Fig. 66.** SEM image at two magnifications of BCY10 at 600 °C in MgO (Ia, Ib), Al<sub>2</sub>O<sub>3</sub> (Ic, Id), YSZ (Ie, If) and 700 °C (e, h), BCY10 at 700 °C in MgO (IIa, IIb), Al<sub>2</sub>O<sub>3</sub> (IIc, IId), YSZ (IIe, IIf) and 700 °C (IIe, IIh)

(I) 600°C

(II) 700°C

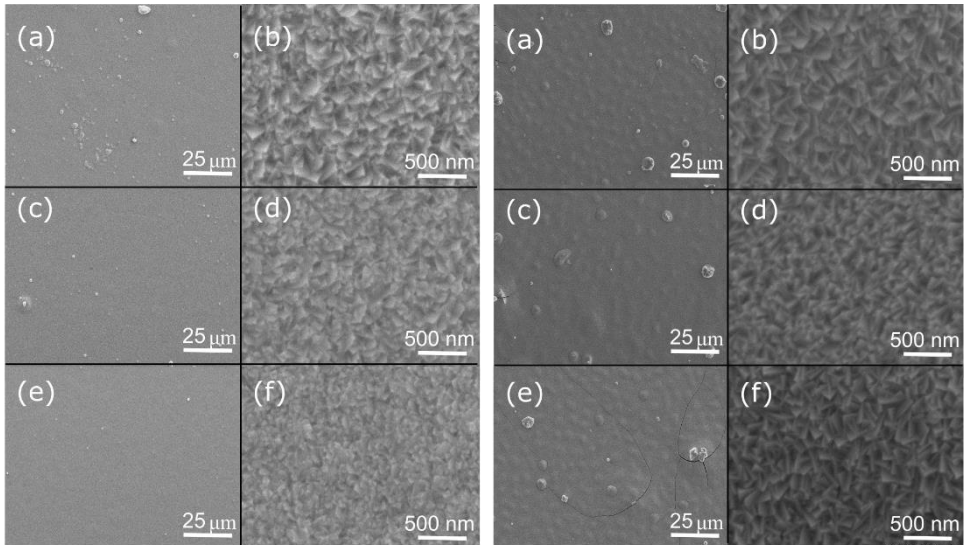


**Fig. 67.** SEM image at two magnifications of BCY20 at 600 °C in MgO (Ia, b), Al<sub>2</sub>O<sub>3</sub> (Ic, Id), YSZ (Ie, If) and 700 °C (e, h), BCY20 at 700 °C in MgO (IIa, IIb), Al<sub>2</sub>O<sub>3</sub> (IIc, IId), YSZ (IIe, IIe) and YSZ (IIe, IIh)

SEM images of BCY20 formed on YSZ, MgO and Al<sub>2</sub>O<sub>3</sub> showed a dense surface morphology attributed to Zone 1 for a deposition temperature of 600 °C that evolves to large grains at 700 °C and Zone 2 (Fig. 67 I, II) on the three substrates. The films formed at 700 °C show the formation of small cracks with rounded features on the surface. A similar behaviour was observed in PZT films: the features were attributed to the increase in roughness starting the residual stress relaxation process with the change in crystal orientation [234]. The residual stress appears to be higher for BCY20 than BCY10. Moreover, the residual stress is suggested to have higher values on metal oxide supports than Inconel 600. Inconel support has higher thermal conductivity, which helps with the relaxation process compared to the metal oxides.

The largest grain size value for BCY10 was 386.2 nm at 700 °C in YSZ (Table 36). YSZ showed the fastest grain growth. The largest grain size value for BCY20 was 249.96 nm at 600 °C on MgO (Table 37) without crack formation. This value is closer to 241 nm formed on Inconel 600 at 500 °C.

**Table 36.** BCY10 grain size at 600 °C and 700 °C on YSZ, Al<sub>2</sub>O<sub>3</sub> and MgO

T(°C)/substrate	Grain size (nm)		
	YSZ	Al <sub>2</sub> O <sub>3</sub>	MgO
<b>600</b>	175.3+/-10.4	324.5+/-0.8	353.6+/-10.3
<b>700</b>	386.2+/-15.8	340.3+/-13.7	353.9+/-16.9

**Table 37.** BCY20 grain size at 600 °C and 700 °C on YSZ, Al<sub>2</sub>O<sub>3</sub> and MgO

T(°C)/substrate	Grain size (nm)		
	YSZ	Al <sub>2</sub> O <sub>3</sub>	MgO
<b>600</b>	131.16+/-3.9	214.33+/-8.1	249.96+/-9.4
<b>700</b>	241.8+/-9.3	213.03+/-6.7	272.1+/-10.10

#### 4.3.4. Electrical properties of the formed BCY thin films

Ionic conductivity measurements show that films formed at 600 °C on Inconel have higher ionic conductivity than samples formed at 700 °C (Fig. 68). The films formed at 600 °C have a higher amount of residual stress compared to the films formed at 700 °C. This effect was previously observed in BaCeO<sub>3</sub> [A4].

The ionic conductivity values of the film were lower than the values reported for the pellets (0.001 S/cm at 400 °C [58] under H<sub>2</sub>). Comparing the film formed at 600 °C and 700 °C (similar unit cell volume and surface morphology), the film highly oriented towards (024) or formed at 700 °C showed the lowest activation energy 0.52 eV (wet/N<sub>2</sub>), or in other words, less oxygen ion conduction compared with the film formed at 600 °C (0.84 eV, wet/N<sub>2</sub>) (Table 38). Thermal stress and its relaxation is the main reason for the change in ionic conductivity. The ionic conductivity and activation energy in dry conditions demonstrate that losing water increments the activation energy values (0.73 eV) and decreases the ionic conductivity values.

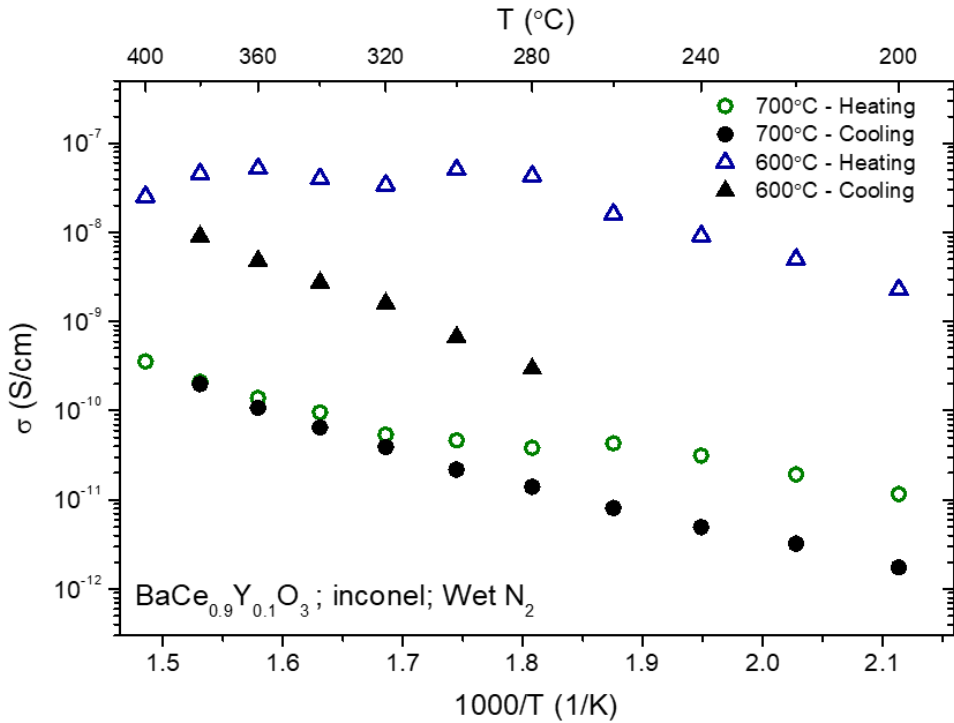


**Fig. 68.** Ionic conductivity on heating and cooling for  $\text{BaCe}_{0.9}\text{Y}_{0.1}\text{O}_3$  formed at 600 °C and 700 °C on Inconel 600, measured in the range between 200 °C and 400 °C in Wet  $\text{N}_2$  [A4]

**Table 38.** Conductivity, activation energy in the dry and wet atmosphere and relaxation temperature in BCY10 formed at 600 °C

Substrate T(°C)	$\sigma_{\text{ion}}$ (300 °C)	$E_a$ (eV) <300 °C	Stress relaxation temperature (°C)
600	$5.04 \times 10^{-8}$ (wet)	0.84	300
	$6.70 \times 10^{-10}$ (dry)	1.10	
700	$4.29 \times 10^{-10}$ (wet)	0.52	300
	$8.10 \times 10^{-11}$ (dry)	0.73	

Compared to  $\text{BaCeO}_3$  with different unit cell values, the thermal stress in BCY10 was observed in the surface morphology and crystal size. Therefore, oxygen ion conduction values are related to the movement in the film microstructure. BCY10 formed at 700 °C with low conductivity values on heating and cooling indicates that the films become stable above 320 °C. However, this as well indicates a loss of water due to the loss of trapping effect that releases water and increases the activation energy.

#### 4.4. Formation and investigation of barium zirconate thin films

A series of thin films was formed from three different powder compositions (BZO, BZY20 and BZCY) and three different temperatures (500 °C, 600 °C and 700 °C).

##### 4.4.1. Elemental composition of the formed barium zirconate thin films

EDS shows that in all three compositions, BZO, BZY20 and BZCY have an excess of Ba. The excess of BaO is reduced with the increase of temperature of the support at 2 Å/s (Table 35). The atomic % ratio Ba/Ce+Y at 500 °C showed that BZY20, which is the composition with higher yttrium concentration, exhibits higher Ba excess. Yttrium could enhance the binding strength with cerium. Undoped barium zirconate showed barium deficiency at 600 °C. The films were stable at room temperature conditions.

**Table 39.** Elemental composition of barium zirconate thin films formed at 500 °C and 600 °C substrate temperatures from EDX and ratio of Ba between Zr, Y and Ce to determine Ba excess in the thin film

Atom/Temperature(°C)	Composition, at. %					
	BZO		BZY20		BCZY	
	500	600	500	600	500	600
<b>Ba</b>	14.99	11.77	13.7	11.29	13.3	11.27
<b>Zr</b>	10.2	13.04	8.1	4.82	12.8	5.81
<b>Y</b>			1.1	1.64	1.0	1.36
<b>Ce</b>					2.8	2.01
<b>O</b>	74.81	75.19	77.10	82.25	70.10	79.55
<b>Ce/Ba</b>	0.72	1.10	0.67	0.57	1.24	0.81

##### 4.4.2. Crystal structure of the formed barium zirconate thin films

XRD diffractograms of BZO, BZY20 and BZCY thin films formed at 500 °C showed a solid mixture formation between precursors (BaO and ZrO<sub>2</sub>) and intermediate phases (Ba<sub>2</sub>ZrO<sub>4</sub>) (Fig. 69). At 600 °C, the crystallinity evolves to BZO and BZY20 with ZrO<sub>2</sub> as an intermediate phase. The phase for BZCY began to form at 700 °C. Compared to barium cerate doped yttrium, the zirconium content strengthens the bond and increases the crystallization energy. Strained hetero-epitaxial films of BZY20 formed by PLD [235] generally form above 700 °C with thicknesses less than 800 nm.

The orientation of the film changes at different temperatures even in the solid-state mixture between secondary, amorphous and crystalline phases. The orientation of the crystal for BZO is towards (200) and evolves towards (110) (Table 40). Despite the growth of the BZY20 films with a (200) orientation at 500 °C, the crystals rearrange their orientation towards (110) at 700 °C. A mixture of intermediate phases

for BZCY was observed at 500 °C and 600 °C. At 700 °C, the crystal shows a preferential orientation towards (200). Similar to BaCeO<sub>3</sub> [A4], the relaxation occurs and modifies the microstructure. Then, the orientation depends on the formation conditions. For example, BZY highly oriented towards (110) was formed earlier at 600 °C on Si (200) support by PLD [236]. Another example is the ultra-thin film of BZY10 that was formed at 600 °C on sapphire and different highly oriented supports with different lattice mismatches with orientations (001), (002), (003) and (004). The same orientations were observed in BZO-MgO formed at 750 °C [130].

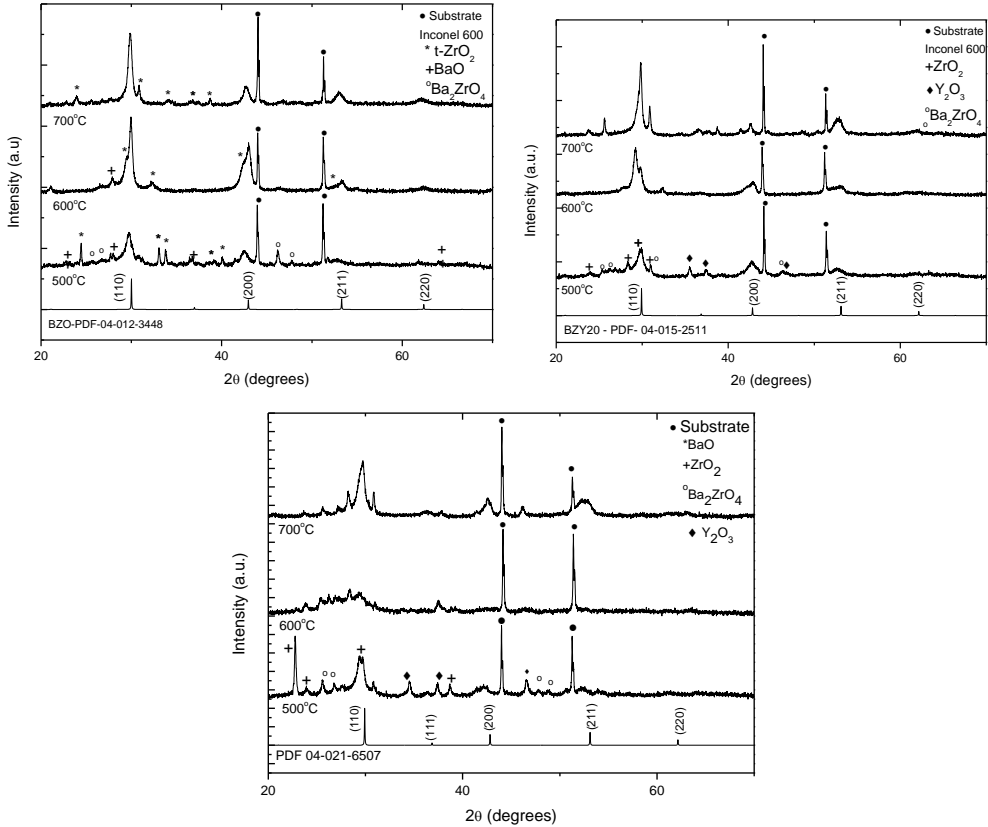


**Fig. 69.** XRD diffractogram of BZO, BZY20 and BZCY thin films formed at 500 °C, 600 °C and 700 °C on Inconel 600

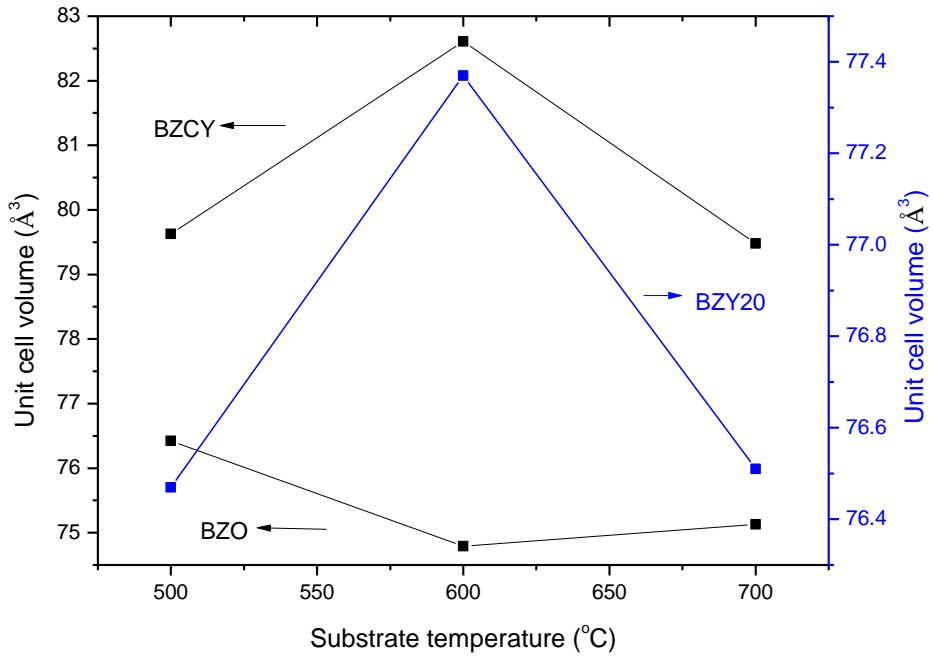


**Fig. 70.** Unit cell volume vs. substrate temperature for BZO, BZY20 and BZCY thin films formed at 500 °C, 600 °C and 700 °C; the lines are for eye guidance

**Table 40.** Texture coefficient for BZO compared with the reference diffractogram of *Pm3m* 04-012-3448, BZY20 compared with the reference diffractogram of *Pm3m* of 04-015-2511 and BZCY *Pm3m* of 04-021-6507 formed at 2Å/s on Inconel 600 at three different temperatures: 500 °C [A3], 600 °C and 700 °C; the main orientation is marked in bold.

Temperature (°C)	Texture coefficient*			
	(110)	(200)	(211)	(220)
<b>BZO</b>				
<b>500</b>	0.88	1.42	0.61	1.07
<b>600</b>	0.95	2.11	0.45	0.48
<b>700</b>	1.24	1.10	0.74	0.90
<b>BZY20</b>				
<b>500</b>	0.83	1.54	0.79	0.82
<b>600</b>	0.87	1.46	0.86	0.78
<b>700</b>	1.42	0.79	1.07	0.70
<b>BZCY</b>				

<b>500</b>	1.10	1.24	0.78	0.87
<b>600</b>	0.78	1.12	0.83	1.25
<b>700</b>	1.10	1.33	1.04	0.51

\*Bolt numbers represent the preferred orientation.

The unit cell volume grows according to the dopant: from BZO < BZY20 < BZCY in a temperature range between 500 °C and 700 °C (Table 41, Fig. 70).

Moreover, the unit cell volume in the film expands compared to the powder values in all the cases [A3]. The unit cell values at different temperatures vary within +/- 2 Å<sup>3</sup>. These values did not follow a linear dependence with temperature. As in the previous results, the main reason is the relaxation of the film at different formation temperatures and support thermal conductivity. The crystal sizes were greater at 700 °C. BZY20 had the largest crystal size with 27.4 nm, BZO with 16.8 nm and BZCY with 11.3 nm.

**Table 41.** Lattice parameter and crystal size for BZO, BZY20 and BZCY initial powder and formed on Inconel 600 at three different temperatures: 500 °C [A3], 600 °C and 700 °C

Substrate temperature (°C)	Lattice parameter (Å)	Unit Cell Volume (Å <sup>3</sup> )	Crystal size (nm)
	a		
<b>BZO</b>			
<b>Powder</b>	4.1915	73.63	125.0
<b>500</b>	4.2436	76.42	12.0
<b>600</b>	4.2132	74.79	9.5
<b>700</b>	4.2196	75.13	16.8
<b>BZY20</b>			
<b>Powder</b>	4.2169	74.98	23.9
<b>500</b>	4.2446	76.47	8.6
<b>600</b>	4.2611	77.37	6.4
<b>700</b>	4.2452	76.51	27.4
<b>BZCY</b>			
<b>Powder</b>	4.2437	76.42	24.1
<b>500</b>	4.3022	79.63	2.4
<b>600</b>	4.3553	82.61	14.2
<b>700</b>	4.2996	79.48	11.3

#### 4.4.3. Microstructure of the formed barium zirconate thin films

Fig. 71 exhibits Stranski–Krastanov growth cross-sections for barium zirconate, signifying a change in chemical potential at the surface compared to barium cerates. Hence, the growth changes to Stranski–Krastanov growth mode. The presence of columnar formation or Zone 1 in the barium zirconate yttrium doped cerium in comparison with the undoped barium zirconate and barium zirconate doped yttrium demonstrates the effect of zirconium and dopants on the microstructure. Cross-sectional images show the deformation at the surface that has a corrugated or wavy surface appearance at 500 °C, which becomes less corrugated at 600 °C as an effect of stress relaxation [237]. The layers that are present in the cross-sections (Fig. 71) could be attributed to yttrium oxide phase. The concentrations greater than 5% of yttrium showed segregation at grain boundaries at sintering temperatures of 1200 °C [238]. The segregation is explained as well by the elastic strain created by the mismatch between ionic radius:  $Y^{3+} = 0.91 \text{ \AA}$  and  $Z^{4+} = 0.72 \text{ \AA}$ .

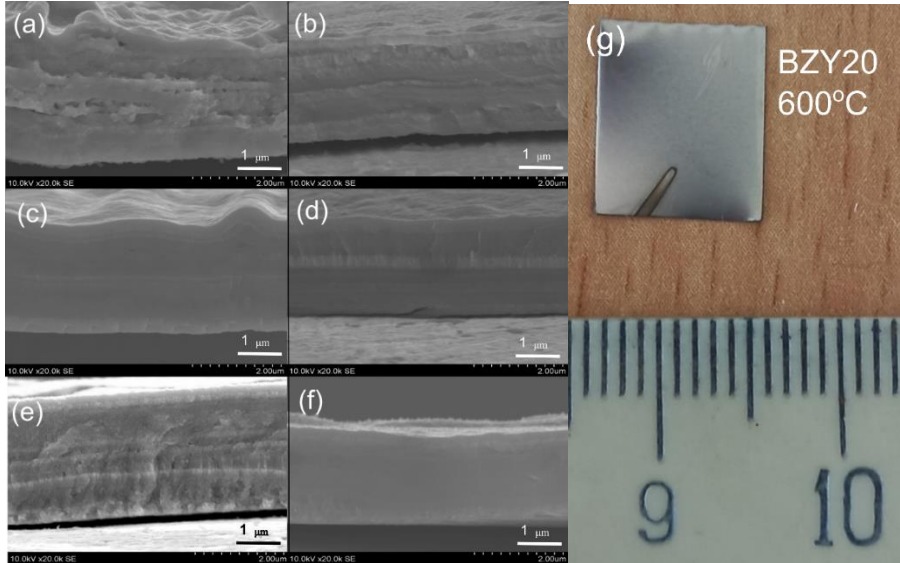


**Fig. 71.** Cross-section of the SEM image of BZO 500 °C (a) [A3] (a) and 600 °C (b), BZY20 500 °C [A3] (c) and 600 °C (d), BZCY 500 °C [A3] (e) and 600 °C (f) formed on Inconel 600 at Å/s, (g) picture of BZY20 formed at 600 °C stable at room conditions

SEM images of the films formed at 500 °C show two types of defects for BZO, corrugate features and cracks on the surface (Fig. 72). The coefficient of thermal expansion for each composition is expected to be different. BZO has a TEC in  $4\text{--}8 \times 10^{-6} \text{ K}^{-1}$  range, BZY20 in  $8\text{--}9 \times 10^{-6} \text{ K}^{-1}$  range and BZCY in  $8 \text{ to } 10 \times 10^{-6} \text{ K}^{-1}$  range [178]. Then, the composition influences the level of residual stress for the same parameters as well.

At 600 °C, there are fewer cracks, and in some cases, they disappear as a result of microstructure change and stress relief. Increasing the forming temperature for BZO and BZCY reduces the defects in the film. Thus, the surfaces are free of cracks (Fig. 72) above 500 °C formation temperature. The cracks and defects for BZY20 were observed at 700 °C. The reason for the formation of cracks varies. High temperatures incorporate more yttrium into the BZO unit cell. The difference in atomic between yttrium and zirconium ( $Y^{3+} = 0.91 \text{ \AA}$  and  $Z^{4+} = 0.72 \text{ \AA}$ ) adds further strain to the film over the already formed stress. As a result, the cracks are formed on the surface. The film surface at 700 °C showed blistering. The blisters form in highly stressed regions.

The grain size values for BZO formed on Inconel grow from 600 °C to 700 °C with values from 113 nm to 134 nm. The grain size values for BZY20 and BZCY dropped at 700 °C (Table 42). The grain size values did not show a dependence on the temperature (Fig. 73). The strain and relaxation process affects the reorganization of the microstructure on the surface. The grain sizes of BZY20 thin films were smaller than those produced by PLD. PLD adds a greater amount of energy from the ionic gas energy transfer, which aids in adatom diffusion.

SEM images of BZO, BZY20 and BZCY on metal oxide supports shows a Stranski–Krastanov growth mode. At 600 °C, the surface undergoes shrinkage formation as a stress relaxation effect due to the sum of Zone 1 at the surface tensile stress, possible TEC mismatch (Fig. 73–75) and the low thermal conductivity in the support to accommodate the microstructure. The growth mode is difficult to distinguish, but it shows a mixture of layer-by-layer with columnar growth or Stranski–Krastanov growth. Buckled features are explained as a delamination effect [239] due to the large amount of stress. Other defects were blistering and cracking. Its possible formation is due to the diffusion of oxygen on the surface, forming different oxides due to the stress. An increase in temperature increases tensile stress, cracks and blisters [240]. The origin of blistering and cracking could be attributed to the effect of radiation [241], but the film is located far from the highly ionized cloud. It is interesting to note that the blister features increase in size with temperature.

The grain sizes in BZO varies with the support (Table 43). The largest grains were observed in MgO at 600 °C (Fig. 73). Their values are reduced with increasing temperature, while they enhance with yttrium dopant and cerium concentration.

The BZY20 film formed on YSZ changes its growth mode from Stranski–Krastanov to layer-by-layer. Although columnar growth appears as a consequence of stress relief, it is suggested that high temperature reduces the stress by reorganizing microstructure. Then, layer-by-layer growth mode without defects is observed (Fig. 74).

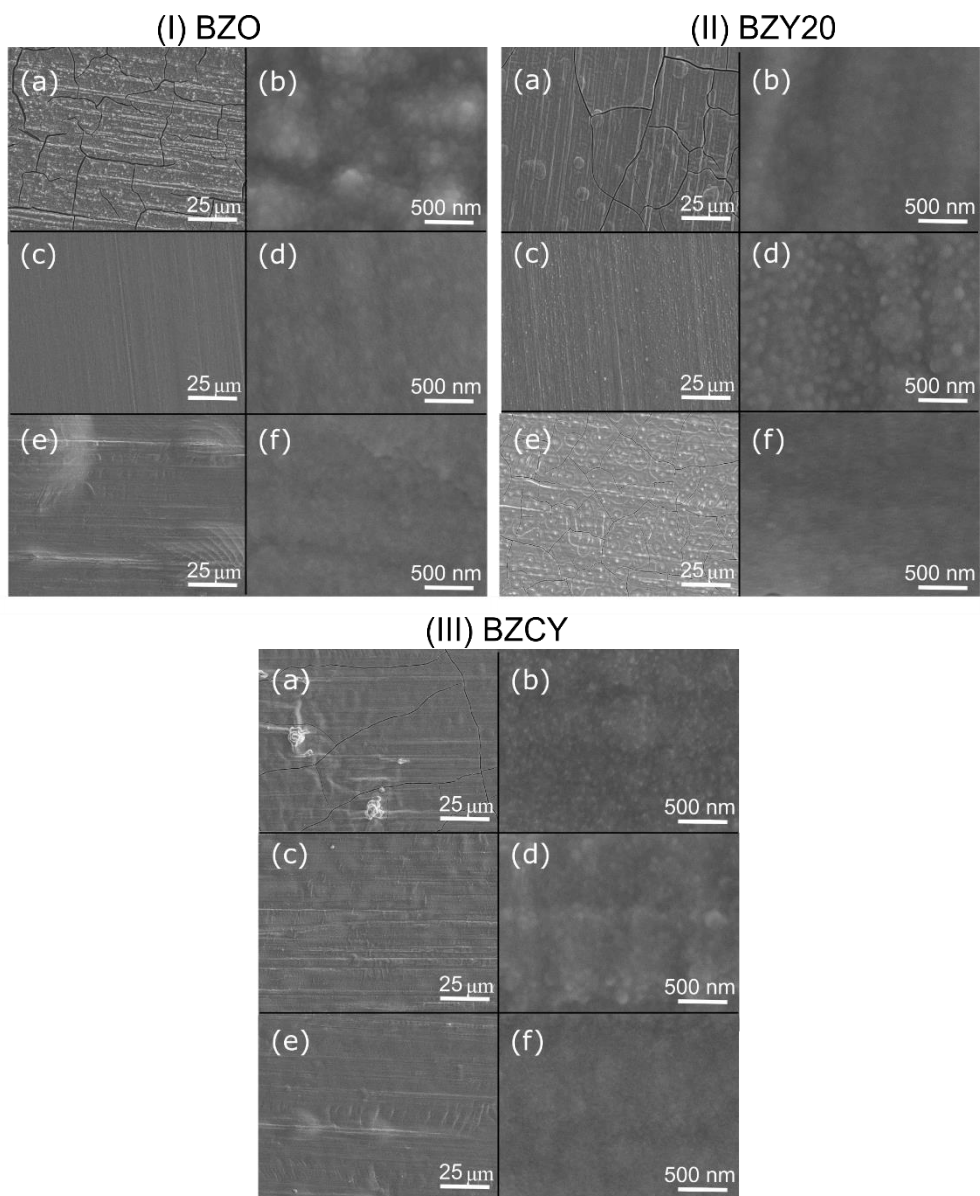


**Fig. 72.** SEM image of (I) BZO formed on Inconel 600 at 500 °C [A3] (a, b), 600 °C (c, d) and 700 °C (e, f), (II) BZY20 at 500 °C [A3] (a, b), 600 °C (c, d) and 700 °C (e, f) and (III) BZCY at 500 °C [A3] (a, b), 600 °C (c, d) and 700 °C (e, f)

**Table 42.** Grain size of BZO, BZY20 and BZCY formed at 500 °C, 600 °C and 700 °C on Inconel 600 at 2 Å/s

	Grain size (nm)		
	BZO	BZY20	BZCY
<b>500</b>	120.33+/-4.5	168+/-8.9	78.3+/-4.6
<b>600</b>	113.53+/-5.2	134.9+/-5.9	115.46+/-8.1
<b>700</b>	134.6+/-5.06	-	75+/-5.0

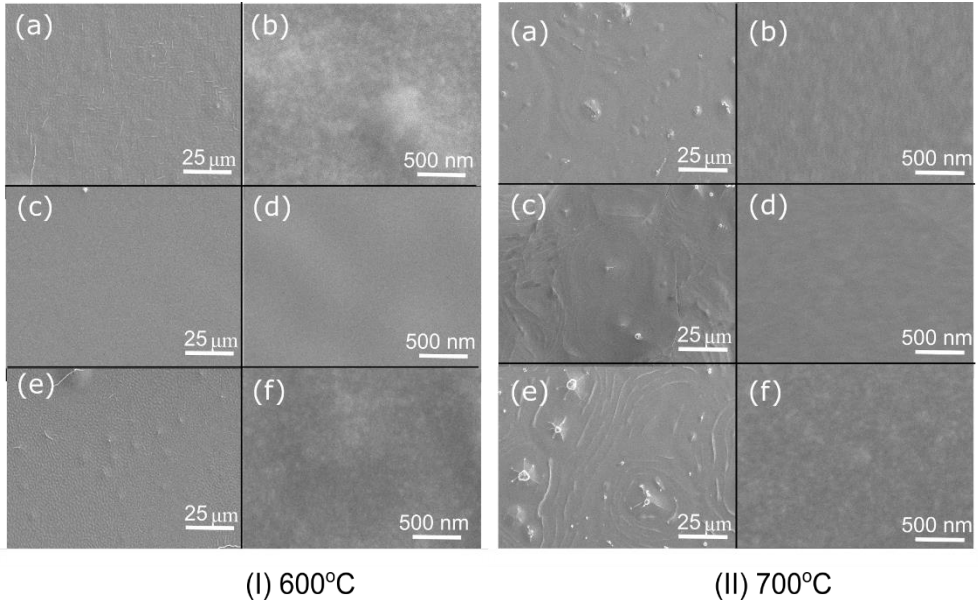


**Fig. 73.** SEM image of BZO formed on MgO (Ia, Ib), Al<sub>2</sub>O<sub>3</sub> (Ic, Id), YSZ (Ie, If) at 600 °C and MgO (IIa, IIb), Al<sub>2</sub>O<sub>3</sub> (IIc, IId), YSZ (IIe, IIf) 700 °C (e-h) at two different magnifications

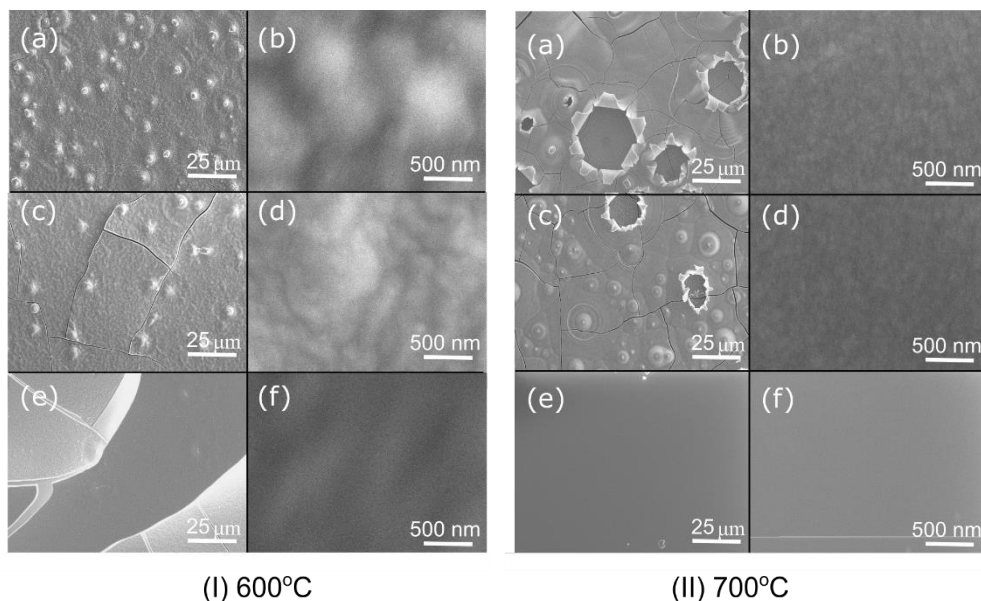


**Fig. 74.** SEM image of BZY20 formed on MgO (Ia, Ib), Al<sub>2</sub>O<sub>3</sub> (Ic, Id), YSZ (Ie, If) at 600 °C and MgO (IIa, IIb), Al<sub>2</sub>O<sub>3</sub> (IIc, IId), YSZ (IIe, IIf) 700 °C (e-h) at two different magnifications

The SEM images for BZCY show layer-by-layer growth with columnar growth on the surface (Stranski–Krastanov) at 600 °C and 700 °C (Fig. 75). Thus, the grain sizes on the surface (Fig. 73, 74 and 75 Ic) with values above 1 μm (Table 43) were observed at high magnification. The grain size values decrease with the addition of high amount of yttrium or cerium. Ultimately, high formation temperatures and high kinetic energies of the particles result in plastic deformation that rearranges the atoms and changes the microstructure of each composition. Thus, barium zirconates exhibit plastic deformation at low temperature <700 °C. Plastic deformation in barium zirconates was reported before at 1235 °C [242].

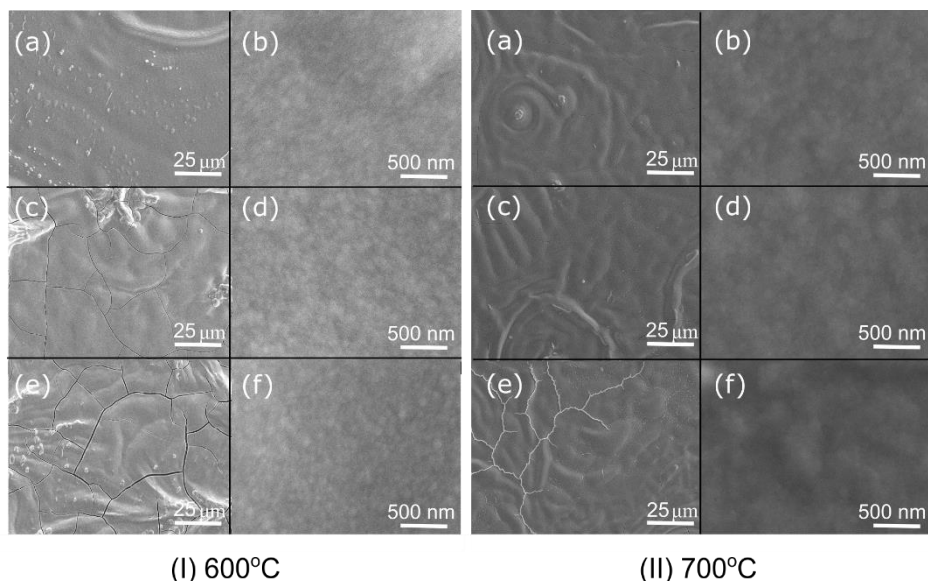


**Fig. 75.** SEM image of BZCY formed on MgO (Ia, Ib), Al<sub>2</sub>O<sub>3</sub> (Ic, Id), YSZ (Ie, If) at 600 °C and MgO (IIa, IIb), Al<sub>2</sub>O<sub>3</sub> (IIc, IIId), YSZ (IIe, IIIf) 700 °C (e-h) at two different magnifications

**Table 43.** Grain size for BZO, BZY20 and BZCY formed on YSZ, Al<sub>2</sub>O<sub>3</sub> and MgO at 600 °C and 2Å/s

Support	Grain size (nm)		
	BZO	BZY20	BZCY
YSZ	1804.7+/-0.07	770.8+/-0.03	135.3+/-0.003
Al <sub>2</sub> O <sub>3</sub>	1139.0+/-0.05	1027.6+/-0.04	160.37+/-0.005
MgO	1599.0+/-0.09	997.9+/-0.05	131.13+/-0.005

The high-density microstructure in barium zirconate showed a preferable layer-by-layer mode with columnar growth on the surface compared to the only columnar growth by PLD [169] with compressive stress. The grain size values were higher than those obtained by PLD at 750 °C at the surface. However, they do not grow towards the cross-section. The supports with different thermal conductivities result in variation on the stress relaxation that affect the final microstructure. TEC mismatch, lattice mismatch, yttrium concentration and supports are the main reasons of stress and its release.

## 5. CONCLUSIONS

The formation of thin films by electron beam evaporation process and control of technological parameters allows to study various mechanisms involved in the microstructural changes of the formed films. The microstructure and its variations are caused by different forces arising from the growth rate of the coating, the temperature of substrate, the mismatch between the thermal expansion coefficient of the coating to be formed and the substrate to be used, the composition of the supports, the thermal properties of the supports and the concentration of impurities and admixtures. The diffusion process alters the growth kinetics of the crystallites, their growth direction, shape, size, crystallisation, residual stresses and the formation of defects at the surface and the coating-substrate interface. The formed barium cerate and barium zirconate thin films had a columnar growth, layer-by-layer and Stranski–Krastanov growth pattern and corresponded to different zones of the Thornton diagram [8]. In summary, the results of this investigation demonstrate that residual stress changes the unit cell volume, influences the diffusion of oxygen ions and affects the proton trapping effect. Then, undoped barium cerate presents mixed proton and oxygen ionic conductivity at tested temperatures below 500 °C. The relaxed microstructure lowers the ionic conductivity as in the case of BaCeO<sub>3</sub>, formed at 700 °C as a consequence of less rearrangement in the microstructure, less diffusion of oxygen ion and less trapping of protons. Then, the change in the residual stress of the barium cerates was first observed by the impedance spectroscopy by following the change in the total conductivity. The Nyquist plot as well showed the mixed proton and oxygen ionic conductivity for undoped BaCeO<sub>3</sub> films at different frequencies. The ionic conductivity values and the activation energies demonstrate the additional oxygen ionic conduction of the supports YSZ, MgO and Al<sub>2</sub>O<sub>3</sub>, which enhance the overall conductivity measured in-plane. In the end, the YSZ support was shown to enhance the oxygen ion conductivity in undoped BaCeO<sub>3</sub> with the formation of oxygen vacancies and transport of oxygen ions.

More specifically:

1. The research demonstrated the formation of crystalline BaCeO<sub>3</sub> thin films above 400 °C, using deposition rates of 2 Å/s and 12 Å/s on Invar, Stainless steel, Glass sealing alloy and Inconel supports. The films remained amorphous from 100 °C to 400 °C at 4 Å/s and 8 Å/s rates. The thermal expansion coefficient (TEC) of the supports and the temperature during the growth cause the additional stress and influence the crystal sizes with a range of 22 nm to 72 nm at 12 Å/s. While unit cell volume values for BaCeO<sub>3</sub> thin films mostly exceeded the reference, the one on Invar's support closely matched it. In addition, the nanoindentation tests measured perpendicular to the thin films highlighted the highest compressive stress in the thin films formed on Inconel 600. The distinct atomic ratios were evident in compositions based on the support temperature, and undoped films closely aligned with stoichiometry.

2. The BaCeO<sub>3</sub> thin films formed at 2 Å/s deposition rate and above 700 °C on Inconel 600 showed an orthorhombic *Pbnm* phase with 1.5–2 μm thickness. Nanograin size values were between 296 nm and 437 nm and the lateral grain sizes, between 39 nm and 215 nm. The cross-sections exhibited columnar growth Zone 2 of Thornton zone diagram with high density above 92%, which is influenced by the higher diffusion of the adatoms during the growth of thin film. The grain size values varied between 283 and 359 nm for the films formed on MgO (001), Al<sub>2</sub>O<sub>3</sub> (0001) and YSZ (001) in the temperature range of 600 °C to 700 °C. The orientation of the support resulted in the variation of the grain shape of the formed BCO thin films.

3. The formed nanograined BCO thin films on Inconel 600 support that were formed at 400 °C exhibit an ionic conductivity of 10<sup>-9</sup> S/cm (400 °C) due to the possible higher amount of the created oxygen vacancies. Dehydration/relaxation onset temperatures were observed, and the activation energies varied from 0.6 eV to 1.13 eV. The thin films formed at 700 °C exhibit ionic conductivity of 10<sup>-7</sup> S/cm (400 °C) due to the higher crystallite size and compression of the unit cell; the thin films formed on YSZ (001) support showed the highest ionic conductivity values (0.13 S/cm at 400 °C) reported until now for the undoped barium cerate.

4. BaCe<sub>0.9</sub>Y<sub>0.10</sub>O<sub>3</sub> (BCY10) thin films deposited at 2 Å/s on Inconel 600 exhibited an orthorhombic *Pbnm* phase. Nanograin sizes ranged from 178 nm to 326 nm on Inconel 600 (500–700 °C) and from 175 nm to 353 nm on YSZ (001), Al<sub>2</sub>O<sub>3</sub> (001) and MgO (001) (600–700 °C). The cross-sections displayed columnar growth (Zone 1 of the Thornton zone diagram), showing that the presence of yttrium dopants decreases the diffusion of adatoms in barium cerates. Crystal sizes on Inconel 600 support, oriented towards (024), varied from 13.2 nm to 33.7 nm (500–700 °C). The ion conductivity of BCY10 formed at 2 Å/s deposition rate and 600 °C on Inconel 600 was 10<sup>-8</sup> S/cm at 400 °C, and BCY10 formed at 700 °C had ion conductivities of 10<sup>-10</sup> S/cm at 400 °C under wet N<sub>2</sub>.

5. The BaCe<sub>0.8</sub>Y<sub>0.20</sub>O<sub>3</sub> (BCY20) thin films formed at 2 Å/s deposition rate on Inconel 600 showed a cubic *Pm3m* with 1.5–2 μm thickness. The grain sizes between 140 nm and 241 nm in the temperature range of 500–700 °C on Inconel 600 and between 131 nm to 272 nm for YSZ (001), Al<sub>2</sub>O<sub>3</sub> (0001), MgO (001) in the temperature range of 500–700 °C. The cross-section showed columnar growth Zone 1 at 500 °C but Zone T of Thornton zone diagram at 600 °C substrate temperature. The crystal size values were between 10.5–14.8 nm on Inconel 600 and oriented towards (211) in the temperature range of 500–700 °C.

6. BaZrO<sub>3</sub> (BZO) thin films formed at 2 Å/s deposition rate on Inconel 600 showed a cubic *Pm3m* with 1.5–2 μm thickness. The grain size values varied between 113 nm and 134 nm in the temperature range of 500–700 °C on Inconel 600, and the values were between 1.13 μm and 1.80 μm on YSZ (001), Al<sub>2</sub>O<sub>3</sub> (0001) and MgO (001) in the temperature range of 600 °C to 700 °C. The large values of grain size on the surface correspond to the Stranski–Krastranov growth with the microstructure of Zone T where it could have been influenced by the

residual stress. The crystal sizes were between 9.5 nm and 16 nm on Inconel 600; the orientation was towards (200) at 500 °C and 600 °C, and with the rise in temperature, it changed to (110) at 700 °C. The crystallites were mixed with ZrO<sub>2</sub>, BaO and Ba<sub>2</sub>ZrO<sub>4</sub> at 500 °C, which were reduced with the increase on temperature. The cross-section investigation showed that thin films growth belongs to Zone T of Thornton zone diagram in the range of 500–700 °C substrate temperature.

7. The BaZr<sub>0.8</sub>Y<sub>0.2</sub>O<sub>3</sub> (BZY20) thin films formed at 2 Å/s deposition rate on Inconel 600 showed a cubic Pm3m with 1.5–2 μm thickness. The grain size values varied between 134 nm and 168 nm in the temperature range of 500–700 °C on Inconel 600. The grain sizes values were between 0.77 μm and 1.02 μm on YSZ (001), Al<sub>2</sub>O<sub>3</sub> (0001) and MgO (001) in the temperature range of 600 °C to 700 °C. The crystal sizes varied between 6.4 nm and 27.4 nm on Inconel 600; the orientation was towards (200) at 500 °C and 600 °C, and it changed to (110) at 700 °C. The crystallites were mixed with ZrO<sub>2</sub>, BaO, Y<sub>2</sub>O<sub>3</sub> and Ba<sub>2</sub>ZrO<sub>4</sub> at 500 °C, which were reduced at high temperature. Cross-section investigation showed that thin films growth belongs to Zone T of Thornton zone diagram in the range of 500–700 °C substrate temperature. The thin films were more attracted to the support that their own atoms forming Stranski-Krastanov growth.

8. The BaZr<sub>0.8</sub>Ce<sub>0.1</sub>Y<sub>0.2</sub>O<sub>3</sub> (BCZY) thin films formed at 2 Å/s deposition rate on Inconel 600 showed a cubic Pm3m with 1.5–2 μm thickness. The grain sizes values varied from 75 nm to 115 nm in the temperature range of 500 °C to 700 °C on Inconel 600. The grain size values varied between 0.13 μm and 0.16 μm on YSZ (001), Al<sub>2</sub>O<sub>3</sub> (0001) and MgO (001). The crystal sizes varied between 2.4 nm and 14.2 nm on Inconel 600, and the orientation was towards (200) at 500 °C and at 700 °C, it changed to (220) at 600 °C for formed thin films. The films showed the presence of ZrO<sub>2</sub>, BaO, Y<sub>2</sub>O<sub>3</sub>, and Ba<sub>2</sub>ZrO<sub>4</sub>, which were reduced at high temperature. Cross-section investigation showed that thin films growth belongs to zone between 1 and T of Thornton zone diagram in the range of 500–700 °C substrate temperature. Presence of Ce enhances the formation of columns.

## 6. SANTRAUKA

### IVADAS

Bario ceratai ir bario cirkonatai yra gana gerai žinomi dėl savo joninio laidumo savybių 200–1000 °C temperatūros aplinkoje. Šios medžiagos gali būti suformuotos kaip atsitiktinai orientuotos ir labai orientuotos heteroepitaksinės plėvelės, tai ir sąlygoja jų savybes. Nors heteroepitaksinės itin plonos plėvelės leidžia išsamiai ištirti paviršiaus ir paviršiaus bei padėklo sąsajas, jose atsiranda įtempiai dėl gardelių parametru neatitikimo, ir tai sąlygoja prastas mechanines savybes. Norint sumažinti atsirandančius įtempius, reikia naudoti papildomus pasluoksnius ar keisti sluoksnių storį. Palyginimui, tekstūrinės plėvelės suteikia pranašumą gauti netradicines mikrostruktūras, pasižyminčias naujomis neiširtomis savybėmis. Tekstūrinių plonų plėvelių ir jų sąveikos su skirtingais pagrindais tyrime siūlomi nauji būdai, kaip pagerinti šių dangų katalitines, mechanines bei elektronines savybes ir cheminį stabilumą, kad būtų pasiektas mikrosistemų ar vidutinės temperatūros mikrokuro elementų, suformuotų iš metalų bei keramikų, didžiausias gamybos našumas. Gaminant mikrosistemas susiduriama su dviem pagrindinėmis problemomis: apdorojimo sąnaudomis ir formuojamų struktūrų matmenų keitimu [3]. Be to, naudojant metalų pagrindu pagamintus kuro elementus, kyla dar kita problema – metalo degradacija ir atomų, pavyzdžiui, Ni, kurie suardo kristalą esant didelei sukepinimo temperatūrai, migracija [4]. Didelė sukepinimo temperatūra yra būtina norint gauti kristalines, tankias ir didelio grūdėtumo plėveles. Fizikiniai nusodinimo metodai (PVD) suteikia pranašumą formuojant kristalines ir tankias plėveles mažesnės temperatūros aplinkoje. Be to, keičiant nusodinimo parametrus, kontroliuojama formuojamų plėvelių mikrostruktūra ir sudėtis. Šiame darbe buvo tirtas bario cerato (BCO), bario cerato, legiruoto 10 % bei 20 % itriu (BCY10, BCY20), bario cirkonato (BZO), bario cirkonato, legiruoto 20 % itriu (BZO), ir bario cirkonato, legiruoto 10 % itriu su 10 % ceriu (BZCY), plonų plėvelių formavimas, taikant vakuuminį garinimą elektronų pluoštu, siekiant nustatyti suformuotų plonų plėvelių įtaką joniniam laidžiui, cheminiam stabilumui ir mechaninėms savybėms. Suformuotos bario cerato ir bario cirkonato plonos plėvelės pasižymėjo tekstūriškumu. Plėvelių mikrostruktūra ir įtempiai keitėsi pagal garų fazėje esančių dalelių kinetinę energiją ir jų greitį garavimo proceso metu [5], [6], padėklo temperatūrą ir relaksacijos procesus. Bario cirkonatų atveju, priemaišų koncentracija taip pat sąlygojo suformuotų plonų plėvelių mikrostruktūrą. Buvo pritaikytos dvi skirtingos plonų plėvelių formavimo metodikos, t. y. buvo panaudoti du skirtingos konstrukcijos kaitintuvai, dirbantys 150–600 °C ir 500–700 °C temperatūrų intervale. Panaudojant kaitintuvą, dirbantį mažesnės temperatūros intervale, buvo nustatyta, kad bario ceratų plonos dangos, remiantis Thorntono zonų diagrama [139], pasižymi mikrostruktūra, būdinga pirmajai zonai, o panaudojant kaitintuvą, dirbantį didesnės temperatūros intervale – antrajai zonai. Jonų laidumas padidėjo plonose dangose, suformuotose panaudojant didesnės temperatūros kaitintuvą, kai padėklo temperatūra buvo 500 °C. Šiose dangose fiksuojamos gniuždančio pobūdžio deformacijos, turinčios įtaką ir kristalinės gardelės parametrams. Bario ceratų plonos plėvelės,

suformuotos  $\text{Al}_2\text{O}_3$  (0001), YSZ (001) bei  $\text{MgO}$  (001) pagrindu, turėjo 2 zonavą būdingą mikrostruktūrą ir pasižymėjo dideliu orientuotu grūdėtumu bei kristališkumu. Didžiausias joninis laidumas ( $\sim 0,1 \text{ S/cm}$ ,  $400 \text{ }^\circ\text{C}$ ), buvo gautas suformuotose BCO plonose dangose, kuriose vyravo lygiagrečios su padėklo paviršiumi (202) orientacijos pailgi grūdėliai. Šios BCO plonos dangos buvo suformuotos ant YSZ  $600 \text{ }^\circ\text{C}$  temperatūros padėklų. Suformuotos mažesnės temperatūros intervale bario cirkonatų plonos dangos buvo nestabilios natūralioje aplinkoje. Tačiau šios plonos dangos, kuriose vyravo Stranskio–Krastanovo augimo pobūdis, pasižymėjo stabilumu. Nustatyta, kad suformuotų plonų dangų mikrostruktūrą bei joninį laidumą sąlygoja nusodinimo parametrai ir skirtingo šiluminio plėtimosi padėklai, kurie paveikia liekamuosius įtempius suformuotose struktūrose.

### **Tyrimo problema**

Dabartiniams tyrimams trūksta informacijos apie bario ceratų ir bario cirkonatų plonų plėvelių formavimą bei suformuotų plonų struktūrų savybes. Ypač trūksta tyrimų, kai nagrinėjamos mažesnės nei  $1 \mu\text{m}$  storio plėvelės. Šios medžiagos pasižymi pakitusiais gardelės parametrais, kai yra auginamos ant skirtingų kristalinių padėklų. Toks reiškinys yra gerai užfiksuotas bario cirkonatų atveju, kai kubinės fazės gardelės parametrai pakinta dėl padėklo gardelės parametru neatitikimo. Priešingai, bario ceratų, turinčių ortorombinę fazę, atveju šis gardelės parametru pokytis dar nėra ištirtas. Bario cirkonatų gardelės parametru pokytis reikšmingai paveikia protonų difuziją ir joninio laidumo vertes. Tačiau įvairių nusodinimo parametru ir priemaišinių medžiagų įtaka fazių susidarymui, mikrostruktūrai, cheminiam stabilumui ir mechaniniam plonų plėvelių, sudarytų iš skirtingos sudėties bario ceratų bei bario cirkonatų, stabilumui anksčiau nebuvo tirta. Ši mokslinių tyrimų spraga ypač aktuali  $25\text{--}700 \text{ }^\circ\text{C}$  padėklo temperatūrų diapazone, kuris sąlygoja plėvelės formavimosi procesą. Be to, bario ceratų ir bario cirkonatų joninio laidumo įvertinimas paprastai atliekamas esant didesnei nei  $600 \text{ }^\circ\text{C}$  temperatūrai. Todėl informacijos apie šių plėvelių elgseną mažesnės nei  $600 \text{ }^\circ\text{C}$  temperatūros aplinkoje taip pat labai trūksta. Apibendrinant galima teigti, kad išsamių tyrimų, kuriuose būtų nagrinėjamas bario ceratų ir bario cirkonatų plonų plėvelių formavimas, jų savybės ir elgsena konkrečiuose temperatūrų diapazonuose, taip pat nusodinimo parametru ir padėklo medžiagos įtaka, trūkumas yra didelė šios srities mokslinių tyrimų problema.

### **Tyrimo tikslas**

Ištirti bario ceratų ir bario cirkonatų plonasluoksnių plėvelių, nusodintų elektroninio garinimo metodu, formavimą bei suformuotų plonų dangų savybes.

### **Tyrimo uždaviniai:**

1. Ištirti bario ceratų ir bario cirkonatų plonų plėvelių, suformuotų esant skirtingiems technologiniams parametrams, mikrostruktūrą.
2. Įvertinti suformuotų bario ceratų bei bario cirkonatų plonųjų plėvelių kristalinę fazę ir vyraujančią orientaciją, taip pat jų priklausomybę nuo technologinių parametru.

3. Iširti pasirinktų bario ceratų ir bario cirkonatų plonųjų plėvelių joninį laidumą mažesnės nei 500 °C temperatūros aplinkoje.

### **Mokslinis naujumas ir praktinė vertė**

Naujumas – gautos naujos žinios apie technologinių parametru (pagrindo temperatūros bei nusodinimo greičio) ir pagrindo tipo įtaką bario ceratų bei bario cirkonatų plonųjų sluoksnių, gautų elektronų spinduliu garinant  $\text{BaCeO}_3$  (BCO),  $\text{BaCe}_{0,9}\text{Y}_{0,1}\text{O}_{3-\delta}$  (BCY10),  $\text{BaCe}_{0,8}\text{Y}_{0,2}\text{O}_{3-\delta}$  (BCY20),  $\text{BaZrO}_3$  (BZO),  $\text{BaZr}_{0,8}\text{Y}_{0,2}\text{O}_{3-\delta}$  (BZY),  $\text{BaZr}_{0,8}\text{Ce}_{0,1}\text{Y}_{0,1}\text{O}_{3-\delta}$  (BZCY) miltelius, charakteristikoms, t. y.:

- a) technologinių parametru įtaką suformuotų bario ceratų ir bario cirkonatų plonųjų plėvelių cheminiam bei mechaniniam stabilumui;
- b) mikrostruktūros kitimą, kuri lemia skirtingi veiksniai, pavyzdžiui, nusodinimo greitis, padėklo temperatūra, bario ceratų bei bario cirkonatų plonos dangos ir naudoto padėklo šiluminio plėtimosi skirtumas, padėklo sudėtis, padėklo šiluminės savybės, legiravimo medžiagos ir jų koncentracija;
- c) kristalinės gardelės parametru, kristalų orientacijos ir grūdelių formos įtaką suformuotų bario ceratų ir bario cirkonatų plonųjų plėvelių joniniam laidumui.

### **Pagrindiniai disertacijos ginamieji teiginiai**

1. Nusodinimo greitis, šiluminio plėtimosi koeficientas (TEC) ir padėklų temperatūra turi įtakos bario ceratų ir bario cirkonatų plonųjų plėvelių, suformuotų taikant garinimą elektronų spinduliu, mikrostruktūrai ir paviršiaus morfologijai.
2. Joninį laidumą galima sąlygoti kontroliuojant liekamuosius įtempius bario ceratų plonose plėvelėse, suformuotose taikant garinimą elektronų spinduliu.
3. Nelegiruotose bario cerato ir bario cerato, legiruoto 10 % itriu, suformuotose plonose dangose, esant mažesnei nei 500 °C padėklo temperatūrai, protonų ir deguonies jonų laidumui didžiausią įtaką turi liekamosios deformacijos.
4. Kontroliuojant nusodinimo parametrus (pagrindo tipą, pagrindo temperatūrą, nusodinimo greitį), bario ceratų plonasluoksnės dangos gali būti formuojamos koloninės struktūros, priklausančios Thorntono zonų diagramos 2 ir  $T$  zonoms, taip pat bario cirkonato plonos dangos, pasižyminčios koloniniu augimu, kurios formuojasi pagal Stranskio–Krastanovo augimo pobūdį.

### **Autorės ir kitų asmenų indėlis**

Autorės indėlis: pagrindinė tyrimo dalis, kurią sudaro eksperimentinis darbas, suformuotų struktūrų tyrimas, matavimai bei skaičiavimai ir duomenų analizė.

Autorės ir kitų asmenų indėlis išsamiau:

- $\text{BaCeO}_3$  plonų dangų formavimas taikant garinimą elektronų pluoštu ant *Invar*, *Inconel 600*, stiklo lydinio (GSA) ir nerūdijančiojo plieno padėklų taikant skirtingą dangos augimo greitį: 2 Å/s, 4 Å/s, 8 Å/s bei 12 Å/s ir esant padėklų temperatūrai 150 °C, 300 °C, 450 °C bei 600 °C;
- $\text{BaCeO}_3$ ,  $\text{BaCe}_{0,9}\text{Y}_{0,1}\text{O}_{3-\delta}$ ,  $\text{BaCe}_{0,8}\text{Y}_{0,2}\text{O}_{3-\delta}$ ,  $\text{BaZrO}_3$ ,  $\text{BaZr}_{0,8}\text{Y}_{0,2}\text{O}_{3-\delta}$ ,  $\text{BaZr}_{0,8}\text{Ce}_{0,1}\text{Y}_{0,1}\text{O}_{3-\delta}$  plonų sluoksnių formavimas garinant elektronų pluoštu, kai dangos augimo greitis buvo 2 Å/s esant 500 °C *Inconel 600* padėklo temperatūrai;

- bendradarbiaujant su dr. Mantu Sriubu,  $\text{BaCeO}_3$ ,  $\text{BaCe}_{0,9}\text{Y}_{0,1}\text{O}_{3-\delta}$ ,  $\text{BaCe}_{0,8}\text{Y}_{0,2}\text{O}_{3-\delta}$ ,  $\text{BaZrO}_3$ ,  $\text{BaZr}_{0,8}\text{Y}_{0,2}\text{O}_{3-\delta}$ ,  $\text{BaZr}_{0,8}\text{Ce}_{0,1}\text{Y}_{0,1}\text{O}_{3-\delta}$  plonų sluoksnių formavimas garinant elektronų pluoštu, kai dangos augimo greitis buvo  $2 \text{ \AA/s}$  esant  $600 \text{ }^\circ\text{C}$  ir  $700 \text{ }^\circ\text{C}$  *Inconel 600*,  $\text{Al}_2\text{O}_3$ , *YZS* ir *MgO* padėklų temperatūrai;
- SEM ir EDS matavimai atlikti bendradarbiaujant su dr. Mantu Sriubu ir dr. Kristina Bočkute;
- XRD matavimai ir analizė atlikta bendradarbiaujant su prof. dr. Maria Gazda (Gdansko universitetas, Lenkija);
- impedansinės spektroskopijos matavimai ir duomenų analizė atlikta bendradarbiaujant su dr. Piotru Winiarzu ir dr. Kacperu Dzierzgowskiu (Gdansko universitetas, Lenkija);
- duomenų analizė, interpretavimas, straipsnių rašymas ir rezultatų pristatymas mokslinėse konferencijose atliktas bendradarbiaujant su dr. Mantu Sriubu, dr. Kristina Bočkute, prof. dr. Marija Gazda, dr. Piotr Winiarz, prof. dr. Giedriumi Laukaičiu.

Visiems šiame darbe atliktiems tyrimams ir pateikiant rezultatus vadovavo prof. dr. Giedrius Laukaitis. Mokslinio plano eksperimentai ir metodika buvo aptarti bendradarbiaujant su visais bendraautoriais.

## PUBLIKACIJŲ IR MOKSLINIŲ KONFERENCIJŲ SĄRAŠAS

### Moksliniai straipsniai, tiesiogiai susiję su daktaro disertacija (recenzuojami ir indeksuojami *Clarivate Analytics WoS*):

[A1]. Monica Susana Campos Covarrubias, Sriubas Mantas, Kristina Bockute, Piotr Winiarz, Tadeusz Miruszewski, Wojciech Skubida, Daniel Jaworski, Michał Bartmański, Marek Szkodo, Maria Gazda and Giedrius Laukaitis,. (2020). Properties of barium cerate thin films formed using e-beam deposition. *Crystals*, 10(12:1152), 1–13. <https://doi.org/10.3390/cryst101211522>. Q2. IF 2.67.

[A2]. Piotr Winiarz, Monica Susana Campos Covarrubias, Mantas Sriubas, Kristina Bockute, Tadeusz Miruszewski, Wojciech Skubida, Daniel Jaworski, Giedrius Laukaitis and Maria Gazda. Properties of barium cerate-zirconate thin films. *Crystals*, 11 (8:1005). <https://doi.org/10.3390/cryst11081005>. Q2. IF 2.67.

[A3]. Monica Susana Campos Covarrubias, Mantas Sriubas, Kristina Bockute, Aurelija Poskaite, Rokas Vazgys, Maria Gazda, and Giedrius Laukaitis. 2022. "Properties on Yttrium-Doped/Undoped Barium Cerate and Barium Zirconate Thin Films Formed by E-Beam Vapor Deposition" *Applied Sciences*, 12 (13: 6422). <https://doi.org/10.3390/app12136422>. Q2. IF. 2.838.

[A4]. Monica Susana Campos Covarrubias, Kristina Bockute, Mantas Sriubas, Kacper Dzierzowski, Maria Gazda & Giedrius Laukaitis . Microstructure and electrical properties of barium cerate thin films. *J Mater Sci* (2023). (Pag. 3909- 3919) <https://doi.org/10.1007/s10853-023-08297-7>. Q1. IF. 4.682.

## Konferencijos, tiesiogiai susijusios su daktaro disertacija

1. Monica Susana Campos Covarrubias, Mantas Sriubas, Kristina Bockute, Aurelija Poskaite, Rokas Vazgys, Giedrius Laukaitis. 18th International conference of young scientist on energy and natural sciences issues, CYSENI 2022, Gegužė 22-24d. Virtuali konferencija. Žodinis pristatymas. 438-441 p.
2. Monica Susana Campos Covarrubias, Mantas Sriubas; Kristina Bočkutė; Giedrius Laukaitis, 5th International conference in applied sciences, Balandis 24-28d., 2022, Palma de Mallorca, Ispanija. Investigation of grain growth induced strains in BaCeO<sub>3</sub> films formed by e-beam vapor deposition. P1.42.
3. Monica Susana Campos Covarrubias, Mantas Sriubas, Kristina Bočkutė, Piotr Winiarz, Maria Gazda ir Giedrius Laukaitis. Influence of dopants on the crystallinity and grain size in barium zirconate cerate thin films formed by e-beam vapor deposition. 14th international symposium on systems with fast ionic transport (ISSFIT14), Liepa 7–9d., 2021. 55 p. Virtuali konferencija.
4. Monica Susana Campos Covarrubias; Mantas Sriubas; Kristina Bockute; Piotr Winiarz; Maria Gazda; Giedrius Laukaitis. Influence of the formation parameters on the properties of yttrium-doped Barium zirconate thin films. E-MRS Spring meeting 2021, Gegužė 31d. - Birželis 4 d. Virtuali konferencija. Stendinis pranešimas.
5. Monica Susana Campos Covarrubias, Mantas Sriubas, Kristina Bockute, Piotr Winiarz, Maria Gazda ir Giedrius Laukaitis. Microstructure properties of formed doped barium cerate thin film formed on different alloy substrates. Functional materials and nanotechnologies: [13th international conference], FM&NT-2020: Vilnius, Lietuva, Lapkritis 23-26 d., 2020. Virtuali konferencija. Stendinis pranešimas.
6. Monica Susana Campos Covarrubias, Mantas Sriubas, Kristina Bockute, Zivile Rutkuniene, Piotr Winiarz, Maria Gazda ir Giedrius Laukaitis. Formation and investigation of barium cerate thin films = Plonasluoksnių bario cerato dangų formavimas ir tyrimas. 43-ioji Lietuvos nacionalinė fizikos konferencija, 2019 m. Spalio 3-5 d., Kaunas: pranešimų medžiaga. Stendinis pranešimas.
7. Piotr Winiarz, Daniel Jaworski, Mirosław Sawczak, Monica Susana Campos Covarrubias, Mantas Sriubas, Kristina Bockute, Zivile Rutkuniene, Giedrius Laukaitis ir Maria Gazda. Electrical properties and protonic conductivity in yttrium-doped barium cerate-zirconate strained thin films. 14th international symposium on systems with fast ionic transport (ISSFIT14), Liepa 7–9d. 2021. Virtuali konferencija. Stendinis pranešimas. 59 p.
8. Piotr Winiarz, Daniel Jaworski, Mirosław Sawczak, Monica Susana Campos Covarrubias, Mantas Sriubas, Kristina Bockute, Zivile Rutkuniene, Giedrius Laukaitis ir Maria Gazda. Selected properties of thermally strained barium cerate – zirconate thin films. SSPC-20: Solid-state proton conductors. Rugsėjis 27d.- Spalio 1d. 2021. Virtuali konferencija. Stendinis pranešimas.

## DISERTACIJOS STRUKTŪRA

Disertaciją sudaro 4 skyriai. Pirmajame skyriuje pristatomas tyrimų aktualumas, atliktų tyrimų tikslas, uždaviniai, tyrimų naujumas, ginamieji teiginiai ir pagrindinės publikacijos. Antrajame (literatūros apžvalgos) skyriuje aptariamos bario ceratų ir bario cirkonatų pagrindinės savybės, mikrostruktūra, formavimo metodai ir įvairių procesų įtaka joniniam laidžiui bei formuojamų plonų dangų mikrostruktūrai. Trečiajame skyriuje aprašomi taikyti tyrimo metodai ir tyrimų metodika. Ketvirtajame skyriuje pateikiami gauti rezultatai, t. y. pirmajame poskyryje pristatomi atlikti tyrimai su suformuotomis nelegiruoto bario cerato plonomis dangomis, antrajame poskyryje pateikiami atlikti tyrimai su suformuotomis legiruoto itriu bario cerato plonomis dangomis, o trečiajame poskyryje pateikiami ir aptariami gauti rezultatai su legiruotomis itriu bei ceriu bario cirkonato plonomis dangomis. Išvados pateikiamos penktajame skyriuje. Disertacijos pabaigoje yra disertacijos santrauka lietuvių kalba (6 skyrius), naudotos literatūros sąrašas (7 skyrius), gyvenimo aprašymas (8 skyrius) ir padėka (9 skyrius).

## EKSPERIMENTINĖ ĮRANGA

Eksperimentinėje dalyje pristatoma bandinių paruošimo metodika, naudoti pagrindai, plonų dangų formavimo įrenginys (elektroninio fizikinio nusodinimo iš garų Sistema – *Kurt J. Lesker 61 EB-PVD 75*, Hastingsas, Jungtinė Karalystė) ir aptariami tyrimams taikyti analizės metodai, t. y. kristalinės struktūros tyrimuose naudotas rentgeno spindulių difraktometras (XRD) *D8 Discover Bruker Cu Ka*  $\lambda = 0,154059$  nm,  $2\theta$  kampas buvo keičiamas nuo  $20^\circ$  iki  $70^\circ$  su  $0,01^\circ$  žingsniu); paviršiaus topografija ir skerspjūvio vaizdai gauti skenuojančiuoju elektroniniu mikroskopu (SEM) *Hitachi S-3400N (Hitachi High-Technologies, Tokijas, Japonija)*; elementinė sudėtis buvo analizuojama taikant energijos dispersinės rentgeno spindulių analizės metodą (EDS) *BrukerXFlash QUAD 5040 (Bruker AXS GmbH, Billerica, Masačusetso valstija, JAV)*; plėvelių elektrinės savybės buvo tiriamos elektrocheminės impedanso spektroskopijos (EIS) metodu naudojant *Gamry Reference 600+* potenciostatą  $1 \text{ Hz}^{-1} \text{ MHz}$  dažnių diapazone drėkintose ir (arba) sausose azoto dujose, kuriose drėkinimo pakopą sudarė nuosekliai sujungti burbuliatorius su dejonizuotu  $\text{H}_2\text{O}$  ( $p_{\text{H}_2\text{O}} = 0,02 \text{ atm}$ ) ir burbuliatorius su dejonizuotu  $\text{H}_2\text{O}$  ir KBr ( $p_{\text{H}_2\text{O}} = 0,02 \text{ atm}$ ).

## REZULTATAI IR JŲ APTARIMAS

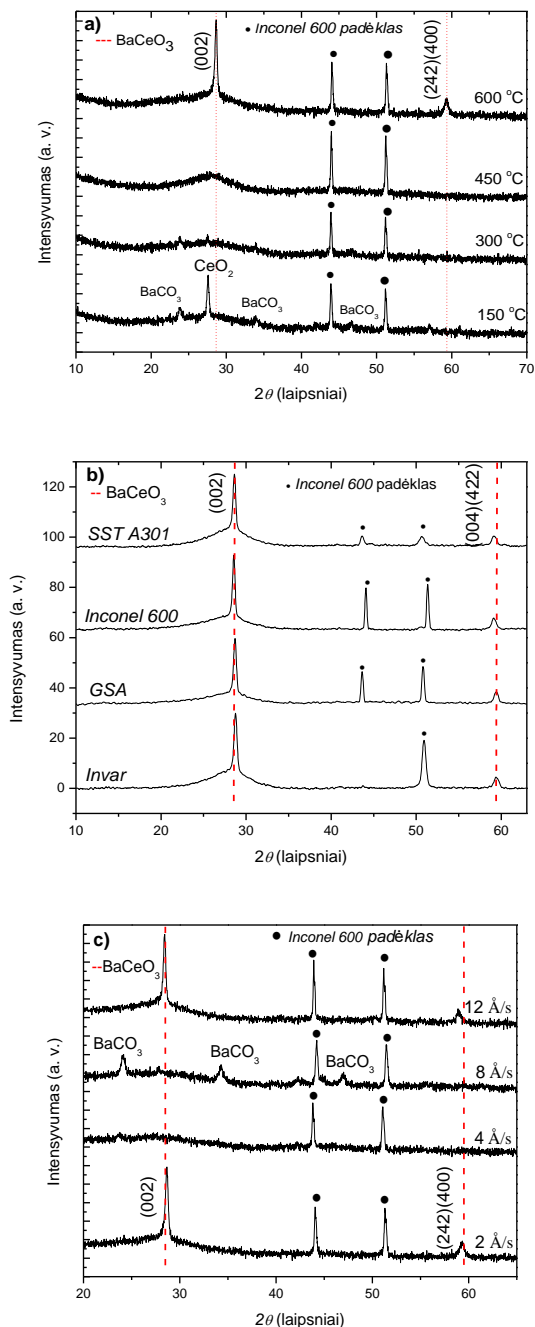
### *Bario cerato plonų dangų formavimas ir tyrimas*

Siekiant optimizuoti suformuotų plonų dangų savybes, bario ceratų (BCO) plonos dangos buvo formuojamos esant keturioms skirtingoms padėklų temperatūroms ( $150^\circ\text{C}$ ,  $300^\circ\text{C}$ ,  $450^\circ\text{C}$  ir  $600^\circ\text{C}$ ) bei esant keturiems skirtingiems dangų užnešimo greičiams ( $2 \text{ \AA/s}$ ,  $4 \text{ \AA/s}$ ,  $8 \text{ \AA/s}$  ir  $12 \text{ \AA/s}$ ) kiekvienos temperatūros sąlygomis. Siekiant įvertinti mikrostruktūrą, suformuotos dangos buvo tiriamos

taikant XRD ir SEM metodus. Paskui buvo įvertintos elektrinės ir mechaninės savybės.

Norint iširti plonos plėvelės sudėtį, buvo analizuojami EDS spektrai. Suformuotų plonų dangų elementinė sudėtis nekito per visą dangos storį ir paviršių. Buvo nustatyta, kad elementinė sudėtis keičiant užnešimo greitį ir esant skirtingai padėklo temperatūrai kinta, t. y. stebimas bario (Ba) perteklius lyginant su pirminių garinamų miltelių sudėtimi (1 lentelė).

XRD matavimai parodė, kad plonų dangų, suformuotų esant 150 °C padėklo temperatūrai, atveju buvo stebimas  $\text{CeO}_2$  ir  $\text{BaCO}_3$  darinių mišinys (1 pav.). Didėjant padėklo temperatūrai, formuojamų dangų kristališkumas didėja,  $\text{CeO}_2$  ir  $\text{BaCO}_3$  darinius atitinkančios smailės sumažėja ir išryškėja  $\text{BaCeO}_3$  junginį atitinkančios smailės. Suformuotų  $\text{BaCeO}_3$  plonų dangų, esant 600 °C padėklo temperatūrai, kristalinė fazė buvo ortorombinė *Pbnm*. Plonų dangų kristalografinės orientacijos buvo (002) ir (242), esant 2 Å/s ir 12 Å/s dangos augimo greičiui (1 pav.). O štai pusiau kristalinės fazės buvo stebimos esant didesniems dangos augimo greičiams, t. y. 8 Å/s ir 12 Å/s. XRD matavimai parodo, kad, esant 2 Å/s bei 12 Å/s nusodinimo greičiui ir 600 °C padėklo temperatūrai, formuojamos  $\text{BaCeO}_3$  dangos pasižymi didžiausiu kristališkumu. Tai galėtų lemti skirtingi dalelių difuzijos procesai ant padėklo dangos formavimo metu [197].



**1 pav.** Suformuotų BaCeO<sub>3</sub> plonų dangų XRD matavimų duomenys, kai: a) padėklo temperatūra dangos formavimo metu buvo 150 °C, 300 °C, 450 °C ir 600 °C; b) dangos buvo suformuotos ant skirtingų padėklų esant 600 °C padėklo temperatūrai; c) dangos buvo

suformuotos ant *Inconel 600* padėklo esant 600 °C temperatūrai, kai dangos augimo greitis buvo 2 Å/s, 4 Å/s, 8 Å/s ir 12 Å/s

Padėklo ir suformuotos plonos dangos temperatūrinio plėtimosi koeficiento skirtumas (2 lentelė) sąlygoja atsirandančius papildomus įtempimus, kurie taip pat sąlygoja vienetinių kristalinių gardelių parametrų pokyčius, t. y. tai gali nulėmti gardelės gniuždymą ar plėtimąsi, kuris ir stebimas gautuose rezultatuose.

**1 lentelė.** Suformuotų ant skirtingos temperatūros (150 °C ir 600 °C) pagrindų plonų BCO dangų elementinė sudėtis

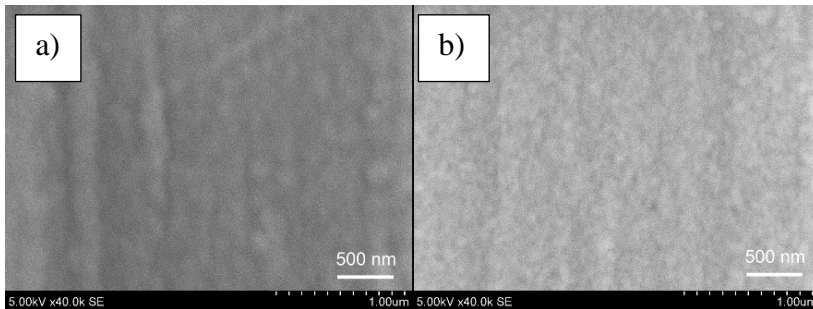
	Užnešimo greitis (Å/s)			
	Padėklo temperatūra 150 °C			
	2	4	8	12
<b>Ba</b>	9,37	10,44	10,83	8,87
<b>Ce</b>	4,43	4,65	4,73	6,01
<b>O</b>	86,2	84,91	84,44	85,12
<b>Ce/Ba</b>	0,47	0,44	0,43	0,67
	Padėklo temperatūra 600 °C			
<b>Ba</b>	15,23	15,42	11,96	14,04
<b>Ce</b>	6,74	7,33	6,08	6,97
<b>O</b>	78,03	77,25	81,96	78,99
<b>Ce/Ba</b>	0,44	0,47	0,50	0,49

**2 lentelė.** Ant skirtingų padėklų suformuotų BaCeO<sub>3</sub> plonų dangų (storis 1 μm, padėklo temperatūra 600 °C, dangos augimo greitis 12 Å/s) kristalinės gardelės parametrų vertės [A1]

Padėklas	Padėklo sudėtis (%)	TEC (×10 <sup>-6</sup> K <sup>-1</sup> )	<i>a</i> (Å)	<i>b</i> (Å)	<i>c</i> (Å)	Tūris, (Å <sup>3</sup> )	Kristalitų dydis (002), (nm)	Santykinis tankis (%)
<i>Invar</i>	Fe 64 % Ni 36 %	1,7	6,2096	8,7640	6,2400	339,59	22	99
<b>GSA</b>	Fe 54 % Ni 29 % Co 17 %	4,8	6,3937	8,7425	6,4578	360,00	25	99
<i>Inconel 600</i>	Fe 8 % Ni 72 % Cr 16 %	11,5	5,5955	8,4463	7,6653	362,27	26	99
<b>SST A301</b>	Fe 76 % Ni 7 % Cr 17 %	17,3	6,1770	8,9109	6,4409	354,17	72	99

Suformuotų BCO plonų dangų ant *Invar*, **GSA** ir *Inconel 600* padėklų (padėklo temperatūra 150 °C, dangos augimo greitis 2 Å/s, 4 Å/s, 8 Å/s ir 12 Å/s) SEM matavimai parodė, kad dangų augimas, remiami Thorntono zonų

diagrama [139], atitinka 1 zoną. Plonos dangos, suformuotos esant 600 °C padėklo temperatūrai ir 2 Å/s bei 12 Å/s dangos augimo greičiui (2 pav.), pasižymėjo mažesniu defektų skaičiumi. BCO dangos, suformuotos esant didesnei nei 300 °C padėklo temperatūrai, turėtų atitikti  $T$  zonos augimo pobūdį.  $T_s/T_m$  santykis leidžia nustatyti ir įvertinti formuojamų dangų mikrostruktūrą Thorntono zonų diagramoje.  $T_m$  – BaCeO<sub>3</sub> lydymosi temperatūra, kuri yra 1743 °C,  $T_s$  – padėklo temperatūra dangos formavimo metu.  $T_s/T_m$  santykis pasikeitė į 0,08; 0,17; 0,26; 0,34, kai padėklo temperatūra buvo atitinkamai 150 °C, 300 °C, 450 °C ir 600 °C. 1 zona atitinka, kai  $T_s/T_m < 0,2$ , o zona  $T$  yra, kai  $T_s/T_m < 0,3$ . 1 zonai būdingos plunksninė ir pluoštinė mikrostruktūros, dėl kurių paviršius yra labai šiurkštus.  $T$  zonos paviršius yra lygus ir labai tankus. Gautų rezultatų atveju,  $T_s/T_m$  santykis neatitiko prognozuojamos mikrostruktūros zonos dangose, suformuotose ant 600 °C temperatūros padėklo. SEM matavimai parodė, kad suformuotos BCO dangos pasižymi dideliu paviršiaus šiurkščiu, tai galėtų būti sąlygota vyraujančių tempimo įtempių formuojamose plonose dangose. Panašus atvejis buvo stebimas ZnO plonose dangose, suformuotose taikant magnetroninio dulkinimo metodą [200]. Gauti SEM vaizdai taip pat parodo, kad ant 150–300 °C temperatūros padėklų suformuotose dangose susidaro įtrūkimų. Tai gali būti sąlygojama atsirandančių deformacijų ir įtempių plonose dangose, kai formuojasi BaCO<sub>3</sub> esant reakcijai tarp laisvojo BaO ir CO<sub>2</sub> iš atmosferos. Suformuotose nestechiometrinėse BCO plonose dangose taip pat gali atsirasti BaO fazė. Norint išvengti BaO fazės formuojamose plonose dangose, padėklo temperatūra turi būti kuo didesnė, t. y. 600 °C ir daugiau.



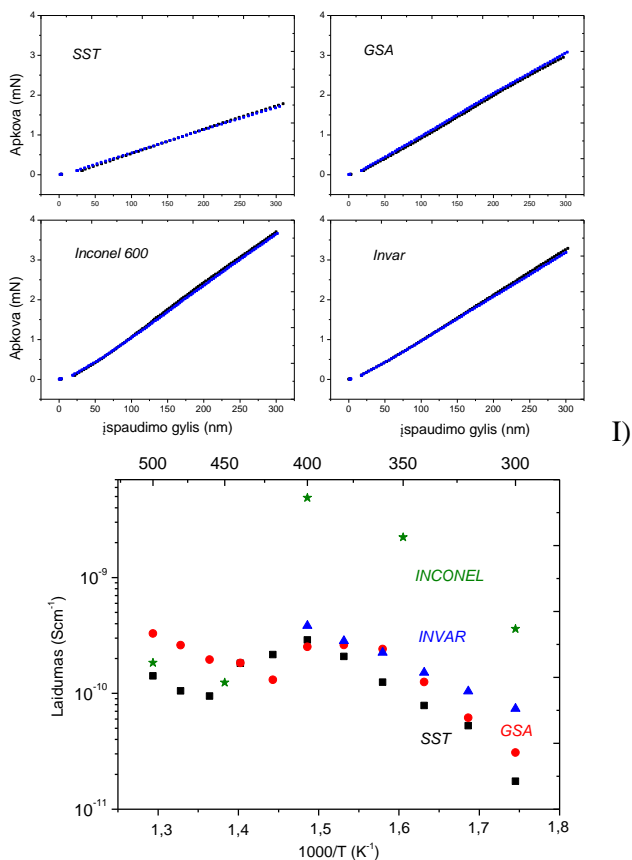
**2 pav.** BCO plonų dangų, suformuotų esant dangų augimo greičiui: a) 2 Å/s ir b) 12 Å/s, SEM vaizdai

BCO plonų dangų, užneštų esant 12 Å/s augimo greičiui ir 600 °C *Invar*, *GSA*, *Inconel 600* ir *SST* padėklų, grūdelių dydžiai buvo atitinkamai 87,87 nm, 85,30 nm, 120,53 nm ir 109,06 nm (3 lentelė). Pastebėtas 35 nm skirtumas tarp mažiausios ir didžiausios vertės. Didelės grūdelių dydžių vertės buvo gautos tada, kai TEC padėklo vertė buvo artimesnė BaCeO<sub>3</sub>, t. y. plonos dangos buvo suformuotos ant *Inconel 600*. Tai parodo, kad, be padėklo temperatūros, grūdelių dydį sąlygoja ir skirtingų padėklų TEC vertės.

**3 lentelė.** BaCeO<sub>3</sub> plonų sluoksnių, suformuotų (dangos augimo greitis 12 Å/s, padėklo temperatūra 600 °C) ant skirtingos rūšies padėklų, grūdelių dydžių vertės

<b>Padėklas</b>	<b>Grūdelių dydis (nm)</b>
<b><i>Invar</i></b>	87,86 ± 3,0
<b>GSA</b>	85,30 ± 3,4
<b><i>Inconel 600</i></b>	120,53 ± 5,3
<b>SST</b>	109,06 ± 4,2

Atlikti nanoįspaudimo matavimų rezultatai rodo kietumo skirtumus (3 pav.) dangose, suformuotose ant skirtingų padėklų. Iš keturių rūšių naudotų padėklų BCO danga, suformuota ant *Inconel 600*, turi didžiausią kietumą. Tai gali būti sąlygota likutinių įtempimų. Dangos, suformuotos ant *Inconel 600* padėklų, lyginant su kitais padėklais, pasižymėjo didžiausiu atsparumu apkrovai. Didelis įspaudimo gylio priklausomybės nuo naudotos apkrovos nuolydis yra susijęs su gniuždymo įtempiais, o mažas nuolydis priskiriamas tempimo įtempiams. Įspaudimo gylio priklausomybės nuo naudotos apkrovos yra tiesinės (3 pav., I). Padėklai, turintys mažesnius nei suformuotos BCO dangos šiluminio plėtimosi koeficientus, pasižymi didelėmis apkrovos vertėmis, lyginant pagal padėklus su didesniu šiluminio plėtimosi koeficientu. BCO dangų, suformuotų ant *Inconel 600* padėklų, pasižymi didžiausiu likutiniu įtempiu, kuris paaiškintų gautas dideles joninio laidumo vertes (3 pav., II) [A4]. Padėklo ir BCO plonos dangos panašios šiluminio plėtimosi koeficiento vertės negarantavo suformuotos plėvelės, kurioje nevyrautų įtempiai. Koloninė suformuotų BCO plonų dangų mikrostruktūra galėtų būti pagrindinė to priežastis. Likutinis įtempis gali būti sąlygotas tiek plonos dangos mikrostruktūros, tiek dangos storio. Dėl didelių liekamųjų įtempimų, sąlygojančių gniuždymą suformuotoje dangoje, buvo pasiektas didžiausias joninis laidumas (3 pav., II).



**3 pav.** I) Apkrovos ir poslinkio kreivės, gautos atliekant nanoįspaudimo matavimus Berkovičiaus indentoriumi, kai BCO plonos dangos (storis 1  $\mu\text{m}$ ) suformuotos ant: a) nerūdijančiojo plieno A301 (SST); b) stiklo sandarinimo lydinio (*Glass sealing alloy*, GSA); c) *Inconel 600* (*Inconel*) lydinio ir d) *Invar* lydinio [A1]; II)  $\text{BaCeO}_3$ , suformuoto ant *Inconel*, *Invar*, GSA ir SST, joninio laidumo priklausomybė nuo temperatūros drėgnoje aplinkoje (0,02 atm  $\text{H}_2\text{O}/\text{Ar}$ )

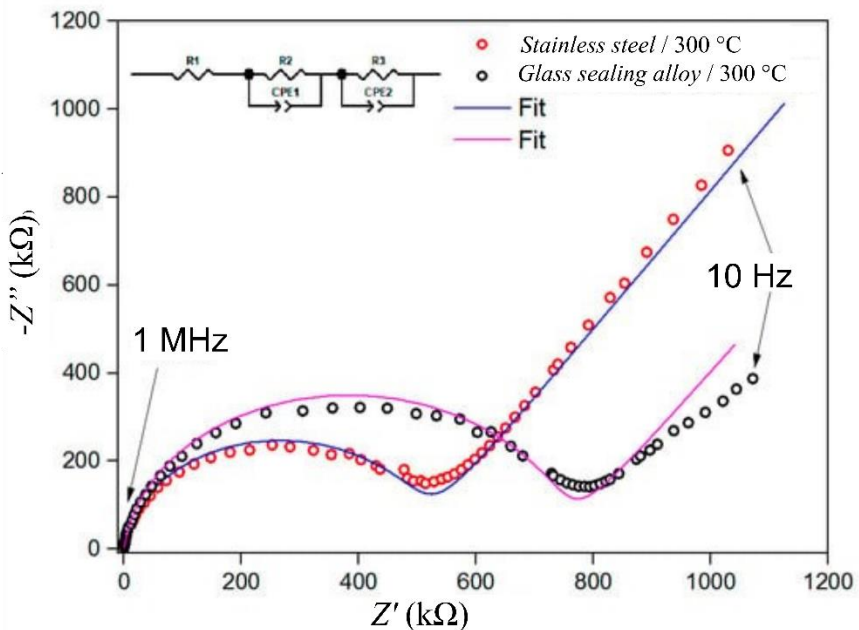
Skirtingų jonų aktyvacijos energija yra skirtinga. Deguonies jonų aktyvacijos energijos vertės yra didesnės nei 0,6 eV, o protonų laidumo – mažesnės nei 0,6 eV. Tačiau abiem atvejais deguonies ir protonų difuzijai įtakos turi gardelės parametrai. Palyginus BCO plonas dangas suformuotas ant *Invar* ir *Inconel 600* padėklų, ant *Invar* padėklų suformuotos BCO plonos dangos turėjo mažiausią aktyvacijos energiją 0,6 eV. O štai BCO plonos dangos, suformuotos ant *Inconel 600* padėklo, aktyvacijos energija buvo 0,9 eV (4 lentelė).

Pusapskritimių atitikimas Nykvisto diagramoje rodo (4 pav.), kad varža kinta pagal liekamojo įtempio dydį suformuotose plonose BCO dangose. Liekamieji įtempiai gali sąlygoti tarpkristalitinėse ribose esančias deguonies vakansijas ir defektus, turinčius įtakos jonų difuzijai ir joniniam laidumui [203]. Nustatyta, kad ant

GSA padėklų suformuotos BCO dangos, kuriose vyrauja didelis gniuždymo įtempis, turi didesnę varžą, palyginti su BCO dangomis, suformuotomis ant SST padėklų. Plonose dangose esantis liekamasis gniuždymo įtempis gali sąlygoti padėklo ir plonos dangos sąsajoje esančius defektus.

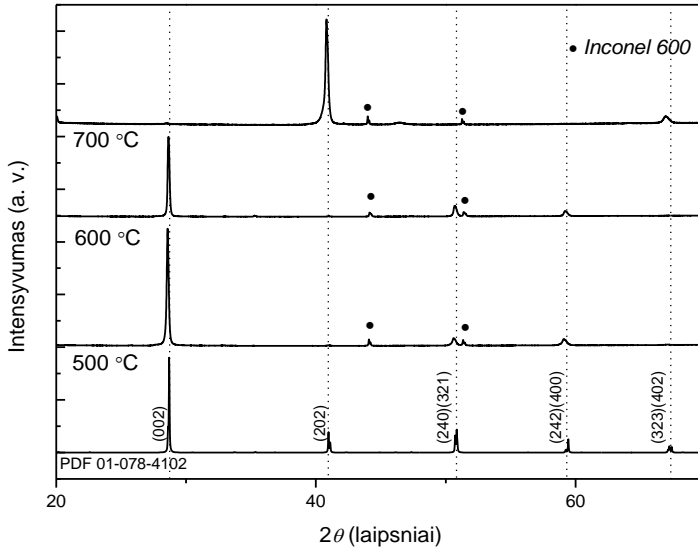
**4 lentelė.** Ant skirtingų padėklų suformuotų BaCeO<sub>3</sub> plonų dangų elektrinės ir mechaninės savybės [A1]

Padėklas	Padėklo elementinė sudėtis	Joninis laidis, $\sigma$ (350 °C), drėgnas Ar (S/cm) $\times 10^{-10}$	Aktyvacijos energija, $E_A$ (eV)	Relaksacijos temperatūra (°C)
<i>Invar</i>	Fe 64 % Ni 36 %	1,9	0,6	400
<b>Stiklo sandarinimo lydinys (GSA)</b>	Fe 54 % Ni 29 % Co 17 %	2,2	1,13	360
<i>Inconel lydinys (600)</i>	Fe 8 % Ni 72 % Cr 16 %	22	0,9	400
<b>Nerūdijantysis plienas (SST)</b>	Fe 76 % Ni 7 % Cr 17 %	1,0	0,95	400



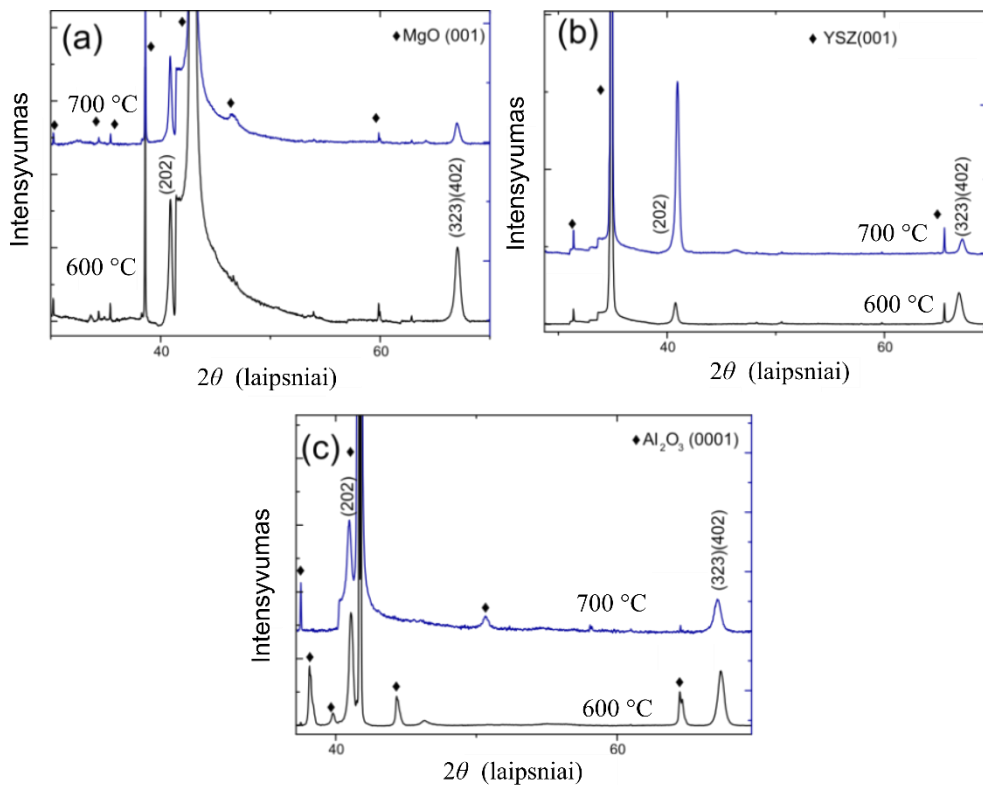
**4 pav.** BCO plonų dangų, suformuotų ant nerūdijančio plieno ir stiklo sandarinimo lydinio padėklų, Nykvisto grafikai ir teorinio skaičiavimo priartėjimo kreivės [A1].

Kristališkumas didėja keičiantis dangos užnešimo technologiniams parametrams ir padėklo fazei. BCO plonų dangų, suformuotų ant 500 °C, 600 °C ir 700 °C temperatūros *Inconel 600* padėklų fazė buvo ortorombinė *Pnma* (5 pav.), o kristalitų dydis, keičiant padėklo temperatūrą nuo 500 °C iki 600 °C, padidėjo nuo 110 nm iki 177 nm atitinkamai. Kristalitų dydis toliau didinant padėklo temperatūrą iki 700 °C sumažėjo iki 68 nm (5 lentelė).



**5 pav.** BCO plonų dangų, suformuotų ant 500 °C, 600 °C ir 700 °C temperatūros *Inconel 600* padėklų, XRD kreivės

Kiekvienos suformuotos BCO dangos atveju esant skirtingai padėklo temperatūrai buvo apskaičiuoti tekstūros koeficientai. Orientacija keičiasi pagal padėklo rūšį ir padėklo temperatūrą dangos formavimo metu. Plonos dangos, suformuotos ant *Inconel 600* padėklo, pasižymi (002) orientacija. Ant metalo oksido padėklų (MgO (001), YSZ (001),  $\text{Al}_2\text{O}_3$  (0001)) orientacija keičiasi į (402)(323) (6 pav.).



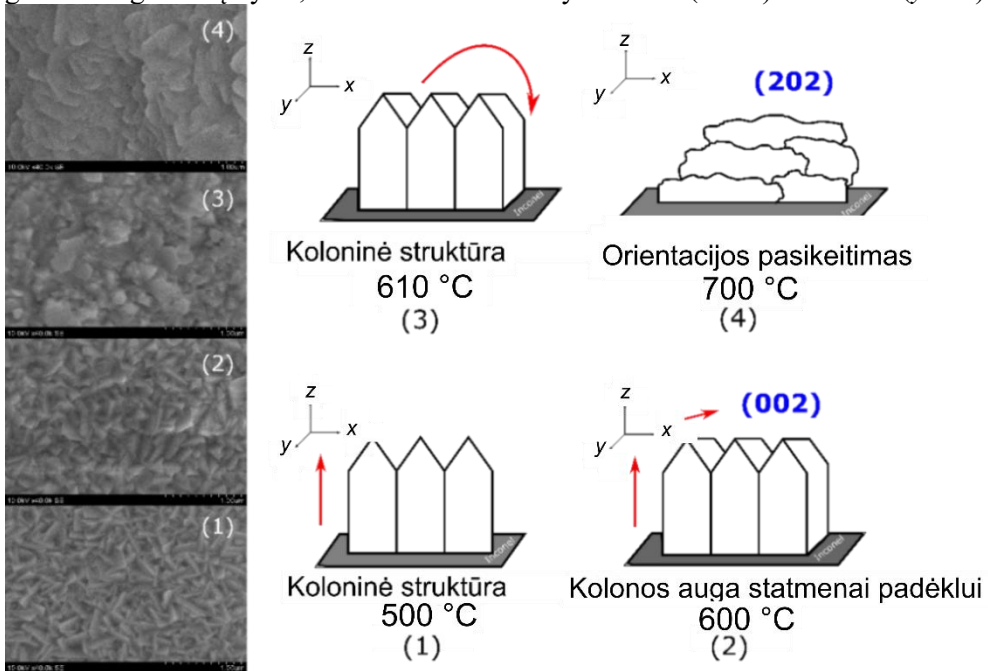
6 pav. BCO plonų dangų, suformuotų ant 600 °C ir 700 °C temperatūros MgO (001) (a), YSZ (001) (b) ir Al<sub>2</sub>O<sub>3</sub> (0001) (c) padėklų, XRD difraktogramos

5 lentelė. BaCeO<sub>3</sub> kristalinės savybės [A4]

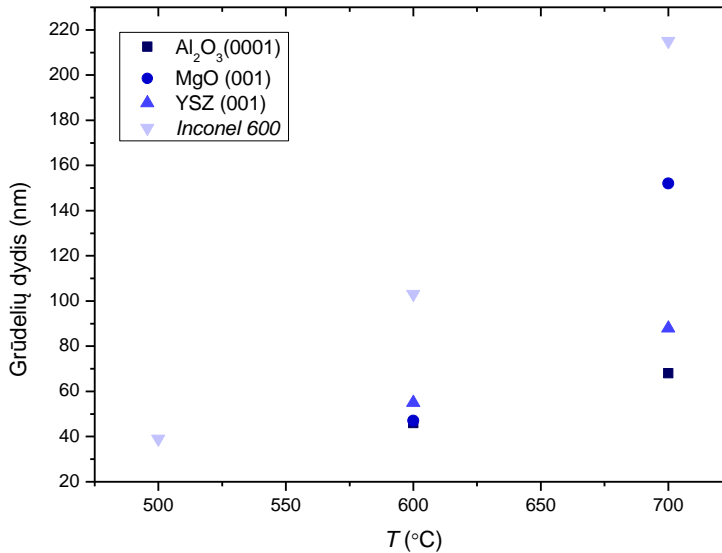
Padėklas	Temperatūra (°C)	Kristalinės gardelės parametrai			Kristalinių dydis (nm)	Vyraujanti orientacija	Kristalinės gardelės tūris (Å <sup>3</sup> )	R <sub>wp</sub> (%)
		a (Å)	b (Å)	c (Å)				
<b>Inconel 600</b>	500	6,2686	8,8188	6,2583	110	(002)	345,97	2,74
	600	6,2339	8,8313	6,2533	177	(002)	344,20	2,81
	610	6,2455	8,8146	6,2385	159	(002)	343,98	2,89
	700	6,2839	8,8223	6,3240	68	(202)	350,60	3,86
<b>Al<sub>2</sub>O<sub>3</sub></b>	500	N/A, daugiafazė struktūra						
	600	6,2910	8,8084	6,1227	34	(202)	339,28	5,73
	700	6,1734	8,9664	6,1415	14	(202)	339,95	9,27
<b>YSZ</b>	500	N/A, daugiafazė struktūra						

	600	6,1378	8,6372	6,4212	16	(202)	340,41	8,80
	700	6,1934	8,7451	6,2768	27	(202)	339,97	9,96
<b>MgO</b>	500	N/A, daugiafazē struktūra						
	600	6,1698	8,6516	6,3616	10	(202)	339,57	7,07
	700	6,1918	8,6584	6,3120	19	(202)	338,40	9,51

*Inconel 600* padēklo atveju, BCO plonų dangų grūdelių dydis ( $x$  ašis) priklauso nuo padēklo temperatūros (7 pav., 8 pav.). Mažiausios grūdelių dydžio vertės buvo gautos 39 nm ( $x$  ašis) ir 296 nm ( $y$  ašis). Didžiausios grūdelių dydžio  $x$  ašyje (437 nm) ir grūdelių dydžio  $y$  ašyje (215 nm) vertės gautos, kai padēklo temperatūra buvo 700 °C.  $Al_2O_3$  padēklo atveju, didelės temperatūros aplinkoje gaunamas grūdelių dydis, kurio minimali vertė yra 68 nm ( $x$  ašis) ir 294 nm ( $y$  ašis).

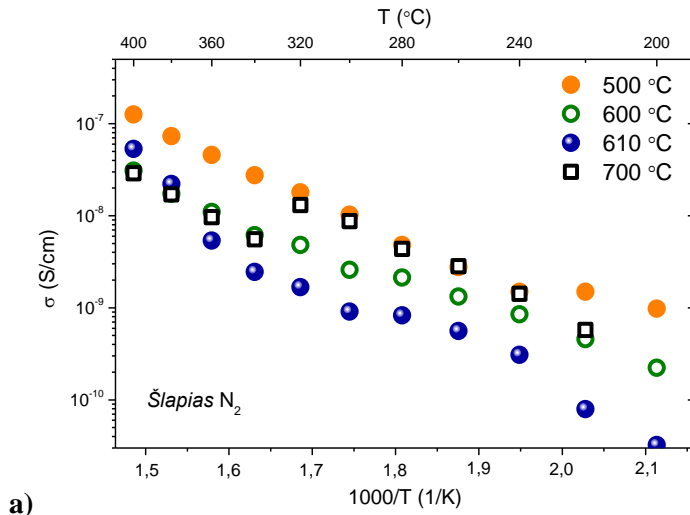


**7 pav.** Padēklo temperatūros įtaka BCO dangų grūdelių dydžiui  $x$  bei  $y$  kryptimis ir mikrostruktūrai esant: (1) 500 °C; (2) 600 °C; (3) 610 °C ir (4) 700 °C padēklo temperatūrai [A4]

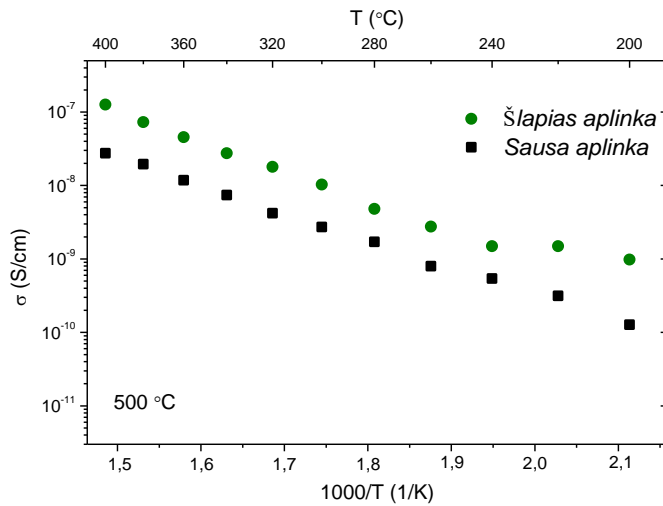


**8 pav.** BCO plonų dangų grūdelių dydžio (šoninis augimas  $x$  kryptimi) priklausomybė nuo padėklo *Inconel 600*, Al<sub>2</sub>O<sub>3</sub>, MgO ir YSZ temperatūros dangų formavimo metu

Joninio laidumo matavimai rodo, kad mikrostruktūros ir kristalitų orientacijos įtaka BaCeO<sub>3</sub> plonų dangų joniniam laidumui, palyginti su keramikomis, gautomis tradiciniais sukepimo metodais, yra didesnė [201] ( $10^{-9}$ – $10^{-10}$  Scm<sup>-1</sup>) (9 pav.). Joninio laidumo vertės taip pat buvo didesnės nei BaCeO<sub>3</sub>, anksčiau suformuoto elektroninio garinimo būdu, kurio grūdelių dydžio vertės buvo tris kartus mažesnės [196]. Joninis laidumas drėgnoje ir sausoje aplinkoje patvirtina deguonies joninį laidumą (sausoje) ir protonų joninį laidumą (drėgnoje) (9 pav.). Kaip ir tikėtasi, plonos dangos drėgnoje aplinkoje parodė didesnį joninį laidumą dėl protonų difuzijos. Sausoje aplinkoje stebimas deguonies jonų laidumas. BaCeO<sub>3</sub> plonos dangos pasižymi protonų laidumu ne tik didelės, bet ir mažesnės temperatūros aplinkoje. BaCeO<sub>3</sub>, suformuotas ant YSZ, pasižymi jonų laidumu be relaksacijos pakopų (10 pav.).

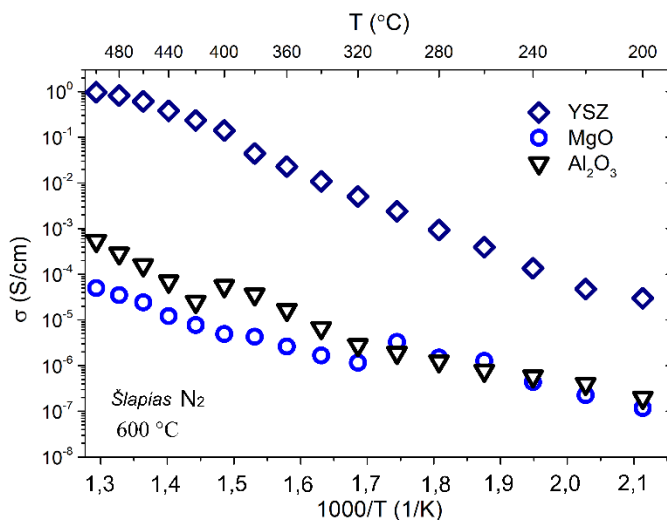


a)



b)

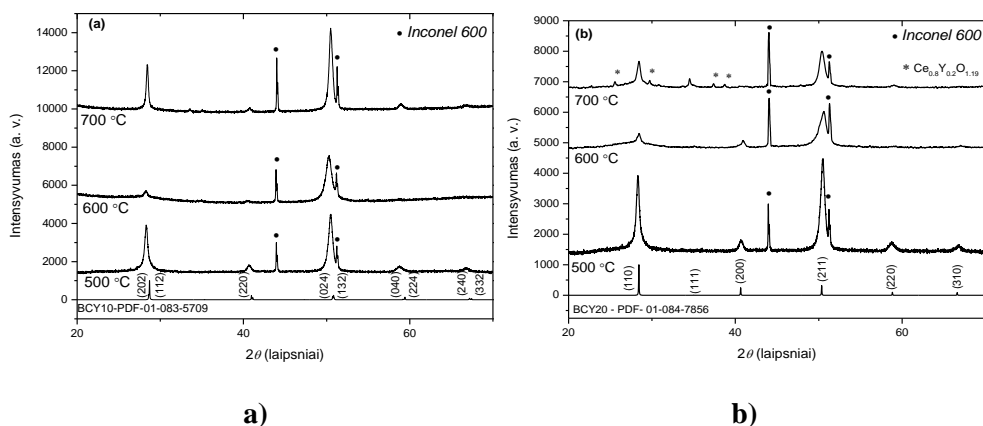
**9 pav.** BCO plonų dangų, suformuotų ant *Inconel 600* 500 °C, 600 °C ir 700 °C temperatūros padėklų: a) joninis laidumas esant 0,02 atm H<sub>2</sub>O/N<sub>2</sub> ir b) joninis laidumas drėgnoje bei sausoje aplinkoje



**10 pav.** BCO plonų dangų, suformuotų ant YSZ, MgO ir Al<sub>2</sub>O<sub>3</sub> padėklų, joninis laidumas (0,02 atm H<sub>2</sub>O/N<sub>2</sub>)

### *Itriu legiruito barrio cerato plonų dangų formavimas ir tyrimas*

Legiruito bario cerato plonos dangos buvo suformuotos taikant didesnę nei 500 °C padėklų temperatūrą. Pradiniuose milteliuose buvo dvi skirtingos itrio koncentracijos – 10 % (BCY10) ir 20 % (BCY20). Padėklo temperatūra buvo pasirinkta 500 °C, 600 °C ir 700 °C. Rentgeno spindulių difrakcijos (XRD) matavimai ir Rietveldo analizė rodo, kad suformuotos BCY10 plonos dangos yra vienfazės, kai padėklo temperatūra yra 500 °C, 600 °C ir 700 °C. BCY10 atveju pastebėta ortorombinė *Pbnm* fazė, o BCY20 atveju – kubinė *Pm3m* fazė (11 pav., 6 lentelė). Kristalitų dydis didėja didėjant temperatūrai (6 lentelė). Be to, didžiausias BCY10 kristalitų dydis buvo 33,7 nm, o BCY20 – 14,8 nm esant 700 °C padėklo temperatūrai. Tai rodo, kad kristalizacijos aktyvacijos energija sumažėjo mažėjant itrio kiekiui. BCY10 kristalų augimas buvo didesnis. Galėtų būti, kad didesnė itrio koncentracija stabilizuoja mikrostruktūrą, todėl BCY20 plonų dangų kristalitų dydis, esant trims skirtingoms padėklų 500 °C, 600 °C ir 700 °C temperatūroms, buvo panašių verčių.



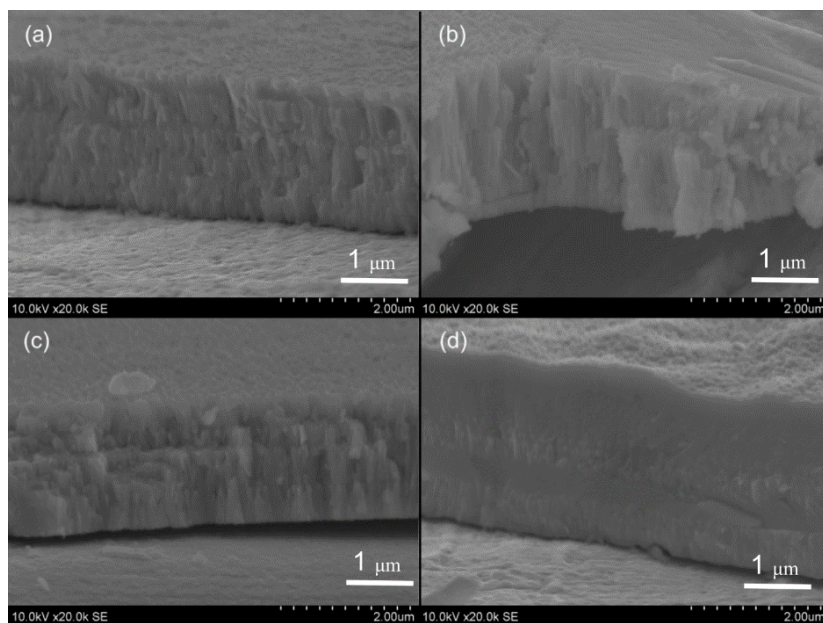
**11 pav.** Suformuotų BCY10 (a) ir BCY20 (b) plonų dangų XRD kreivės, kai *Inconel 600* padėklo temperatūra buvo 500 °C, 600 °C ir 700 °C [A2]

**6 lentelė.** BCY10 ( $\text{BaCe}_{0,9}\text{Y}_{0,1}\text{O}_{3-\delta}$ , *Pbnm* fazė) ir BCY20 ( $\text{BaCe}_{0,8}\text{Y}_{0,2}\text{O}_{3-\delta}$ , *Pm3m* fazė), plonų dangų, suformuotų ant 500 °C, 600 °C ir 700 °C temperatūros *Inconel 600* padėklų, kristalinės gardelės parametria [A3]

Padėklo temperatūra (°C)	Kristalinė fazė	Kristalinės gardelės parametrai			Vienetinės gardelės tūris (Å <sup>3</sup> )	Rwp (%)	GOF	Kristalitių dydis (nm)
		a (Å)	b (Å)	c (Å)				
<b>BCY10</b>								
<b>Baziniai milteliai</b>	<i>Pbnm</i>	6,3033	6,2473	8,6764	341,66	3,80	1,27	24,2
<b>500</b>	<i>Pbnm</i>	6,7349	6,2173	8,8036	368,63	3,63	1,16	18,6
<b>600</b>	<i>Pbnm</i>	5,7928	6,2915	9,5774	349,06	3,35	1,07	13,2
<b>700</b>	<i>Pbnm</i>	6,2194	6,2523	8,9257	347,08	3,39	1,11	33,7
<b>BCY20</b>								
<b>Baziniai milteliai</b>	<i>Pm3m</i>	4,4393			87,48	3,67	1,31	10,3
<b>500</b>	<i>Pm3m</i>	4,4410			87,59	3,46	1,10	10,5
<b>600</b>	<i>Pm3m</i>	4,4249			86,70	3,32	1,13	10,1

<b>700</b>	<i>Pm3m</i>	4,4291			86,88	4,04	1,25	14,8
------------	-------------	--------	--	--	-------	------	------	------

Suformuotų BCY10 plonų dangų, esant padėklo temperatūrai 500 °C, skerspjūvio SEM vaizdai rodo, kad dangų mikrostruktūra atitinka 1 zoną Thorntono diagramoje. Kai padėklo temperatūra 600 °C, grūdelių dydis didėja statmenai padėklui ir pereina į 2 zoną (12 pav.).



**12 pav.** BCY10 plonų dangų, suformuotų ant 500 °C (a) ir 600 °C (b) temperatūros padėklo bei BCY20 plonų dangų, suformuotų ant 500 °C (c) ir 600 °C (d) temperatūros padėklo, SEM skerspjūvio vaizdai

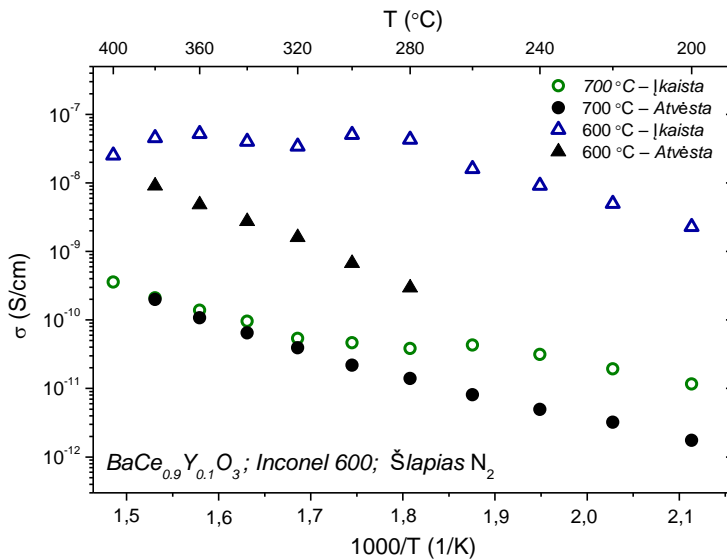
Grūdelių dydžio reikšmės suformuotose dangose kito pagal padėklo temperatūrą ir legiravimo medžiagos koncentraciją (7 lentelė).

**7 lentelė.** BCY10 ir BCY20 plonų dangų, suformuotų ant *Inconel 600* padėklų, esant 2 Å/s dangos augimo greičiui, grūdelių dydis

Padėklo temperatūra (°C)	Grūdelių dydis (nm)	
	BCY10	BCY20
<b>500</b>	307,6 ± 10,8	241,86 ± 6,2
<b>600</b>	178,73 ± 10,6	140,26 ± 7,1

<b>700</b>	$326,4 \pm 11,0$	$189,56 \pm 7,5$
------------	------------------	------------------

Suformuotų BCY10 plonų dangų joninio laidumo vertės buvo gautos mažesnės (0,001 S/cm esant 400 °C temperatūrai) nei literatūroje rastos klasikiniu sukepimo metodu gautų keramikų joninio laidumo vertės (13 pav.). Sumažinus plonų dangų storį, joninis laidumas galėtų padidėti daugiau kaip dviem eilėmis [232]. Kristalitams didėjant taip pat galima padidinti joninį laidumą. Maža to, BCY10 ir BCY20 plonų dangų struktūroje gali būti ir amorfinių fazių, kurios gali sumažinti joninį laidumą.



**13 pav.** BCY10 plonų dangų, suformuotų ant 600 °C ir 700 °C temperatūros padėklo, joninis laidumas [A4]

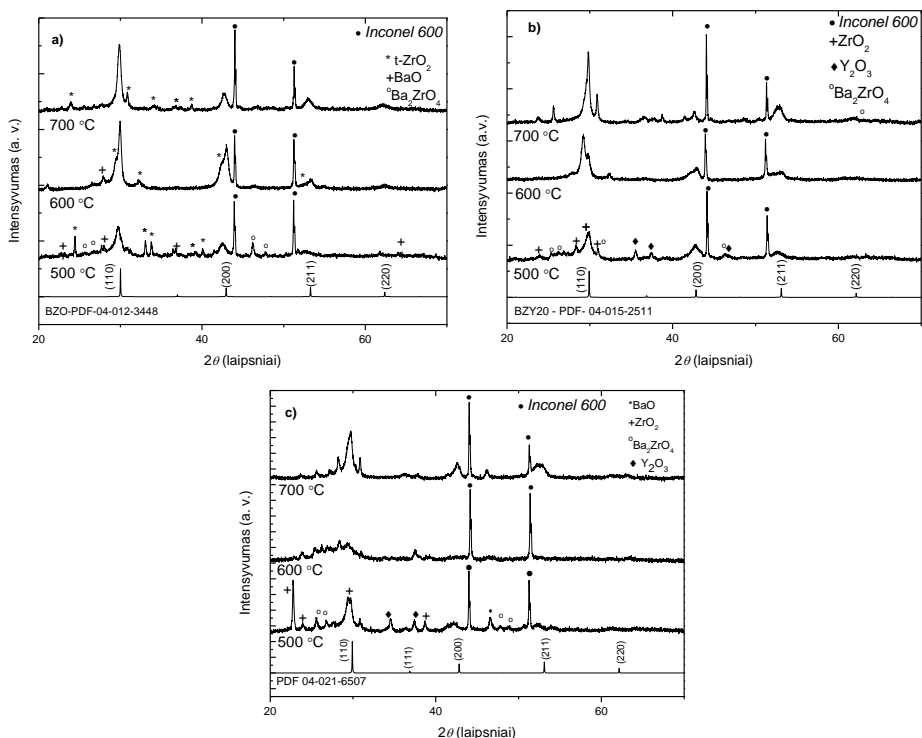
### ***Bario cirkonato plonų dangų formavimas ir tyrimas***

Bario cirkonato plonos dangos buvo suformuotos taikant didesnę nei 500 °C padėklų temperatūrą. Plonos dangos buvo formuojamos garinant trijų rūšių skirtingos sudėties miltelius (BZO, BZY20 ir BZCY) esant trims skirtingoms padėklų temperatūroms (500 °C, 600 °C ir 700 °C). Plonos dangos, suformuotos esant žemesnei nei 500 °C padėklo temperatūrai, buvo gautos nestabilios. EDS matavimai parodė, kad suformuotose BZO, BZY20 ir BZCY plonose dangose yra Ba perteklius. Šis perteklius sumažėja padidėjus padėklo temperatūrai esant 2 Å/s dangos augimo greičiui (8 lentelė).

**8 lentelė.** Bario cirkonato (BZO, BZY20 ir BZCY) plonų dangų, suformuotų ant 500 °C ir 600 °C temperatūros padėklo, elementinė sudėtis, gauta iš EDS matavimų

	Elementinė sudėtis (atominės masės %)					
	BZO		BZY20		BCZY	
	500	600	500	600	500	600
<b>Ba</b>	14,99	11,77	13,7	11,29	13,30	11,27
<b>Zr</b>	10,20	13,04	8,10	4,82	12,80	5,81
<b>Y</b>			1,10	1,64	1,00	1,36
<b>Ce</b>					2,80	2,01
<b>O</b>	74,81	75,19	77,10	82,25	70,10	79,55
<b>Ce/Ba</b>	0,72	1,10	0,67	0,57	1,24	0,81

BZO, BZY20 ir BZCY plonų dangų, suformuotų ant 500 °C temperatūros padėklo, XRD difraktogramos parodė, kad susidaro kietasis mišinys, kuriame yra pirminė garinamos medžiagos fazė ir tarpinė fazė ( $Ba_2ZrO_4$ ). Plonose dangose, suformuotose esant 600 °C padėklo temperatūrai, BZO ir BZY20 plonų dangų kristalinė fazė pereina į *Pm3m* fazę su tarpine  $ZrO_2$  faze. BZCY fazė pradeda formotis, kai padėklo temperatūra yra 700 °C (14 pav.). Gautus tyrimo rezultatus lyginant su itriu legiruoto bario cerato rezultatais, cirkonio kiekis sustiprina ryšį ir padidina kristališkumą. Esant įtempiams suformuotose heteroepitaksinėse BZY20 dangose, suformuotose naudojant PLD [233], kristalinės fazės paprastai susidaro padėklo temperatūrai esant aukštesnei nei 700 °C, kai dangų storis yra mažesnis nei 800 nm.



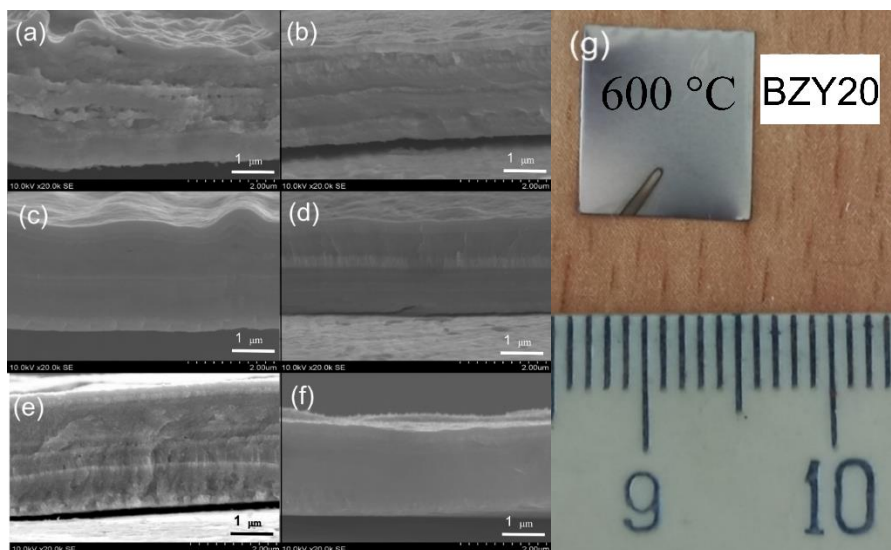
**14 pav.** a) BZO, b) BZY20 ir c) BZCY plonų dangų, suformuotų ant 500 °C, 600 °C ir 700 °C temperatūros *Inconel 600* padėklų, XRD kreivės

**9 lentelė.** Bario cirkonato (BZO, BZY20 ir BZCY) plonų dangų, suformuotų ant 500 °C ir 600 °C *Inconel 600* temperatūros padėklo esant 2 Å/s dangos augimo greičiui, tekstūros koeficientai. Jie apskaičiuoti lyginant su duomenų bazėse pateiktais etalonais, t. y. BZO-*Pm3m*, 04-012-3448, BZY20-*Pm3m*, 04-015-2511 ir BZCY-*Pm3m*, 04-021-6507. Vyraujanti tekstūra patamsinta.

Padėklo temperatūra (°C)	Tekstūros koeficientas			
	(110)	(200)	(211)	(220)
<b>BZO</b>				
<b>500</b>	0,88	<b>1,42</b>	0,61	1,07
<b>600</b>	0,95	<b>2,11</b>	0,45	0,48
<b>700</b>	<b>1,24</b>	1,10	0,74	0,90
<b>BZY20</b>				
<b>500</b>	0,83	<b>1,54</b>	0,79	0,82
<b>600</b>	0,87	<b>1,46</b>	0,86	0,78
<b>700</b>	<b>1,42</b>	0,79	1,07	0,70
<b>BZCY</b>				

<b>500</b>	1,10	<b>1,24</b>	0,78	0,87
<b>600</b>	0,78	1,12	0,83	<b>1,25</b>
<b>700</b>	1,10	<b>1,33</b>	1,04	0,51

Suformuotų dangų kristalinė orientacija kinta keičiant padėklo temperatūrą. BZO plonose dangose vyrauja (200), o didėjant padėklo temperatūrai pereina į (110) (9 lentelė). Nors BZY20 plonos dangos auga su (200) orientacija esant 500 °C padėklo temperatūrai, kristalai persiorientuoja į (110) esant 700 °C temperatūrai. BZCY tarpinių fazių mišinys buvo stebimas, kai padėklo temperatūra buvo 500 °C ir 600 °C. Esant 700 °C padėklo temperatūrai, kristalitų augimo pobūdis vyrauja (200). Panašiai kaip BaCeO<sub>3</sub> [A4], vyksta įtempių relaksacija ir modifikuojama mikrostruktūra. Vyraujanti kristalitų orientacija priklauso nuo formavimo sąlygų. Skerspjuvyje matomas sluoksnis po sluoksnio ir Stranskio–Krastanovo dangoms būdingas augimas (15 pav.). Suformuotų plonų dangų skerspjūvio nuotraukose matomos paviršiaus deformacijos, kurios esant 500 °C temperatūrai atrodo kaip gofruotas arba banguotas paviršius, o esant 600 °C temperatūrai, galimai dėl įtempių relaksacijos, tampa mažiau banguotas. Atrodo, kad BZO ir BZY20 augimo režimas keičiasi nuo sluoksnio po sluoksnio iki stulpelinio augimo dėl liekamųjų įtempių, sąlygotų padėklo ir formuojamos dangos medžiagos kristalinės gardelės parametru neatitikimo, relaksacijos [235]. Priešingai nei BZO ir BZY20 atveju, BZCY plonų dangų atveju koloninis augimo pobūdis (1 zona) keičiasi į augimo sluoksnis po sluoksnio pobūdį.

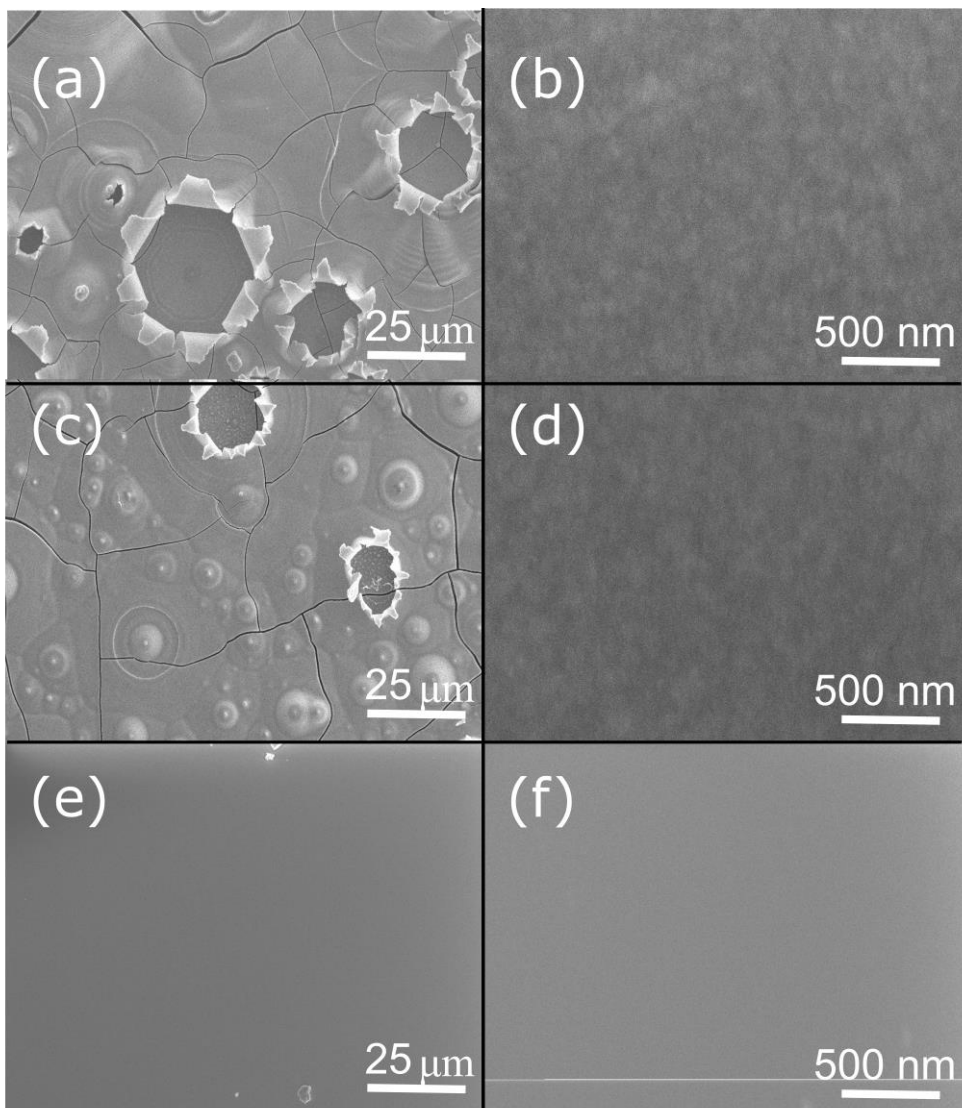


**15 pav.** BZO 500 °C [A3] (a) ir 600 °C (b), BZY20 500 °C [A3] (c) ir 600 °C (d), BZCY 500 °C [229] (e) ir 600 °C (f), suformuotų ant *Inconel 600* padėklo, skerspjūvio SEM nuotraukos (dangų augimo greitis 2 Å/s), (g) BZY20, suformuoto esant 600 °C padėklo temperatūrai, nuotrauka

**10 lentelė.** Bario cirkonato (BZO, BZY20 ir BZCY) plonų dangų, suformuotų ant 500 °C ir 600 °C temperatūros *Inconel 600* padėklo esant 2 Å/s dangos augimo greičiui, grūdelių dydis

Padėklo temperatūra (°C)	Grūdelių dydis, nm		
	BZO	BZY20	BZCY
<b>500</b>	120,3 ± 4,5	168,0 ± 8,9	78,3 ± 4,6
<b>600</b>	113,5 ± 5,2	134,9 ± 5,9	115,5 ± 8,1
<b>700</b>	134,6 ± 5,1	–	75,0 ± 5,0

BZY20 atveju augimo pobūdis, kintant padėklo temperatūrai, keičiasi iš Stranskio–Krastanovo į sluoksnis po sluoksnio (16 pav.). Be to, galime stebėti deformacijos pokyčius. Dėl įtempių sąlygotos deformacijos atsiranda įtrūkimų plonose dangose, kurių augimo pobūdis atitinka Stranskio–Krastanovo augimo režimą, o plonos dangos neįtrūksta, kai augimo pobūdis atitinka augimo sluoksnis po sluoksnio režimą.



**16 pav.** BZY20 plonų sluoksnių, suformuotų ant YSZ (001) 600 °C (a)–(d) ir 700 °C (e)–(h) temperatūros padėklo, SEM vaizdai esant dviem skirtingiems didinimams

### *Gautų rezultatų apibendrinimas ir išvados*

Plonų dangų formavimas, taikant garinimą elektronų spinduliu ir valdant technologinius parametrus, leidžia tirti įvairius mechanizmus, susijusius su formuojamų dangų mikrostruktūros pokyčiais. Mikrostruktūrą ir jos kitimą sukelia skirtingos jėgos, atsirandančios dėl dangos augimo greičio, padėklo temperatūros, šiluminio plėtimosi koeficiento neatitikimo tarp formuojamos dangos ir naudojamo padėko, padėklo sudėties, padėklo šiluminių savybių, priemaišų tipo ir jų

koncentracijos. Difuzijos procesas keičia kristalitų augimo kinetiką, jų augimo kryptį, formą, dydį, kristalizaciją, liekamuosius įtempius ir defektų susidarymą paviršiuje bei dangos sąsajoje su padėklu. Suformuotos bario cerato ir bario cirkonato plonos dangos turėjo sluoksnis po sluoksnio ir Stranski-Krastanov augimo pobūdį, taip pat atitiko įvairias Thorntono diagramos zonas [8]. Apibendrinant galima teigti, kad šio tyrimo rezultatai rodo, jog liekamieji įtempiai keičia kristalinės gardelės tūrį, daro įtaką deguonies jonų difuzijai ir protonų sulaikymo efektui. Be to, esant mažesnei nei 500 °C temperatūrai, nelegiruotas bario ceratas pasižymi mišriu protonų ir deguonies joniniu laidumu. Dėl mikrostruktūros pokyčio sumažėja aktyvacijos energija, kaip ir 700 °C temperatūros aplinkoje suformuoto BaCeO<sub>3</sub> atveju, nes mažiau kinta mikrostruktūra, mažiau difunduoja deguonies jonai ir mažiau sulaikomi protonai. Bario ceratų plonose dangose liekamojo įtempio pokytis pirmiausia buvo stebimas impedanso spektroskopijos metodu, sekant bendrojo laidumo pokytį. Nykvisto grafikas taip pat parodė mišrų protonų ir deguonies joninį laidumą nelegiruotose BaCeO<sub>3</sub> plonose plėvelėse esant skirtingiems dažniams. Joninio laidumo vertės ir aktyvacijos energija rodo papildomą YSZ, MgO ir Al<sub>2</sub>O<sub>3</sub> padėklų deguonies joninį laidumą, kuris padidina bendrąjį laidumą, išmatuotą plokštumoje. Galiausiai nustatyta, kad YSZ padėklas padidina deguonies joninį laidumą nelegiruotose BaCeO<sub>3</sub> plonose dangose, kai susidaro deguonies vakansijos ir pernešami deguonies jonai.

### **Išsamios išvados:**

1. Tyrimai parodė, kad amorfinės BaCeO<sub>3</sub> plonos dangos susidarė 400 °C temperatūroje, naudojant 2 Å/s ir 12 Å/s nusodinimo greitį ant invaro, nerūdijančiojo plieno, stiklo sandarinimo lydinio ir *Inconel 600* padėklų. Panašiai, esant nuo 100 °C iki 400 °C padėklo temperatūrai, plonos dangos išliko amorfinės, kai buvo taikomas 4 Å/s ir 8 Å/s nusodinimo greitis. Terminio plėtimosi koeficientas (TEC) ir padėklo temperatūra, sąlygojantys papildomus įtempius, turėjo įtakos kristalų dydžiui, kai padėklo temperatūra buvo 400 °C, o nusodinimo greitis 12 Å/s, kuris kito nuo 22 nm iki 72 nm. Nors BaCeO<sub>3</sub> plonų dangų kristalinės gardelės tūrio vertės dažniausiai viršijo etalonines, ant invaro padėklo suformuotos plonos dangos jas beveik atitiko. Suformuotų plonų dangų elementinė sudėtis priklauso nuo padėklo temperatūros, o nelegiruotose plonose dangose atitiko stochiometrinę sudėtį.
2. BaCeO<sub>3</sub> plonos dangos, suformuotos 2 Å/s nusodinimo greičiu ant *Inconel 600* padėklo, buvo ortorombinės su *Pbnm* faze ir 1,5–2 μm storio. Nanodarinių dydžio vertės buvo nuo 296 nm iki 437 nm, o išilginiai grūdelių dydžiai – nuo 39 nm iki 215 nm. Skerspjūviuose matomas koloninis augimas, atitinkantis Thorntono zonų diagramos 2 zoną, kurios tankis viršija 92 %, jam įtakos galėjo turėti didesnė adatomų difuzija dangos augimo metu. Grūdelių dydžio vertės svyravo nuo 283 nm iki 359 nm dangose, suformuotose ant MgO (001), Al<sub>2</sub>O<sub>3</sub> (0001) ir YSZ (001) padėklų, esant 600–700 °C temperatūrai. Padėklo orientacija sąlygoja suformuotų BCO plonų plėvelių grūdelių formą.

3. Ant *Inconel 600* padėklo suformuotos BCO plonos dangos pasižymi didžiausiu joniniu laidumu ( $10^{-9}$  S/cm) 400 °C temperatūros aplinkoje, galimai sąlygotu didesnio deguonies vakansijų skaičiaus. Buvo stebima dehidratacijos / relaksacijos pradžios temperatūra, o aktyvacijos energijos vertės svyravo nuo 0,6 eV iki 1,13 eV. Bet štai BCO plonos dangos, suformuotos ant 700 °C temperatūros padėklų, pasižymi  $10^{-7}$  S/cm (400 °C) joniniu laidumu, sąlygotu didesnio kristalitų dydžio ir kristalinės gardelės suspaudimo. Plonos dangos, suformuotos ant YSZ (001) padėklo, pasižymėjo didžiausia (0,13 S/cm esant 400 °C temperatūrai) joninio laidumo verte, būdinga nelegiruotam BCO.
4.  $\text{BaCe}_{0,9}\text{Y}_{0,10}\text{O}_3$  (BCY10) 1,5–2  $\mu\text{m}$  storio plonose dangose, suformuotose esant 2 Å/s augimo greičiui ant *Inconel 600* padėklo, vyravo ortorombinė *Pbnm* fazė. Grūdelių dydis keitėsi intervale nuo 178 nm iki 326 nm keičiant padėklo *Inconel 600* temperatūrą nuo 500 °C iki 700 °C. Plonų dangų skerspjuvio analizė parodė, kad danga yra koloninės struktūros, atitinkanti 1 Thorntono diagramos zoną, o tai parodo, kad itrio priemaišų buvimas sumažina adatomų difuziją bario ceratuose. Nanogrūdelių dydis kito nuo 175 nm iki 353 nm, kai danga buvo suformuota ant YSZ (001),  $\text{Al}_2\text{O}_3$  (001) ir MgO (001) 600–700 °C temperatūros padėklų. Kristalitų, orientuotų (024) kryptimi, dydis kito nuo 13,2 nm iki 33,7 nm, kai plonos dangos buvo suformuotos ant 500–700 °C temperatūros *Inconel 600* padėklų. BCY10 plonų dangų, suformuotų esant 2 Å/s augimo greičiui ant 600 °C temperatūros *Inconel 600* padėklų, joninis laidumas drėgnoje  $\text{N}_2$  aplinkoje buvo  $10^{-8}$  S/cm (esant 400 °C temperatūrai), o plonų dangų, suformuotų esant 700 °C padėklo temperatūrai, joninis laidumas drėgnoje  $\text{N}_2$  aplinkoje buvo  $10^{-9}$  S/cm (400 °C).
5.  $\text{BaCe}_{0,8}\text{Y}_{0,20}\text{O}_3$  (BCY20) 1,5–2  $\mu\text{m}$  storio plonose dangose, suformuotose esant 2 Å/s augimo greičiui ant *Inconel 600* padėklo, vyravo ortorombinė *Pm3m* fazė. Grūdelių dydis keitėsi intervale nuo 140 nm iki 241 nm keičiant padėklo *Inconel 600* temperatūrą nuo 500 °C iki 700 °C ir keitėsi intervale nuo 131 nm iki 272 nm keičiant padėklų YSZ (001),  $\text{Al}_2\text{O}_3$  (0001), MgO (001) temperatūrą nuo 500 °C iki 700 °C. Plonų dangų skerspjuvio analizė parodė, kad danga yra koloninės struktūros, atitinkanti 1 zoną Thorntono diagramoje, kai padėklų temperatūra 500 °C, ir pereina į zoną *T*, kai padėklo temperatūra pasiekia 600 °C. Kristalitų, orientuotų (211) kryptimi, dydis kito nuo 10,5 nm iki 14,8 nm, kai plonos dangos buvo suformuotos ant 500–700 °C temperatūros *Inconel 600* padėklų.
6.  $\text{BaZrO}_3$  (BZO) 1,5–2  $\mu\text{m}$  storio plonose dangose, suformuotose esant 2 Å/s augimo greičiui ant *Inconel 600* padėklo, vyravo ortorombinė *Pm3m* fazė. Grūdelių dydis keitėsi intervale nuo 113 nm iki 120 nm keičiant padėklo *Inconel 600* temperatūrą nuo 500 °C iki 700 °C ir keitėsi intervale nuo 1,13  $\mu\text{m}$  iki 1,80  $\mu\text{m}$  keičiant padėklų YSZ (001),  $\text{Al}_2\text{O}_3$  (0001), MgO (001) temperatūrą nuo 500 °C iki 700 °C. Didelės grūdelių dydžio reikšmės paviršiuje atitinka Stranskio–Krastanovo augimą su *T* zonos mikrostruktūra, kur liekamasis įtempis galėjo turėti tam įtakos. Kristalitų, orientuotų (200) kryptimi, dydis kito nuo

9,5 nm iki 16,0 nm, kai plonos dangos buvo suformuotos ant 500 °C ir 600 °C temperatūros *Inconel 600* padėklų, ir vyraujanti orientacija pasikeitė į (110), kai padėklo temperatūra buvo 700 °C. Stebėti ZrO<sub>2</sub>, BaO ir Ba<sub>2</sub>ZrO<sub>4</sub> mišrios fazės kristalitimai esant 500 °C padėklo temperatūrai. Plonų dangų skerspjūvio analizė parodė, kad danga yra koloninės struktūros, atitinkanti 1 zoną Thorntono diagramoje, kai padėklų temperatūra 500 °C, ir pereina į zoną T, kai padėklo temperatūra yra 600 °C.

7. BaZr<sub>0,8</sub>Y<sub>0,2</sub>O<sub>3</sub> (BZY20) 1,5–2 μm storio plonose dangose, suformuotose esant 2 Å/s augimo greičiui ant *Inconel 600* padėklo, vyravo ortorombinė *Pm3m* fazė. Grūdelių dydis keitėsi intervale nuo 134 nm iki 168 nm keičiant padėklo *Inconel 600* temperatūrą nuo 500 °C iki 700 °C ir keitėsi intervale nuo 0,77 μm iki 1,02 μm keičiant padėklų YSZ (001), Al<sub>2</sub>O<sub>3</sub> (0001), MgO (001) temperatūrą nuo 600 °C iki 700 °C. Kristalitimų, orientuotų (200) kryptimi, dydis kito nuo 6,4 nm iki 27,4 nm, kai plonos dangos buvo suformuotos ant 500 °C ir 600 °C temperatūros *Inconel 600* padėklų ir vyraujanti orientacija pasikeitė į (110), kai padėklo temperatūra buvo 700 °C. Stebėti ZrO<sub>2</sub>, BaO ir Ba<sub>2</sub>ZrO<sub>4</sub> mišrios fazės kristalitimai esant 500 °C padėklo temperatūrai. Plonų dangų skerspjūvio analizė parodė, kad dangos mikrostruktūra atitinka T zoną Thorntono diagramoje, kai padėklų temperatūra yra 500–700 °C.
8. BaZr<sub>0,8</sub>Ce<sub>0,1</sub>Y<sub>0,2</sub>O<sub>3</sub> (BCZY) 1,5–2 μm storio plonose dangose, suformuotose esant 2 Å/s augimo greičiui ant *Inconel 600* padėklo, vyravo ortorombinė *Pm3m* fazė. Grūdelių dydis keitėsi intervale nuo 75 nm iki 115 nm keičiant padėklo *Inconel 600* temperatūrą nuo 500 °C iki 700 °C ir keitėsi intervale nuo 0,13 μm iki 0,16 μm keičiant YSZ (001), Al<sub>2</sub>O<sub>3</sub> (0001), MgO (001) padėklų temperatūrą nuo 600 °C iki 700 °C. Kristalitimų, orientuotų (200) kryptimi, dydis kito nuo 2,4 nm iki 14,2 nm, kai plonos dangos buvo suformuotos ant 500 °C ir 700 °C temperatūros *Inconel 600* padėklų, ir vyraujanti orientacija pasikeitė į (220), kai padėklo temperatūra buvo 600 °C. Stebėtos ZrO<sub>2</sub>, BaO ir Ba<sub>2</sub>ZrO<sub>4</sub> mišrios kristalografinės fazės, kai padėklo temperatūra buvo žemesnė nei 700 °C. Plonų dangų skerspjūvio analizė parodė, kad dangos mikrostruktūra atitinka I ir T zonas Thorntono diagramoje, kai padėklų temperatūra yra 500–700 °C.

## 7. LITERATURE

- [1] W. Zhang and Y. H. Hu, 'Progress in proton-conducting oxides as electrolytes for low-temperature solid oxide fuel cells: From materials to devices', *Energy Sci. Eng.*, vol. 9, no. 7, pp. 984–1011, 2021, doi: 10.1002/ese3.886.
- [2] B. Suherman, F. Nurosyid, Khairuddin, D. K. Sandi, and Y. Irian, 'Impacts of low sintering temperature on microstructure, atomic bonds, and dielectric constant of barium titanate (BaTiO<sub>3</sub>) prepared by co-precipitation technique', *J. Phys. Conf. Ser.*, vol. 2190, no. 1, p. 012006, Mar. 2022, doi: 10.1088/1742-6596/2190/1/012006.
- [3] S. Lobe, A. Bauer, S. Uhlenbruck, and D. Fattakhova-Rohlfing, 'Physical Vapor Deposition in Solid-State Battery Development: From Materials to Devices', *Adv. Sci.*, vol. 8, no. 11, p. 2002044, 2021, doi: 10.1002/advs.202002044.
- [4] D. Jennings, S. Ricote, J. M. Caicedo, J. Santiso, and I. Reimanis, 'The effect of Ni and Fe on the decomposition of yttrium doped barium zirconate thin films', *Scr. Mater.*, vol. 201, p. 113948, Aug. 2021, doi: 10.1016/j.scriptamat.2021.113948.
- [5] A. Anders, 'A structure zone diagram including plasma-based deposition and ion etching', *Thin Solid Films*, vol. 518, no. 15, pp. 4087–4090, May 2010, doi: 10.1016/j.tsf.2009.10.145.
- [6] S. Shao, Z. Fan, J. Shao, and H. He, 'Evolutions of residual stress and microstructure in ZrO<sub>2</sub> thin films deposited at different temperatures and rates', *Thin Solid Films*, vol. 445, no. 1, pp. 59–62, Nov. 2003, doi: 10.1016/j.tsf.2003.08.051.
- [7] J. A. Thornton, 'Influence of apparatus geometry and deposition conditions on the structure and topography of thick sputtered coatings', *J. Vac. Sci. Technol.*, vol. 11, no. 4, pp. 666–670, Jul. 1974, doi: 10.1116/1.1312732.
- [8] J. A. Thornton, 'Structure-Zone Models Of Thin Films', presented at the 31st Annual Technical Symposium, M. R. Jacobson, Ed., San Diego, CA, United States, Feb. 1988, p. 95. doi: 10.1117/12.941846.
- [9] E. Kusano, 'Structure-Zone Modeling of Sputter-Deposited Thin Films: A Brief Review', *Appl. Sci. Converg. Technol.*, vol. 28, no. 6, pp. 179–185, Nov. 2019, doi: 10.5757/ASCT.2019.28.6.179.
- [10] L. Lei, J. Zhang, R. Guan, J. Liu, F. Chen, and Z. Tao, 'Energy storage and hydrogen production by proton conducting solid oxide electrolysis cells with a novel heterogeneous design', *Energy Convers. Manag.*, vol. 218, p. 113044, Aug. 2020, doi: 10.1016/j.enconman.2020.113044.
- [11] L. Mazzei *et al.*, 'Local structure and vibrational dynamics in indium-doped barium zirconate', *J. Mater. Chem. A*, Nov. 2018, doi: 10.1039/C8TA06202A.
- [12] R. Sažinas *et al.*, 'Surface reactivity and cation non-stoichiometry in BaZr<sub>1-x</sub>Y<sub>x</sub>O<sub>3-δ</sub> (x = 0–0.2) exposed to CO<sub>2</sub> at elevated temperature', *J. Mater. Chem. A*, Jan. 2019, doi: 10.1039/C8TA11021B.
- [13] S. H. Morejudo *et al.*, 'Direct conversion of methane to aromatics in a catalytic cationic membrane reactor', *Science*, vol. 353, no. 6299, pp. 563–566, Aug. 2016, doi: 10.1126/science.aag0274.
- [14] C. Duan *et al.*, 'Readily processed protonic ceramic fuel cells with high performance at low temperatures', *Science*, vol. 349, no. 6254, pp. 1321–1326, Sep. 2015, doi: 10.1126/science.aab3987.
- [15] J. A. Kilner and M. Burriel, 'Materials for Intermediate-Temperature Solid-Oxide Fuel Cells', *Annu. Rev. Mater. Res.*, vol. 44, no. 1, pp. 365–393, 2014, doi: 10.1146/annurev-matsci-070813-113426.

- [16] L. Malavasi, C. A. J. Fisher, and M. S. Islam, 'Oxide-ion and proton conducting electrolyte materials for clean energy applications: structural and mechanistic features', *Chem. Soc. Rev.*, vol. 39, no. 11, pp. 4370–4387, Oct. 2010, doi: 10.1039/B915141A.
- [17] S. Wang, J.-L. Luo, A. R. Sanger, and K. T. Chuang, 'Performance of Ethane/Oxygen Fuel Cells Using Yttrium-Doped Barium Cerate as Electrolyte at Intermediate Temperatures', *J. Phys. Chem. C*, vol. 111, no. 13, pp. 5069–5074, Apr. 2007, doi: 10.1021/jp066690w.
- [18] R. K. Ahluwalia and J. K. Peng, 'Automotive hydrogen storage system using cryo-adsorption on activated carbon', *Int. J. Hydrog. Energy*, vol. 34, no. 13, pp. 5476–5487, Jul. 2009, doi: 10.1016/j.ijhydene.2009.05.023.
- [19] W. A. Meulenbergh, M. E. Ivanova, J. M. Serra, and S. Roitsch, '17 - Proton-conducting ceramic membranes for solid oxide fuel cells and hydrogen (H<sub>2</sub>) processing', in *Advanced Membrane Science and Technology for Sustainable Energy and Environmental Applications*, A. Basile and S. P. Nunes, Eds., in Woodhead Publishing Series in Energy. Woodhead Publishing, 2011, pp. 541–567. doi: 10.1533/9780857093790.4.541.
- [20] Y. Yang, Y. Zeng, B. S. Amirkhiz, J.-L. Luo, and N. Yan, 'Promoting the ambient-condition stability of Zr-doped barium cerate: Toward robust solid oxide fuel cells and hydrogen separation in syngas', *J. Power Sources*, vol. 378, pp. 134–138, Feb. 2018, doi: 10.1016/j.jpowsour.2017.12.036.
- [21] S. Cheng *et al.*, 'A Dual-Phase Ceramic Membrane with Extremely High H<sub>2</sub> Permeation Flux Prepared by Autoseparation of a Ceramic Precursor', *Angew. Chem. Int. Ed.*, vol. 55, no. 36, pp. 10895–10898, 2016, doi: 10.1002/anie.201604035.
- [22] A. Eftekhari and B. Fang, 'Electrochemical hydrogen storage: Opportunities for fuel storage, batteries, fuel cells, and supercapacitors', *Int. J. Hydrog. Energy*, vol. 42, no. 40, pp. 25143–25165, Oct. 2017, doi: 10.1016/j.ijhydene.2017.08.103.
- [23] F. Jiao and B. Xu, 'Electrochemical Ammonia Synthesis and Ammonia Fuel Cells', *Adv. Mater.*, vol. 31, no. 31, p. 1805173, 2019, doi: 10.1002/adma.201805173.
- [24] B. Wang, T. Li, F. Gong, M. H. D. Othman, and R. Xiao, 'Ammonia as a green energy carrier: Electrochemical synthesis and direct ammonia fuel cell - a comprehensive review', *Fuel Process. Technol.*, vol. 235, p. 107380, Oct. 2022, doi: 10.1016/j.fuproc.2022.107380.
- [25] C.-Y. Yoo *et al.*, 'Role of Protons in Electrochemical Ammonia Synthesis Using Solid-State Electrolytes', *ACS Sustain. Chem. Eng.*, vol. 5, no. 9, pp. 7972–7978, Sep. 2017, doi: 10.1021/acssuschemeng.7b01515.
- [26] N. Shimoda, Y. Kimura, Y. Kobayashi, J. Kubota, and S. Satokawa, 'Ammonia synthesis over yttrium-doped barium zirconate and cerate-based perovskite-type oxide supported ruthenium catalysts', *Int. J. Hydrog. Energy*, vol. 42, no. 50, pp. 29745–29755, Dec. 2017, doi: 10.1016/j.ijhydene.2017.10.108.
- [27] C. Duan *et al.*, 'Highly durable, coking and sulfur tolerant, fuel-flexible protonic ceramic fuel cells', *Nature*, vol. 557, no. 7704, Art. no. 7704, May 2018, doi: 10.1038/s41586-018-0082-6.
- [28] R. O'Hayre, S.-W. Cha, W. Colella, and F. B. Prinz, *Fuel Cell Fundamentals*. John Wiley & Sons, 2016.
- [29] Y. Li *et al.*, 'Impact of syngas from biomass gasification on solid oxide fuel cells: A review study for the energy transition', *Energy Convers. Manag.*, vol. 250, p. 114894, Dec. 2021, doi: 10.1016/j.enconman.2021.114894.
- [30] T. Chen, W. G. Wang, H. Miao, T. Li, and C. Xu, 'Evaluation of carbon deposition behavior on the nickel/yttrium-stabilized zirconia anode-supported fuel cell fueled with simulated syngas', *J. Power Sources*, vol. 196, no. 5, pp. 2461–2468, Mar. 2011, doi: 10.1016/j.jpowsour.2010.11.095.

- [31] N. Bausá, S. Escolástico, and J. M. Serra, 'Direct CO<sub>2</sub> conversion to syngas in a BaCe<sub>0.2</sub>Zr<sub>0.7</sub>Y<sub>0.1</sub>O<sub>3-δ</sub>-based proton-conducting electrolysis cell', *J. CO<sub>2</sub> Util.*, vol. 34, pp. 231–238, Dec. 2019, doi: 10.1016/j.jcou.2019.05.037.
- [32] X. Xia, H. Zhou, Y. Zhang, and H. Jiang, 'Innovative steam methane reforming for coproducing CO-free hydrogen and syngas in proton conducting membrane reactor', *AIChE J.*, vol. 65, no. 11, p. e16740, 2019, doi: 10.1002/aic.16740.
- [33] X.-Z. Fu, J.-L. Luo, A. R. Sanger, N. Luo, and K. T. Chuang, 'Y-doped BaCeO<sub>3-δ</sub> nanopowders as proton-conducting electrolyte materials for ethane fuel cells to co-generate ethylene and electricity', *J. Power Sources*, vol. 195, no. 9, pp. 2659–2663, May 2010, doi: 10.1016/j.jpowsour.2009.10.069.
- [34] J.-Y. Lin, L. Shao, F.-Z. Si, X.-Z. Fu, and J.-L. Luo, 'Multiple-doped barium cerate proton-conducting electrolytes for chemical-energy cogeneration in solid oxide fuel cells', *Int. J. Hydrog. Energy*, vol. 43, no. 42, pp. 19704–19710, Oct. 2018, doi: 10.1016/j.ijhydene.2018.08.204.
- [35] S. McIntosh and R. J. Gorte, 'Direct Hydrocarbon Solid Oxide Fuel Cells', *Chem. Rev.*, vol. 104, no. 10, pp. 4845–4866, Oct. 2004, doi: 10.1021/cr020725g.
- [36] Y. Meng, J. Gao, Z. Zhao, J. Amoroso, J. Tong, and K. S. Brinkman, 'Review: recent progress in low-temperature proton-conducting ceramics', *J. Mater. Sci.*, vol. 54, no. 13, pp. 9291–9312, Jul. 2019, doi: 10.1007/s10853-019-03559-9.
- [37] K. H. Ryu and S. M. Haile, 'Chemical stability and proton conductivity of doped BaCeO<sub>3</sub>-BaZrO<sub>3</sub> solid solutions', *Solid State Ion.*, vol. 125, no. 1, pp. 355–367, Oct. 1999, doi: 10.1016/S0167-2738(99)00196-4.
- [38] H. Iwahara, 'Proton conducting ceramics and their applications', *Solid State Ion.*, vol. 86–88, pp. 9–15, Jul. 1996, doi: 10.1016/0167-2738(96)00087-2.
- [39] D. S. Aidhy and W. J. Weber, 'Microstructure design for fast oxygen conduction', *J. Mater. Res.*, vol. 31, no. 1, pp. 2–16, Jan. 2016, doi: 10.1557/jmr.2015.327.
- [40] D. Pergolesi *et al.*, 'High proton conduction in grain-boundary-free yttrium-doped barium zirconate films grown by pulsed laser deposition', *Nat. Mater.*, vol. 9, no. 10, pp. 846–852, Oct. 2010, doi: 10.1038/nmat2837.
- [41] D. Konwar, B. J. Park, P. Basumatary, and H. H. Yoon, 'Enhanced performance of solid oxide fuel cells using BaZr<sub>0.2</sub>Ce<sub>0.7</sub>Y<sub>0.1</sub>O<sub>3-δ</sub> thin films', *J. Power Sources*, vol. 353, pp. 254–259, Jun. 2017, doi: 10.1016/j.jpowsour.2017.04.010.
- [42] K. Thabet, A. Le Gal La Salle, E. Quarez, and O. Joubert, 'Chapter 4 - Protonic-based ceramics for fuel cells and electrolyzers', in *Solid Oxide-Based Electrochemical Devices*, M. Lo Faro, Ed., Academic Press, 2020, pp. 91–122. doi: 10.1016/B978-0-12-818285-7.00004-6.
- [43] K. D. Kreuer, 'Aspects of the formation and mobility of protonic charge carriers and the stability of perovskite-type oxides', *Solid State Ion.*, vol. 125, no. 1, pp. 285–302, Oct. 1999, doi: 10.1016/S0167-2738(99)00188-5.
- [44] A. Satapathy and E. Sinha, 'A comparative proton conductivity study on Yb-doped BaZrO<sub>3</sub> perovskite at intermediate temperatures under wet N<sub>2</sub> environment', *J. Alloys Compd.*, vol. 772, pp. 675–682, Jan. 2019, doi: 10.1016/j.jallcom.2018.08.329.
- [45] S. Hossain, A. M. Abdalla, S. N. B. Jamain, J. H. Zaini, and A. K. Azad, 'A review on proton conducting electrolytes for clean energy and intermediate temperature-solid oxide fuel cells', *Renew. Sustain. Energy Rev.*, vol. 79, pp. 750–764, Nov. 2017, doi: 10.1016/j.rser.2017.05.147.
- [46] P. Du *et al.*, 'Cooperative origin of proton pair diffusivity in yttrium substituted barium zirconate', *Commun. Phys.*, vol. 3, no. 1, pp. 1–9, Nov. 2020, doi: 10.1038/s42005-020-00464-5.
- [47] Z. Lin, S. Lin, Y. Tian, A. Van Bokkelen, M. Valerio, and M. A. Gomez, 'Oxygen Vacancies Altering the Trapping in the Proton Conduction Landscape of Doped Barium

Zirconate', *J. Phys. Chem. C*, vol. 124, no. 51, pp. 27954–27964, Dec. 2020, doi: 10.1021/acs.jpcc.0c09461.

[48] A. Kruth and J. T. S. Irvine, 'Water incorporation studies on doped barium cerate perovskites', *Solid State Ion.*, vol. 162–163, pp. 83–91, Sep. 2003, doi: 10.1016/S0167-2738(03)00252-2.

[49] W. G. Coors and D. W. Readey, 'Proton Conductivity Measurements in Yttrium Barium Cerate by Impedance Spectroscopy', *J. Am. Ceram. Soc.*, vol. 85, no. 11, pp. 2637–2640, 2002, doi: 10.1111/j.1151-2916.2002.tb00507.x.

[50] Y. Yamazaki *et al.*, 'Proton trapping in yttrium-doped barium zirconate', *Nat. Mater.*, vol. 12, no. 7, pp. 647–651, Jul. 2013, doi: 10.1038/nmat3638.

[51] J. Kong *et al.*, 'Temperature dependence of ion diffusion coefficients in NaCl electrolyte confined within graphene nanochannels', *Phys. Chem. Chem. Phys.*, vol. 19, no. 11, pp. 7678–7688, Mar. 2017, doi: 10.1039/C6CP08752C.

[52] E. Matsushita and H. Senki, 'Application of Proton Diffusion Analysis in Perovskite-Type Oxides', in *2007 Sixteenth IEEE International Symposium on the Applications of Ferroelectrics*, May 2007, pp. 301–304. doi: 10.1109/ISAF.2007.4393248.

[53] K. Singh, J. Nowotny, and V. Thangadurai, 'Amphoteric oxide semiconductors for energy conversion devices: a tutorial review', *Chem. Soc. Rev.*, vol. 42, no. 5, pp. 1961–1972, Feb. 2013, doi: 10.1039/C2CS35393H.

[54] N. Bonanos, 'Transport properties and conduction mechanism in high-temperature protonic conductors', *Solid State Ion.*, vol. 53–56, pp. 967–974, Jul. 1992, doi: 10.1016/0167-2738(92)90278-W.

[55] A. S. Babu and R. Bauri, 'Synthesis, phase stability and conduction behavior of rare earth and transition elements doped barium cerates', *Int. J. Hydrog. Energy*, vol. 39, no. 26, pp. 14487–14495, Sep. 2014, doi: 10.1016/j.ijhydene.2014.03.249.

[56] J. Bu, P. G. Jönsson, and Z. Zhao, 'Ionic conductivity of dense BaZr<sub>0.5</sub>Ce<sub>0.3</sub>Ln<sub>0.2</sub>O<sub>3-δ</sub> (Ln = Y, Sm, Gd, Dy) electrolytes', *J. Power Sources*, vol. 272, pp. 786–793, Dec. 2014, doi: 10.1016/j.jpowsour.2014.09.056.

[57] P. Sawant, S. Varma, B. N. Wani, and S. R. Bharadwaj, 'Synthesis, stability and conductivity of BaCe<sub>0.8-x</sub>Zr<sub>x</sub>Y<sub>0.2</sub>O<sub>3-δ</sub> as electrolyte for proton conducting SOFC', *Int. J. Hydrog. Energy*, vol. 37, no. 4, pp. 3848–3856, Feb. 2012, doi: 10.1016/j.ijhydene.2011.04.106.

[58] V. C. D. Graça, F. J. A. Loureiro, L. I. V. Holz, S. M. Mikhalev, and D. P. Fagg, 'Toward improved chemical stability of yttrium-doped barium cerate by the introduction of nickel oxide', *J. Am. Ceram. Soc.*, vol. n/a, no. n/a, doi: 10.1111/jace.18600.

[59] Z. Luo *et al.*, 'A New Class of Proton Conductors with Dramatically Enhanced Stability and High Conductivity for Reversible Solid Oxide Cells', *Small*, vol. n/a, no. n/a, p. 2208064, doi: 10.1002/sml.202208064.

[60] K. Xie *et al.*, 'A new stable BaCeO<sub>3</sub>-based proton conductor for intermediate-temperature solid oxide fuel cells', *J. Alloys Compd.*, vol. 472, no. 1, pp. 551–555, Mar. 2009, doi: 10.1016/j.jallcom.2008.05.036.

[61] L. Bi, S. Zhang, S. Fang, Z. Tao, R. Peng, and W. Liu, 'A novel anode supported BaCe<sub>0.7</sub>Ta<sub>0.1</sub>Y<sub>0.2</sub>O<sub>3-δ</sub> electrolyte membrane for proton-conducting solid oxide fuel cell', *Electrochem. Commun.*, vol. 10, no. 10, pp. 1598–1601, Oct. 2008, doi: 10.1016/j.elecom.2008.08.024.

[62] F. Zhao, S. Wang, L. Dixon, and F. Chen, 'Novel BaCe<sub>0.7</sub>In<sub>0.2</sub>Yb<sub>0.1</sub>O<sub>3-δ</sub> proton conductor as electrolyte for intermediate temperature solid oxide fuel cells', *J. Power Sources*, vol. 196, no. 18, pp. 7500–7504, Sep. 2011, doi: 10.1016/j.jpowsour.2011.04.036.

[63] P. Ranran, W. Yan, Y. Lizhai, and M. Zongqiang, 'Electrochemical properties of intermediate-temperature SOFCs based on proton conducting Sm-doped BaCeO<sub>3</sub> electrolyte

thin film', *Solid State Ion.*, vol. 177, no. 3, pp. 389–393, Jan. 2006, doi: 10.1016/j.ssi.2005.11.020.

[64] Y. Guo, B. Liu, Q. Yang, C. Chen, W. Wang, and G. Ma, 'Preparation via microemulsion method and proton conduction at intermediate-temperature of  $\text{BaCe}_{1-x}\text{Y}_x\text{O}_{3-\alpha}$ ', *Electrochem. Commun.*, vol. 11, no. 1, pp. 153–156, Jan. 2009, doi: 10.1016/j.elecom.2008.10.038.

[65] W. B. Wang, J. W. Liu, Y. D. Li, H. T. Wang, F. Zhang, and G. L. Ma, 'Microstructures and proton conduction behaviors of Dy-doped  $\text{BaCeO}_3$  ceramics at intermediate temperature', *Solid State Ion.*, vol. 181, no. 15, pp. 667–671, Jun. 2010, doi: 10.1016/j.ssi.2010.04.008.

[66] C. Chen and G. Ma, 'Proton conduction in  $\text{BaCe}_{1-x}\text{Gd}_x\text{O}_{3-\alpha}$  at intermediate temperature and its application to synthesis of ammonia at atmospheric pressure', *J. Alloys Compd.*, vol. 485, no. 1, pp. 69–72, Oct. 2009, doi: 10.1016/j.jallcom.2009.05.108.

[67] Y.-P. Fu and C.-S. Weng, 'Effect of rare-earth ions doped in  $\text{BaCeO}_3$  on chemical stability, mechanical properties, and conductivity properties', *Ceram. Int.*, vol. 40, no. 7, Part B, pp. 10793–10802, Aug. 2014, doi: 10.1016/j.ceramint.2014.03.069.

[68] D. Pergolesi *et al.*, 'High proton conduction in grain-boundary-free yttrium-doped barium zirconate films grown by pulsed laser deposition', *Nat. Mater.*, vol. 9, no. 10, pp. 846–852, Oct. 2010, doi: 10.1038/nmat2837.

[69] E. Fabbri, L. Bi, H. Tanaka, D. Pergolesi, and E. Traversa, 'Chemically Stable Pr and Y Co-Doped Barium Zirconate Electrolytes with High Proton Conductivity for Intermediate-Temperature Solid Oxide Fuel Cells', *Adv. Funct. Mater.*, vol. 21, no. 1, pp. 158–166, Jan. 2011, doi: 10.1002/adfm.201001540.

[70] Y. Yamazaki, R. Hernandez-Sanchez, and S. M. Haile, 'High Total Proton Conductivity in Large-Grained Yttrium-Doped Barium Zirconate', *Chem. Mater.*, vol. 21, no. 13, pp. 2755–2762, Jul. 2009, doi: 10.1021/cm900208w.

[71] W. Sun, L. Yan, Z. Shi, Z. Zhu, and W. Liu, 'Fabrication and performance of a proton-conducting solid oxide fuel cell based on a thin  $\text{BaZr}_{0.8}\text{Y}_{0.2}\text{O}_{3-\delta}$  electrolyte membrane', *J. Power Sources*, vol. 195, no. 15, pp. 4727–4730, Aug. 2010, doi: 10.1016/j.jpowsour.2010.02.012.

[72] Z. Sun, E. Fabbri, L. Bi, and E. Traversa, 'Lowering grain boundary resistance of  $\text{BaZr}_{0.8}\text{Y}_{0.2}\text{O}_{3-\delta}$  with  $\text{LiNO}_3$  sintering-aid improves proton conductivity for fuel cell operation', *Phys. Chem. Chem. Phys.*, vol. 13, no. 17, pp. 7692–7700, Apr. 2011, doi: 10.1039/C0CP01470B.

[73] S. Wienströer and H.-D. Wiemhöfer, 'Investigation of the influence of zirconium substitution on the properties of neodymium-doped barium cerates', *Solid State Ion.*, vol. 101–103, pp. 1113–1117, Nov. 1997, doi: 10.1016/S0167-2738(97)00163-X.

[74] B. Lin, M. Hu, J. Ma, Y. Jiang, S. Tao, and G. Meng, 'Stable, easily sintered  $\text{BaCe}_{0.5}\text{Zr}_{0.3}\text{Y}_{0.16}\text{Zn}_{0.04}\text{O}_{3-\delta}$  electrolyte-based protonic ceramic membrane fuel cells with  $\text{Ba}_{0.5}\text{Sr}_{0.5}\text{Zn}_{0.2}\text{Fe}_{0.8}\text{O}_{3-\delta}$  perovskite cathode', *J. Power Sources*, vol. 183, no. 2, pp. 479–484, Sep. 2008, doi: 10.1016/j.jpowsour.2008.05.075.

[75] X. Wang, J. Yin, J. Xu, H. Wang, and G. Ma, 'Chemical Stability, Ionic Conductivity of  $\text{BaCe}_{0.9-x}\text{Zr}_x\text{Sm}_{0.10}\text{O}_{3-\alpha}$  and Its Application to Ammonia Synthesis at Atmospheric Pressure', *Chin. J. Chem.*, vol. 29, no. 6, pp. 1114–1118, Jun. 2011, doi: 10.1002/cjoc.201190209.

[76] Y.-C. Tsai, S.-Y. Chen, J.-H. Wang, P.-W. Wu, and P.-C. Chen, 'Chemical stability and electrical conductivity of  $\text{BaCe}_{0.4}\text{Zr}_{0.4}\text{Gd}_{0.1}\text{Dy}_{0.1}\text{O}_{3-\delta}$  perovskite', *Ceram. Int.*, vol. 41, no. 9, Part A, pp. 10856–10860, Nov. 2015, doi: 10.1016/j.ceramint.2015.05.026.

[77] X. Ma, J. Dai, H. Zhang, and D. E. Reisner, 'Protonic conductivity nanostructured ceramic film with improved resistance to carbon dioxide at elevated temperatures', *Surf. Coat. Technol.*, vol. 200, no. 5, pp. 1252–1258, Nov. 2005, doi: 10.1016/j.surfcoat.2005.07.099.

- [78] J. Lv, L. Wang, D. Lei, H. Guo, and R. V. Kumar, 'Sintering, chemical stability and electrical conductivity of the perovskite proton conductors  $\text{BaCe}_{0.45}\text{Zr}_{0.45}\text{M}_{0.1}\text{O}_{3-\delta}$  (M=In, Y, Gd, Sm)', *J. Alloys Compd.*, vol. 467, no. 1, pp. 376–382, Jan. 2009, doi: 10.1016/j.jallcom.2007.12.103.
- [79] Y. Li *et al.*, 'Stable and easily sintered  $\text{BaCe}_{0.5}\text{Zr}_{0.3}\text{Y}_{0.2}\text{O}_{3-\delta}$  electrolytes using ZnO and  $\text{Na}_2\text{CO}_3$  additives for protonic oxide fuel cells', *Electrochimica Acta*, vol. 95, pp. 95–101, Apr. 2013, doi: 10.1016/j.electacta.2013.02.023.
- [80] J. Yin, X. Wang, J. Xu, H. Wang, F. Zhang, and G. Ma, 'Ionic conduction in  $\text{BaCe}_{0.85-x}\text{Zr}_x\text{Er}_{0.15}\text{O}_{3-\alpha}$  and its application to ammonia synthesis at atmospheric pressure', *Solid State Ion.*, vol. 185, no. 1, pp. 6–10, Mar. 2011, doi: 10.1016/j.ssi.2010.12.018.
- [81] N. T. Q. Nguyen and H. H. Yoon, 'Preparation and evaluation of  $\text{BaZr}_{0.1}\text{Ce}_{0.7}\text{Y}_{0.1}\text{Yb}_{0.1}\text{O}_{3-\delta}$  (BZCYYb) electrolyte and BZCYYb-based solid oxide fuel cells', *J. Power Sources*, vol. 231, pp. 213–218, Jun. 2013, doi: 10.1016/j.jpowsour.2013.01.011.
- [82] L. Yang *et al.*, 'Enhanced sulfur and coking tolerance of a mixed ion conductor for SOFCs:  $\text{BaZr}_{0.1}\text{Ce}_{0.7}\text{Y}_{0.2-x}\text{Yb}_x\text{O}_{3-\delta}$ ', *Science*, vol. 326, no. 5949, pp. 126–129, Oct. 2009, doi: 10.1126/science.1174811.
- [83] X. Zhou *et al.*, 'Ionic conductivity, sintering and thermal expansion behaviors of mixed ion conductor  $\text{BaZr}_{0.1}\text{Ce}_{0.7}\text{Y}_{0.1}\text{Yb}_{0.1}\text{O}_{3-\delta}$  prepared by ethylene diamine tetraacetic acid assisted glycine nitrate process', *J. Power Sources*, vol. 196, no. 11, pp. 5000–5006, Jun. 2011, doi: 10.1016/j.jpowsour.2011.01.092.
- [84] N. Radenahmad, A. Afif, M. I. Petra, S. M. H. Rahman, S. Eriksson, and A. K. Azad, 'High conductivity and high density proton conducting  $\text{Ba}_{1-x}\text{Sr}_x\text{Ce}_{0.5}\text{Zr}_{0.35}\text{Y}_{0.1}\text{Sm}_{0.05}\text{O}_{3-\delta}$  (x = 0.5, 0.7, 0.9, 1.0) perovskites for IT-SOFC', *Int. J. Hydrog. Energy*, vol. 41, no. 27, pp. 11832–11841, Jul. 2016, doi: 10.1016/j.ijhydene.2016.02.073.
- [85] K. Yang *et al.*, 'Synthesis, sintering behavior and electrical properties of  $\text{Ba}(\text{Zr}_{0.1}\text{Ce}_{0.7}\text{Y}_{0.2})\text{O}_{3-\delta}$  and  $\text{Ba}(\text{Zr}_{0.1}\text{Ce}_{0.7}\text{Y}_{0.1}\text{Yb}_{0.1})\text{O}_{3-\delta}$  proton conductors', *Ceram. Int.*, vol. 40, no. 9, Part B, pp. 15073–15081, Nov. 2014, doi: 10.1016/j.ceramint.2014.06.115.
- [86] C.-J. Tseng *et al.*, 'Potassium doping optimization in proton-conducting  $\text{Ba}_{1-x}\text{K}_x\text{Ce}_{0.6}\text{Zr}_{0.2}\text{Y}_{0.2}\text{O}_{3-\delta}$  oxides for fuel cell applications', *J. Alloys Compd.*, vol. 696, pp. 251–256, Mar. 2017, doi: 10.1016/j.jallcom.2016.11.249.
- [87] M. Amsif, D. Marrero-Lopez, J. C. Ruiz-Morales, S. N. Savvin, M. Gabás, and P. Nunez, 'Influence of rare-earth doping on the microstructure and conductivity of  $\text{BaCe}_{0.9}\text{Ln}_{0.1}\text{O}_{3-\delta}$  proton conductors', *J. Power Sources*, vol. 7, no. 196, pp. 3461–3469, 2011, doi: 10.1016/j.jpowsour.2010.11.120.
- [88] C. Zhang and H. Zhao, 'Influence of In content on the electrical conduction behavior of Sm- and In-co-doped proton conductor  $\text{BaCe}_{0.80-x}\text{Sm}_{0.20}\text{In}_x\text{O}_{3-\delta}$ ', *Solid State Ion.*, vol. 206, pp. 17–21, Jan. 2012, doi: 10.1016/j.ssi.2011.10.026.
- [89] A. Radojković *et al.*, 'Co-doping as a strategy for tailoring the electrolyte properties of  $\text{BaCe}_{0.9}\text{Y}_{0.1}\text{O}_{3-\delta}$ ', *Ceram. Int.*, vol. 45, no. 7, Part A, pp. 8279–8285, May 2019, doi: 10.1016/j.ceramint.2019.01.134.
- [90] F. Zhao, S. Wang, L. Dixon, and F. Chen, 'Novel  $\text{BaCe}_{0.7}\text{In}_{0.2}\text{Yb}_{0.1}\text{O}_{3-\delta}$  proton conductor as electrolyte for intermediate temperature solid oxide fuel cells', *J. Power Sources*, vol. 196, no. 18, pp. 7500–7504, Sep. 2011, doi: 10.1016/j.jpowsour.2011.04.036.
- [91] Y.-P. Fu and C.-S. Weng, 'Effect of rare-earth ions doped in  $\text{BaCeO}_3$  on chemical stability, mechanical properties, and conductivity properties', *Ceram. Int.*, vol. 40, no. 7, Part B, pp. 10793–10802, Aug. 2014, doi: 10.1016/j.ceramint.2014.03.069.
- [92] W. Sun, L. Yan, Z. Shi, Z. Zhu, and W. Liu, 'Fabrication and performance of a proton-conducting solid oxide fuel cell based on a thin  $\text{BaZr}_{0.8}\text{Y}_{0.2}\text{O}_{3-\delta}$  electrolyte membrane', *J. Power Sources*, vol. 195, no. 15, pp. 4727–4730, Aug. 2010, doi: 10.1016/j.jpowsour.2010.02.012.

- [93] T. Ohzeki, S. Hasegawa, M. Shimizu, and T. Hashimoto, 'Analysis of phase transition behavior of BaCeO<sub>3</sub> with thermal analyses and high temperature X-ray diffraction', *Solid State Ion.*, vol. 180, no. 17, pp. 1034–1039, Jul. 2009, doi: 10.1016/j.ssi.2009.05.019.
- [94] B.-T. Melekh *et al.*, 'Structure, phase transitions and optical properties of pure and rare earth doped BaCeO<sub>3</sub>, SrCeO<sub>3</sub> prepared by inductive melting', *Solid State Ion.*, vol. 97, no. 1, pp. 465–470, May 1997, doi: 10.1016/S0167-2738(97)00093-3.
- [95] K. S. Knight, 'Structural phase transitions in BaCeO<sub>3</sub>', *Solid State Ion.*, vol. 74, no. 3, pp. 109–117, Dec. 1994, doi: 10.1016/0167-2738(94)90199-6.
- [96] K. S. Knight, 'Structural phase transitions, oxygen vacancy ordering and protonation in doped BaCeO<sub>3</sub>: results from time-of-flight neutron powder diffraction investigations', *Solid State Ion.*, vol. 145, no. 1, pp. 275–294, Dec. 2001, doi: 10.1016/S0167-2738(01)00952-3.
- [97] S. Yamanaka, T. Hamaguchi, T. Oyama, T. Matsuda, S. Kobayashi, and K. Kurosaki, 'Heat capacities and thermal conductivities of perovskite type BaZrO<sub>3</sub> and BaCeO<sub>3</sub>', *J. Alloys Compd.*, vol. 359, no. 1, pp. 1–4, Sep. 2003, doi: 10.1016/S0925-8388(03)00137-3.
- [98] K. Takeuchi, C.-K. Loong, J. W. Richardson, J. Guan, S. E. Dorris, and U. Balachandran, 'The crystal structures and phase transitions in Y-doped BaCeO<sub>3</sub>: their dependence on Y concentration and hydrogen doping', *Solid State Ion.*, vol. 138, no. 1, pp. 63–77, Dec. 2000, doi: 10.1016/S0167-2738(00)00771-2.
- [99] X.-T. Su, Q.-Z. Yan, X.-H. Ma, W.-F. Zhang, and C.-C. Ge, 'Effect of co-dopant addition on the properties of yttrium and neodymium doped barium cerate electrolyte', *Solid State Ion.*, vol. 177, no. 11, pp. 1041–1045, Apr. 2006, doi: 10.1016/j.ssi.2006.02.047.
- [100] M. Amsif, D. Marrero-Lopez, J. C. Ruiz-Morales, S. N. Savvin, M. Gabás, and P. Nunez, 'Influence of rare-earth doping on the microstructure and conductivity of BaCe<sub>0.9</sub>Ln<sub>0.1</sub>O<sub>3-δ</sub> proton conductors', *J. Power Sources*, vol. 7, no. 196, pp. 3461–3469, 2011, doi: 10.1016/j.jpowsour.2010.11.120.
- [101] G. Accardo, D. Frattini, and S. P. Yoon, 'Enhanced proton conductivity of Gd–Co bi-doped barium cerate perovskites based on structural and microstructural investigations', *J. Alloys Compd.*, vol. 834, p. 155114, Sep. 2020, doi: 10.1016/j.jallcom.2020.155114.
- [102] J. Tong, D. Clark, L. Bernau, A. Subramaniyan, and R. O'Hayre, 'Proton-conducting yttrium-doped barium cerate ceramics synthesized by a cost-effective solid-state reactive sintering method', *Solid State Ion.*, vol. 181, no. 33, pp. 1486–1498, Oct. 2010, doi: 10.1016/j.ssi.2010.08.022.
- [103] S. Likhittaphon, T. Pukkrueapun, P. Seeharaj, U. Wetwathana Hartley, N. Laosiripojana, and P. Kim-Lohsoontorn, 'Effect of sintering additives on barium cerate based solid oxide electrolysis cell for syngas production from carbon dioxide and steam', *Fuel Process. Technol.*, vol. 173, pp. 119–125, May 2018, doi: 10.1016/j.fuproc.2018.01.019.
- [104] A. Lacz, 'Effect of microstructure on chemical stability and electrical properties of BaCe<sub>0.9</sub>Y<sub>0.1</sub>O<sub>3-δ</sub>', *Ionics*, vol. 22, no. 8, pp. 1405–1414, Aug. 2016, doi: 10.1007/s11581-016-1665-6.
- [105] N. W. Mazlan, N. Osman, and O. H. Hassan, 'Thermal expansion and lattice parameter of solid electrolyte based on cerate-zirconate ceramics', presented at the AIP Conference Proceedings, 2018. doi: 10.1063/1.5066970.
- [106] D. Chen, Q. Wang, Y. Liu, and X. Ning, 'Microstructure, thermal characteristics, and thermal cycling behavior of the ternary rare earth oxides (La<sub>2</sub>O<sub>3</sub>, Gd<sub>2</sub>O<sub>3</sub>, and Yb<sub>2</sub>O<sub>3</sub>) co-doped YSZ coatings', *Surf. Coat. Technol.*, vol. 403, p. 126387, Dec. 2020, doi: 10.1016/j.surfcoat.2020.126387.
- [107] E. Gorbova, V. Maragou, D. Medvedev, A. Demin, and P. Tsiakaras, 'Investigation of the protonic conduction in Sm doped BaCeO<sub>3</sub>', *J. Power Sources*, vol. 181, no. 2, pp. 207–213, Jul. 2008, doi: 10.1016/j.jpowsour.2008.01.036.

- [108] S. U. Dubal, C. H. Bhosale, and L. D. Jadhav, 'Performance of spray deposited Gd-doped barium cerate thin films for proton conducting SOFCs', *Ceram. Int.*, vol. 41, no. 4, pp. 5607–5613, May 2015, doi: 10.1016/j.ceramint.2014.12.142.
- [109] N. Maffei, L. Nossova, M. J. Turnbull, G. Caravaggio, and R. Burich, 'Doped barium cerate perovskite catalysts for simultaneous NO<sub>x</sub> storage and soot oxidation', *Appl. Catal. Gen.*, vol. 600, p. 117465, Jun. 2020, doi: 10.1016/j.apcata.2020.117465.
- [110] M. W. Kadi and R. M. Mohamed, 'Synthesis of BaCeO<sub>3</sub> nanoneedles and the effect of V, Ag, Au, Pt doping on the visible light hydrogen evolution in the photocatalytic water splitting reaction', *J. Sol-Gel Sci. Technol.*, May 2019, doi: 10.1007/s10971-019-05018-y.
- [111] J. Sarabut *et al.*, 'Effect of strontium and zirconium doped barium cerate on the performance of proton ceramic electrolyser cell for syngas production from carbon dioxide and steam', *Int. J. Hydrog. Energy*, vol. 44, no. 37, pp. 20634–20640, Aug. 2019, doi: 10.1016/j.ijhydene.2018.07.121.
- [112] S. Bhowmick, J. Basu, Y. Xue, and C. B. Carter, 'Hydrothermal Synthesis of Nanocrystalline Barium Cerate Using Hexamethylenetetramine', *J. Am. Ceram. Soc.*, vol. 93, no. 12, pp. 4041–4046, 2010, doi: 10.1111/j.1551-2916.2010.03998.x.
- [113] Y. Luo, Y. Li, N. Zhang, Y. Ding, H. Li, and W. Huang, 'Electrical properties of the nanostructured BaCe<sub>0.8</sub>Gd<sub>0.2</sub>O<sub>3-δ</sub> electrolyte', *Ionics*, Aug. 2020, doi: 10.1007/s11581-020-03733-z.
- [114] Z. Khani, M. Taillades-Jacquin, G. Taillades, M. Marrony, D. J. Jones, and J. Rozière, 'New synthesis of nanopowders of proton conducting materials. A route to densified proton ceramics', *J. Solid State Chem.*, vol. 182, no. 4, pp. 790–798, Apr. 2009, doi: 10.1016/j.jssc.2008.12.020.
- [115] S. D. Flint, M. Hartmanová, J. S. Jones, and R. C. T. Slade, 'Microstructure of Ca-doped barium cerate electrolytes BaCe<sub>1-x</sub>Ca<sub>x</sub>O<sub>3-x</sub> (= 0, 0.02, 0.05, 0.10 and 0.15)', *Solid State Ion.*, vol. 86–88, pp. 679–683, Jul. 1996, doi: 10.1016/0167-2738(96)00365-7.
- [116] E. Gorbova, V. Maragou, D. Medvedev, A. Demin, and P. Tsiakaras, 'Influence of sintering additives of transition metals on the properties of gadolinium-doped barium cerate', *Solid State Ion.*, vol. 179, no. 21, pp. 887–890, Sep. 2008, doi: 10.1016/j.ssi.2008.02.065.
- [117] C. Zhang, G. Luo, J. Zhang, Y. Dai, Q. Shen, and L. Zhang, 'Synthesis and thermal conductivity improvement of W-Cu composites modified with WC interfacial layer', *Mater. Des.*, vol. 127, pp. 233–242, Aug. 2017, doi: 10.1016/j.matdes.2017.04.090.
- [118] Z. Liu *et al.*, 'Multiple Effects of Iron and Nickel Additives on the Properties of Proton Conducting Yttrium-Doped Barium Cerate-Zirconate Electrolytes for High-Performance Solid Oxide Fuel Cells', *ACS Appl. Mater. Interfaces*, Oct. 2020, doi: 10.1021/acsami.0c14523.
- [119] D. A. Medvedev, A. A. Murashkina, and A. K. Demin, 'Formation of dense electrolytes based on BaCeO<sub>3</sub> and BaZrO<sub>3</sub> for application in solid oxide fuel cells: The role of solid-state reactive sintering', *Rev. J. Chem.*, vol. 5, no. 3, pp. 193–214, Jul. 2015, doi: 10.1134/S2079978015030024.
- [120] R. Köferstein, L. Jäger, and S. G. Ebbinghaus, 'Sintering of a fine-grained BaCeO<sub>3</sub> powder obtained from a co-precipitation method', *J. Mater. Sci.*, vol. 45, no. 23, pp. 6521–6527, 2010, doi: 10.1007/s10853-010-4741-8.
- [121] E. Gorbova, V. Maragou, D. Medvedev, A. Demin, and P. Tsiakaras, 'Influence of Cu on the properties of gadolinium-doped barium cerate', *J. Power Sources*, vol. 181, no. 2, pp. 292–296, Jul. 2008, doi: 10.1016/j.jpowsour.2007.11.049.
- [122] G. Meng, P. Wang, Y. Gu, and D. Peng, 'Preparation and characterization of barium cerate-based thick membranes using a screen printing process', *Solid State Ion.*, vol. 136–137, pp. 209–213, Nov. 2000, doi: 10.1016/S0167-2738(00)00312-X.

- [123] A. Subramaniyan, J. Tong, R. P. O'Hayre, and N. M. Sammes, 'Sintering Studies on 20 mol% Yttrium-Doped Barium Cerate', *J. Am. Ceram. Soc.*, vol. 94, no. 6, pp. 1800–1804, 2011, doi: 10.1111/j.1551-2916.2010.04303.x.
- [124] M. Amsif, D. Marrero-López, A. Magrasó, J. Peña-Martínez, J. C. Ruiz-Morales, and P. Núñez, 'Synthesis and characterisation of BaCeO<sub>3</sub>-based proton conductors obtained from freeze-dried precursors', *J. Eur. Ceram. Soc.*, vol. 29, no. 1, pp. 131–138, Jan. 2009, doi: 10.1016/j.jeurceramsoc.2008.06.001.
- [125] F. Chen, O. T. Sørensen, G. Meng, and D. Peng, 'Preparation of Nd-doped barium cerate through different routes', *Solid State Ion.*, vol. 100, no. 1, pp. 63–72, Sep. 1997, doi: 10.1016/S0167-2738(97)00265-8.
- [126] N. Maffei, L. Pelletier, J. P. Charland, and A. McFarlan, 'A Direct Ammonia Fuel Cell Using Barium Cerate Proton Conducting Electrolyte Doped With Gadolinium and Praseodymium', *Fuel Cells*, vol. 7, no. 4, pp. 323–328, 2007, doi: 10.1002/face.200600038.
- [127] A. S. Patra *et al.*, 'Combined Experimental and Theoretical Insights into the Synergistic Effect of Cerium Doping and Oxygen Vacancies in BaZrO<sub>3-δ</sub> Hollow Nanospheres for Efficient Photocatalytic Hydrogen Production', *J. Phys. Chem. C*, Nov. 2018, doi: 10.1021/acs.jpcc.8b10626.
- [128] S. Imashuku, T. Uda, Y. Nose, G. Taniguchi, Y. Ito, and Y. Awakura, 'Dependence of Dopant Cations on Microstructure and Proton Conductivity of Barium Zirconate', *J. Electrochem. Soc.*, vol. 156, no. 1, p. B1, Oct. 2008, doi: 10.1149/1.2999335.
- [129] R. Sažinas, C. Bernuy-López, M.-A. Einarsrud, and T. Grande, 'Effect of CO<sub>2</sub> Exposure on the Chemical Stability and Mechanical Properties of BaZrO<sub>3</sub>-Ceramics', *J. Am. Ceram. Soc.*, vol. 99, no. 11, pp. 3685–3695, Jul. 2016, doi: 10.1111/jace.14395.
- [130] A. Fluri *et al.*, 'Enhanced Proton Conductivity in Y - Doped BaZrO<sub>3</sub> via Strain Engineering', *Adv. Sci.*, vol. 4, no. 12, Oct. 2017, doi: 10.1002/advs.201700467.
- [131] A. Magrasó, B. Ballesteros, R. Rodríguez-Lamas, M. F. Sunding, and J. Santiso, 'Optimisation of growth parameters to obtain epitaxial Y-doped BaZrO<sub>3</sub> proton conducting thin films', *Solid State Ion.*, vol. 314, pp. 9–16, Jan. 2018, doi: 10.1016/j.ssi.2017.11.002.
- [132] E. Fabbri, L. Bi, H. Tanaka, D. Pergolesi, and E. Traversa, 'Chemically Stable Pr and Y Co-Doped Barium Zirconate Electrolytes with High Proton Conductivity for Intermediate-Temperature Solid Oxide Fuel Cells', *Adv. Funct. Mater.*, vol. 21, no. 1, pp. 158–166, Jan. 2011, doi: 10.1002/adfm.201001540.
- [133] U. Aarthi and K. S. Babu, 'Grain boundary space charge modulation in BaZr<sub>0.8</sub>Y<sub>0.2-x</sub>M<sub>x</sub>O<sub>3-δ</sub> with transition metal (M= Ni, Co, Fe, and Zn) co-doping', *Int. J. Hydrog. Energy*, Aug. 2020, doi: 10.1016/j.ijhydene.2020.07.207.
- [134] D. Han, K. Shinoda, and T. Uda, 'Dopant Site Occupancy and Chemical Expansion in Rare Earth-Doped Barium Zirconate', *J. Am. Ceram. Soc.*, vol. 97, no. 2, pp. 643–650, 2014, doi: 10.1111/jace.12681.
- [135] E. Gilardi *et al.*, 'Effect of Dopant-Host Ionic Radii Mismatch on Acceptor-Doped Barium Zirconate Microstructure and Proton Conductivity', *J. Phys. Chem. C*, vol. 121, no. 18, pp. 9739–9747, May 2017, doi: 10.1021/acs.jpcc.7b02163.
- [136] M. Irshad *et al.*, 'Evaluation of BaZr<sub>0.8</sub>X<sub>0.2</sub> (X= Y, Gd, Sm) proton conducting electrolytes sintered at low temperature for IT-SOFC synthesized by cost effective combustion method', *J. Alloys Compd.*, vol. 815, p. 152389, Jan. 2020, doi: 10.1016/j.jallcom.2019.152389.
- [137] Z. Sun, E. Fabbri, L. Bi, and E. Traversa, 'Lowering grain boundary resistance of BaZr<sub>0.8</sub>Y<sub>0.2</sub>O<sub>3-δ</sub> with LiNO<sub>3</sub> sintering-aid improves proton conductivity for fuel cell operation', *Phys. Chem. Chem. Phys.*, vol. 13, no. 17, pp. 7692–7700, Apr. 2011, doi: 10.1039/C0CP01470B.

- [138] S. Wang, Y. Liu, J. He, F. Chen, and K. S. Brinkman, ‘Spark-plasma-sintered barium zirconate based proton conductors for solid oxide fuel cell and hydrogen separation applications’, *Int. J. Hydrog. Energy*, vol. 40, no. 16, pp. 5707–5714, May 2015, doi: 10.1016/j.ijhydene.2015.02.116.
- [139] V. L. Tassev and S. R. Vangala, ‘Thick Hydride Vapor Phase Heteroepitaxy: A Novel Approach to Growth of Nonlinear Optical Materials’, *Crystals*, vol. 9, no. 8, Art. no. 8, Aug. 2019, doi: 10.3390/cryst9080393.
- [140] G. Abadias and R. Daniel, ‘7 - Stress in physical vapor deposited thin films: Measurement methods and selected examples’, in *Handbook of Modern Coating Technologies*, M. Aliofkhaezai, N. Ali, M. Chipara, N. Bensaada Laidani, and J. Th. M. De Hosson, Eds., Amsterdam: Elsevier, 2021, pp. 359–436. doi: 10.1016/B978-0-444-63239-5.00008-1.
- [141] M. Ohring, *Materials Science of Thin Films: Deposition and Structure*. Elsevier, 2001.
- [142] A. Anders, ‘A structure zone diagram including plasma based deposition and ion etching’, Apr. 2010, Accessed: Aug. 02, 2022. [Online]. Available: <https://escholarship.org/uc/item/3261x4bm>
- [143] Z. Huang *et al.*, ‘Fast crystallization of amorphous  $Gd_2Zr_2O_7$  induced by thermally activated electron-beam irradiation’, *J. Appl. Phys.*, vol. 118, no. 21, Dec. 2015, doi: 10.1063/1.4936785.
- [144] N. Kaiser, ‘Review of the fundamentals of thin-film growth’, *Appl. Opt.*, vol. 41, no. 16, pp. 3053–3060, Jun. 2002, doi: 10.1364/ao.41.003053.
- [145] D. D. Hass, J. F. Groves, and H. N. G. Wadley, ‘Reactive vapor deposition of metal oxide coatings’, *Surf. Coat. Technol.*, vol. 146–147, pp. 85–93, Sep. 2001, doi: 10.1016/S0257-8972(01)01368-8.
- [146] J. T. Gudmundsson, A. Anders, and A. von Keudell, ‘Foundations of physical vapor deposition with plasma assistance’, *Plasma Sources Sci. Technol.*, vol. 31, no. 8, p. 083001, Sep. 2022, doi: 10.1088/1361-6595/ac7f53.
- [147] Y. H. Lee *et al.*, ‘Thin Film Solid Oxide Fuel Cells Operating Below 600°C: A Review’, *Int. J. Precis. Eng. Manuf.-Green Technol.*, vol. 5, no. 3, pp. 441–453, Jul. 2018, doi: 10.1007/s40684-018-0047-0.
- [148] A. M. Engwall, Z. Rao, and E. Chason, ‘Origins of residual stress in thin films: Interaction between microstructure and growth kinetics’, *Mater. Des.*, vol. 110, pp. 616–623, Nov. 2016, doi: 10.1016/j.matdes.2016.07.089.
- [149] M. A. P. Yazdi, P. Briois, and A. Billard, ‘Influence of the annealing conditions on the structure of  $BaCe_{1-x}Y_xO_{3-a}$  coatings elaborated by DC magnetron sputtering at room temperature’, *Mater. Chem. Phys.*, vol. 117, no. 1, pp. 178–182, Sep. 2009, doi: 10.1016/j.matchemphys.2009.05.032.
- [150] N. Kaiser, ‘Some Fundamentals of Optical Thin Film Growth’, in *Optical Interference Coatings*, N. Kaiser and H. K. Pulker, Eds., in Springer Series in Optical Sciences. Berlin, Heidelberg: Springer, 2003, pp. 59–80. doi: 10.1007/978-3-540-36386-6\_3.
- [151] Y. B. Kim, T. M. Gür, H.-J. Jung, S. Kang, R. Sinclair, and F. B. Prinz, ‘Effect of crystallinity on proton conductivity in yttrium-doped barium zirconate thin films’, *Solid State Ion.*, vol. 198, no. 1, pp. 39–46, Sep. 2011, doi: 10.1016/j.ssi.2011.07.004.
- [152] K. Bae, D. Y. Jang, H. J. Jung, J. W. Kim, J.-W. Son, and J. H. Shim, ‘Micro ceramic fuel cells with multilayered yttrium-doped barium cerate and zirconate thin film electrolytes’, *J. Power Sources*, vol. 248, pp. 1163–1169, Feb. 2014, doi: 10.1016/j.jpowsour.2013.10.057.
- [153] K. Bae *et al.*, ‘High-Performance Protonic Ceramic Fuel Cells with Thin-Film Yttrium-Doped Barium Cerate–Zirconate Electrolytes on Compositionally Gradient Anodes’, *ACS Appl. Mater. Interfaces*, vol. 8, no. 14, pp. 9097–9103, Apr. 2016, doi: 10.1021/acsami.6b00512.

- [154] R. A. Powell and S. M. Rossmagel, Eds., ‘Chapter 2 Physics of sputtering’, in *Thin Films*, in PVD for Microelectronics, vol. 26. Elsevier, 1999, pp. 23–49. doi: 10.1016/S1079-4050(99)80005-2.
- [155] S. Luo *et al.*, ‘Growth and microstructure of columnar Y-doped SrZrO<sub>3</sub> films deposited on Pt-coated MgO by pulsed laser deposition’, *J. Appl. Phys.*, vol. 118, no. 3, p. 035310, Jul. 2015, doi: 10.1063/1.4927158.
- [156] G. Koster, D. H. A. Blank, and G. A. J. H. M. Rijnders, ‘Oxygen in Complex Oxide Thin Films Grown by Pulsed Laser Deposition: a Perspective’, *J. Supercond. Nov. Magn.*, vol. 33, no. 1, pp. 205–212, Jan. 2020, doi: 10.1007/s10948-019-05276-5.
- [157] W. S. Choi, J. Yi, and B. Hong, ‘The effect of cerium doping in barium zirconate titanate thin films deposited by rf magnetron sputtering system’, *Mater. Sci. Eng. B*, vol. 109, no. 1, pp. 146–151, Jun. 2004, doi: 10.1016/j.mseb.2003.10.081.
- [158] S. Barison, L. Doubova, and A. Sanson, ‘RF sputtering deposition of BCZY proton conducting electrolytes’, presented at the Presented at 9th European Solid Oxide Fuel Cell Forum, 2010.
- [159] T. Sato, T. Inoue, D. Ichinose, H. Funakubo, and K. Uchiyama, ‘Fabrication of highly (110)-oriented BaCeO<sub>3</sub>-based proton-conductive oxide thin films by RF magnetron sputtering method’, *Jpn. J. Appl. Phys.*, vol. 55, no. 2S, p. 02BC19, Jan. 2016, doi: 10.7567/JJAP.55.02BC19.
- [160] L.-J. Wu, J.-M. Wu, H.-E. Huang, and H.-Y. Bor, ‘Electric tunable behavior of sputtered lead barium zirconate thin films’, *Appl. Phys. Lett.*, vol. 90, no. 7, p. 072901, Feb. 2007, doi: 10.1063/1.2472564.
- [161] Y. Li, P.-C. Su, L. M. Wong, and S. Wang, ‘Chemical stability study of nanoscale thin film yttria-doped barium cerate electrolyte for micro solid oxide fuel cells’, *J. Power Sources*, vol. 268, pp. 804–809, Dec. 2014, doi: 10.1016/j.jpowsour.2014.06.128.
- [162] N. Yang *et al.*, ‘Deposition and electrochemical characterization of Yttrium doped Barium cerate and zirconate heterostructures’, *Thin Solid Films*, vol. 562, pp. 264–268, Jul. 2014, doi: 10.1016/j.tsf.2014.04.073.
- [163] E. Fabbri *et al.*, ‘Design and fabrication of a chemically-stable proton conductor bilayer electrolyte for intermediate temperature solid oxide fuel cells (IT-SOFCs)’, *Energy Environ. Sci.*, vol. 1, no. 3, p. 355, 2008, doi: 10.1039/b806655h.
- [164] I. Chang, J. Y. Paek, and S. W. Cha, ‘Parametric study of Y-doped BaZrO<sub>3</sub> thin film deposited via pulsed laser deposition’, *J. Vac. Sci. Technol. A*, vol. 33, no. 2, p. 021515, Mar. 2015, doi: 10.1116/1.4905775.
- [165] J. Ding *et al.*, ‘Influence of Nonstoichiometry on Proton Conductivity in Thin-Film Yttrium-Doped Barium Zirconate’, *ACS Appl. Mater. Interfaces*, vol. 10, no. 5, pp. 4816–4823, Feb. 2018, doi: 10.1021/acsami.7b16900.
- [166] R. V. Chopdekar, E. Arenholz, and Y. Suzuki, ‘Orientation and thickness dependence of magnetization at the interfaces of highly spin-polarized manganite thin films’, *Phys. Rev. B*, vol. 79, no. 10, p. 104417, Mar. 2009, doi: 10.1103/PhysRevB.79.104417.
- [167] Y. Li, S. Wang, and P.-C. Su, ‘Proton-conducting Micro-solid Oxide Fuel Cells with Improved Cathode Reactions by a Nanoscale Thin Film Gadolinium-doped Ceria Interlayer’, *Sci. Rep.*, vol. 6, no. 1, Art. no. 1, Feb. 2016, doi: 10.1038/srep22369.
- [168] Y. Xiao, R. Waser, and T. Schneller, ‘Highly-oriented proton conducting BaZr<sub>0.9</sub>Y<sub>0.1</sub>O<sub>3-x</sub> ceramic thin films prepared by chemical solution deposition’, *J. Eur. Ceram. Soc.*, vol. 42, no. 7, pp. 3245–3253, Jul. 2022, doi: 10.1016/j.jeurceramsoc.2022.02.019.
- [169] D. Pergolesi, E. Fabbri, and E. Traversa, ‘Chemically stable anode-supported solid oxide fuel cells based on Y-doped barium zirconate thin films having improved performance’,

*Electrochem. Commun.*, vol. 12, no. 7, pp. 977–980, Jul. 2010, doi: 10.1016/j.elecom.2010.05.005.

[170] A. Fluri, C. W. Schneider, and D. Pergolesi, ‘5 - In situ stress measurements of metal oxide thin films’, in *Metal Oxide-Based Thin Film Structures*, N. Pryds and V. Esposito, Eds., in *Metal Oxides*. Elsevier, 2018, pp. 109–132. doi: 10.1016/B978-0-12-811166-6.00005-4.

[171] F. J. A. Loureiro *et al.*, ‘Proton conductivity in yttrium-doped barium cerate under nominally dry reducing conditions for application in chemical synthesis’, *J. Mater. Chem. A*, vol. 7, no. 30, pp. 18135–18142, Jul. 2019, doi: 10.1039/C9TA04584H.

[172] M. Li *et al.*, ‘Carbon-tolerant Ni-based cermet anodes modified by proton conducting yttrium- and ytterbium-doped barium cerates for direct methane solid oxide fuel cells’, *J. Mater. Chem. A*, vol. 3, no. 43, pp. 21609–21617, Oct. 2015, doi: 10.1039/C5TA06488K.

[173] J. H. Oh *et al.*, ‘Side reaction in the hydrogen and carbothermal reductions of BaO and BaCO<sub>3</sub>: The role of an infinitesimal amount of water’, *Curr. Appl. Phys.*, vol. 34, pp. 19–23, Feb. 2022, doi: 10.1016/j.cap.2021.10.008.

[174] R. Sažinas, C. Bernuy-López, M.-A. Einarsrud, and T. Grande, ‘Effect of CO<sub>2</sub> Exposure on the Chemical Stability and Mechanical Properties of BaZrO<sub>3</sub>-Ceramics’, *J. Am. Ceram. Soc.*, vol. 99, no. 11, pp. 3685–3695, 2016, doi: 10.1111/jace.14395.

[175] D. Han, K. Kishida, K. Shinoda, H. Inui, and T. Uda, ‘A comprehensive understanding of structure and site occupancy of Y in Y-doped BaZrO<sub>3</sub>’, *J. Mater. Chem. A*, vol. 1, no. 9, pp. 3027–3033, Feb. 2013, doi: 10.1039/C2TA00675H.

[176] D. Jennings, S. Ricote, J. Santiso, and I. Reimanis, ‘The formation of oriented barium carbonate from the decomposition of yttria-doped barium zirconate films’, *Scr. Mater.*, vol. 186, pp. 401–405, Sep. 2020, doi: 10.1016/j.scriptamat.2020.05.028.

[177] D. Ciria *et al.*, ‘Mechanical degradation under hydrogen of yttrium doped barium zirconate electrolyte material prepared with NiO additive’, *J. Power Sources*, vol. 321, pp. 226–232, Jul. 2016, doi: 10.1016/j.jpowsour.2016.05.001.

[178] A. Løken, S. Ricote, and S. Wachowski, ‘Thermal and Chemical Expansion in Proton Ceramic Electrolytes and Compatible Electrodes’, *Crystals*, vol. 8, no. 9, p. 365, Sep. 2018, doi: 10.3390/cryst8090365.

[179] F. Volmer *et al.*, ‘How to solve problems in micro- and nanofabrication caused by the emission of electrons and charged metal atoms during e-beam evaporation’, *J. Phys. Appl. Phys.*, vol. 54, no. 22, p. 225304, Jun. 2021, doi: 10.1088/1361-6463/abe89b.

[180] D. Chaleix, P. Choquet, A. Bessaudou, L. Frugier, and J. Machet, ‘A spatial distribution study of a beam vapour emitted by electron-beam-heated evaporation sources’, *J. Phys. Appl. Phys.*, vol. 29, no. 1, p. 218, Jan. 1996, doi: 10.1088/0022-3727/29/1/032.

[181] Yu. G. Yushkov, A. V. Tyunkov, E. M. Oks, and D. B. Zolotukhin, ‘Electron beam evaporation of boron at forevacuum pressures for plasma-assisted deposition of boron-containing coatings’, *J. Appl. Phys.*, vol. 120, no. 23, p. 233302, Dec. 2016, doi: 10.1063/1.4972268.

[182] E. Bakan, D. E. Mack, G. Mauer, R. Vaßen, J. Lamon, and N. P. Padture, ‘1 - High-temperature materials for power generation in gas turbines’, in *Advanced Ceramics for Energy Conversion and Storage*, O. Guillon, Ed., in Elsevier Series on Advanced Ceramic Materials. Elsevier, 2020, pp. 3–62. doi: 10.1016/B978-0-08-102726-4.00001-6.

[183] J. T. Gudmundsson, ‘Ionization mechanism in the high power impulse magnetron sputtering (HiPIMS) discharge’, *J. Phys. Conf. Ser.*, vol. 100, no. 8, p. 082013, Mar. 2008, doi: 10.1088/1742-6596/100/8/082013.

[184] U. Helmersson, M. Lattemann, J. Bohlmark, A. P. Ehiasarian, and J. T. Gudmundsson, ‘Ionized physical vapor deposition (IPVD): A review of technology and applications’, *Thin Solid Films*, vol. 513, no. 1, pp. 1–24, Aug. 2006, doi: 10.1016/j.tsf.2006.03.033.

- [185] B. Wu *et al.*, ‘Tailoring of titanium thin film properties in high power pulsed magnetron sputtering’, *Vacuum*, vol. 150, pp. 144–154, Apr. 2018, doi: 10.1016/j.vacuum.2018.01.039.
- [186] M. Ohring, ‘Chapter 10 - Characterization of Thin Films and Surfaces’, in *Materials Science of Thin Films (Second Edition)*, M. Ohring, Ed., San Diego: Academic Press, 2002, pp. 559–640. doi: 10.1016/B978-012524975-1/50013-6.
- [187] N. S. Murthy, ‘9 - Techniques for analyzing biomaterial surface structure, morphology and topography’, in *Surface Modification of Biomaterials*, R. Williams, Ed., in Woodhead Publishing Series in Biomaterials. Woodhead Publishing, 2011, pp. 232–255. doi: 10.1533/9780857090768.2.232.
- [188] R. S. Gedam, N. T. Kalyani, and S. J. Dhoble, ‘Chapter 1 - Energy materials: Fundamental physics and latest advances in relevant technology’, in *Energy Materials*, S. J. Dhoble, N. T. Kalyani, B. Vengadaesvaran, and A. Kariem Arof, Eds., Elsevier, 2021, pp. 3–26. doi: 10.1016/B978-0-12-823710-6.00010-8.
- [189] A. L. Bail, ‘Whole powder pattern decomposition methods and applications: A retrospection’, *Powder Diffr.*, vol. 20, no. 4, pp. 316–326, Dec. 2005, doi: 10.1154/1.2135315.
- [190] B. H. Toby, ‘R factors in Rietveld analysis: How good is good enough?’, *Powder Diffr.*, vol. 21, no. 1, pp. 67–70, Mar. 2006, doi: 10.1154/1.2179804.
- [191] L. Reimer, *Scanning Electron Microscopy: Physics of Image Formation and Microanalysis*. Springer, 2013.
- [192] S. Anand, M. Y. Toriyama, C. Wolverton, S. M. Haile, and G. J. Snyder, ‘A Convergent Understanding of Charged Defects’, *Acc. Mater. Res.*, vol. 3, no. 7, pp. 685–696, Jul. 2022, doi: 10.1021/accountsmr.2c00044.
- [193] B. A. Boukamp, ‘A Nonlinear Least Squares Fit procedure for analysis of immittance data of electrochemical systems’, *Solid State Ion.*, vol. 20, no. 1, pp. 31–44, Feb. 1986, doi: 10.1016/0167-2738(86)90031-7.
- [194] P. Braun, C. Uhlmann, A. Weber, H. Störmer, D. Gerthsen, and E. Ivers-Tiffée, ‘Separation of the bulk and grain boundary contributions to the total conductivity of solid lithium-ion conducting electrolytes’, *J. Electroceramics*, vol. 38, no. 2, pp. 157–167, Jun. 2017, doi: 10.1007/s10832-016-0061-y.
- [195] W. Choi, H.-C. Shin, J. M. Kim, J.-Y. Choi, and W.-S. Yoon, ‘Modeling and Applications of Electrochemical Impedance Spectroscopy (EIS) for Lithium-ion Batteries’, *J. Electrochem. Sci. Technol.*, vol. 11, no. 1, pp. 1–13, Jan. 2020, doi: 10.33961/jecst.2019.00528.
- [196] S. Wang, J. Zhang, O. Gharbi, V. Vivier, M. Gao, and M. E. Orazem, ‘Electrochemical impedance spectroscopy’, *Nat. Rev. Methods Primer*, vol. 1, no. 1, Art. no. 1, Jun. 2021, doi: 10.1038/s43586-021-00039-w.
- [197] J. T. S. Irvine, D. C. Sinclair, and A. R. West, ‘Electroceramics: Characterization by Impedance Spectroscopy’, *Adv. Mater.*, vol. 2, no. 3, pp. 132–138, 1990, doi: 10.1002/adma.19900020304.
- [198] A. Greco, E. Sgambitterra, and F. Furgiuele, ‘A new methodology for measuring residual stress using a modified Berkovich nano-indenter’, *Int. J. Mech. Sci.*, vol. 207, p. 106662, Oct. 2021, doi: 10.1016/j.ijmecsci.2021.106662.
- [199] T. Götsch, W. Wallisch, M. Stöger-Pollach, B. Klötzer, and S. Penner, ‘From zirconia to yttria: Sampling the YSZ phase diagram using sputter-deposited thin films’, *AIP Adv.*, vol. 6, no. 2, p. 025119, Feb. 2016, doi: 10.1063/1.4942818.
- [200] C. W. Schneider, M. Döbeli, C. Richter, and T. Lippert, ‘Oxygen diffusion in oxide thin films grown on SrTiO<sub>3</sub>’, *Phys. Rev. Mater.*, vol. 3, no. 12, p. 123401, Dec. 2019, doi: 10.1103/PhysRevMaterials.3.123401.

- [201] M. Sriubas, K. Pamakštys, and G. Laukaitis, 'Investigation of microstructure and electrical properties of Sm doped ceria thin films', *Solid State Ion.*, vol. 302, pp. 165–172, Apr. 2017, doi: 10.1016/j.ssi.2016.11.007.
- [202] W. Harbich, 'Collision of Clusters with Surfaces: Deposition, Surface Modification and Scattering', in *Metal Clusters at Surfaces: Structure, Quantum Properties, Physical Chemistry*, K.-H. Meiwes-Broer, Ed., in Springer Series in Cluster Physics. Berlin, Heidelberg: Springer, 2000, pp. 107–150. doi: 10.1007/978-3-642-57169-5\_4.
- [203] M. S. Jackson and L. Che-yu, 'Stress relaxation and hillock growth in thin films', *Acta Metall.*, vol. 30, no. 11, pp. 1993–2000, Nov. 1982, doi: 10.1016/0001-6160(82)90103-1.
- [204] V. Tvarozek, I. Novotny, P. Sutta, S. Flickyngerova, K. Schtereva, and E. Vavrinsky, 'Influence of sputtering parameters on crystalline structure of ZnO thin films', *Thin Solid Films*, vol. 515, no. 24, pp. 8756–8760, Oct. 2007, doi: 10.1016/j.tsf.2007.03.125.
- [205] D.-J. Xue *et al.*, 'Regulating strain in perovskite thin films through charge-transport layers', *Nat. Commun.*, vol. 11, no. 1, Art. no. 1, Mar. 2020, doi: 10.1038/s41467-020-15338-1.
- [206] S. Ricote, N. Bonanos, M. C. Marco de Lucas, and G. Caboche, 'Structural and conductivity study of the proton conductor  $\text{BaCe}_{(0.9-x)}\text{Zr}_x\text{Y}_{0.1}\text{O}_{(3-\delta)}$  at intermediate temperatures', *J. Power Sources*, vol. 193, no. 1, pp. 189–193, Aug. 2009, doi: 10.1016/j.jpowsour.2008.11.080.
- [207] D. Shima and S. M. Haile, 'The influence of cation non-stoichiometry on the properties of undoped and gadolinia-doped barium cerate', *Solid State Ion.*, vol. 97, no. 1, pp. 443–455, May 1997, doi: 10.1016/S0167-2738(97)00029-5.
- [208] S.-H. Yoon, C. A. Randall, and K.-H. Hur, 'Influence of Grain Size on Impedance Spectra and Resistance Degradation Behavior in Acceptor (Mg)-Doped  $\text{BaTiO}_3$  Ceramics', *J. Am. Ceram. Soc.*, vol. 92, no. 12, pp. 2944–2952, 2009, doi: 10.1111/j.1551-2916.2009.03305.x.
- [209] A. Beiranvand, E. Rivasto, H. Huhtinen, and P. Paturi, 'Strain-Induced Domain Structure and Its Impact on Magnetic and Transport Properties of  $\text{Gd}_{0.6}\text{Ca}_{0.4}\text{MnO}_3$  Thin Films', *ACS Omega*, vol. 6, no. 50, pp. 34572–34579, Dec. 2021, doi: 10.1021/acsomega.1c04904.
- [210] S. Fop *et al.*, 'High oxide ion and proton conductivity in a disordered hexagonal perovskite', *Nat. Mater.*, vol. 19, no. 7, Art. no. 7, Jul. 2020, doi: 10.1038/s41563-020-0629-4.
- [211] M. Coduri, M. Karlsson, and L. Malavasi, 'Structure–property correlation in oxide-ion and proton conductors for clean energy applications: recent experimental and computational advancements', *J. Mater. Chem. A*, vol. 10, no. 10, pp. 5082–5110, 2022, doi: 10.1039/D1TA10326A.
- [212] S. M. Haile, G. Staneff, and K. H. Ryu, 'Non-stoichiometry, grain boundary transport and chemical stability of proton conducting perovskites', *J. Mater. Sci.*, vol. 36, no. 5, pp. 1149–1160, Mar. 2001, doi: 10.1023/A:1004877708871.
- [213] M. Sriubas, D. Virbukas, N. Kainbayev, K. Bockute, and G. Laukaitis, 'Structural and Electrochemical Properties of Scandia Alumina Stabilized Zirconia Thin Films', *Coatings*, vol. 11, no. 7, Art. no. 7, Jul. 2021, doi: 10.3390/coatings11070800.
- [214] A. González-González, G. M. Alonzo-Medina, A. I. Oliva, C. Polop, J. L. Sacedón, and E. Vasco, 'Morphology evolution of thermally annealed polycrystalline thin films', *Phys. Rev. B*, vol. 84, no. 15, p. 155450, Oct. 2011, doi: 10.1103/PhysRevB.84.155450.
- [215] Y. Li, P.-C. Su, L. M. Wong, and S. Wang, 'Chemical stability study of nanoscale thin film yttria-doped barium cerate electrolyte for micro solid oxide fuel cells', *J. Power Sources*, vol. 268, pp. 804–809, Dec. 2014, doi: 10.1016/j.jpowsour.2014.06.128.
- [216] A. Gangulee, 'Strain-relaxation in thin films on substrates', *Acta Metall.*, vol. 22, no. 2, pp. 177–183, Feb. 1974, doi: 10.1016/0001-6160(74)90008-X.

- [217] D. Lee *et al.*, ‘Stretching Epitaxial  $\text{La}_{0.6}\text{Sr}_{0.4}\text{CoO}_{3-\delta}$  for Fast Oxygen Reduction’, *J. Phys. Chem. C*, vol. 121, no. 46, pp. 25651–25658, Nov. 2017, doi: 10.1021/acs.jpcc.7b06374.
- [218] M. A. Reddy and M. Fichtner, ‘20 - Ionic Conductivity of Nanocrystalline Metal Fluorides’, in *Photonic and Electronic Properties of Fluoride Materials*, A. Tressaud and K. Poeppelmeier, Eds., Boston: Elsevier, 2016, pp. 449–463. doi: 10.1016/B978-0-12-801639-8.00020-9.
- [219] P. P. Khirade, A. V. Raut, R. C. Alange, W. S. Barde, and A. R. Chavan, ‘Structural, electrical and dielectric investigations of cerium doped barium zirconate ( $\text{BaZrO}_3$ ) nanoceramics produced via green synthesis: Probable candidate for solid oxide fuel cells and microwave applications’, *Phys. B Condens. Matter*, vol. 613, p. 412948, Jul. 2021, doi: 10.1016/j.physb.2021.412948.
- [220] T. Prodromakis and C. Papavassiliou, ‘Engineering the Maxwell–Wagner polarization effect’, *Appl. Surf. Sci.*, vol. 255, no. 15, pp. 6989–6994, May 2009, doi: 10.1016/j.apsusc.2009.03.030.
- [221] N. Yang *et al.*, ‘Defective Interfaces in Yttrium-Doped Barium Zirconate Films and Consequences on Proton Conduction’, *Nano Lett.*, vol. 15, no. 4, pp. 2343–2349, Apr. 2015, doi: 10.1021/acs.nanolett.5b00698.
- [222] A. Subramaniyan, J. Tong, R. P. O’Hayre, and N. M. Sammes, ‘Sintering Studies on 20 mol% Yttrium-Doped Barium Cerate’, *J. Am. Ceram. Soc.*, vol. 94, no. 6, pp. 1800–1804, 2011, doi: 10.1111/j.1551-2916.2010.04303.x.
- [223] O. Kraft and H. Gao, ‘Measurement of Stresses in Thin Films and Their Relaxation’, in *Diffusion Processes in Advanced Technological Materials*, D. Gupta, Ed., Berlin, Heidelberg: Springer, 2005, pp. 365–404. doi: 10.1007/978-3-540-27470-4\_8.
- [224] L. S.-J. Peng, X. X. Xi, B. H. Moeckly, and S. P. Alpay, ‘Strain relaxation during in situ growth of  $\text{SrTiO}_3$  thin films’, *Appl. Phys. Lett.*, vol. 83, no. 22, pp. 4592–4594, Dec. 2003, doi: 10.1063/1.1631055.
- [225] F. Bechstedt, ‘Defects’, in *Principles of Surface Physics*, F. Bechstedt, Ed., in Advanced Texts in Physics. Berlin, Heidelberg: Springer, 2003, pp. 293–315. doi: 10.1007/978-3-642-55466-7\_7.
- [226] T. Sato, T. Inoue, D. Ichinose, H. Funakubo, and K. Uchiyama, ‘Fabrication of highly (110)-oriented  $\text{BaCeO}_3$ ’, *Jpn J Appl Phys*, vol. 55, no. 2, p. 02BC19, Jan. 2016, doi: 10.7567/JJAP.55.02BC19.
- [227] A. Yamaguchi, A. Hirohata, and B. J. H. Stadler, Eds., ‘Chapter 1 - Nano/micro-structured magnetism’, in *Nanomagnetic Materials*, in Micro and Nano Technologies. Elsevier, 2021, pp. 1–55. doi: 10.1016/B978-0-12-822349-9.00007-9.
- [228] A. Kerrigan *et al.*, ‘Nano-faceted stabilization of polar-oxide thin films: The case of  $\text{MgO}(111)$  and  $\text{NiO}(111)$  surfaces’, *Appl. Surf. Sci.*, vol. 596, p. 153490, Sep. 2022, doi: 10.1016/j.apsusc.2022.153490.
- [229] U. Smith, N. Kristensen, F. Ericson, and J. Schweitz, ‘Local stress relaxation phenomena in thin aluminum films’, *J. Vac. Sci. Technol. A*, vol. 9, no. 4, pp. 2527–2535, Jul. 1991, doi: 10.1116/1.577268.
- [230] Q. Hérault, I. Gozhyk, M. Balestrieri, H. Montigaud, S. Grachev, and R. Lazzari, ‘Kinetics and mechanisms of stress relaxation in sputtered silver thin films’, *Acta Mater.*, vol. 221, p. 117385, Dec. 2021, doi: 10.1016/j.actamat.2021.117385.
- [231] F. W. Dynys, M. H. Berger, and A. Sayir, ‘Laser processed protonic ceramics’, *J. Eur. Ceram. Soc.*, vol. 28, no. 12, pp. 2433–2440, Aug. 2008, doi: 10.1016/j.jeurceramsoc.2008.03.038.
- [232] D. E. Wolfe, J. Singh, R. A. Miller, J. I. Eldridge, and D.-M. Zhu, ‘Tailored microstructure of EB-PVD 8YSZ thermal barrier coatings with low thermal conductivity and

- high thermal reflectivity for turbine applications’, *Surf. Coat. Technol.*, vol. 190, no. 1, pp. 132–149, Jan. 2005, doi: 10.1016/j.surfcoat.2004.04.071.
- [233] S. Yazdani *et al.*, ‘Thermal transport in phase-stabilized lithium zirconate phosphates’, *Appl. Phys. Lett.*, vol. 117, no. 1, p. 011903, Jul. 2020, doi: 10.1063/5.0013716.
- [234] J. H. Lee, K. S. Hwang, and T. S. Kim, ‘The Microscopic Origin of Residual Stress for Flat Self-Actuating Piezoelectric Cantilevers’, *Nanoscale Res Lett*, vol. 6, no. 1, p. 55, Sep. 2010, doi: 10.1007/s11671-010-9810-z.
- [235] D. Pergolesi *et al.*, ‘High proton conduction in grain-boundary-free yttrium-doped barium zirconate films grown by pulsed laser deposition’, *Nat. Mater.*, vol. 9, no. 10, pp. 846–852, Oct. 2010, doi: 10.1038/nmat2837.
- [236] S. Ji, I. Chang, Y. H. Lee, M. H. Lee, and S. W. Cha, ‘Performance enhancement of thin-film ceramic electrolyte fuel cell using bi-layered yttrium-doped barium zirconate’, *Thin Solid Films*, vol. 539, pp. 117–121, Jul. 2013, doi: 10.1016/j.tsf.2013.05.063.
- [237] H. C. Ong and G. T. Du, ‘The evolution of defect emissions in oxygen-deficient and -surplus ZnO thin films: the implication of different growth modes’, *J. Cryst. Growth*, vol. 265, no. 3, pp. 471–475, May 2004, doi: 10.1016/j.jcrysgro.2004.02.010.
- [238] A. Uthayakumar, A. Pandiyan, and S. B. Krishna Moorthy, ‘Yttrium dependent space charge effect on modulating the conductivity of barium zirconate electrolyte for solid oxide fuel cell’, *Int. J. Hydrog. Energy*, vol. 43, no. 52, pp. 23488–23499, Dec. 2018, doi: 10.1016/j.ijhydene.2018.10.185.
- [239] C. H. Zhou *et al.*, ‘Oxidation Kinetics Researches under the Condition of Compressive Loading’, *IOP Conf. Ser. Mater. Sci. Eng.*, vol. 389, no. 1, p. 012017, Jul. 2018, doi: 10.1088/1757-899X/389/1/012017.
- [240] X. Chen, X. Pang, J. Meng, and H. Yang, ‘Thermal-induced blister cracking behavior of annealed sandwich-structured TiN/CrAlN films’, *Ceram. Int.*, vol. 44, no. 6, pp. 5874–5879, Apr. 2018, doi: 10.1016/j.ceramint.2017.12.014.
- [241] V. V. Uglov, G. Abadias, S. V. Zlotski, N. T. Kvasov, I. A. Saladukhin, and A. A. Malashevich, ‘Blister formation in ZrN/SiN multilayers after He irradiation’, *Surf. Coat. Technol.*, vol. 344, pp. 170–176, Jun. 2018, doi: 10.1016/j.surfcoat.2018.02.095.
- [242] D. Ciria, M. Jiménez-Melendo, V. Aubin, and G. Dezanneau, ‘High-temperature mechanical behavior of proton-conducting yttrium-doped barium zirconate perovskite’, *J. Eur. Ceram. Soc.*, vol. 41, no. 2, pp. 1374–1383, Feb. 2021, doi: 10.1016/j.jeurceramsoc.2020.09.069.

## 8. CURRICULUM VITAE

**Monica Susana Campos Covarrubias**

monica.campos@ktu.lt

### **Education**

2006–2012 Bachelor's degree in Industrial Chemistry in Faculty of Chemical Engineering, Merida, Yucatán, Mexico.

2014–2016 Double Master's degree in Science, University of Bordeaux and University of Augsburg for the program of Functionalized Advanced Materials and Engineering.

2018–2023 PhD in Physics in Kaunas University of Technology, Kaunas, Lithuania.

### **Professional experience**

2011 Internship in the laboratories in the Center of Research for Applied Chemistry (CIQA), Saltillo, Nuevo Leon, Mexico.

2012–2013 Technician at the Faculty of Chemical Engineering in the Laboratory of Chemistry of Materials. Merida, Yucatán, Mexico.

2013–2014 Technician in the company H<sub>2</sub>O for water quality control.

2016 Internship on the laboratory of Organic Polymeric Chemistry in the group of polymers for electronics. Bordeaux, France.

2019–2020 Internship at the Institute of Nanotechnology and Materials Engineering, Gdansk, Poland.

2018–2023 Lithuanian Energy Institute, Kaunas, Lithuania.

### **Research interests**

Material Science, Hybrid Materials, Ceramics, Thin Films, Physical Vapor Deposition, Electrochemistry.

## 9. LIST OF PUBLICATIONS AND SCIENTIFIC CONFERENCES

### Scientific papers directly related to the doctoral dissertation (peer-reviewed and indexed in Clarivate Analytics Wos)

[A1]. Monica Susana Campos Covarrubias, Sriubas Mantas, Kristina Bockute, Piotr Winiarz, Tadeusz Miruszewski, Wojciech Skubida, Daniel Jaworski, Michał Bartmański, Marek Szkodo, Maria Gazda and Giedrius Laukaitis. 2020. Properties of barium cerate thin films formed using e-beam deposition. *Crystals*, 10 (12:1152), 1–13. <https://doi.org/10.3390/cryst101211522>. Q2, IF 2.67.

[A2]. Piotr Winiarz, Monica Susana Campos Covarrubias, Mantas Sriubas, Kristina Bockute, Tadeusz Miruszewski, Wojciech Skubida, Daniel Jaworski, Giedrius Laukaitis and Maria Gazda. Properties of barium cerate-zirconate thin films. *Crystals*, 11 (8:1005). <https://doi.org/10.3390/cryst11081005>. Q2, IF 2.67.

[A3]. Monica Susana Campos Covarrubias, Mantas Sriubas, Kristina Bockute, Aurelija Poskaite, Rokas Vazgys, Maria Gazda and Giedrius Laukaitis. 2022. Properties on Yttrium-Doped/Undoped Barium Cerate and Barium Zirconate Thin Films Formed by E-Beam Vapor Deposition. *Applied Sciences*, 12 (13:6422). <https://doi.org/10.3390/app12136422>. Q2, IF. 2.838.

[A4]. Monica Susana Campos Covarrubias, Kristina Bockute, Mantas Sriubas, Kacper Dzierzgowski, Maria Gazda and Giedrius Laukaitis. Microstructure and electrical properties of barium cerate thin films. *J Mater Sci* (2023). (pp. 3909–3919) <https://doi.org/10.1007/s10853-023-08297-7>. Q1, IF. 4.682.

### Conferences directly related to the doctoral dissertation

1. Monica Susana Campos Covarrubias; Mantas Sriubas; Kristina Bockute; Aurelija Poskaite; Rokas Vazgys; Giedrius Laukaitis. 18th International conference of young scientist on energy and natural sciences issues, CYSENI 2022, May 22–24th. Virtual conference. Oral presentation.

2. Monica Susana Campos Covarrubias; Mantas Sriubas; Kristina Bočkutė; Giedrius Laukaitis. 5th International conference in applied sciences, April 24–28th, 2022, Palma de Mallorca, Spain. *Investigation of grain growth induced strains in BaCeO<sub>3</sub> films formed by e-beam vapor deposition*. P1.42. Poster presentation.

3. Monica Susana Campos Covarrubias; Mantas Sriubas; Kristina Bočkutė; Piotr Winiarz; Maria Gazda; Giedrius Laukaitis. 14th international symposium on systems with fast ionic transport (ISSFIT14), 7–9 July 2021, online. *Influence of dopants on the crystallinity and grain size in barium zirconate cerate thin films formed by e-beam vapor deposition*. Virtual conference. Poster presentation.

4. Monica Susana Campos Covarrubias; Mantas Sriubas; Kristina Bockute; Piotr Winiarz; Maria Gazda; Giedrius Laukaitis. *Influence of the formation parameters on the properties of yttrium-doped Barium zirconate thin films*. E-MRS Spring meeting 2021, May 31–June 4, virtual conference. Poster presentation.

5. Monica Susana Campos Covarrubias; Mantas Sriubas; Kristina Bockute; Piotr Winiarz; Maria Gazda; Giedrius Laukaitis. *Microstructure properties of formed doped barium cerate thin film formed on different alloy substrates. Functional materials and nanotechnologies: [13th international conference]*, FM&NT-2020:

virtual Vilnius, Lithuania, 23–26 November, 2020: abstract book / [organized by the ISSP of University of Latvia, University of Tartu and Vilnius University]. Virtual conference. Poster presentation.

6. Monica Susana Campos Covarrubias; Mantas Sriubas; Kristina Bockute; Zivile Rutkuniene; Piotr Winiarz; Maria Gazda; Giedrius Laukaitis. *Formation and investigation of barium cerate thin films = Plonasluoksnių 173 bario cerato dangų formavimas ir tyrimas*. 43-ioji Lietuvos nacionalinė fizikos konferencija, 2019 m. spalio 3–5 d., Kaunas: pranešimų medžiaga. Poster presentation.

7. Piotr Winiarz; Daniel Jaworski; Mirosław Sawczak; Monica Susana Campos Covarrubias; Mantas Sriubas; Kristina Bockute; Zivile Rutkuniene; Giedrius Laukaitis; Maria Gazda. Electrical properties and protonic conductivity in yttrium-doped barium cerate-zirconate strained thin films. 14th international symposium on systems with fast ionic transport (ISSFIT14), 7–9 July 2021. Virtual conference. Poster presentation.

8. Piotr Winiarz; Daniel Jaworski; Mirosław Sawczak; Monica Susana Campos Covarrubias; Mantas Sriubas; Kristina Bockute; Zivile Rutkuniene; Giedrius Laukaitis; Maria Gazda. Selected properties of thermally strained barium cerate – zirconate thin films. SSPC-20: Solid-state proton conductors September 27–August 1, 2021. Virtual conference. Poster presentation.

## 10. ACKNOWLEDGEMENTS

I am grateful to Prof. Dr. Giedrius Laukaitis for his patience, time and knowledge to guide me to be a better scientist. Moreover, I want to express my gratitude to Dr. Mantas Sriubas for his patience, time and help in the characterization of the films and Dr. Kristina Bockute for contributing to this research. The author of the dissertation thanks the group of hydrogen energy technologies of Lithuanian Energy Institute, especially Dr. Marius Urbanavičius, Dr. Šarūnas Varnagiris and Dr. Martynas Lelis, for their help in the use of facilities. I would like to thank the group of Prof. Dr. Maria Gazda from Gdansk, Poland, for collaboration and contribution to this research. I am thankful to Dr. Jurgita Laurikaitienė, Dr. Tomas Tamulevičius and Dr. Šarūnas Meškinis for their corrections and reviews in order to make this dissertation better. Finally, I thank the Lithuanian Research Council for the scholarship, which gave me the opportunity to contribute to the advancement of fuel cell technologies in Lithuania.

To my husband Andrius  
and my family in Mexico



UDK [539.216 + 661.844] (043.3)

SL 344. 2023-10-03, \* leidyb. apsk. I. Tiražas 14 egz. Užsakymas MI2040-523.  
Išleido Kauno technologijos universitetas, K. Donelaičio g. 73, 44249 Kaunas  
Spausdino leidyklos „Technologija“ spaustuvė, Studentų g. 54, 51424 Kaunas

